DYNAMICAL PROCESSES IN THE SOLAR ATMOSPHERE

P. J. Cargill

A Thesis Submitted for the Degree of PhD
at the
University of St Andrews

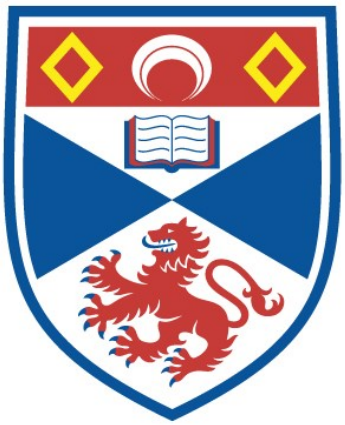

1982

DYNAMICAL PROCESSES IN THE SOLAR ATMOSPHERE

P. J. Cargill

Thesis submitted for the Degree of Doctor of Philosophy of the University of St. Andrews.

DYNAMICAL PROCESSES IN THE SOLAR ATMOSPHERE

Abstract

It has become clear that the closed-field regions of the solar atmosphere are not static (as was once thought) but that many types of steady and unsteady flows and other dynamical processes such as flares are continually occurring in them. This thesis investigates some theoretical aspects of these dynamical phenomena.

Steady, one-dimensional flow along a coronal loop is investigated first of all. Such a flow may be driven by a pressure difference between the footpoints, and a wide range of shocked and unshocked flows are found. The presence of steady flows removes the symmetry present in most static loop models, and these models are shown to form only one class of a much wider range of dynamic solutions to the equations of motion.

Thermal non-equilibrium in hot coronal loops occurs if the pressure in a loop becomes too big. The non-linear evolution of this non-equilibrium state is followed, and the loop is found to cool from of order 10^6 K to below 10^5 K in a few hours. An upflow is driven, and non-equilibrium is suggested as a means of formation of either cool loop cores or prominences.

Thermal non-equilibrium is also discussed as a possible mechanism for the simple-loop flare. It is suggested that a cool equilibrium at a temperature of a few times 10^4 K can flare to over 10^7 K if the mechanical heating in the cool loop becomes too large. The evolution is followed and the

loop is found to flare to over 10^7 K in approximately 5 minutes.

Magnetohydrodynamic shock waves have long been regarded as a potentially efficient heating mechanism. Their behaviour is re-examined here, and it is found that certain types of shock can release very large amounts of energy. These results are then applied to the heating of "post"-flare loops, for which temperatures of 10^7 K at the loop summit may be obtained.

Finally, some solutions of the magnetostatic equation are discussed, and it is pointed out that if the gas pressure is too big then magnetostatic equilibrium will break down. It is suggested that the subsequent evolution may give rise to a surge or other mass ejection.

CERTIFICATE

I certify that Peter J. Cargill has satisfied the conditions of the Ordinance and Regulations and is qualified to submit the accompanying application for the Degree of Doctor of Philosophy.

DECLARATION

I declare that the following thesis is a record of research work carried out by me, that the thesis is my own composition, and that it has not been previously presented in application for a higher degree.

(Peter John Cargill)

POSTGRADUATE CAREER

I was admitted into the University of St. Andrews as a research student under Ordinance General No. 12 in October 1978 to work on Dynamical Processes in the Solar Atmosphere under the supervision of Dr. E. R. Priest. I was admitted under the above resolution as a candidate for the degree of Ph.D. in October 1979.

ACKNOWLEDGEMENT

I would like to thank Dr.Eric Priest for his continual supervision, encouragement and enthusiasm during the past three years. I am also greatly indebted to Drs. Alan Hood and Bernard Roberts with whom much of the work in this thesis has been discussed. I am grateful to my colleagues in the Applied Mathematics Department, Drs. Terry Forbes, Iain Rae, Andrew Webb and Michael Kragg for helpful discussions, and I also wish to thank Dr. G. W. Pneuman for helpful correspondence.

I wish to thank the Science Research Council for financial support and also for providing funds to enable me to attend the Culham Plasma Physics summer school in July, 1979 and the NATO ASI at Bonas, France, August-September, 1980. Thanks is also due to the CNRS of France for funds toward my attendance of their workshop on Noise-storms in March, 1980 at Gordes.

Finally, I wish to thank Drs. T. Forbes, A. Hood and I.Rae for providing comments on the first draft of this thesis and Mrs. Baillie for typing it so promptly and efficiently.

CONTENTS

A note on Units

In general, we have used standard mks units throughout this thesis with the following exceptions.

(1) Lengths are sometimes referred to in megameters (Mm). $1 Mm = 10^6$ m.

(2) Magnetic fields are always referred to in Gauss. $1 G = 10^{-4}$ Tesla.

Chapter 1: INTRODUCTION

The recent Skylab and Solar Maximum Mission (S.M.M.)satellites have stressed that the solar atmosphere is not a quiet homogeneous structure but an active dynamic region containing many steady and unsteady flows. Observations have concentrated on coronal loops and solar flares, and it is the object of this thesis to examine the dynamic behaviour of such regions.

We begin by describing the basic equations in Section 1.1. Sections 1.2 - 1.4 then provide a review of coronal loop observations, flows in the transition zone and corona, and solar flares. Section 1.5 provides a very brief review of the aims of this thesis. However, in order to keep each chapter relatively self-contained, some of the observations outlined in this chapter are repeated in subsequent chapters and, where necessary, expanded.

1.1 The basic equations

The basic equations for the behaviour of an ionised gas (or plasma) are the kinetic equations (Boyd and Sanderson, 1969). They describe the particle distribution but, for most purposes, may be approximated by the fluid equations. This approximation holds provided the length-scales are much greater than the mean free path and the time-scales are much longer than the collision time. In this section, we state the equations of electromagnetism, fluid dynamics, and energy, and finally combine them to obtain the equations of magneto-hydrodynamics (referred to as M.H.D.).

1.1.1 Electromagnetic equations

In an inertial frame the equations of electromagnetism are Maxwell's equations:

$$\nabla \times \underline{E} = -\frac{\partial \underline{B}}{\partial t} \quad , \tag{1.1}$$

$$\nabla \times \underline{B} = \mu \underline{J} + \mu \varepsilon \frac{\partial \underline{E}}{\partial t} \quad , \tag{1.2}$$

$$\nabla . \underline{E} = \varrho_c / \varepsilon \quad , \tag{1.3}$$

$$\nabla . \underline{B} = 0 \quad , \tag{1.4}$$

where $\underline{E}$ is the electric field, $\underline{B}$ is the magnetic induction (generally referred to as the magnetic field), $\underline{J}$ is the electric current density and ϱ_c is the electric charge density. μ and ε are the magnetic permeability ($4\pi \times 10^{-7}$ H m^{-1}) and dielectric constant (8.85×10^{-12} F m^{-1}) in a vacuum.

These equations are supplemented by Ohm's law in the form

$$\underline{J} = \sigma (\underline{E} + \underline{v} \times \underline{B}) \quad , \tag{1.5}$$

where σ is the electrical conductivity and $\underline{v}$ is the plasma velocity. It is a greatly simplified version of the general Ohm's law (Boyd and Sanderson, equation 3.61).

1.1.2 Fluid equations

The fluid equations are the continuity equation

$$\frac{\partial \rho}{\partial t} + \nabla . (\rho \underline{v}) = 0 \quad , \tag{1.6}$$

and the momentum equation

$$\rho \left(\frac{\partial}{\partial t} + \underline{v} . \nabla \right) \underline{v} = - \nabla p + \rho \underline{g} + \underline{F} \quad , \tag{1.7}$$

where p is the gas pressure, ρ is the mass density and $\underline{F}$ is any general force acting on the plasma (e.g. viscosity or the Lorentz force). The force acting due to an electromagnetic field is

$$\underline{F} = \rho_c \underline{E} + \underline{J} \times \underline{B} \quad . \tag{1.8}$$

The pressure and density are related to the temperature, T, by the equation of state

$$p = \frac{R \rho T}{\tilde{\mu}} \quad ,$$

where R is the gas constant (8.26×10^3 J kg^{-1}K^{-1}) and $\tilde{\mu}$ is the mean molecular weight (taken as 0.5 for a fully ionised hydrogen plasma). It is often more convenient to work in terms of the number density, n, rather than the mass density ρ.

If a hydrogen plasma is fully ionised ($n_e \approx n_p$) then

$$\rho = n_p m_p + n_e m_e \quad ,$$

$$\approx n_p m_p \approx n_e m_H \quad ,$$

where m_H is the mass of a hydrogen atom. The equation of state is then

$$p = 2nk_BT, \tag{1.9}$$

where k_B ($= R/m_H$) is Boltzmann's constant (1.38×10^{-23} J K^{-1}). We shall generally drop the subscript 'e' in the density so that n will be assumed to mean the electron number density.

1.1.3 Magnetohydrodynamic equations

We now combine the equations stated in Section (1.1.1) and (1.1.2) to give the equations of M.H.D. The M.H.D. approximation holds if the characteristic speeds are non-relativistic. Then, comparing the terms on the right-hand side of (1.2) gives

$$\left|\frac{\mu \underline{J}}{\mu\varepsilon \partial \underline{E}/\partial t}\right| \approx \left|\frac{B/l}{vB/c^2\tau}\right| = \left|\frac{c^2}{v^2}\right| \gg 1 ,$$

provided $v \ll c$. In this expression, v is a typical velocity, l a typical length and τ a typical time. Equation (1.2) then reduces to

$$\nabla \times \underline{B} = \mu \underline{J} , \tag{1.10}$$

Similarly, (1.8) becomes

$$\underline{F} = \underline{J} \times \underline{B} = (\nabla \times \underline{B}) \times \frac{\underline{B}}{\mu} , \tag{1.11}$$

and the momentum equation is thus

$$m_H n \left(\frac{\partial}{\partial t} + \underline{v}.\nabla\right)\underline{v} = -\nabla p + m_H n \underline{g} + \underline{J} \times \underline{B} .$$

Taking the curl of Ohm's law (1.5) and using (1.10) and (1.1) gives

$$\frac{\partial \underline{B}}{\partial t} = \nabla \times (\underline{v} \times \underline{B}) - \nabla \times (\eta \nabla \times \underline{B}) , \qquad (1.12)$$

which is called the induction equation.

η is the magnetic diffusivity and is defined as

$$\eta = \frac{1}{\mu \sigma} .$$

If η is taken uniform, then equation (1.12) reduces to

$$\frac{\partial \underline{B}}{\partial t} = \nabla \times (\underline{v} \times \underline{B}) + \eta \nabla^2 \underline{B} . \qquad (1.13)$$

The ratio of the two terms on the right-hand side of (1.13) is known as the magnetic Reynolds number, R_m, defined as

$$R_m = \frac{v l}{\eta} .$$

If $R_m \gg 1$, then (1.13) simplifies to

$$\frac{\partial \underline{B}}{\partial t} = \nabla \times (\underline{v} \times \underline{B}) . \qquad (1.14)$$

In this case, the magnetic flux in a closed contour moving with the plasma is constant, which implies that the lines of magnetic force move with the plasma and are said to be frozen into the plasma. If $R_m \ll 1$, then (1.13) becomes

$$\frac{\partial \underline{B}}{\partial t} = \nabla^2 \underline{B} , \qquad (1.15)$$

the well-known diffusion equation. In this case, the field diffuses away on a timescale

$$\tau \sim l^2 / \eta .$$

1.1.4 The energy equation

The system of equations discussed in the previous three

sections is not closed unless the temperature is prescribed. In general, a further equation is then required which is the energy equation. In its simplest form it is

$$\frac{n^\gamma}{\gamma-1}\left(\frac{\partial}{\partial t}+\underline{v}.\nabla\right)\left(\frac{p}{n^\gamma}\right) = -L(n,T) , \qquad (1.16)$$

where $\gamma = c_p/c_v$, the ratio of the specific heats and L(n, T) represents the energy losses or gains. If L = 0 then (1.16) implies

$$p/n^\gamma = \text{const of motion}, \qquad (1.17)$$

the familiar adiabatic law.

We shall consider three terms in L, namely thermal conduction (which may be a gain or a loss), energy loss due to radiation and energy gain due to mechanical heating.

(a) Thermal conduction

The thermal conductive gain or loss is written as

$$L_{cond} = \nabla.(\underline{\underline{K}}\nabla T) ,$$

where $\underline{\underline{K}}$ is the conductivity tensor.

For present purposes, $\underline{\underline{K}}$ can be considered as having two components, one along the magnetic field ($K_{||}$) and one perpendicular to it ($K_\perp$), defined for sufficiently strong magnetic fields as

$$K_{||} = 1.95\times10^{-4}\frac{\xi\delta_T T^{5/2}}{Z\log\Lambda} \quad W\,m^{-1}\,K^{-1} , \qquad (1.18)$$

$$K_\perp = 3.54\times10^{-25}\frac{A_i^{1/2}Z^2 n_i^2 \log\Lambda}{T^{1/2}B^2} \quad W\,m^{-1}\,K^{-1} , \qquad (1.19)$$

Z is the particle charge, A_i the positive ion mass and $\log\Lambda$ is the coulomb logarithm which depends weakly on n and T. ξ and δ_T are both dependent on Z (Spitzer, 1962). For a

hydrogen plasma and typical coronal values of n and T,

$$\left.\begin{aligned} K_{\parallel} &= 10^{-11} T^{5/2} \ \mathrm{W\,m^{-1}\,K^{-1}}, \\ K_{\perp} &= \frac{2\times 10^{-31} n^2}{T^3 B^2} K_{\parallel} \ \mathrm{W\,m^{-1}\,K^{-1}}. \end{aligned}\right\} \qquad (1.20)$$

Priest (1978) has shown that, if l is a typical length across the field and L a length along the field, then

$$\frac{K_{\perp} L^2}{K_{\parallel} l^2} = \frac{2\times 10^{-31} n^2}{B^2 T^3} \left(\frac{L}{l}\right)^2 \ll 1 ,$$

if $L/l \approx 10$, $n \approx 10^{15}\ \mathrm{m^{-3}}$, $T \approx 10^6\ \mathrm{K}$ and $B \approx 10^{-2}\ \mathrm{T}$. Thus, conduction across a magnetic field is, for these parameters, negligible in the solar corona.

(b) Radiation

The optically thin radiative loss from a plasma is represented by (Summers and McWhirter, 1979)

$$\left.\begin{aligned} L_{rad} &= n_e n_H Q(T) \ \mathrm{W\,m^{-3}}, \\ \text{where} \quad Q(T) &= Q(H) + \sum_i \frac{n(X_i)}{n_H} Q(X_i) . \end{aligned}\right\} \qquad (1.21)$$

$Q(H)$ is the radiated loss from hydrogen and Q_i is that from element X_i. A large number of authors have calculated the loss function, their results being shown in Figure 1.1. However, the loss is generally approximated by a piecewise continuous function; that of Rosner et al. (1978) is given in Table 1.1.

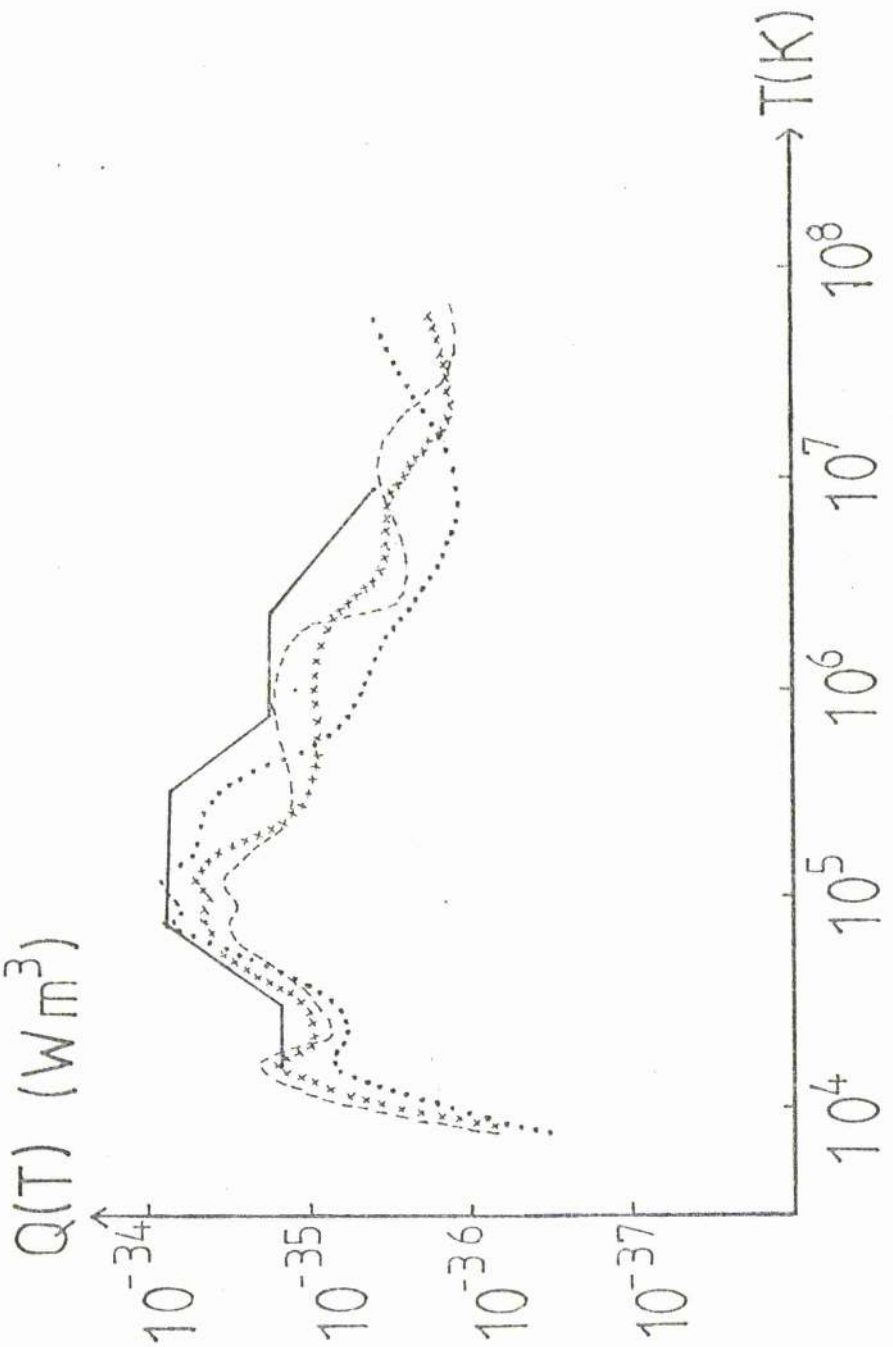

Figure 1.1 The optically thin radiative loss function as calculated by Cox and Tucker (1969) (·····), Raymond Cox and Smith (1976) (××××) and Summers and McWhirter (1979) (----). The approximation to these calculations used in thesis due to Rosner et al. (1978) is also shown (——).

Table 1.1

The values of χ and α in the optically thin radiative loss function $n^2 \chi T^{\alpha}$ as a function of temperature as calculated by Rosner et al. (1978).

Temperature Range	χ	α
$2 \times 10^4 K < T < 4 \times 10^4 K$	1.12×10^{-35}	0
$4 \times 10^4 K < T < 8 \times 10^4 K$	10^{-44}	2
$8 \times 10^4 K < T < 2.5 \times 10^5 K$	6.3×10^{-35}	0
$2.5 \times 10^5 K < T < 5.6 \times 10^5 K$	3.98×10^{-24}	-2
$5.6 \times 10^5 K < T < 2 \times 10^6 K$	1.15×10^{-35}	0
$2 \times 10^6 K < T < 10^7 K$	1.86×10^{-31}	$-2/3$

The function is defined as

$$Q(T) = \chi T^{\alpha} , \qquad (1.22)$$

where χ and α are given in Table 1. It should be noted that only 10% of this radiation comes from hydrogen, thus the accuracy of Q(T) depends on how well solar abundances are known. In fact, (1.22) is accurate to only a factor of 2 or 3.

(c) Mechanical heating

This term (denoted by E_H) represents all the heat sources in the energy equation. In the corona, the heating is thought to be due to both waves propagating upward from the photosphere and ohmic dissipation at a rate J^2/σ. However, the dependence of the heating function on the local parameters is not clear and so E_H is written as

$$E_H = H \rho^d T^e , \qquad (1.23)$$

where H, d and e are constants. In this thesis, two cases

of (1.23) are considered, namely heating constant per unit mass (d = 1, e = -1) and heating constant per unit volume (d = e = 0), so that

$$E_H = \frac{h\rho}{T} \quad , \tag{1.24a}$$

or

$$E_H = H \quad . \tag{1.24b}$$

Our energy equation is thus

$$\frac{n^\gamma}{\gamma-1}\left(\frac{\partial}{\partial t} + \underline{v}.\nabla\right)\left(\frac{p}{n^\gamma}\right) = -L_{rad} + E_H + L_{cond} \quad ,$$

and the closed set of equations is

$$m_H n\left(\frac{\partial}{\partial t} + \underline{v}.\nabla\right)\underline{v} = -\nabla p + m_H n \underline{g} + \underline{J} \times \underline{B} \quad , \tag{1.25}$$

$$\frac{\partial n}{\partial t} + \nabla.(n\underline{v}) = 0 \quad , \tag{1.26}$$

$$p = 2nk_B T \quad , \tag{1.27}$$

$$\nabla.\underline{B} = 0 \quad , \tag{1.28}$$

$$\frac{\partial \underline{B}}{\partial t} = \nabla \times (\underline{v} \times \underline{B}) + \eta \nabla^2 \underline{B} \quad , \tag{1.29}$$

$$\frac{n^\gamma}{\gamma-1}\left(\frac{\partial}{\partial t} + \underline{v}.\nabla\right)\left(\frac{p}{n^\gamma}\right) = -n^2 \Lambda T^\alpha + E_H \rho^\beta T^\varepsilon + \nabla.(\underline{\underline{k}}\nabla T) \quad , \tag{1.30}$$

where $\underline{E}$ and $\underline{J}$ are given by

$$\underline{E} = -\underline{v} \times \underline{B} + \underline{J}/\sigma \quad , \tag{1.31}$$

$$\underline{J} = \frac{\nabla \times \underline{B}}{\mu} \quad . \tag{1.32}$$

1.2 Observations of coronal loops

Since the launch of the Skylab satellite it has become apparent that, instead of being a static, plane-stratified atmosphere, the solar corona is a highly structured medium. It consists of open structures (coronal holes), which are the source of the solar wind, and closed structures, which are seen in E.U.V. and X-rays as loops. These loops typically have temperatures in excess of 10^6K, implying some form of energy deposition or heating to balance losses due to radiation and thermal conduction. We now outline their properties briefly and discuss in Section (1.3) the nature of steady and transient flows observed in loops and in the transition zone.

The most concise recent review of the properties of loops is given by Priest (1978) which we follow closely. He splits loops up into roughly five classifications, the properties of which are summarised in Table 1.2.

Table 1.2

Typical length (Mm), Temperature (K) and electron number density (m^{-3}) for different types of loops.

	Inter-connecting	Quiet Region	Active Region	"Post"-flare	Simple flare
L	20-700	20-700	10-100	10-100	5-50
T	$2\text{-}3\times10^6$	1.8×10^6	$10^4\text{-}25\times10^6$	$10^4\text{-}4\times10^6$	$\lesssim 4\times10^7$
n	7×10^{14}	$2\text{-}10\times10^{14}$	$.5\text{-}5\times10^{15}$	10^{17}	$\lesssim 10^{18}$

"Post"-flare and simple flare loops are discussed in Section 1.4.

Interconnecting loops link different active regions, are seen in E.U.V. (Sheeley et al., 1975) and X-Rays (Chase et al.,

1975, Svestka et al., 1977). They are rooted in regions of strong magnetic field at the edge of active regions and typically have a lifetime of a day, but a system of such loops may last for several solar rotations.

Quiet-region loops are similar to interconnecting loops except that they are somewhat cooler and do not connect active regions.

Active-region loops are somewhat more interesting than the previous ones: they have been studied extensively by Foukal (1975) using Skylab E.U.V. data. He finds cool loop cores ($T \lesssim 10^5$ K) nested inside regions at coronal temperatures. The density of such a cool core is approximately equal to that of the corona, and so the pressure in the core must be a tenth of the coronal pressure. Similar properties have been found by Jordan (1975) and discussed further by Foukal (1976).

1.3 Observations of steady and transient flows in the transition zone and corona

Since the advent of space telescopes, a large range of flows have been observed in the solar transition zone and corona. These and the older ground-based observations are now summarised.

1.3.1 Ground-based

(a) One of the earliest flows observed on the sun was the Evershed flow in sunspots. This is a two-way flow, being directed out of the sunspot at photosphere levels and into it at the chromosphere (e.g. Schröter (1967)). Outward Evershed flow starts at the edge of the photosphere umbra and moves radially through the penumbra at a few km s^{-1}. Maltby (1975) has described inward (chromospheric) Evershed flow along

superpenumbral fibrils that reach an altitude of 5Mm. The flow speed decreases abruptly in the penumbra to an undetectable value at a brightening. Speeds along superpenumbral fibrils can be as much as 25-50 km s^{-1} and the flow lifetime is between ½ hour and 2 hours. (See Haugen, 1967, Loughhead, 1966).

(b) Coronal rain is seen as cool downflowing material along strongly curved trajectories into active regions, velocities being typically 50-100 km s^{-1}. A good illustration is provided in Bruzek and Durrant (1977) on page 101. Foukal (1976) discusses coronal rain moving down both legs of a loop at speeds in excess of 45 km s^{-1} from a condensation near the loop summit.

(c) Somewhat more transient effects are due to surges. These are streams of plasma ejected upwards from the leading edge of an active region with speeds of typically 20-30 km s^{-1}, but sometimes as fast as 200 km s^{-1}. They follow curved paths and often return to the surface along the same path.

(d) Spicules are jets of gas ejected from the low chromosphere at the boundary of supergranular cells. Their speeds are typically 20-30 km s^{-1} and they attain a height of approximately 10Mm before returning to the surface.

1.3.2 Spacecraft observations

Persistent chromospheric and transition region flows lasting several hours have been observed on OSO-8, by Lites et al.(1976). They describe an upflow of 6-10 km s^{-1} at 50° to the vertical around a filament, downflows of 2-5 km s^{-1} over the network and downflows over a sunspot of 4-6 km s^{-1}

at 35^{o} to the normal. Bruner et al. (1976) observed these transient downflows at five minute intervals; they may well be coronal rain falling through the field of view with a velocity of 30 km s^{-1}. More transient phenomenon include small-scale downward flows over sunspots of up to 150 km s^{-1}, micro-surges over a plage of 30 km s^{-1} (both upward and downward) and explosions with upward or downward motions of 100 km s^{-1}. (See Priest (1981b) for more details).

Flows in the upper transition zone and corona are somewhat harder to detect and X-Ray observations of coronal loops have not yet identified flows but recent eclipse results (Livingston and Harvey, 1981) have suggested that steady flows occur in coronal loops, the velocities lying between 3 and 15 km s^{-1}. However, Levine and Withbroe (1977) witnessed the rapid evacuation of a coronal loop in which large downflows were observed: the (possibly) "post"-flare nature of this event makes interpretation difficult. Flare-related flows are discussed in Section 1.4.

We are only starting to become aware of the highly dynamic nature of the upper solar atmosphere, and future observations, in particular from the S.M.M., should provide a vast new range of data.

1.4 Solar flare observations

In this section, we aim to give a general review of solar flare observations: more detailed analyses are given in the relevant chapters. Good reviews of observations are given by Svestka (1976) and Brown et al. (1981), and recent theory is summarised in Priest (1981a) and Spicer and Brown (1981).

A solar flare is often crudely defined as a brightening on the Sun but this is a simplistic viewpoint. More explicitly flares can be classified into two main types:

(a) simple-loop (or compact) flares,

(b) two-ribbon flares.

and we discuss these separately.

1.4.1 Two-ribbon flares

The large, two-ribbon flare occurs when an active-region filament, often lying along the polarity inversion line, erupts and two bright bands of H_α emission move out from the filament site. The H_α ribbons are joined by loops - called "post"-flare loops - whose properties were stated in Table 1.2. In fact, the words "post"-flare are a misnomer, since energy release probably continues throughout the main phase.

Svestka (1976) lists many observations of flares and states 37 properties that flares generally appear to possess. Clearly, any single flare theory cannot explain all of these and in this thesis we shall not be concerned with a considerable number of them - such as those concerned with particle behaviour.

Priest (1976) has given a representation of the flare intensity in various wavelengths and we reproduce this in Figure 1.2. The flare is typically split into 4 regions:- preflare, impulsive, flash and main phases. During the preflare phase (typically 1-10 minutes) an increase in intensity in X-ray and E.U.V. emission is seen. The flare itself begins in two stages: the flash phase and the impulsive phase. The flash phase lasts approximately five minutes: during this time, the intensity and flare area increase rapidly. During this phase, some flares also exhibit an impulsive phase,

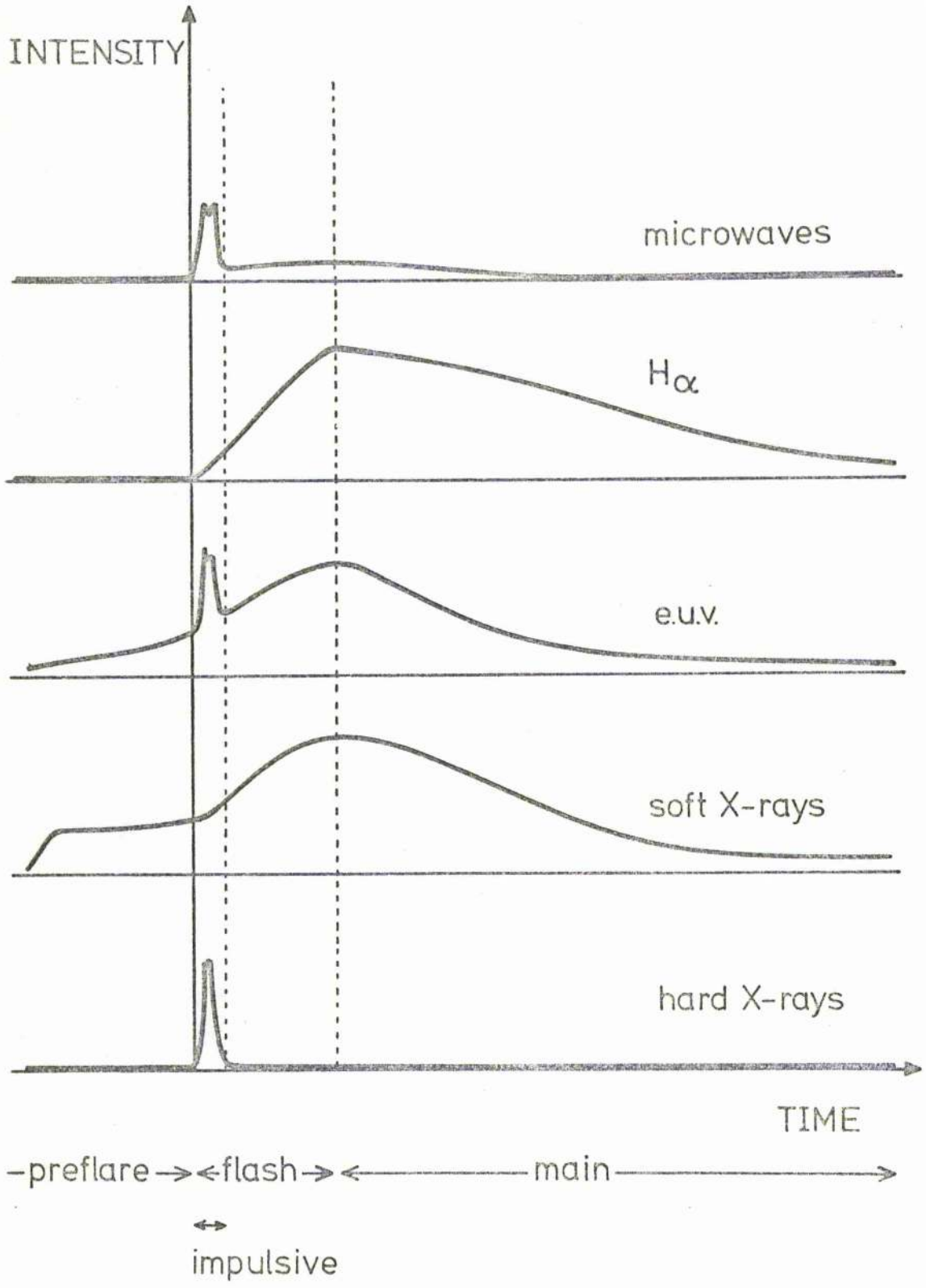

Figure 1.2 A schematic representation of the flare intensity in several wavelengths. Typical time-scales for the various phases are: preflare - ten minutes; impulsive - 1 minute; flash - five minutes; main phase - 1 hour. (From Priest, 1976).

characterised by hard X-ray bursts and microwave emission. The main phase follows the flash phase; during it the intensity decreases, typically in about 1 hour.

We now summarise the basic observations of magnetic field, temperature and density as listed by Svestka (1976).

(a) A bipolar field is a necessary condition for flare occurrence.

(b) The response of the corona to an emerging bipolar field is heating above the emerging flux. This gives rise to an X-Ray bright point.

(c) Flares tend to occur when an active region approaches maximum development.

(d) The biggest flares occur in regions where the original bipolar structure has become magnetically complex.

(e) The initial flare brightenings in the chromosphere occur near the zero line of longitudinal magnetic field.

(f) In big flares, the bright patches merge and form regular chromospheric ribbons. (So-called two-ribbon flares).

(g) The quiescent filament often disappears and the chromospheric ribbons form along both sides of its site.

(h) These ribbons travel outwards at velocities between 1 and 10 km s^{-1}.

(i) The ribbons mark the footpoints of coronal loops ("post"-flare loops).

(j) Changing magnetic fields are characteristic of active regions giving rise to flares.

(k) Flares tend to occur when new flux emerges inside active regions.

(l) After the flare, the magnetic structure is somewhat simplified.

(m) In the preflare phase, the quiescent filament is activated minutes or tens of minutes before the flare occurs. This can be interpreted as a change in the field before the flare onset, and this change is of a non-eruptive nature.

(n) Pre-flare heating (seen in soft X-rays) is evident ten minutes before the flare.

(o) The earliest manifestation of the flare is an increase in soft X-ray and E.U.V. emission reflecting a heating in the transition zone or corona.

(p) The sequence of maxima during a flare is :

(1) maximum in coronal temperature;

(2) maximum in H_α light;

(3) maximum in emission measure.

(q) The maximum temperature deduced from soft X-rays is $1 - 4 \times 10^7$ K with a mean electron density of 3×10^{16} m^{-3}.

(r) The electron density in the chromosphere during a flare is 10^{19} m^{-3}, but it can be as high as 4×10^{19} m^{-3}.

(s) The density of hydrogen in a chromospheric flare is 10^{20} m^{-3}.

(t) The density decreases with height: it is 10^{18} m^{-3} just above the chromosphere, and 10^{16} m^{-3} at a height of 20,000 km above the chromospheric base.

(u) The density is two orders of magnitude higher than in the quiet sun.

The total energy released in a flare is of order 10^{22} J for a small flare and up to 3×10^{25} J for a large event. Priest (1976) has estimated the various contributions for a large flare as

Electromagnetic radiation up to X-rays	10^{25} J
Interplanetary blast wave	10^{25} J
Hard X-rays (fast particles)	5×10^{24} J
Subrelativistic nuclei	2×10^{24} J
Relativistic nuclei	3×10^{24} J
Total energy output	3×10^{25} J.

Brown (1975) has estimated that hard X-rays may contribute up to 2×10^{25} J. This energy release is equivalent to annihalating a magnetic field of 500 Gauss in a cube of side 3×10^{7} m.

1.4.2 Simple-loop (compact) flares

One outstanding result of the Skylab observations was the realisation that the compact flare occurred in a magnetic loop or arch (Cheng and Widing, 1975). The structure of this loop does not appear to change much during the flare and it has a typical height of a few Mm.

During the flare, the temperature in the loop rises to over 2×10^{7} K and the density (deduced from the emission measure) reaches values of over 10^{17} m^{-3}. There is a time-lag of about five minutes between the temperature and density maxima. An extensive analysis of such flares by Moore and Datlowe (1975) showed that the X-ray emitting region had a temperature of between 1.1×10^{7} K and 1.8×10^{7} K, it was visible for between 3 and 40 minutes and was approximately 10 - 80 Mm long. A similar analysis by Milkey et al. (1971) gave maximum temperatures in the range 2.5 - 3.5 x 10^{7} K, and oscillations in the temperature appeared in the cooling of the X-ray plasma (presumably due to radiative and conductive effects).

Cheng and Widing (1975) also observed some evidence of

so-called 'Thermal Flares'. These are flares which, in the words of Cheng and Widing "no obvious evidence of violent dynamical processes or particle acceleration" was found. They comment that such a flare must possess an instability which results in heating only.

More recent observations by Lites et al. (1981) have detected downflows of order 80 km s^{-1} in the transition zone and Cheng et al. (1981) have suggested that such flows are driven by a pressure gradient between loop summit and base.

1.5 Aims of this thesis

In this chapter, a brief review of the M.H.D. equations and observations of coronal loops and solar flares has been presented. Observations of steady and transient flows in the transition zone and corona have also been discussed, and the dynamic nature of the solar corona is stressed throughout this thesis.

Chapter 2 presents a review of the behaviour of shock-waves, which are of importance later in the thesis. The properties of M.H.D. shocks whose incident flow and field are non-aligned is reinvestigated, and it is found that substantial extra energy release is allowed if the input parameters take on certain values.

Chapters 3, 4 and 5 are concerned with the behaviour of steady and unsteady flows in coronal loops. A general theory of steady-state siphon flows is developed in Chapters 3 and 4. In Chapter 3, an adiabatic energy equation is employed, and the general characteristics of the flow are investigated, whereas Chapter 4 extends the analysis to

include a full energy equation. The effects of different boundary conditions and loop geometries are investigated, and the non-existence of solutions in certain cases is briefly discussed.

Chapter 5 investigates the non-linear evolution of thermal non-equilibrium in a coronal loop, which may occur if the loop pressure is too large. It is suggested that this could account for the formation of the observed cool loop cores.

Chapters 6 and 7 are concerned with the solar flare problem. In Chapter 6, we suggest that the simple-loop flare is due to thermal non-equilibrium in a cool coronal loop or filament, and carry out a simple non-linear calculation to demonstrate this suggestion's viability.

Chapter 7 discusses the heating of "post"-flare loops in the context of the Kopp-Pneuman (1976) model for their formation. The results of Chapter 2 are used to propose a simple slow-shock heating model. An incompressible global reconnection model is also discussed.

Chapter 8 discusses magnetostatic equilibrium in coronal structures and suggests that its breakdown could be responsible for surges and explosive flares.

Chapter 2: SHOCK WAVES

2.1 Introduction

In this thesis, shock waves will occur in several problems, and so it is convenient to summarise their behaviour here and also to present some results in a new light. In an ordinary gas, a disturbance will propagate at the sound speed, c_s (where $c_s^2 = 2\gamma k_B T/m_H$); these sound waves may be described by linear theory, but when a wave possesses a finite amplitude, it steepens due to the effect of the non-linear terms. Eventually, the crest catches up with the trough and there then exists a region of large velocity, density and pressure gradients in which dissipative terms in the momentum and energy equations become important. This is known as a shock wave. It travels in excess of the local sound speed, so information cannot propagate ahead to indicate its arrival. The gas is decelerated and also compressed and heated (by viscous dissipation) as it passes through a shock.

If the gas is electrically conducting, then the presence of a magnetic field may be important. It is then necessary to add terms to the momentum and energy equations representing a Lorentz force and Poynting vector flux. The ideal time-dependent equations are then,

$$\frac{\partial \rho}{\partial t} + \nabla \cdot (\rho \underline{v}) = 0, \tag{2.1}$$

$$\rho \left(\frac{\partial}{\partial t} + \underline{v} \cdot \nabla \right) \underline{v} = -\nabla p + \frac{(\nabla \times \underline{B}) \times \underline{B}}{\mu}, \tag{2.2}$$

$$\underline{E} = -\underline{v} \times \underline{B} \quad , \tag{2.3}$$

$$\nabla . \underline{B} = 0 \quad , \tag{2.4}$$

$$\left(\frac{\partial}{\partial t} + \underline{v} . \nabla \right) \left(\frac{p}{\rho^{\gamma}} \right) = 0 \quad . \tag{2.5}$$

Linearising these equations for disturbances about a uniform plasma and magnetic field, perturbed quantities may be Fourier analysed as

$$e^{i(\omega t + \underline{k} . \underline{r})} \quad ,$$

and three types of wave result (e.g. Parker, 1979, Priest, 1982) which have dimensionless phase velocities

$$V_p^2 = \frac{1}{2} \left[\frac{c_s^2}{v_A^2} + 1 \pm \left\{ \left(\frac{c_s^2}{v_A^2} - 1 \right)^2 + 4 \frac{c_s^2}{v_A^2} \sin^2 \theta \right\}^{1/2} \right] \quad , \tag{2.6}$$

$$V_p^2 = \cos^2 \theta \quad , \tag{2.7}$$

where

$$V_p^2 = \frac{\omega^2}{k^2 v_A^2} \quad ,$$

$$\underline{k} . \underline{B}_0 = k B_0 \cos \theta \quad ,$$

k is the wavenumber, ω is the circular wave frequency and v_A is the Alfvén speed defined as

$$V_A = \frac{B_0}{(\mu \rho_0)^{1/2}} \quad .$$

The positive root gives the fast magnetoacoustic wave, the negative root the slow magnetoacoustic wave; and (2.7) represents the Alfvén wave.

Only the fast and slow magnetoacoustic waves can steepen to form shocks; the Alfven wave can propagate without steepening (e.g. Priest, 1982).

An important parameter in equation (2.2) is the plasma beta, defined as the ratio of gas (p) to magnetic pressure ($B^2/2\mu$),

$$\beta = \frac{2\mu p}{B^2} = \frac{2}{\gamma}\frac{c_s^2}{v_A^2} .$$

In terms of β, equation (2.6) is

$$\omega^2 = \frac{k^2 v_A^2}{2}\left[\frac{\gamma\beta}{2} + 1 \pm \left\{\left(\frac{\gamma\beta}{2} - 1\right)^2 + 2\gamma\beta\sin^2\theta\right\}^{1/2}\right] . \qquad (2.8)$$

If $\beta \ll 1$, the fast and slow magnetoacoustic waves become

$$\begin{aligned} \omega^2 &= k^2 v_A^2 , \quad \text{(fast)} \\ \omega^2 &= k^2 c_s^2 \cos^2\theta . \quad \text{(slow)} \end{aligned} \qquad (2.9)$$

Hence, the slow magnetoacoustic wave can propagate very slowly at almost 90° to the field, but never exactly perpendicular to it.

If $\beta \gg 1$, then the fast and slow modes are

$$\begin{aligned} \omega^2 &= k^2 c_s^2 , \quad \text{(fast)} \\ \omega^2 &= k^2 v_A^2 \cos^2\theta \quad \text{(slow)} . \end{aligned} \qquad (2.10)$$

2.2 Gas dynamic shocks

The simplest type of shock-wave is the plane gas shock, the theory of which has been understood for over a century. If we assume that variables change in the direction normal to the shock only, equation (2.2) is

$$m_H n \frac{\partial v}{\partial t} + m_H n v \frac{\partial v}{\partial s} = -\frac{\partial p}{\partial s} , \qquad (2.11)$$

where s is the coordinate normal to the shock.

Integrating from $s=-\varepsilon$ to $s=+\varepsilon$ and letting $\varepsilon \to 0$ gives

$$\int_{-\varepsilon}^{\varepsilon} \left(n m_H \frac{\partial v}{\partial t} + n m_H v \frac{\partial v}{\partial s} + \frac{\partial p}{\partial s} \right) ds =$$

$$= \int_{-\varepsilon}^{\varepsilon} n m_H \frac{\partial v}{\partial t} ds + \left[n m_H v^2 + p \right]_{-\varepsilon}^{+\varepsilon} =$$

$$= \left[n m_H v^2 + p \right]_1^2 = 0 \quad , \qquad (2.12)$$

where the integral of any quantity <u>without</u> a spatial derivative is identically zero.

Similarly equations (2.1) and (2.5) become

$$\left[nv \right]_1^2 = 0 \quad , \qquad (2.13)$$

and

$$\left[m_H n v \left(\frac{1}{2} v^2 + \frac{\gamma p}{\gamma - 1 \, n m_H} \right) \right]_1^2 = 0 \, , \qquad (2.14)$$

where

$$\left[f \right]_1^2 = f(2) - f(1) \, ,$$

and '1' denotes an unshocked quantity, '2' a shocked one. Equations (2.12) - (2.14) are known as the <u>Rankine - Hugeniot jump relations</u>, and they represent the conservation of momentum, mass and energy across the shock. Inside the shock, the dissipative terms neglected in (2.1) - (2.5) such as viscosity and thermal conduction are dominant: a complicated analysis is then needed to determine the shock structure (See Curle, 1971, p.81-85).

Equations (2.12) - (2.14) may be combined with the equation of state to give the following expressions for the density, pressure and temperature ratios across the shock:

$$\frac{\rho_2}{\rho_1} = \frac{v_1}{v_2} = \frac{(\gamma+1)M_1^2}{2+(\gamma-1)M_1^2} \quad , \tag{2.15}$$

$$\frac{p_2}{p_1} = \frac{2\gamma M_1^2 - (\gamma-1)}{(\gamma+1)} \quad , \tag{2.16}$$

$$\frac{T_2}{T_1} = \frac{(2\gamma M_1^2 - (\gamma-1))(2+(\gamma-1)M_1^2)}{(\gamma+1)^2 M_1^2} \quad , \tag{2.17}$$

where

$$M_1 = \frac{v_1}{c_{s_1}} \quad ,$$

is the incident Mach number.

(2.15) - (2.17) are supplemented by the constraint that the entropy, defined as

$$S = c_v \log\left(\frac{p}{\rho^\gamma}\right) + \text{const.} \quad , \tag{2.18}$$

must never decrease.

The change in entropy across a shock is

$$\Delta S = S_2 - S_1 = c_v \log\left[\frac{p_2}{\rho_2^\gamma}\frac{\rho_1^\gamma}{p_1}\right] \quad , \tag{2.19}$$

and differentiating gives

$$\frac{d(\Delta S)}{dM_1^2} = \frac{2c_v(\gamma-1)(M_1^2-1)^2}{M_1^2(2\gamma M_1^2-(\gamma-1))(2+(\gamma-1)M_1^2)} \quad ,$$

which is positive provided $M_1^2 > 1$. Equations (2.15) - (2.17) then imply that density, pressure and temperature all increase across the shock.

The maximum density jump possible ($M_1 \to \infty$) is given by

$$\left(\frac{\rho_2}{\rho_1}\right)_{max} = \frac{(\gamma+1)}{(\gamma-1)} \quad ,$$

which is approximately 4 for a monatomic gas. The jumps in pressure and temperature for strong shocks are directly proportional to M_1^2.

Finally, it is worth noting that for oblique shocks, results (2.15) - (2.17) are modified by replacing M_1^2 by $M_1^2 \cos^2\delta_1$ where δ_1 is the angle of incidence of the flow to the shock normal. The flow is deflected away from the normal on passage through the shock.

2.3 M.H.D. Shocks

In Section 2.1, it was shown that the characteristic velocity of propagation in a gas, c_s, is modified by the presence of a magnetic field and so the behaviour of shocks will likewise change. Magnetohydrodynamic (M.H.D.) shocks are of great relevence in astrophysics, particularly in certain aspects of solar flare theory. Shock waves in general heat a plasma and certain classes of M.H.D. shocks are extremely efficient at doing this. They are of importance to the problem of steady reconnection by the Petschek (1964) mechanism and are responsible for most of the plasma heating in that theory. The compressible Petschek mechanism has only recently become well understood (Soward and Priest, 1982), and the results of this section are of some relevance to their calculations.

We do not intend to develop the theory of M.H.D. shocks along the well-trodden path of assuming that the incident flow and field are aligned (Bazer and Ericson, 1959, Jeffrey and Taniuti, 1964), but instead we set up and solve the full, non-aligned, jump relations. To the author's knowledge, this has only been attempted by Lynn (1966) who solved the equations in terms of the flow deflection angle. On the other hand, we intend to solve the equations as a function of the input parameters, giving a clearer understanding of how external conditions affect the properties of the shock and the energy

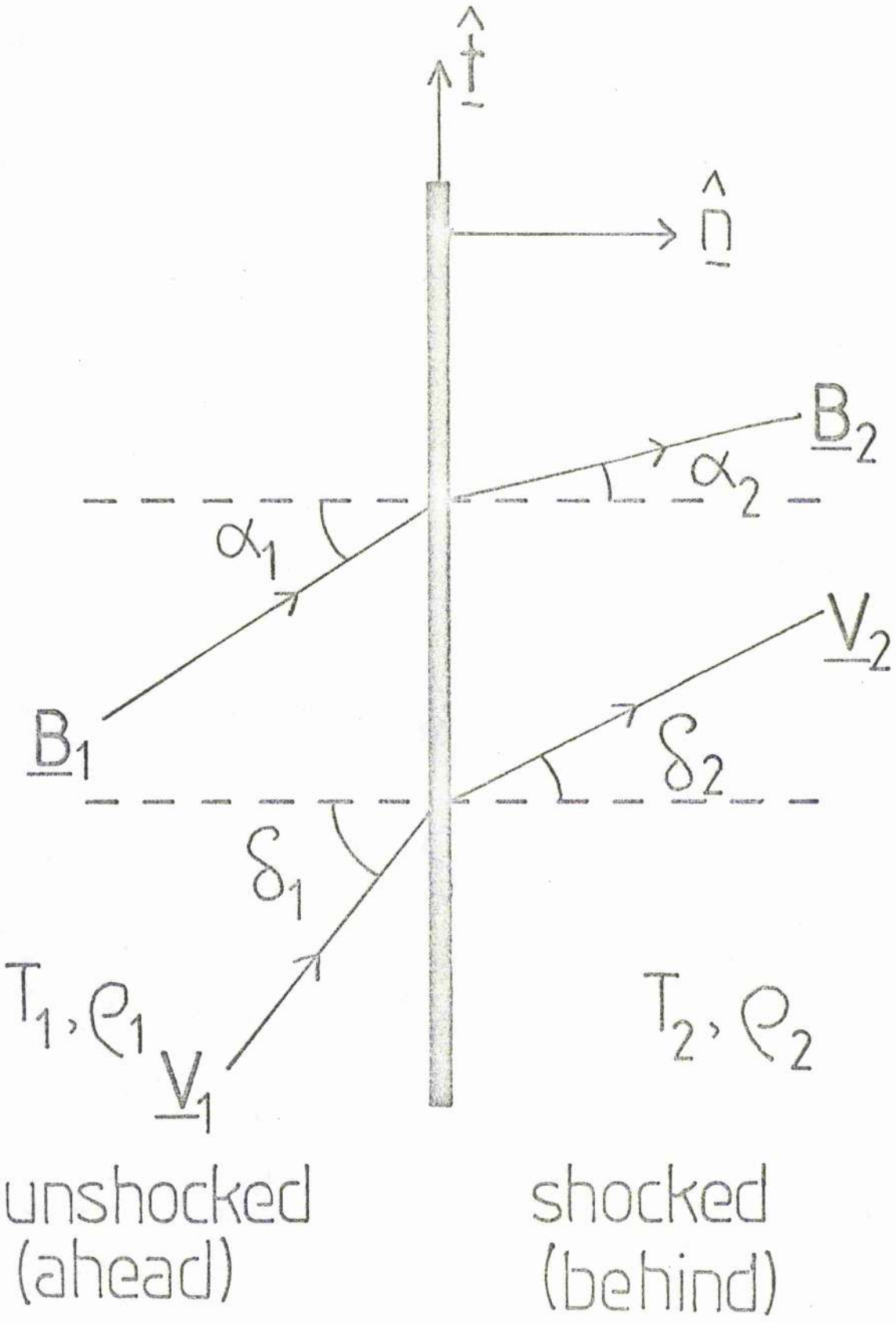

Figure 2.1 The notation across a slow M.H.D. shock. Incident and shocked quantities are denoted by subscripts 1 and 2 respectively.

release generated by it.

We consider a straight, oblique shock with the incident flow and field aligned at angles of δ_1 and α_1 to the normal, respectively, (Figure 2.1) and integrate the dissipationless equations across a thin layer as outlined in Section 2.2. The conservation of normal magnetic field component, mass flux, normal and tangential components of momentum, energy and tangential electric field are required, and in differential form they may be written

$$\frac{d}{ds} B_n = 0 , \tag{2.20}$$

$$\frac{d}{ds} (m_H n v_n) = 0 , \tag{2.21}$$

$$m_H n v_n \frac{dv_n}{ds} + \frac{dp}{ds} + \frac{d}{ds}\left(\frac{B_t^2}{2\mu}\right) = 0 , \tag{2.22}$$

$$m_H n v_n \frac{dv_t}{ds} - B_n \frac{dB_t}{ds} = 0 , \tag{2.23}$$

$$\frac{d}{ds}\left[m_H n v_n \left(\frac{1}{2}v^2 + \frac{\gamma}{\gamma-1}\frac{p}{m_H n}\right)\right] + v_n B_t \frac{dB_t}{ds} - v_t B_n \frac{dB_t}{ds} = 0 , \tag{2.24}$$

$$\oint \underline{E} \cdot \underline{dl} = 0 , \tag{2.25}$$

where subscripts n and t denote normal and tangential components, respectively.

The jump relations are then

$$[B_n]_1^2 = 0 , \tag{2.26}$$

$$[m_H n v]_1^2 = 0 , \tag{2.27}$$

$$\left[m_H n v_n^2 + p + \frac{B_t^2}{2\mu}\right]_1^2 = 0 , \tag{2.28}$$

$$\left[m_H \rho v_n v_t - \frac{B_n B_t}{\mu} \right]_1^2 = 0 , \tag{2.29}$$

$$\left[m_H \rho v_n \left(\frac{1}{2} v^2 + \frac{\gamma}{\gamma - 1} \frac{p}{m_H \rho} \right) + v_n \frac{B_t^2}{\mu} - \right.$$
$$\left. - \frac{B_n B_t}{\mu} v_t \right]_1^2 = 0 , \tag{2.30}$$

$$\left[(\underline{v} \times \underline{B})_t \right]_1^2 = 0 , \tag{2.31}$$

where subscripts 1 and 2 denote unshocked and shocked quantities, respectively. The equations are non-dimensionalised in terms of

$$X = \frac{\rho_2}{\rho_1} , \quad \beta_1 = \frac{2 \mu p_1}{B_1^2} , \quad m_1 = \frac{v_1}{c_{s1}} ,$$

$$\tan \delta_1 = \frac{v_{1t}}{v_{1n}} , \quad \tan \alpha_1 = \frac{B_{1t}}{B_{1n}} , \quad c_{s1} = \frac{\gamma p_1}{m_H \rho_1} .$$

Upon use of (2.26) and (2.27), (2.28) - (2.31) reduce to the following dimensionless forms:

$$\frac{\gamma m_{1n}^2}{X} + X \left(\frac{T_2}{T_1} + \frac{\tan^2 \alpha_2 \cos^2 \alpha_1}{X \beta_1} \right) = \gamma m_{1n}^2 +$$
$$+ \left(1 + \frac{\sin^2 \alpha_1}{\beta_1} \right) , \tag{2.32}$$

$$m_{1n}^2 \left(\frac{\tan \delta_2}{X} - \tan \delta_1 \right) = \frac{2}{\gamma \beta_1} \cos^2 \alpha_1 (\tan \alpha_2 - \tan \alpha_1) , \tag{2.33}$$

$$\frac{T_2}{T_1} = 1 - \frac{(\gamma - 1) m_{1n}^2}{2} \left[\frac{1 + \tan^2 \delta_2}{X^2} - (1 + \tan^2 \delta_1) \right] -$$
$$- \frac{2(\gamma - 1)}{\gamma \beta_1} \cos^2 \alpha_1 (\tan \alpha_2 - \tan \alpha_1) * \tag{2.34}$$
$$* (\tan \alpha_1 - \tan \delta_1) ,$$

and

$$(\tan \delta_2 - \tan \alpha_2) = X (\tan \delta_1 - \tan \alpha_1) . \tag{2.35}$$

Further, (2.33) and (2.35) may be combined to give

$$\tan\delta_2 = \left[\frac{2X}{\gamma\beta_1}\cos^2\alpha_1\tan\alpha_1(X-1) + X\tan\delta_1\left(M_{in}^2 - \frac{2X}{\gamma\beta_1}\cos^2\alpha_1\right)\right] \Big/ \left(M_{in}^2 - \frac{2X}{\gamma\beta_1}\cos^2\alpha_1\right) \qquad (2.36)$$

and

$$\tan\alpha_2 = \frac{X\tan\alpha_1\left(\frac{2}{\gamma\beta_1}\cos^2\alpha_1 - M_{in}^2\right)}{\left(\frac{2X}{\gamma\beta_1}\cos^2\alpha_1 - M_{in}^2\right)} \qquad (2.37)$$

(2.34), (2.36) and (2.37) may be substituted into (2.32) to produce an equation for X alone:

$$\frac{\gamma M_{in}^2}{X} + X - \frac{X(\gamma-1)M_{in}^2}{2}\left[\frac{1+\tan^2\delta_2}{X^2} - (1+\tan^2\delta_1)\right] - \frac{2X(\gamma-1)}{\gamma\beta_1}\cos^2\alpha_1(\tan\alpha_2 - \tan\alpha_1)(\tan\alpha_1 - \tan\delta_1) + X^2\sin^2\alpha_1\frac{\left(\frac{2}{\gamma\beta_1}\cos^2\alpha_1 - M_{in}^2\right)^2}{\beta_1\left(\frac{2X}{\gamma\beta_1}\cos^2\alpha_1 - M_{in}^2\right)^2} = \gamma M_{in}^2 + \left(1 + \frac{\sin^2\alpha_1}{\beta_1}\right). \qquad (2.38)$$

A factor of (X - 1) may be removed from (2.38) to give a cubic in X,

$$\left(\frac{2X}{\gamma}\cos^2\alpha_1 - M_{in}^2\beta_1\right)^2\left[X\left(1+(\gamma-1)\frac{M_{in}^2}{2}\right) - (\gamma+1)\frac{M_{in}^2}{2}\right] + \frac{2X^2}{\gamma}M_{in}^2\cos\alpha_1\sin\alpha_1(\gamma-1)\left[\frac{X}{\gamma}\cos^2\alpha_1(2\tan\delta_1 - \tan\alpha_1) - \beta_1 M_{in}^2\tan\delta_1 + \frac{\cos\alpha_1\sin\alpha_1}{\gamma}\right] + 2X^2(\gamma-1)\cos\alpha_1\sin\alpha_1 M_{in}^2 * (\tan\alpha_1 - \tan\delta_1)\left(\frac{2X}{\gamma}\cos^2\alpha_1 - \beta_1 M_{in}^2\right) + X\sin^2\alpha_1 M_{in}^2 * * \left[X\left(\beta_1 M_{in}^2 - 4\frac{\cos^2\alpha_1}{\gamma}\right) + \beta_1 M_{in}^2\right] = 0. \qquad (2.39)$$

The aim of the present analysis is to determine the shocked quantities ($T_2, \rho_2, \beta_2, \alpha_2, \delta_2, v_2$) as functions of the unshocked (or incident) ones ($T_1, \rho_1, \beta_1, \alpha_1, \delta_1, v_1$). In theory, one can just solve equation (2.39) for X numerically and then deduce the other results, but it is instructive to first consider the general method of shock classification and also some special cases.

2.3.1 M.H.D. shock classification and conditions for existence

In Section 2.1 we outlined the three basic modes of propagation of M.H.D. waves in a uniform medium. It will be recalled that of these modes, two (the fast and slow magnetoacoustic waves) could steepen and form shocks. M.H.D. shocks can be classified in an analogous way in terms of fast and slow M.H.D. shocks.

Figure 2.1 and equation (2.37) show that

$$\frac{B_{2t}}{B_{1t}} = \frac{X\left(\frac{2}{\gamma\beta_1}\cos^2\alpha_1 - M_{1n}^2\right)}{\left(\frac{2X}{\gamma\beta_1}\cos^2\alpha_1 - M_{1n}^2\right)} \qquad (2.40)$$

and the total change in magnetic field across the shock is given by

$$\frac{B_2^2}{B_1^2} = \frac{(1+\tan^2\alpha_2)}{(1+\tan^2\alpha_1)} \qquad (2.41)$$

From equation (2.40), it can be seen that different types of shocks will arise, depending upon the signs of the numerator and denominator; Bazer and Ericson (1958) based their method of shock classification upon such an analysis.

They assumed that, provided the entropy increased across the shock, it would propagate no matter what happened to the direction of the magnetic field. However, Jeffrey and Taniuti (1964, p. 220-238) pointed out that satisfying the entropy condition was not sufficient for an M.H.D. shock to propagate and that a stronger condition involving the behaviour of the magnetic field was needed:- this is called the evolutionary condition. Based on the theory of characteristics, this arises if one considers the behaviour of small perturbations at the shock front: we just content ourselves with stating the result. In simplest terms, it is that the tangential component of the magnetic field cannot reverse across a shock.

Thus, if we demand that the shock is compressive ($X > 1$), the allowed solutions to (2.40) are

$$M_{10}^2 \geq \frac{2X}{\gamma\beta_1}\cos^2\alpha_1 > \frac{2\cos^2\alpha_1}{\gamma\beta_1}, \qquad (2.42)$$

and

$$M_{10}^2 \leq \frac{2}{\gamma\beta_1}\cos^2\alpha_1 < \frac{2X\cos^2\alpha_1}{\gamma\beta_1}. \qquad (2.43)$$

These correspond to fast and slow magnetoacoustic shocks, respectively. The fast shock propagates above the fast magnetoacoustic speed and the slow shock propagates at a speed between the slow magnetoacoustic wave speed and the Alfvén speed. The basic properties of these shocks are

(a) Fast shocks: $\alpha_2 > \alpha_1$,

$\delta_2 > \delta_1$,

$\beta_2 > \beta_1$;

(b) Slow shocks: $\alpha_2 < \alpha_1$,

$\delta_2 < \delta_1$,

$\beta_2 < \beta_1$.

Also, if the equality in (2.42) or (2.43) holds, then we have the switch-off or switch-on shocks. The switch-off shock occurs when the slow shock propagates at the Alfvén speed and hence the tangential magnetic field vanishes (equation 2.40). The switch-on shock occurs when the fast shock propagates at a velocity $m^2_{\infty} = 2\times\omega_s^2\alpha_1/(\gamma\beta_1)$. In this case, there is no incident tangential magnetic field, and the effect of the shock is to "switch-on" a tangential component.

We have not discussed other types of discontinuity such as contact discontinuities (a situation in which the velocity is zero on either side of the discontinuity but the magnetic field may change across it (such as a current sheet) or the intermediate wave (which just corresponds to the Alfvén wave discussed in Section 2.1).

2.3.2 Special cases

Equations (2.34), (2.36), (2.37) and (2.38) may be solved analytically for some special cases. Due to the large number of parameters ($m_\infty, \alpha_1, \delta_1, \beta_1$), one can discuss many such cases depending upon the problem that one is trying to solve. We now outline some of the more interesting ones - bearing in mind our interest in the properties of slow shocks.

(a) $\beta_1 \to \infty$

In this limit, equation (2.38) reduces to the standard gas shocks outlined in Section 2.2. This is the case of a negligible field and outlines the fundamental difference

between fast and slow shocks. The fast shock is just a modification of the gas shock in that the flow is rotated away from the normal as is the field. The slow shock is totally different in that the flow is rotated toward the shock normal and the shock disappears in the limit $\beta_1 \to \infty$.

(b) Switch-off shock

Here, the equality in equation (2.42) holds and equations (2.36) and (2.37) become

$$\left.\begin{aligned} \tan\delta_2 &= X(\tan\delta_1 - \tan\alpha_1), \\ \tan\alpha_2 &= 0 . \end{aligned}\right\} \qquad (2.44)$$

(2.34) is then

$$\frac{T_2}{T_1} = 1 + (\gamma-1)\frac{\cos^2\alpha_1}{\gamma\beta_1}\left[1 - \frac{1}{X^2} + \tan^2\alpha_1\right], \qquad (2.45)$$

and equation (2.38) reduces to

$$X^2\left(1 + \frac{(\gamma-1)}{\gamma\beta_1}\right) - X\left(\frac{\cos^2\alpha_1}{\beta_1} + 1 + \frac{1}{\beta_1}\right) + \\ + \cos^2\alpha_1\frac{(\gamma+1)}{\gamma\beta_1} = 0 . \qquad (2.46)$$

Equation (2.45) shows that large plasma heating can be expected for the case of small plasma beta. The case of α_1 close to $\pi/2$ is of interest, since it is the limit of the slow shock as its propagation speed becomes small (equation 2.9). Then,

$$X \approx \frac{(2+\beta_1)}{2\left(\beta_1 + \frac{(\gamma-1)}{\gamma}\right)}\left[1 \pm \left\{1 - 4(\gamma+1)\frac{\left(\beta_1 + \frac{(\gamma-1)}{\gamma}\right)}{\gamma(2+\beta_1)^2}\right\}^{1/2}\right],$$

and

$$\frac{T_2}{T_1} \approx 1 + \frac{(\gamma+1)}{\gamma\beta_1} \quad . \tag{2.47}$$

For a plasma beta of 0.01, this indicates that a switch-off shock is a very effective heating mechanism. This is because in a switch-off shock, the entire energy of the tangential magnetic field is being converted into thermal and kinetic energy, and, if α_1 is near $\pi/2$, this represents an almost total conversion of magnetic to thermal and kinetic energy. The ratio of inflowing magnetic energy converted to thermal energy may be easily derived for the case of $\alpha_1 \to \pi/2$ and $\beta_1 \ll 1$. The unshocked magnetic energy is

$$W_m = \frac{B_1^2}{2\mu} \quad ,$$

and the shocked thermal energy ($m_H n_2 e_2$) is

$$m_H n_2 e_2 = \frac{B_1^2}{2\mu}\frac{(\gamma-1)}{\gamma} \quad ,$$

and so the ratio of incident magnetic to shocked thermal energy is

$$\frac{e_2}{W_m} = 0.4 \quad .$$

(c) Strong magnetic field ($\beta_1 \ll 1$)

In many regions of the solar corona, the local magnetic pressure dominates the gas pressure so that the plasma beta is small. The behaviour of shocks in these regions is of interest. One could solve equation (2.39) in terms of an expansion of X in powers of beta, but this analysis is lengthy Instead, information can be gained from equations (2.34) - (2.37).

If $\beta_1 \ll 1$, and $m_{in}^2 = O(1)$ then (2.36) becomes

$$\tan\delta_2 = \tan\delta_1 (1-X) + X \tan\delta_1 , \qquad (2.48)$$

while (2.37) gives

$$\tan\alpha_2 = \tan\alpha_1 + \frac{\beta_1 m_{in}^2 \gamma (1-X)}{2X \cos^2\alpha_1} \tan\alpha_1 , \qquad (2.49)$$

and so $\alpha_2 < \alpha_1$ and $\beta_2 < \beta_1$.

One can also see that

$$\frac{T_2}{T_1} = 1 + \frac{(\gamma-1) m_{in}^2 (1-\tan^2\alpha_1)(X^2-1)}{2X^2} , \qquad (2.50)$$

which is valid provided $\beta_1 \ll \cos^2\alpha_1$.

For now we shall leave X undetermined in these equations, since X is always a bounded quantity, given by

$$X = \frac{m_{in}^2 (\gamma+1)(1+\tan^2\alpha_1)}{2 + (\gamma-1) m_{in}^2 (1+\tan^2\alpha_1)} + O(\beta_1) \qquad (2.51)$$

Hence, as α_1 increases, the temperature jump rises: this is only true provided α_1 is not close to $\pi/2$, otherwise one cannot neglect terms of order $\beta_1/\cos^2\alpha_1$.

2.3.3 Numerical solution of M.H.D. shock relations

Equation (2.39) was solved for X as a function of α_1, δ_1, β_1, m_{in}, and then T_2, δ_2 and α_2 were deduced from equations (2.34), (2.36) and (2.37), respectively. The variations of T_2, δ_2 and α_2 with m_1 are shown in Figures 2.2, 2.3 and 2.4 for an external plasma beta of 0.1 and a normal incident flow. The solid dots denote the lower limit on m_1

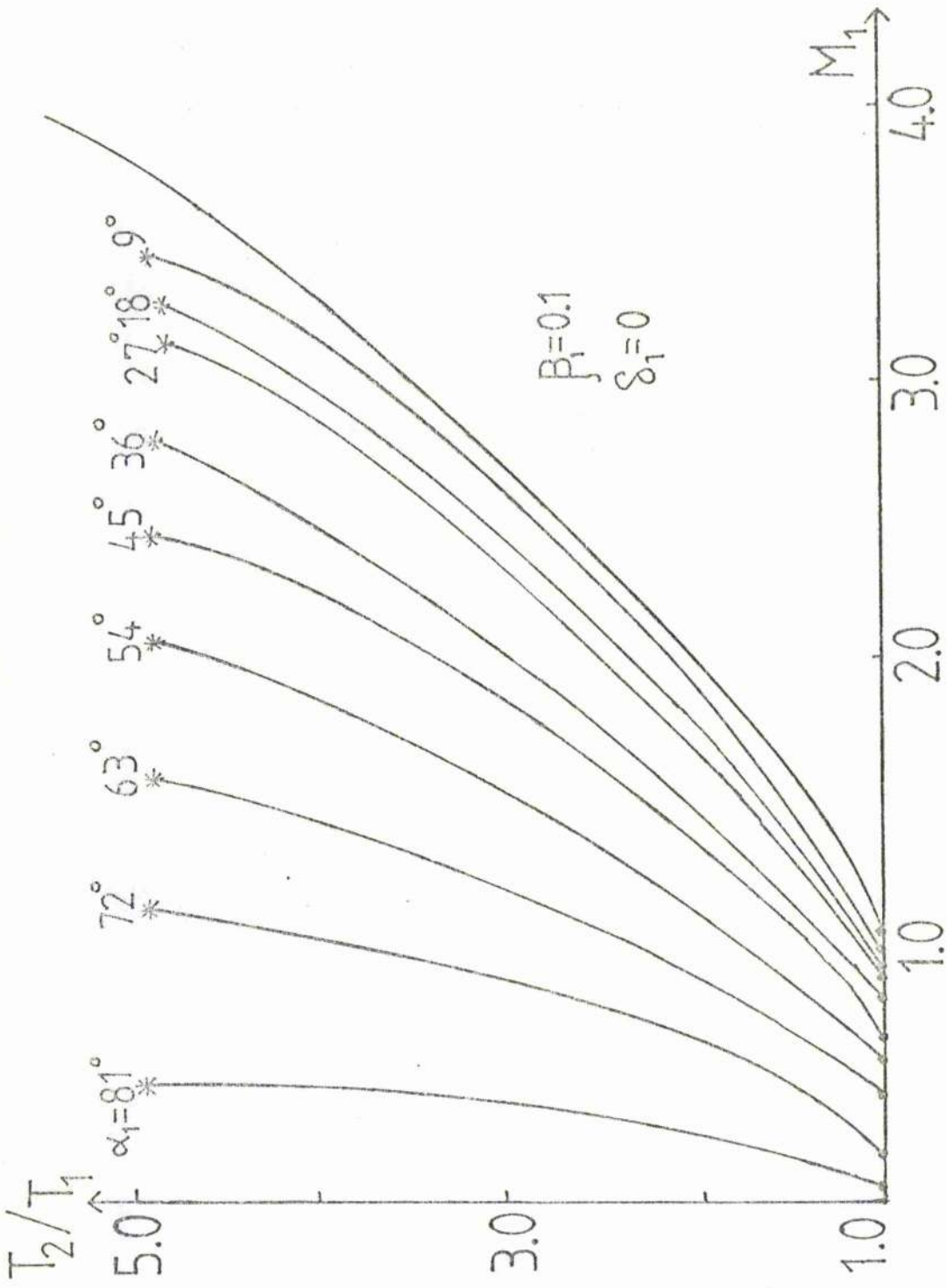

Figure 2.2 The variation with the incident magnetic field angle (α_1) and the inflow Mach number (M_1) of the shocked flow temperature T_2. The incident flow is normal to the shock ($\delta_1 = 0$) with a plasma beta of 0.1. Dots indicate when the incident speed equals the slow magnetoacoustic wave speed, while the stars show where the tangential magnetic field component is "switched off". (A typical value of T_1 may be 2×10^6 K).

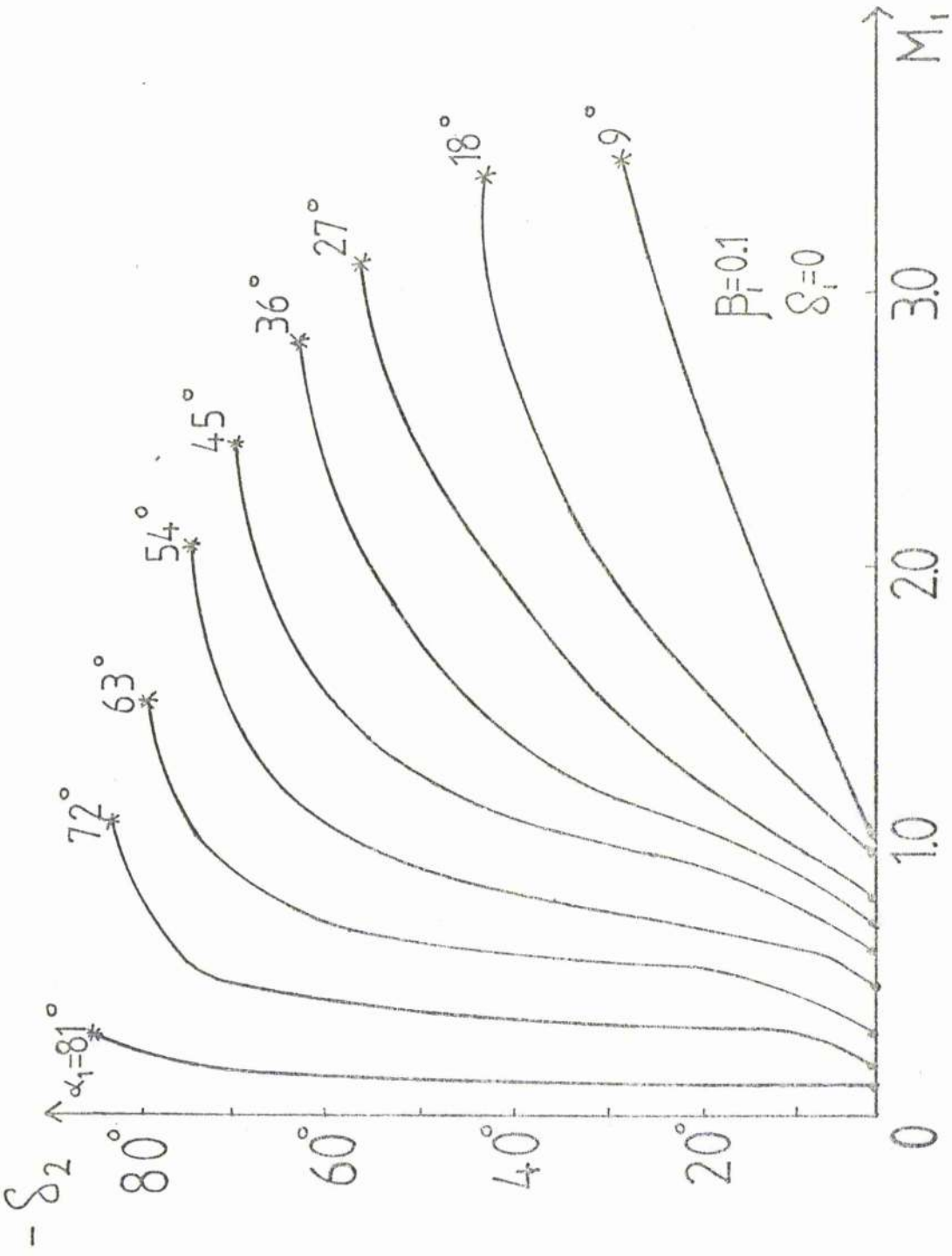

Figure 2.3 The variation with the incident magnetic field angle (α_1) and the inflow Mach number (M_1) of the angle of the shocked flow to the normal(δ_2). The notation is the same as Figure 2.2.

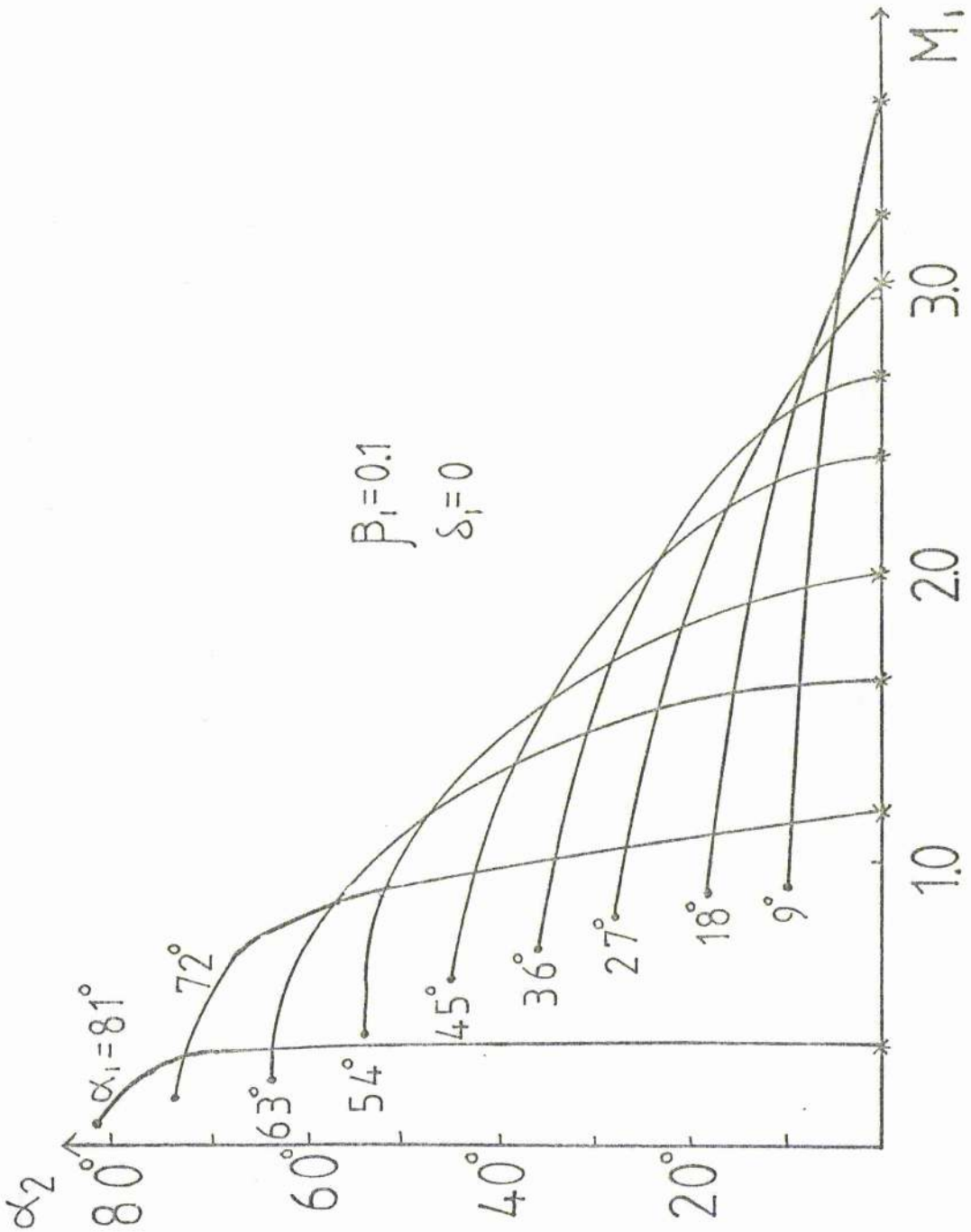

Figure 2.4 The variation with the incident magnetic field angle (α_1) and the inflow Mach number (M_1) of angle of the shocked field to the normal(α_2). The notation is the same as Figure 2.2.

for the formation of a shock. At this point, the propagation speed is equal to the slow magnetoacoustic wave speed and so $T_2 = T_1$, $\alpha_2 = \alpha_1$ and $\delta_2 = \delta_1$. The asterisks denote a "switch-off" shock, when $\alpha_2 = 0$. As was shown analytically, the effect of increasing α_1 is to increase the maximum temperature jump, occurring when the tangential magnetic field is switched off. For α_1 close to $\pi/2$, the expression (2.47) was derived and for $\beta_1 = 0.1$, $T_2/T_1 \approx 5$. This is in good agreement with numerical results. One interesting point is that the switch-off temperature jump appears to be approximately independent of α_1.

Figure 2.3 shows that δ_2 is always negative for a slow shock, as is clear from equation (2.36). Thus, the flow is turned in a clockwise direction through the shock. Also, as the tangential magnetic field is increased, the flow is turned through a larger angle.

In Figure 2.5, we have relaxed the constraint that $\delta_1 = 0$ and held $M_1 = 1$. As the inflow angle increases then the temperature jump falls. The effect of decreasing β_1 may be deduced from Section 2.3. Decreasing β_1 for a fixed M_1 moves the shock further from being 'switch-off'. Equations (2.36 and (2.37) imply that as β_1 decreases, then both α_1 and δ_1 decrease and so the flow and field are rotated through smaller angles. The temperature jump for a given M_1 remains roughly fixed for $\beta_1 \ll 1$ (equation 2.50) but as M_1 is increased, smaller values of β_1 permit much higher temperature jumps. This is simply because the switch-off speed has increased and the shock can then propagate more quickly. If $\beta_1 = 0.01$, T_2/T_1 may be as large as 40 if α_1 and δ_1 are close to $\pi/2$ and $\alpha_1 > \delta_1$.

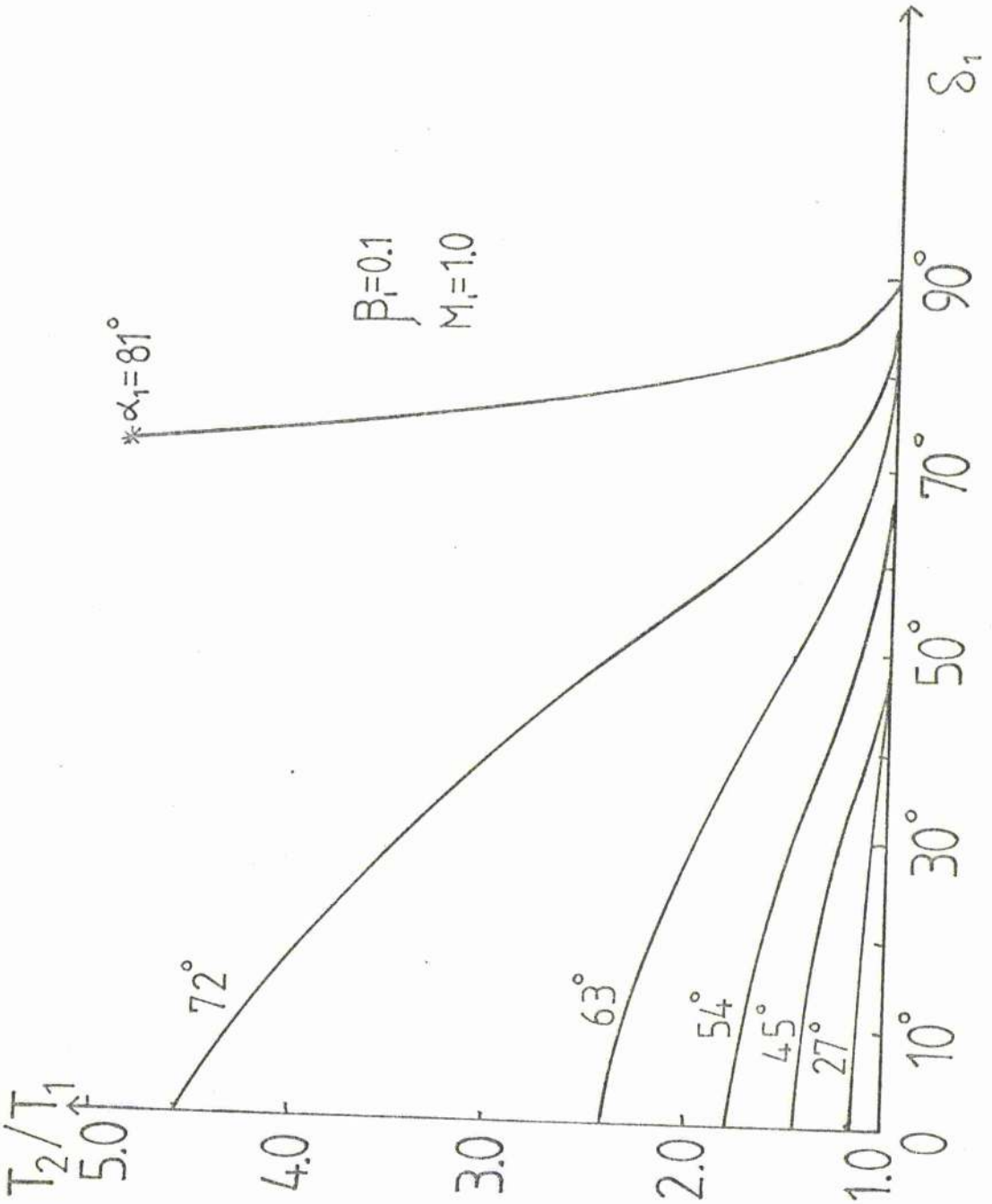

Figure 2.5 The jump in temperature across a slow M.H.D. shock as a function of the angle of flow incidence δ_1, for several values of α_1. The incident Mach number (M_1) is 1.0 and the plasma beta (β_1) is 0.1. (A typical value for T_1 is 2×10^6 K).

2.3.4 The role of slow M.H.D. shocks in the solar corona

In Chapter 7 of this thesis, we consider one particular role of shocks in some detail, namely the heating of post-flare loops, but it is convenient to discuss the role of slow shocks as a general heating mechanism. In the last few sections, it has been shown that slow shocks can release a large amount of magnetic energy as heat in a plasma. The maximum temperature rise across such a shock depends on the local plasma beta, and in the corona, where the beta is small, this temperature jump is especially large. Thus, slow-shock heating may well be one of the mechanisms responsible for maintaining the high coronal temperature.

It is generally considered (e.g. Priest, 1981b) that the corona is an active, dynamic structure with small-scale motions of magnetic field and plasma continually occurring. In such a medium, small current sheets may well be frequently set up, and, if reconnection occurs, it may proceed by the Petschek mechanism in its compressible form (Soward and Priest, 1982). Since slow shocks are an integral part of this mechanism, the results of the last few sections are relevant. These shocks are almost "switch-off" and have values of δ_1 close to $\pi/2$ and $S_1 \simeq 0$. If the plasma beta is 0.01, say, then such reconnection is an effective heating mechanism. This is seen by a simple shock analysis without the need for the complex solution undertaken by Soward and Priest.

It is thus important to consider the general analysis of M.H.D. shocks which has been considered here rather than the severely restrictive analysis generally attempted in which the flow and field are considered parallel.

2.4 Shocks in non-uniform media

The general theory of shocks involves an analysis of the jump relations (as earlier in this Chapter) and an investigation of the internal structure of the shock. However, a third important problem is to consider how a shock behaves in a medium in which dissipation (such as thermal or electrical conduction) is important outside the shock front. Since these shocks are only used briefly in this thesis, we shall give only a brief discussion of their behaviour.

If thermal conduction is important outside the shock front, then, for a field-free gas, the steady-state one-dimensional energy equation is

$$\frac{d}{ds}\left[m_0 n v\left(\frac{1}{2}v^2 + \frac{\gamma P}{(\gamma-1)m_0 n}\right) - 10^{-11}T^{5/2}\frac{dT}{ds}\right] = 0, \qquad (2.52)$$

and the energy jump relation becomes

$$\left[m_0 n v\left(\frac{1}{2}v^2 + \frac{\gamma P}{(\gamma-1)m_0 n}\right) - 10^{-11}T^{5/2}\frac{dT}{ds}\right]_1^2 = 0. \qquad (2.53)$$

So, as well as the velocity, pressure, density and temperature jumping, it appears that the temperature gradient jumps as well.

Similarly, if a magnetic field is present and the plasma is not infinitely conducting outside the shock, then a term $\eta\, dG/ds$ must be added to Ohm's law. Marshall (1955) and Ludford (1958) analysed such an M.H.D. shock and concluded that while the magnetic field gradient could be discontinuous across the shock, the field itself had to be continuous. This can be referred to as an Isomagnetic shock.

An analogous result for a gas shock with finite conduction

is derived by Landau and Lifschitz (1958), so that the temperature gradient can be discontinuous but the temperature itself is continuous (Roseneau and Frankenthal, 1976, 1978):

$$T_2 = T_1 \ . \tag{2.54}$$

The expression (2.15) for the density jump now becomes

$$\frac{\rho_2}{\rho_1} = m_1^2 \ , \tag{2.55}$$

since the energy jump relation decouples from the other two. Finally, the shocked conductive flux is given by

$$10^{-11} T_1^{5/2} \left(\frac{\partial T}{\partial s}\right)_2 = 10^{-11} T_1^{5/2} \left(\frac{\partial T}{\partial s}\right)_1 + \\ + (m_1^4 - 1) \frac{1}{2} m_1 n v_1^3 \ . \tag{2.56}$$

This is known as an Isothermal shock. It is clear that if one did allow a jump in temperature, then the temperature gradient across such a shock would behave as a delta function which is not realistic. The Isothermal shock may be regarded as spreading out the temperature variation around the shock rather than simply allowing it to jump.

2.5 Discussion and conclusions

In this chapter the basic theory of shock waves has been discussed with the needs of subsequent chapters of this thesis in mind. However, some cases of slow M.H.D. shocks have been looked at in more detail. In the view of the author, the literature on shocks whose incident flow and field are non-aligned is inadequate (with the exception of the work of Lynn, 1966) and these shocks have been explored from the viewpoint of the temperature jump across them. The aligned case in fact

overlooks many of the most interesting features of flow and field topology such as the reversal of flow direction in a shock. Substantial temperature jumps are also found particularly in the case of the switch-off shock and such shocks may be of importance in coronal heating.

The case of slow M.H.D. shocks has been examined to the exclusion of other types. Fast shocks, intermediate waves and contact discontinuities are of great importance but are not involved in the work of this thesis.

CHAPTER 3: STEADY-STATE FLOWS IN CORONAL MAGNETIC LOOPS

I:- ISOTHERMAL AND ADIABATIC THEORY

3.1 Introduction

In Chapter 1, it was noted that the closed-field regions of the solar corona are now known to be structured as loops. In the following two chapters, we examine the theoretical nature of steady-state siphon flows in such loops. One may pose the problem as follows:- given a loop of length 2L, what steady-state flows can be driven along the loop by prescribed foot-point temperatures and pressures?

The thermal conduction perpendicular to a magnetic field is negligible (Chapter 1), and so each field line is thermally isolated from its neighbours and may be examined separately provided the field is force-free, and any flows are sub-Alfvénic. Large pressures may distort the field and make a full M.H.D. calculation necessary. This problem does not generally arise in the modelling of coronal loops, but it may be relevant during simple-loop flares when extremely high temperatures and densities arise.

Taking the scalar product of $\underline{B}$ with the steady-state momentum equation gives

$$m_H n v \frac{dv}{ds} = -\frac{dp}{ds} - n m_H g \, \hat{\underline{z}} \cdot \hat{\underline{s}} \quad , \tag{3.1}$$

where s is the coordinate along a magnetic field line. The importance of gravity is measured by both the ratio of the loop length to the scale-height and by the angle the loop makes

with the vertical. In a low-lying loop ($\hat{z}\cdot\hat{s} \approx 0$), one can effectively neglect gravity. The other equations for flow along a field line are continuity (1.26), flux conservation (1.28), state (1.27) in the form

$$\frac{d}{ds}(nvA) = 0 , \tag{3.2}$$

$$\frac{d}{ds}(BA) = 0 , \tag{3.3}$$

$$p = 2nk_B T , \tag{3.4}$$

and energy, (1.30)

$$\frac{n^\gamma}{\gamma-1} v \frac{d}{ds}\left(\frac{p}{n^\gamma}\right) - \frac{1}{A}\frac{d}{ds}\left(k_\parallel A \frac{dT}{ds}\right) = n h - n^2 \chi T^\alpha , \tag{3.5}$$

where A(s) is the loop cross-sectional area and the mechanical heating has been taken proportional to density. This set of equations just approximates a loop by a rigid tube if the loop area and geometry are prescribed. We wish to solve these equations subject to the following boundary conditions:

$$\left.\begin{aligned} s = 0 , \quad & n = n_0 , \quad T = T_0 , \\ s = 2L , \quad & n = n_2 , \quad T = T_2 . \end{aligned}\right\} \tag{3.6}$$

Several authors have solved equations (3.1) - (3.6) using various approximations as follows.

Meyer and Schmidt (1968) modelled steady Evershed flow out of sunspots (See Chapter 1) in a low-lying loop structure

under the assumption that it is driven by a pressure difference between the two footpoints. They solved the equations of continuity, momentum and state but do not make clear what energy equation is taken. It is found that the flow becomes sonic at an appropriate point along the loop and is slowed down by a shockwave in the downflowing leg. The calculated outflow speed is typically 6-7 km s^{-1} at a distance of 15 Mm from the sunspot centre. Meyer and Schmidt only obtained flows involving sonic points and shocks.

Yeh (1977), on the other hand, considered only subsonic flows. He modelled a symmetric interplanetary loop, rising a solar radius above the surface and having a length of approximately 1500 Mm.

The equations of continuity, state, momentum and energy, were solved numerically, the energy equation containing terms involving convection and conduction (but no heating and radiation). Yeh finds a large range of subsonic flows exist corresponding to different values of the boundary conditions, but he claims that supersonic flows cannot occur. He states that, if a subsonic-supersonic transition occurs, the plasma is rarefied to a vacuum at the transition point. This is true everywhere except at the sonic point, which is the only physically relevant transition point. It allows one to satisfy the boundary conditions by using a discontinuity. Yeh claims that this solution will never arise and states that the flux tube geometry will adjust to give rise to a subsonic flow due to lateral force balance. However, this balance will, to zeroth order, be force-free, and so the flux tube is unable to adjust. The work of Yeh is, however, important in that he

was first to point out that, although a loop is in static equilibrium if $n_o = n_2$ and $T_o = T_2$, such boundary conditions are extremely unlikely to arise and so a flow will in general be present along the loop. Whether such a flow is steady or transient in practice is still a very open question.

More recent attempts at the siphon flow problem have been made by Glencross (1980) and Noci (1981). Glencross has modelled upflows in small coronal loops (of height 5 Mm): he solves the equations of continuity and motion for a prescribed temperature profile. However, Glencross only considers half a loop (i.e. up to the summit), and so he does not need to invoke shock waves. Noci (1981) has studied (independently of the present author) the problem of siphon flows in coronal loops. He approximates the energy equation by the polytropic law, in the form

$$p = \text{const.}\ n^{\alpha} \quad , \tag{3.7}$$

and solves this together with the equations of continuity, state and momentum. He considers loops of uniform cross-sectional area and goes on to predict the E.U.V. emission measure.

In this Chapter, we solve equations (3.1) - (3.4) together with equation (3.5) in the form

$$\frac{p}{n^{\gamma}} = \text{const.} \quad , \tag{3.8}$$

and so we neglect any energy sources and sinks. Approximation (3.8) enables us to outline the main features of the flow and gives a good background to the solution of the full steady-state problem in Chapter 4.

3.2 General solution

The equations of adiabatic and isothermal siphon flow along a coronal loop are (3.1) - (3.5) in the form

$$m_H n v \frac{dv}{ds} = - \frac{dp}{ds} - m_H n g \cos\left(\frac{\pi s}{2L}\right), \qquad (3.9)$$

$$n v A = M, \qquad (3.10)$$

$$BA = \Phi, \qquad (3.11)$$

$$p = 2nk_B T, \qquad (3.12)$$

$$p = k n^{\gamma}, \qquad (3.13)$$

where M is the mass flux, Φ is the magnetic flux, γ is the ratio of specific heats ($5/3$ for adiabatic flow, 1 for isothermal flow) and the term $\cos(\pi s/2L)$ in the momentum equation represents the flux tube geometry (in this case a semi-circular loop as shown in Figure 3.1). It is worth pointing out that the steady-state assumption is true provided the footpoint pressures remain fixed for a few sound travel-times. The sound travel-time, (τ_s) is defined as

$$\tau_s = L / c_s$$

and Table 3.1 shows how τ_s varies with L and c_s.

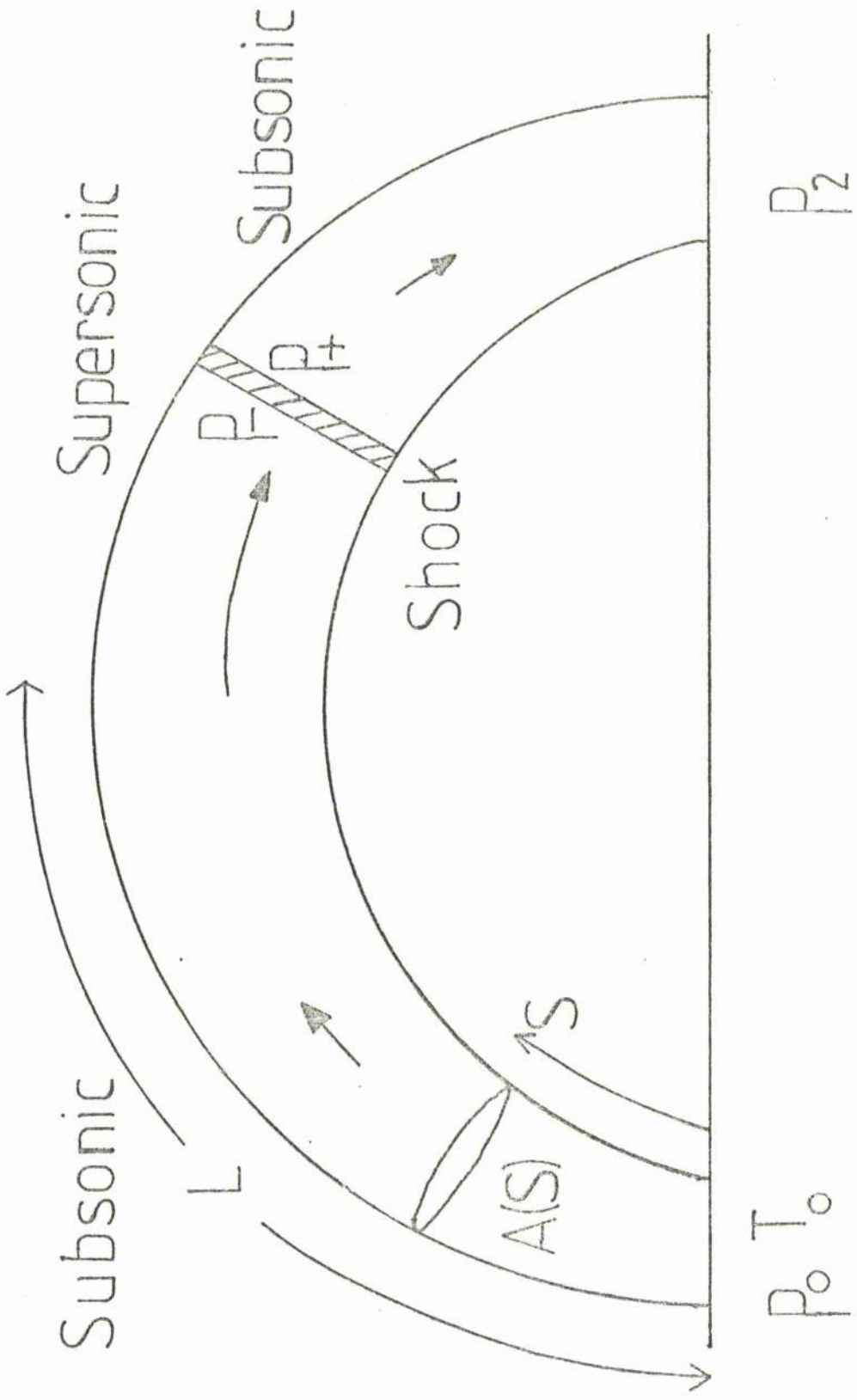

Figure 3.1 The notation for a loop of length 2L with the position from one footpoint measured by the coordinate s. Shown here is the case when the cross-sectional area A(s) is symmetric about the loop summit. The flow is subsonic up to the summit and supersonic between the summit and a shock wave.

Table 3.1

The variation of the sound-travel time, τ_s (in seconds) with the loop half-length, L, (Mm) and the sound speed, c_s (km s^{-1}).

L \ c_s	50	100	150	200
10	200	100	66	50
25	500	250	166	125
50	1000	500	333	250
100	2000	1000	666	500
150	3000	1500	1000	750
200	4000	2000	1333	1000

The boundary conditions must also be altered since, by neglecting thermal conduction, the order of the equations has been reduced by one. Equation (3.6) is thus replaced by

$$\left.\begin{aligned} p = p_0 , \quad T = T_0 \quad &\text{at} \quad s = 0 , \\ p = p_2 , \quad &\text{at} \quad s = 2L , \end{aligned}\right\} \tag{3.14}$$

and so T_2 is free. Yeh (1977) claims that one should still apply the full boundary conditions (3.6) and that γ (or, in the polytropic case, α) should be deduced from them, so that one finds

$$\gamma = 1 + \frac{\log (T_2/T_1)}{\log (n_2/n_1)} .$$

In effect, he has overprescribed the problem, and we note that γ (or α) should not be determined in this way, but should be

free to be prescribed. It will be found that, for some values of these boundary conditions, a continuous solution is impossible and a flow discontinuity must arise at some location. The conservation relations across such a shock are given by equations (2.12) - (2.14).

Defining the local sound speed (c_s) by

$$c_s^2 = \frac{2\gamma k_B T}{m_H} ,$$

equations (3.9), (3.10), (3.12) and (3.13) can be combined, to give a differential equation for v(s):

$$\left(v - \frac{c_s^2}{v}\right)\frac{dv}{ds} = -g\cos\left(\frac{\pi s}{2L}\right) + \frac{c_s^2}{A}\frac{dA}{ds} . \qquad (3.15)$$

In (3.15), one can replace v by -v and still get the same equation. Thus, subsonic flows may occur along the loop either from left to right or right to left. For shocked flows, such a reversal is not possible because the entropy must increase across the shock. If we impose $p_2 > p_o$ rather than $p_2 < p_o$, the supersonic flow will be reversed with the shock still in the downflowing leg.

It is convenient to non-dimensionalise the equations as follows,

$$\bar{v} = \frac{v}{c_{so}} , \quad \bar{s} = \frac{s}{L} , \quad \bar{A} = \frac{A}{A_o} , \quad \bar{g} = \frac{L}{\Lambda_o} ,$$

where zero subscripts refer to values at s = 0 and Λ_o is the scale-height at the base of the loop defined as

$$\Lambda_o = \frac{p_o}{m_H n_o g} = \frac{c_{so}^2}{\gamma g} .$$

Equation (3.15) may then be written as

$$\left[\bar{v} - \frac{1}{\bar{v}}\left(\frac{\bar{v}_o}{\bar{v}\bar{A}}\right)^{\gamma-1}\right]\frac{d\bar{v}}{d\bar{s}} = -\frac{\bar{q}}{\gamma}\cos\left(\frac{\pi\bar{s}}{2}\right) + \left(\frac{\bar{v}_o}{\bar{v}\bar{A}}\right)^{\gamma-1}\frac{1}{\bar{A}}\frac{d\bar{A}}{d\bar{s}} \quad . \tag{3.16}$$

If we assume that

$$\bar{v} = \bar{v}_o \quad \text{at} \quad \bar{s} = 0 ,$$

(3.16) integrates to give

$$\frac{1}{2}(\bar{v}^2 - \bar{v}_o^2) + \frac{1}{\gamma-1}\left[\left(\frac{\bar{v}_o}{\bar{v}\bar{A}}\right)^{\gamma-1} - 1\right] = -\frac{2\bar{q}}{\gamma\pi}\sin\left(\frac{\pi\bar{s}}{2}\right) , \tag{3.17}$$

which is just Bernoulli's equation.

Equation (3.17) gives the velocity $\bar{v}(\bar{s})$ along the loop for a given base velocity $\bar{v}_o$ and cross-sectional area $\bar{A}(\bar{s})$. The density, pressure and temperature are then determined by

$$\left.\begin{aligned} \bar{\rho} &= \frac{\bar{v}_o}{\bar{v}\bar{A}} , \\ \bar{p} &= \bar{\rho}^{\gamma} , \\ \bar{T} &= \bar{\rho}^{\gamma-1} . \end{aligned}\right\} \tag{3.18}$$

Further examination of (3.16) shows that a critical (or sonic) point (when $d\bar{v}/d\bar{s}$ is undefined) occurs at a velocity $\bar{v}_c$ and location $\bar{s}_c$ given by

$$\bar{v}_c = \left(\frac{\bar{v}_o^*}{\bar{A}_c}\right)^{\frac{\gamma-1}{\gamma+1}} , \tag{3.19}$$

and

$$\cos\left(\frac{\pi \bar{s}_c}{2}\right) = \frac{\gamma}{\bar{g}} \left(\frac{\bar{v}_o^*}{\bar{v}_c \bar{A}_c}\right)^{\gamma-1} \frac{1}{\bar{A}_c} \left(\frac{d\bar{A}}{d\bar{s}}\right)_c \quad . \tag{3.20}$$

The corresponding footpoint velocity $\bar{v}_o^*$ that gives a solution passing through the critical point satisfies

$$\frac{1}{2}\left(\bar{v}_c^2 - \bar{v}_o^{*2}\right) + \frac{1}{\gamma-1}\left[\left(\frac{\bar{v}_o^*}{\bar{v}_c \bar{A}_c}\right)^{\gamma-1} - 1\right] + \frac{2\bar{g}}{\gamma\pi} \sin\left(\frac{\pi \bar{s}_c}{2}\right) = 0 \quad , \tag{3.21}$$

and one can then solve (3.19) - (3.21) for $\bar{s}_c$, $\bar{v}_c$ and $\bar{v}_o^*$.

There is only one free parameter in the problem, namely $\bar{g}$, the ratio of the loop half-length to the base scale-height. For a base temperature of $T_o = 10^6$K, the scale height, Λ_o, is about 50Mm ($=5\times10^4$km), whereas coronal loop lengths lie typically between about 5Mm and 700Mm. Thus $\bar{g}$ varies between about .05 and 7, but we shall concentrate in particular on the value $\bar{g} = 1$.

It is worth noting that (3.16), (3.17) and (3.19) - (3.21) are very similar to the solar wind equations (Parker, 1963). One has the same feature of a sonic point and a range of transonic and wholly subsonic solutions and one must also match the wind onto the interstellar medium.

3.3 Isothermal flow

3.3.1 Uniform area

A loop whose temperature and area are both uniform outside

the shock is the simplest possible case to consider and so illustrates the basic physical ideas behind the siphon flow model. After putting $\bar{A}(\bar{s}) \equiv 1$ and taking the limit of γ tending to 1, equations (3.16) and (3.17) reduce to

$$\left(\bar{v} - \frac{1}{\bar{v}}\right)\frac{d\bar{v}}{d\bar{s}} = -\bar{g}\cos\left(\frac{\pi\bar{s}}{2}\right), \tag{3.22}$$

$$\frac{1}{2}(\bar{v}^2 - \bar{v}_0^2) + \log\left(\frac{\bar{v}_0}{\bar{v}}\right) = -\frac{2\bar{g}}{\pi}\sin\left(\frac{\pi\bar{s}}{2}\right), \tag{3.23}$$

respectively. Equation (3.22) has a critical point at the loop summit ($\bar{s}=1$) where the flow becomes sonic ($\bar{v}=1$), as indicated in Figure 3.2. The starting velocity ($\bar{v}_0^*$) for flow to pass through the critical point depends on $\bar{g}$ and is given by the solution of

$$\frac{1}{2}(1 - \bar{v}_0^{*2}) + \log \bar{v}_0^* = -\frac{2\bar{g}}{\pi},$$

after putting $\bar{v} = 1$, $\bar{s} = 1$ in (3.23).

For initial speeds ($\bar{v}_0$) slower than $\bar{v}_0^*$, the flow is subsonic and symmetric about the top of the loop and the pressure ratio $\bar{p}_2/\bar{p}_0$ is unity. For $\bar{v}_0 = \bar{v}_0^*$, the flow becomes supersonic after the loop summit and, for $\bar{v}_0 > \bar{v}_0^*$, the results have no physical meaning. We shall not be concerned with flows that start out supersonically. Clearly the infinite range of subsonic solutions is a result of the model. If one included a full energy equation, the symmetry of equation (3.15) would be lost and the infinite range of solutions would vanish.

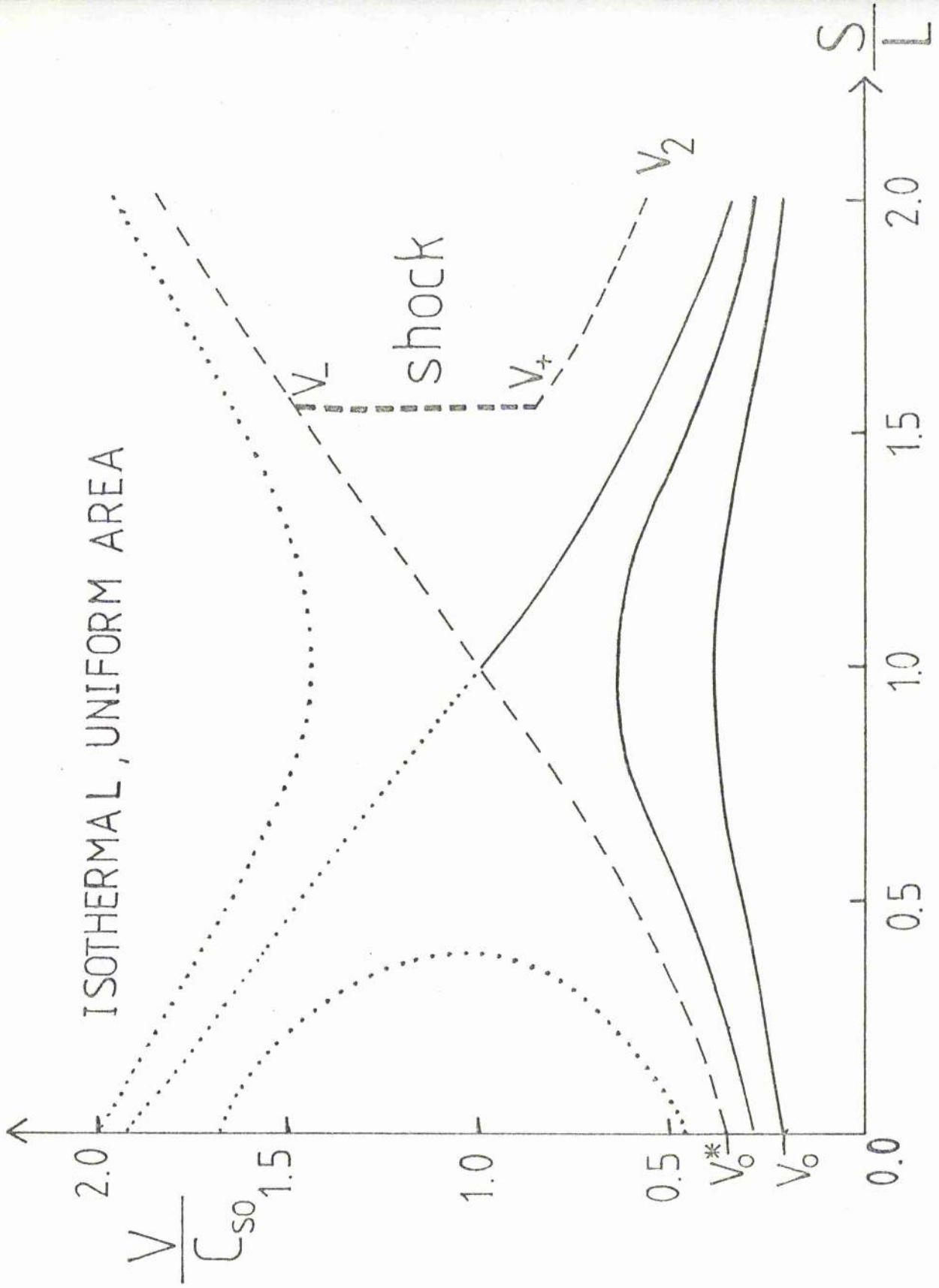

Figure 3.2 The flow speed ($\tilde{v}$) at a distance $\tilde{s}$ along a loop of half-length (L) equal to 50 Mm (i.e. $\tilde{g}=1$). The loop has uniform cross-sectional area and the (unshocked) flow is isothermal with sound speed c_{so}. Subsonic flows (solid) have initial speeds $\tilde{v}_0$ less than $\tilde{v}_0^*$. Flow (dashed) with initial speed $\tilde{v}_0^*$ become supersonic at the loop summit (s=L) and are slowed from $\tilde{v}_-$ to $\tilde{v}_+$ by a shock wave. Beyond the shock the flow has enhanced temperature T_+ and slows to $\tilde{v}_2$ at the footpoint. Dotted lines indicate unphysical or wholly supersonic solutions.

Indeed this is what is found in Chapter 4.

When there is no pressure difference between the ends of the loop ($\bar{p}_2/\bar{p}_0=1$), any of the subsonic flows may occur. However, an imposed pressure difference forces the flow to become supersonic beyond the loop summit and then to be decelerated at a shock wave that is located at some position on the downflowing leg (Figure 3.1). The effect of imposing different pressure differences is to change the location and strength of the shock wave and the values of the downstream speed $\bar{v}_2$ (Figure 3.2). These solutions may be constructed in an inverse manner by imposing the position of the shock and deducing the necessary pressure difference, as follows. For a given shock position, as indicated in Figure 3.2, we have prescribed the value of $\bar{v}_1$, the speed ahead of the shock. This in turn determines the Mach number (M) and so from (2.15) the value of the speed (v_2) just behind the shock. Furthermore, the temperature (T_2) behind the shock is given by (2.17), and so the isothermal downstream flow follows one of the trajectories of (3.23), with temperature T_2 inserted in (3.22). In particular, (3.23) gives the flow speed ($\bar{v}_2$) and the pressure ($\bar{p}_2$) at the footpoint follows.

Figure 3.3 is plotted for a loop of half-length 50Mm so that $\bar{g} = 1$. It can be seen that supersonic flows are possible when the upflow base speed $\bar{v}_0^*$ is 0.34. Also the smallest allowable pressure ratio $\bar{p}_2/\bar{p}_0$ is 0.75. For smaller values, the shock moves below the footpoint and our model fails (except in the case of unshocked transonic flow when $\bar{p}_2/\bar{p}_0 = 0.18$). (The model fails because it is not possible to construct steady solutions with the required pressure ratio: if such a prescribed

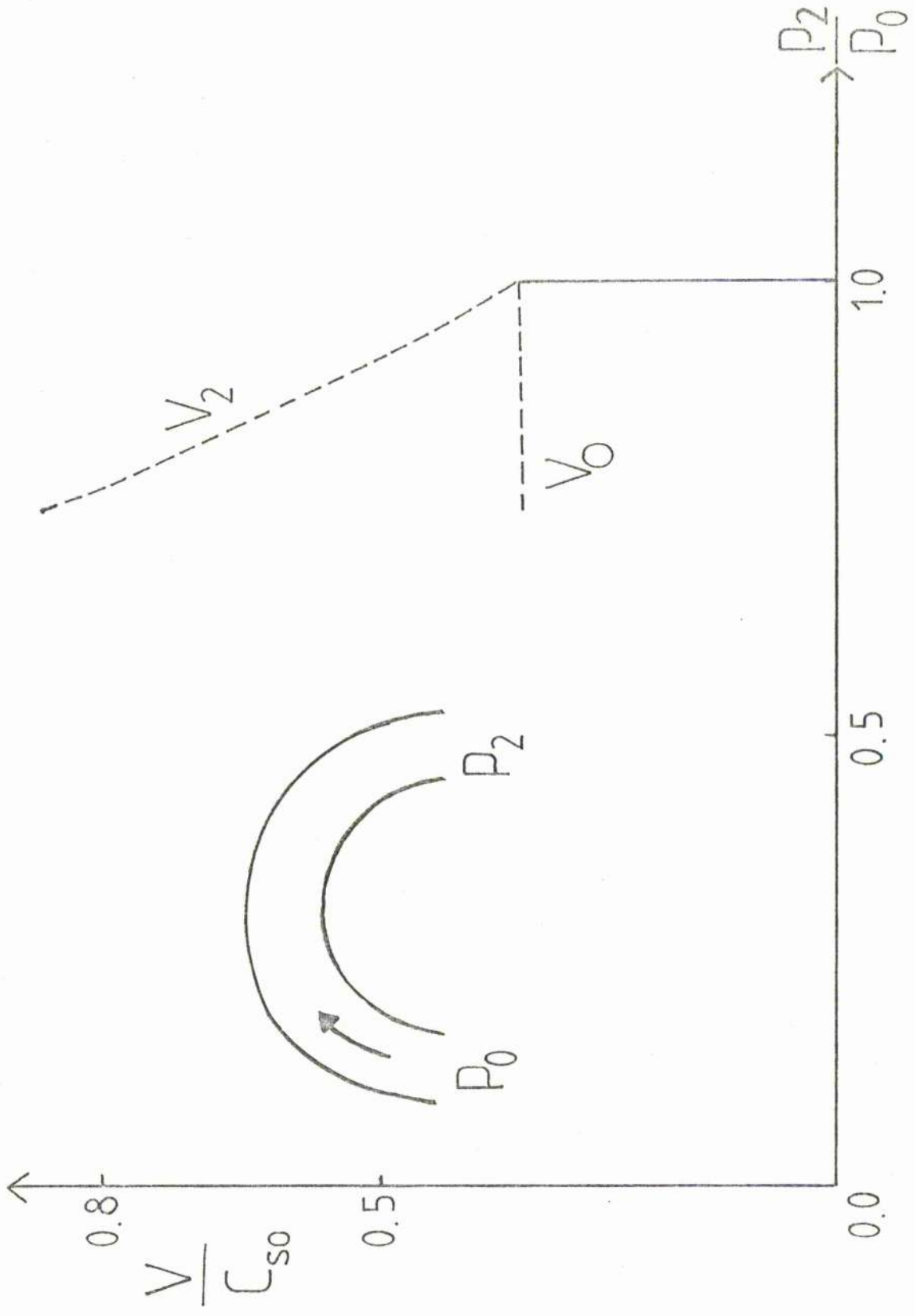

Figure 3.3 The flow speeds $\bar{v}_0$, $\bar{v}_2$ as a function of the imposed pressure ratio p_2/p_0 for Figure 3.2. The solid line denotes subsonic flows ($\bar{v}_0=\bar{v}_2$) while the dashed lines denote flows containing shock waves. When p_2/p_0 is less

pressure ratio is switched on, a shock wave will propagate down the loop; when it propagates out of the end of the loop the pressure $\bar{p}_2$ is changed to the value $0.18\bar{p}_0$ by the passage of the shock and the previous value is not maintained.) Longer loops give a wider range of possible pressure ratios and a lower base speed, as indicated in Table 3.2.

Table 3.2

The variation of critical starting velocity and minimum pressure ratio with loop half-length (L), for isothermal flow in a loop of uniform area. (The coronal scale-height is taken as 50Mm.)

L(Mm)	5	10	25	50	100	200
$\bar{v}_0^*$	0.760	0.667	0.500	0.340	0.175	0.048
$\left(\frac{p_2}{p_0}\right)_{min}$	1.000	1.000	0.927	0.752	0.479	0.166

3.3.2 The effect of a varying area

When the temperature is isothermal but the cross-sectional area varies, (3.16) and (3.17) become

$$\left(\bar{v} - \frac{1}{\bar{v}}\right)\frac{d\bar{v}}{d\bar{s}} = -\bar{g}\cos\left(\frac{\pi\bar{s}}{2}\right) + \frac{1}{\bar{A}}\frac{d\bar{A}}{d\bar{s}}\,, \qquad (3.24)$$

$$\frac{1}{2}\left(\bar{v}^2 - \bar{v}_0^2\right) + \log\left(\frac{\bar{v}_0}{\bar{v}\bar{A}}\right) + \frac{2\bar{g}}{\pi}\sin\left(\frac{\pi\bar{s}}{2}\right) = 0\,, \qquad (3.25)$$

respectively. Equation (3.24) has a critical (sonic) point at

$$\left.\begin{aligned} \bar{v} &= 1 \ , \\ \cos\left(\frac{\pi\bar{s}}{2}\right) &= \frac{1}{\bar{A}}\frac{d\bar{A}}{d\bar{s}} \ . \end{aligned}\right\} \qquad (3.26)$$

For a given form $\bar{A}(\bar{s})$ of the area, (3.26) determines the location $\bar{s}_c$ of the critical point along the loop, and then the corresponding speed $\bar{v}_0^*$ follows from

$$\frac{1}{2}\left(1-\bar{v}_0^{*2}\right) + \log\left(\frac{\bar{v}_0^*}{\bar{A}_c}\right) + \frac{2\bar{g}}{\pi}\sin\left(\frac{\pi\bar{s}_c}{2}\right) \ .$$

In particular, if $d\bar{A}/d\bar{s}$ is positive, the sonic point lies before the loop summit, whereas if $d\bar{A}/d\bar{s}$ is negative it lies beyond the summit. When the variation of the loop area is symmetric about the loop summit and is not too great, the results are very similar to those in Figures 3.2 and 3.3, but with slight changes of scale on the axes. Converging and diverging loops, however, produce new features.

Consider a converging loop whose cross-sectional area decreases with distance such that

$$\bar{A}(\bar{s}) = 1 + \frac{(a-1)}{2}\bar{s} \ , \qquad 0 < a < 1 \ .$$

The solutions to (3.25) for $\bar{v}(\bar{s})$ are shown in Figure 3.4 for the case a = 0.5. The way that the footpoint speeds $\bar{v}_0$, $\bar{v}_2$ vary with the pressure difference is given in Figure 3.5a. The presence of asymmetry in Figure 3.4 means that the subsonic flows are now driven by a small non-zero pressure difference. If the pressure difference is large enough, $\bar{v}_0$ becomes equal to $\bar{v}_0^*$ and shocked solutions result. It is clear from the nature of the asymmetry in Figure 3.4 that $\bar{v}_2$ always exceeds $\bar{v}_0$, which implies that n_0 exceeds n_2 and p_0 exceeds p_2, so

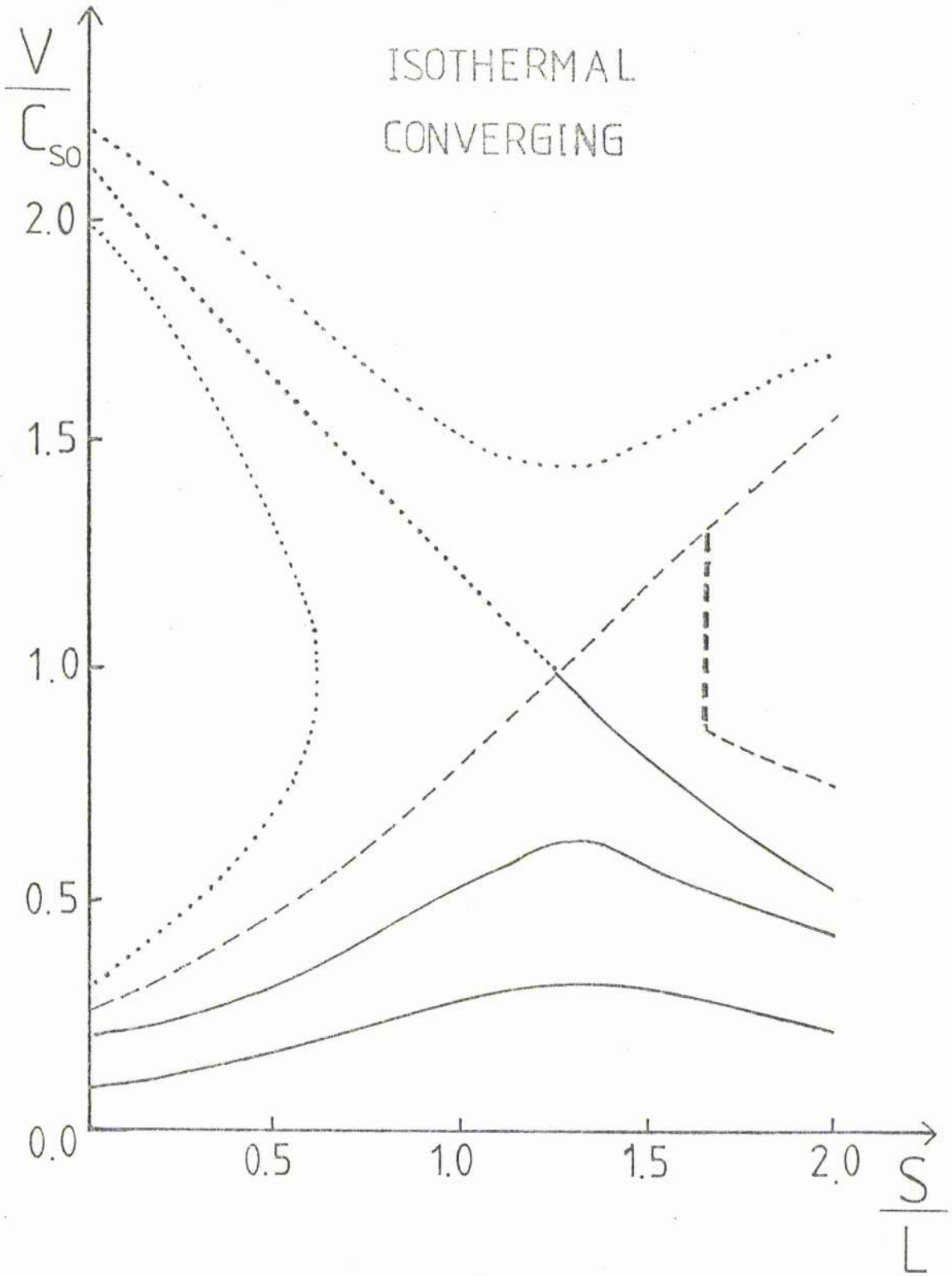

Figure 3.4 Phase plane $\bar{v}(\bar{s})$ for isothermal flow in a converging loop with half length 50Mm ($\bar{p}$=1) and whose cross-sectional area varies as $A=A_0(1-s/(4L))$.

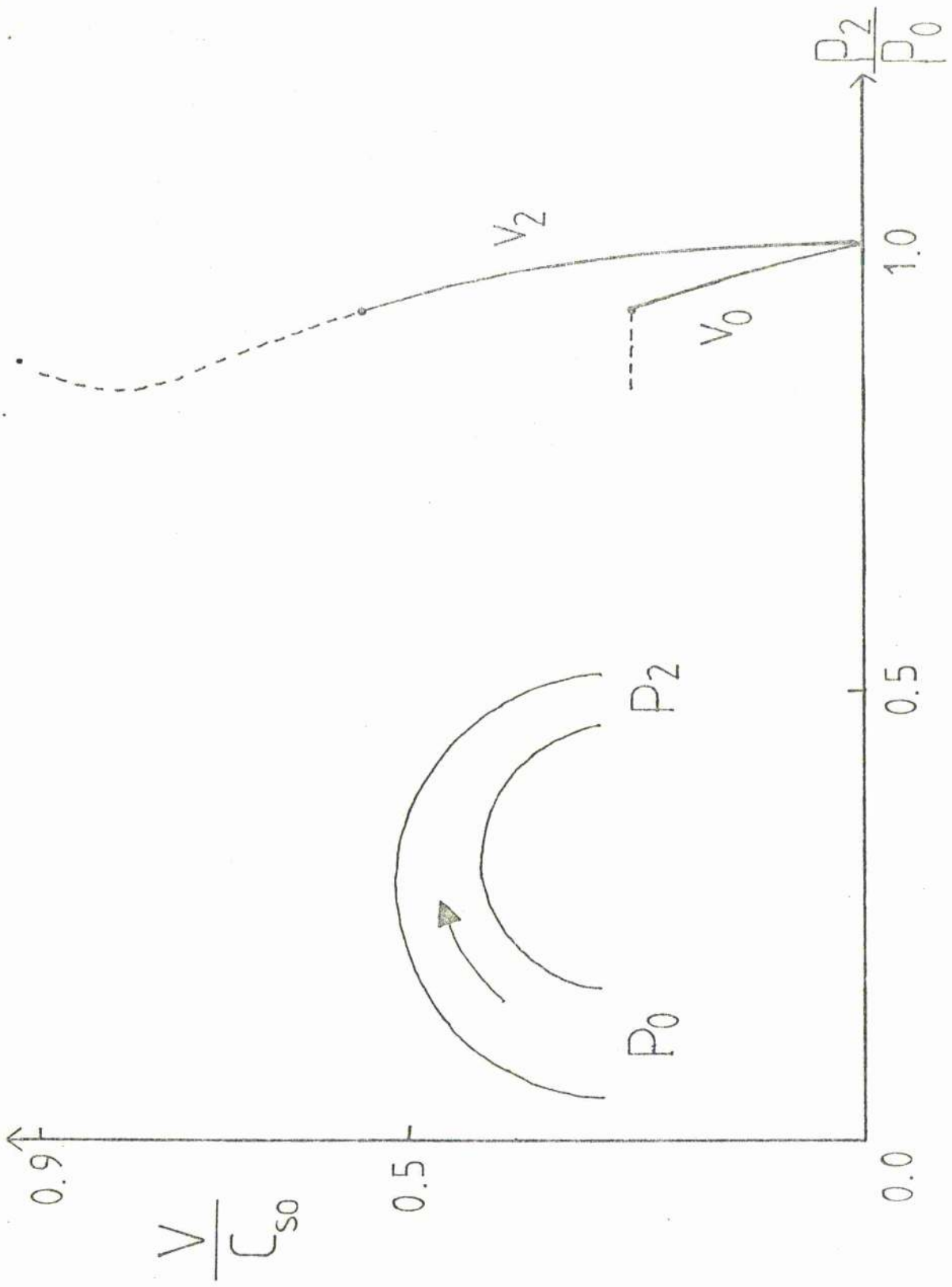

Figure 3.5a The flow speeds $\bar{v}_0$, $\bar{v}_2$ at the loop footpoints as a function of the imposed pressure ratio of isothermal flow in a converging loop with $\bar{A} = A_s/(4L)$. Solid lines denote subsonic flows and dashed lines indicate shocked flows. The loops have a half-length equal to the scale-height (i.e. $\bar{g} = 1$).

that the flow is accelerated into the converging loop. This can be shown from (3.25) and the equation of state which is

$$\frac{\bar{p}_2}{\bar{p}_0} = \frac{\bar{v}_0}{\bar{v}_2 \bar{A}_2},$$

for an isothermal loop. (3.25) gives

$$\bar{v}_2 = \frac{\bar{v}_0}{\bar{A}_2} \exp\left(\tfrac{1}{2}(\bar{v}_1^2 - \bar{v}_0^2)\right),$$

and so

$$\frac{\bar{p}_2}{\bar{p}_0} = \exp\left(-\tfrac{1}{2}(\bar{v}_2^2 - \bar{v}_0^2)\right).$$

Thus, if $\bar{A}$ converges, and $v_2 > v_0$, then clearly $p_2 < p_0$. Similarly, if $\bar{A}$ diverges, and $v_2 < v_0$, then $p_2 > p_0$. The effect of increasing the convergence by decreasing a is to make the sonic point move further away from the loop summit and increase the range of values of p_2/p_0 that generate subsonic flows. Table 3.3 shows allowed range of p_2/p_0 for subsonic and shocked flows.

Table 3.3

The variation with a of the critical starting velocity ($\bar{v}_0^*$), the range of pressure ratios and the sonic point location ($\bar{s}_c$) for isothermal flow in a loop of length 50Mm. a is the ratio of the loop areas at the two footpoints. For converging loops $a < 1$ and for diverging loops $a > 1$.

a	0.33	0.5	0.8	1.0	1.2	1.5	2.0
$\bar{v}_0^*$	0.199	0.238	0.301	0.340	0.378	0.435	0.534
$\left(\frac{p_2}{p_0}\right)_{min}$	0.703	0.840	0.790	0.752	0.725	0.696	0.667
$\left(\frac{p_2}{p_0}\right)_{max}$	1.000	1.000	1.000	1.000	1.022	1.057	1.120
$\bar{s}_c$	1.429	1.236	1.071	1.000	0.942	0.868	0.764

Diverging loops with

$$\bar{A}(\bar{s}) = 1 + \left(\frac{a-1}{2}\right)\bar{s} \quad , \quad a > 1$$

give a phase-plane that may be obtained from Figure 3.4 by rotating the solutions about the loop summit $\bar{s} = 1$. The corresponding footpoint flow speeds are shown in Figure 3.5b. All the subsonic flows now have $\bar{v}_2$ smaller than $\bar{v}_0$ so that $\bar{p}_2$ exceeds $\bar{p}_0$. The plasma is moving in the direction of increasing pressure, and so the flow is decelerated out of the diverging loop. For $\bar{p}_2 > \bar{p}_0$, there is also a shocked solution, so it is unclear which of the two possibilities will occur in practice. When $\bar{p}_2 < \bar{p}_0$, the flow is accelerated and only shocked solutions are possible. In Figure 3.5b, it should be noted that for some values of $\bar{p}_2/\bar{p}_0$ there are <u>two</u> possible shocked flows, similarly in Figure 3.5a, there are values of $\bar{p}_2/\bar{p}_0$ where there exist <u>both</u> subsonic and shocked flows. On the basis of the present model, both flows are feasible. However, it may transpire that one of the flows is unstable, and, in any case, which one occurs may depend on how they are set up.

It is worth pointing out that our loop area profiles are highly idealised, but one can visualise such fields being set up as follows. Given a uniform-area loop, continual photospheric motions will tend to twist up and compress the loop footpoints giving different magnetic fields and hence different areas at either end of a loop.

3.4 Adiabatic flow

In this section we extend our model from the simple isothermal case to one where the energy equation is approximated

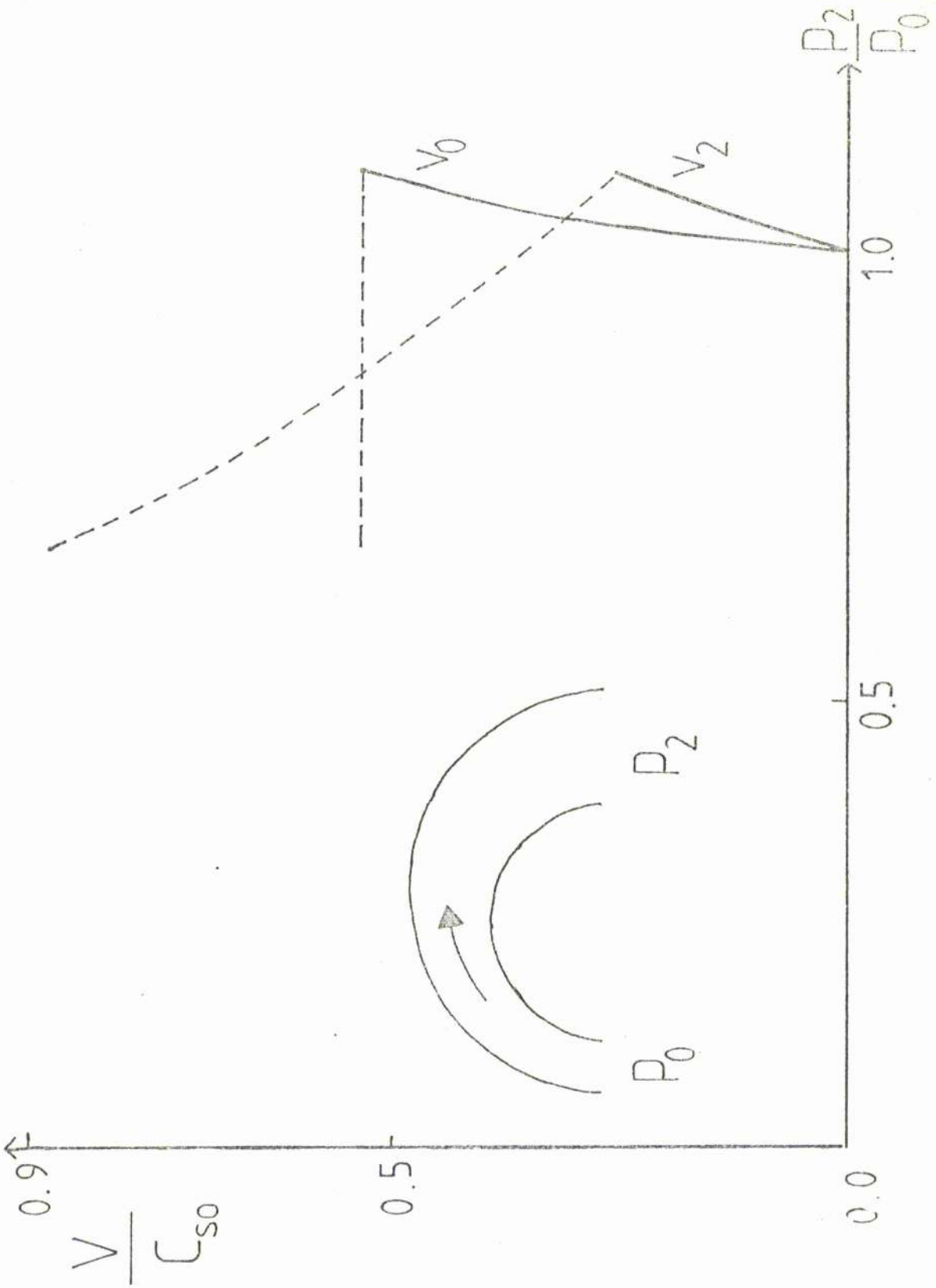

Figure 3.5b The flow speeds $\bar{v}_0$, $\bar{v}_2$ at the loop footpoints as a function of the imposed pressure ratio for isothermal flow in a diverging loop with $\tilde{A} = 1 + s/(2L)$. The notation is the same as Figure 3.5a.

by the adiabatic law. The equation of motion is now (3.17) and the critical point is determined by (3.19) - (3.21). By comparison with the isothermal case, the temperature is lower at the loop summit, which reduces the pressure gradient and hence also the flow speed.

3.4.1 Uniform Area

Consider first the simplest case, namely a loop whose cross-sectional area is constant with $\bar{A} \equiv 1$. The equation (3.17) becomes, on assuming $\gamma = \frac{5}{3}$,

$$\frac{1}{2}(\bar{v}^2 - \bar{v}_0^2) + \frac{3}{2}\left[\left(\frac{\bar{v}_0}{\bar{v}}\right)^{2/3} - 1\right] + \frac{6\bar{q}}{5\pi}\sin\left(\frac{\pi\bar{s}}{2}\right) = 0 \quad . \tag{3.27}$$

Equation (3.27) possesses a critical point at the loop summit ($\bar{s}=1$) with a flow speed

$$\bar{v}_c = \bar{v}_0^{1/4} \quad . \tag{3.28}$$

Substitution of (3.28) into (3.21) determines the corresponding base speed ($\bar{v}_0^*$) from

$$2\bar{v}_0^{*1/2} - \frac{1}{2}\bar{v}_0^{*2} - \frac{3}{2} + \frac{6\bar{q}}{5\pi} = 0 \quad . \tag{3.29}$$

For the particular case $\bar{q} = 1$, one finds $\bar{v}_0^* = 0.347$. Figure 3.6 shows the resulting velocity, temperature and pressure variations along the loop for a range of subsonic and shocked solutions. It can be seen that the effect of the flow is to reduce the loop temperature by typically a factor of 2 and to reduce the pressure by up to a factor of 10.

The effect of increasing the length of the loop through $\bar{q}$ is to decrease the value of $\bar{v}_0^*$ and thus increase the range

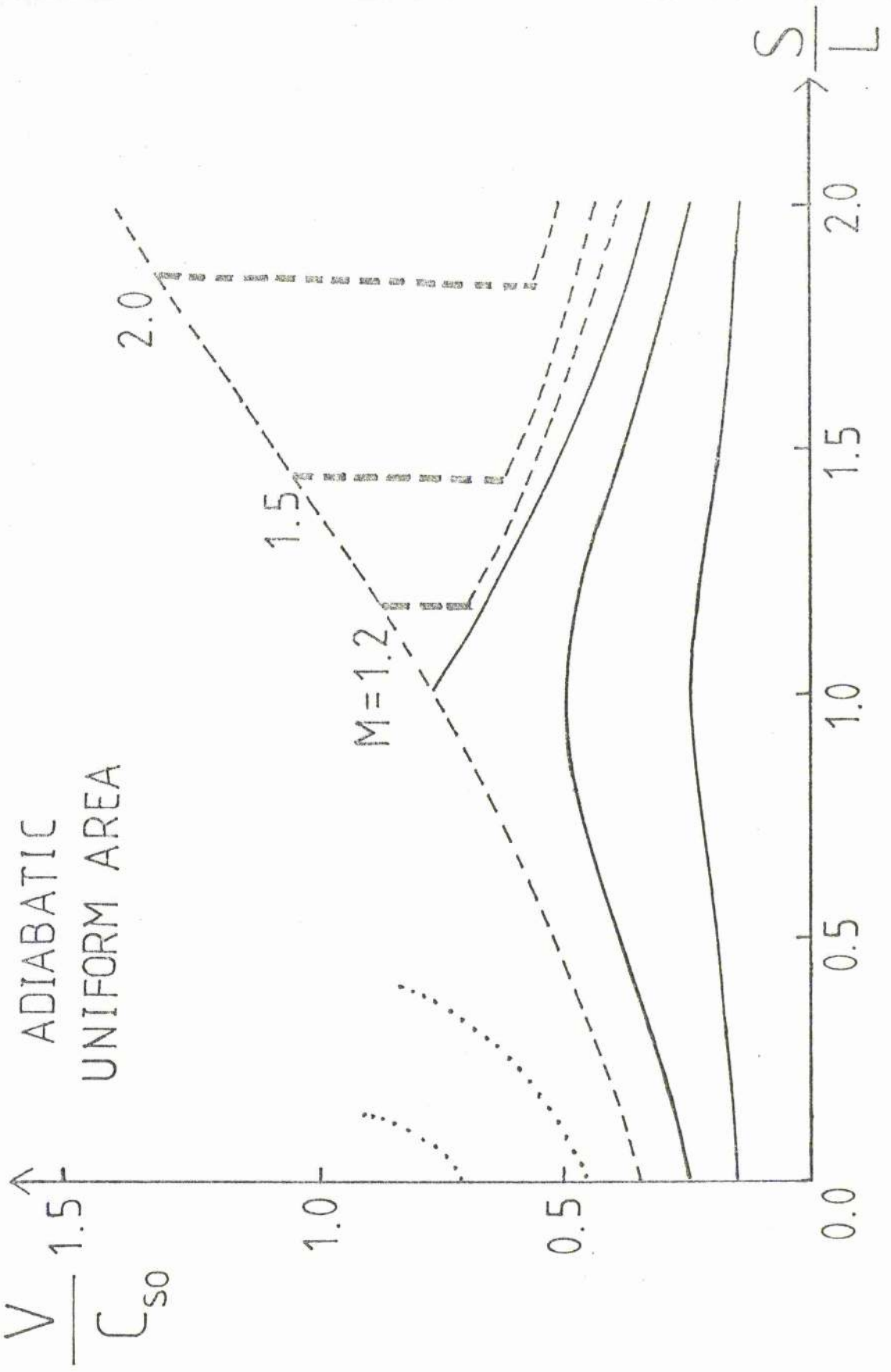

Figure 3.6a The velocity profile for adiabatic flow in a loop of uniform area and half-length 50Mm ($\bar{g}$=1). The sound speed (c_{so}) is 151 kms^{-1}. For the shocked solutions, the shock strength (M) is indicated. The base temperature and density are $T_0 = 10^6 K$, $n_0 = 7 \times 10^{14} m^{-3}$.

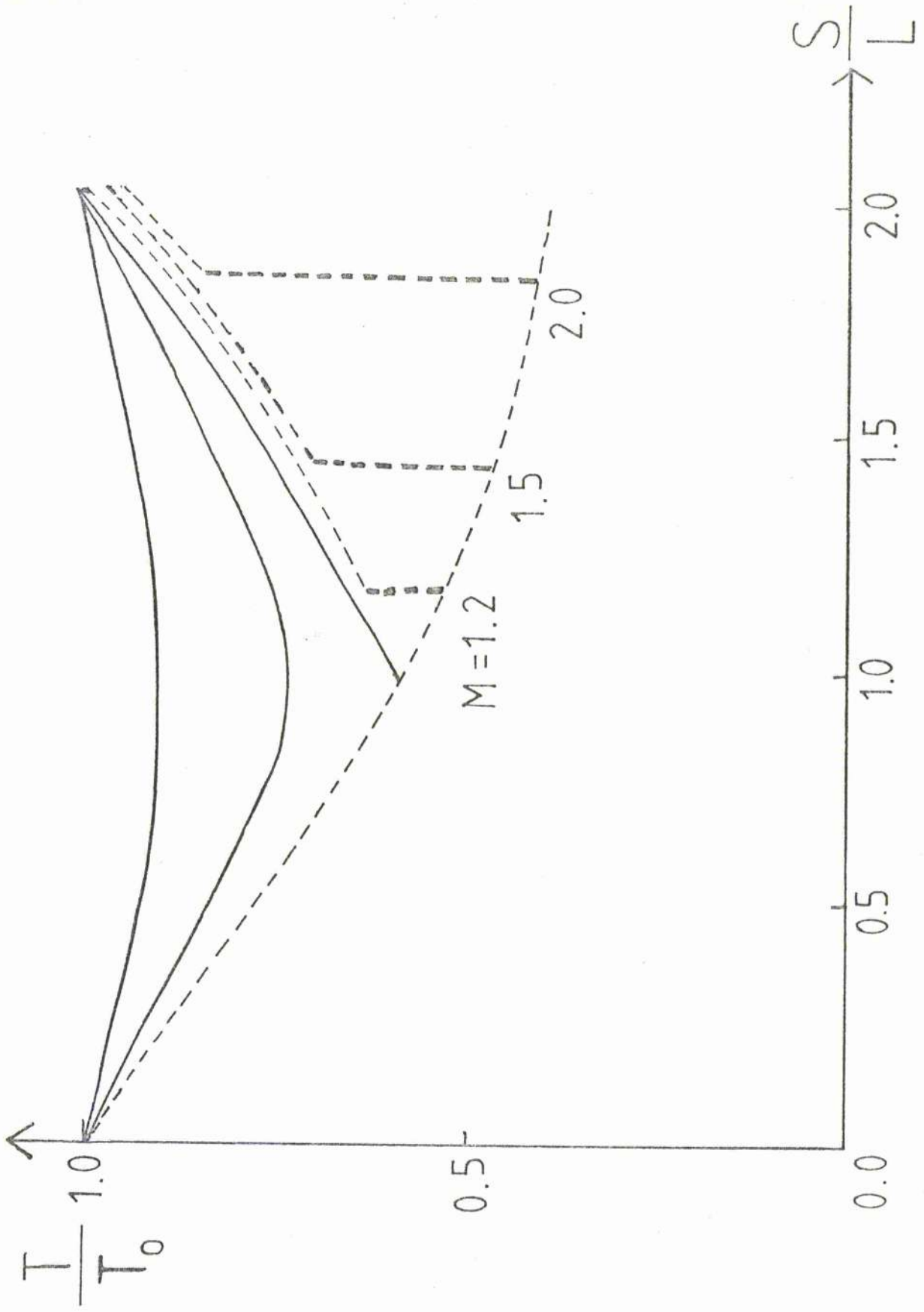

Figure 3.6b The temperature profile for adiabatic flow in a loop of uniform area and half-length 50mm. The notation is the same as Figure 3.6a.

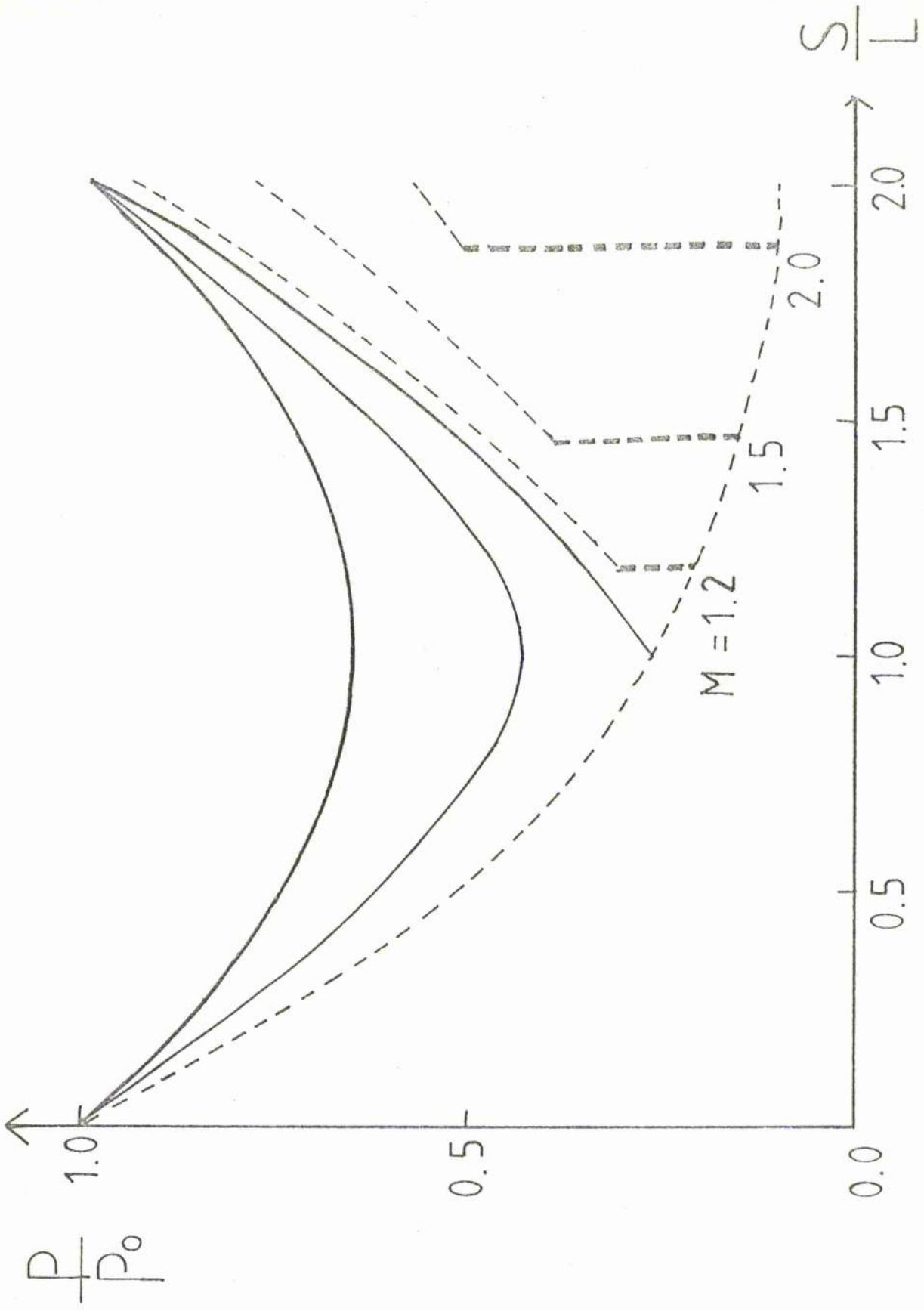

Figure 3.6c The pressure profile for adiabatic flow in a loop of uniform area and half-length 50mm. The notation is the same as Figure 3.6a.

of pressure ratios as shown in Table 3.4.

Table 3.4

The variation with loop half-length L(Mm) of the critical starting velocity ($\bar{v}_0^*$) and the minimum pressure ratio for adiabatic flow in a loop of uniform area.

L(Mm)	5	25	50	100	150
v_0^*	0.780	0.522	0.349	0.150	0.031
$\left(\frac{p_2}{p_0}\right)_{min}$	0.966	0.772	0.580	0.283	0.061

If, however, the loop is so long that $\bar{g}$ exceeds $5\pi/4$, the increasing solution through the critical point starts from the $\bar{s}$-axis rather than the $\bar{v}$-axis and so only the wholly supersonic solutions are possible.

3.4.2 Symmetric loops with varying area

Now suppose the loop possesses a cross-sectional area that varies along the loop but is symmetric about its top. The sonic point remains at the loop summit ($\bar{s}_c=1$), but according to (3.19), the flow speed there is

$$\bar{v}_c = \left(\frac{\bar{v}_0^*}{\bar{A}(1)}\right)^{1/4} . \qquad (3.30)$$

Equation (3.21) for the limiting initial speed becomes

$$2\left(\frac{\bar{v}_0^*}{\bar{A}(1)}\right)^{1/2} - \frac{1}{2}\bar{v}_0^{*2} - \frac{3}{2} + \frac{6\bar{g}}{5\pi} = 0 . \qquad (3.31)$$

If the loop is so long that $\bar{g} > \frac{5\pi}{4}$ this possesses only one solution, which, for moderate area increases is supersonic so that, as before, only supersonic solutions exist.

If the loop is so small that $\bar{g} < \frac{5\pi}{4}$ and the area does not increase too rapidly towards the summit, (3.31) possesses two solutions for $\bar{v}_0^*$ and subsonic flows do exist. However, when

$$1 < \bar{A}(1) < (1 - 0.6\bar{g}/\pi)^{-2} , \qquad (3.32)$$

one solution is less than 1 and the other greater than one. Furthermore, when

$$\bar{A}(1) > (1 - 0.8\bar{g}/\pi)^{-3/2} , \qquad (3.33)$$

there are no solutions to (3.31). These features are similar to those discussed by Kopp and Holzer (1976) for rapidly diverging coronal holes. For loops expanding up to the summit so much that $\bar{A}(1) > (1-0.6\bar{g}/\pi)^{-2}$, 4 additional critical points occur as shown in Figure 3.7b. However, if (3.33) is satisfied as well, the form of the phase-plane changes as in Kopp and Holzer (Figure 2). The critical solution no longer passes through the sonic point at the loop summit but through one near the base of the loop. The following example illustrates these features.

Consider for example an area which varies as

$$\bar{A}(\bar{s}) = 1 + (k-1)\sin^2\left(\frac{\pi\bar{s}}{2}\right) , \qquad (3.34)$$

and in particular set k = 20, so that the loop is twenty times as wide at the top as it is at the base. Then the critical flow speed at the loop summit is

$$\bar{v}_c = \left(\frac{\bar{v}_0^*}{\bar{v}_{c0}}\right)^{1/2}, \tag{3.35}$$

For the particular case $\bar{g} = 3.5$ (i.e. L = 175Mm) $\bar{v}_0^*$ follows from

$$2\left(\frac{\bar{v}_0^*}{\bar{v}_{c0}}\right)^{1/2} - \frac{1}{2}\bar{v}_0^{*2} - \frac{3}{2} + \frac{4.2}{\bar{v}_0^*} = 0, \tag{3.36}$$

and both solutions for $\bar{v}_0^*$ are subsonic. The first solution of (3.36) is $\bar{v}_0^* = 0.15$ and gives the phase plane shown in Figure 3.7a. This value for $\bar{v}_0^*$ is larger than the corresponding one for a loop of uniform area. One effect of the large increase in area from the footpoint is to make the velocity first decrease to a minimum value of 0.059 before increasing. Initial speeds ($\bar{v}_0$) lower than 0.15 give purely subsonic flows as expected, while those somewhat higher than 0.15 give unphysical solutions. The variation of some of the flow properties with the area factor k is shown in Table 3.5.

Table 3.5

The variation of $\bar{v}_0^*$, $(p_2/p_0)_{min}$ and $\bar{v}_{min}$ with k for adiabatic flow in a symmetric loop of half-length 175Mm ($\bar{g}$=3.5), whose area varies as $\bar{A} = 1 + (k-1)\sin^2\frac{1}{2}\bar{s}\pi$.

k	1	2	5	10	20
$\bar{v}_0^*$	0.007	0.013	0.038	0.068	0.150
$\left(\frac{p_2}{p_0}\right)_{min}$	0.016	0.038	0.090	0.139	0.286
$\bar{v}_{min}$	v_0^*	v_0^*	v_0^*	0.050	0.059

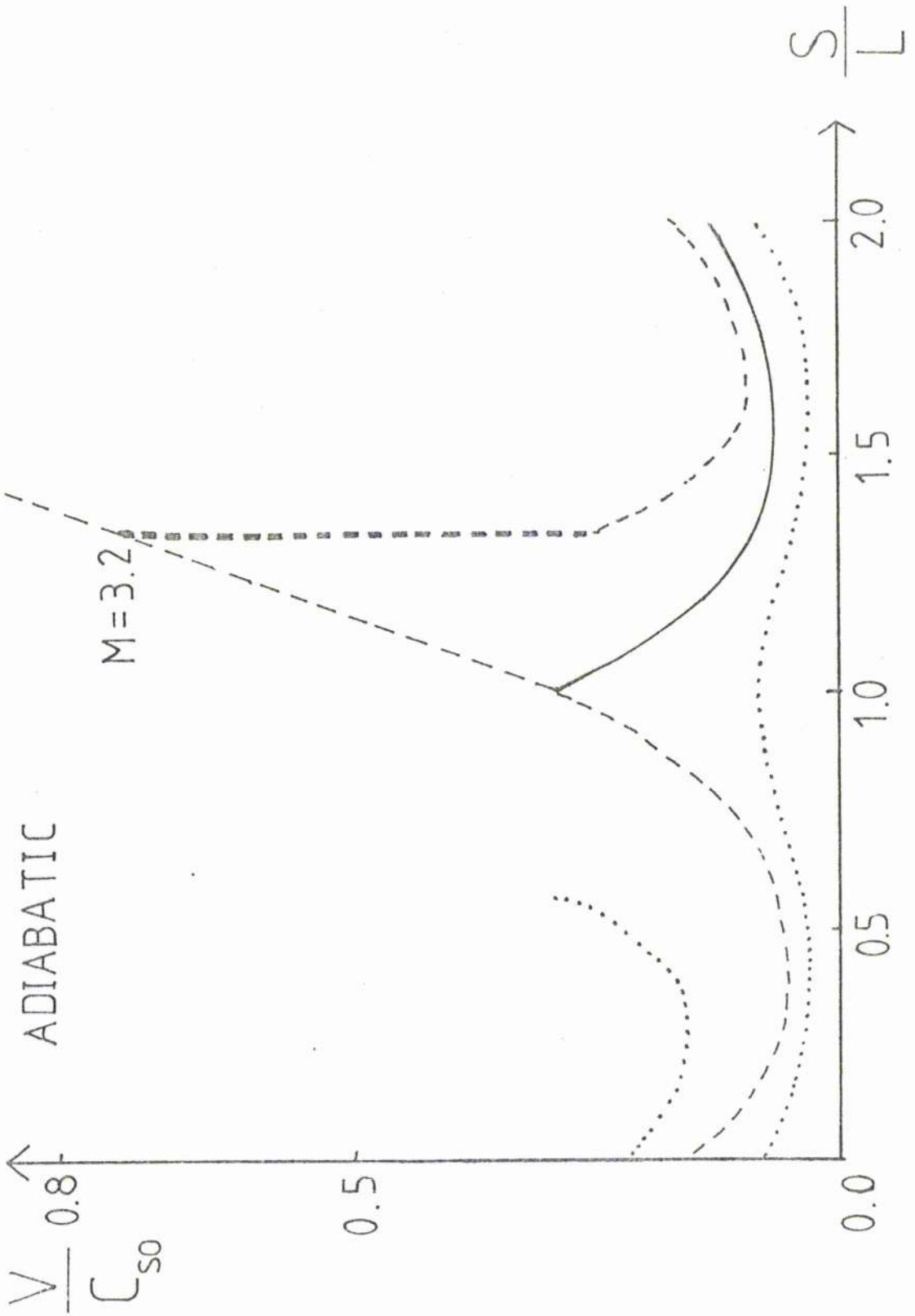

Figure 3.7a The phase plane for adiabatic flow along a symmetric loop whose cross-sectional area varies as $1 + 19\sin^{4}\frac{1}{2}s\pi$. The half-length of the loop is 175Mm ($\bar{s}=3.5$) and the sound speed c_{so} = 151 kms^{-1}. The starting speed is $\bar{v}_0^* = 0.15$.

The second solution to (3.36) is $\bar{v}_0^* = 0.61$ and also leads to shocked solutions of the subsonic-supersonic-shock-subsonic form. The phase plane is shown in Figure 3.7b and is symmetric about $\bar{s} = 1$ although the topology in the region $\bar{s} > 1$ has been omitted for clarity. In contrast to the isothermal solutions, the adiabatic flows give a phase-plane that depends on $\bar{v}_0$ and we have indicated the neighbouring topology by dotted curves. It is noticeable that additional X- and O-type critical points are present in Figure 3.7b the X-type point being at approximately $\bar{s} = 0.026$. Such a complicated topology was also found by Kopp and Holzer (1976) when modelling coronal hole expansion. One effect of the closed trajectories on the solutions for $\bar{v}_0^* = 0.61$ is to allow shocked solutions only for a small range of pressure ratios. Shocks that are located at $\bar{s} < 1.91$ give rise to unacceptable solutions that end up on closed trajectories. The acceptable solutions possess a pressure ratio in the range

$$0.817 < \bar{p}_2/\bar{p}_1 < 0.847 .$$

For initial speeds $\bar{v}_0$ between 0.61 and 0.91, the flows are purely subsonic, and then, above $\bar{v}_0 = 0.91$, the solutions become unphysical again. It should be noted that the pressure ratios for $\bar{v}_0^* = 0.61$ are also possible if $\bar{v}_0^* = 0.15$; which will occur may depend on how the flow is set up.

3.4.3 Asymmetric loops

A loop whose cross-sectional area increases or decreases continuously with distance gives results that are similar to those in Section 3.3.2, except that now the temperature varies. The location ($\bar{s}_c$) of the critical point, is the solution of

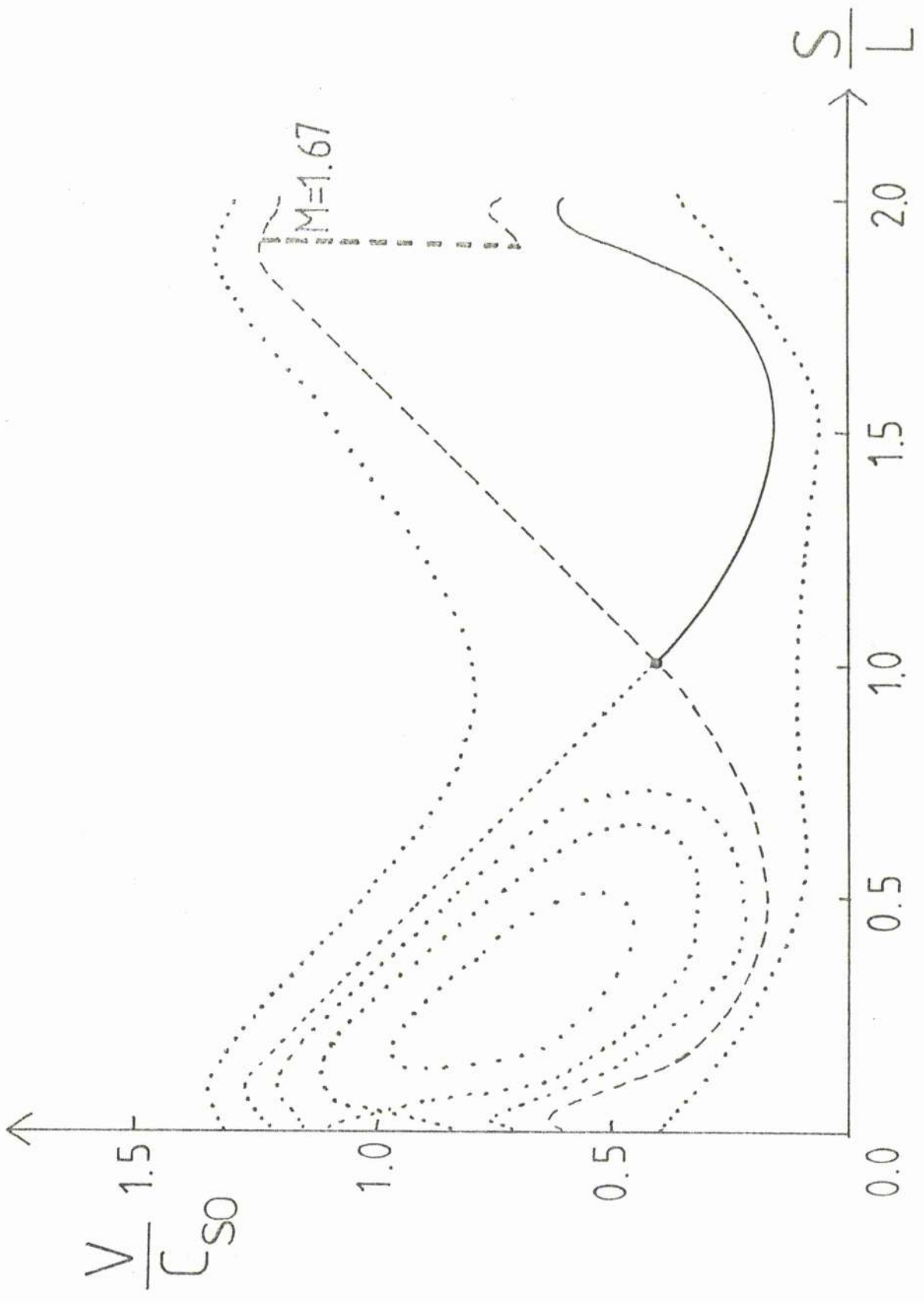

Figure 3.7b The phase plane for the symmetric loop shown in Figure 3.7a with $\bar{v}_0^* = 0.615$.

the following equation, obtained by eliminating $\bar{v}_c$ and $\bar{v}_0^*$ between (3.19 - 3.21):

$$4\left(\frac{d\bar{A}}{d\bar{s}}\right)^3_{\bar{s}=\bar{s}_c}\frac{3\bar{g}}{5}\cos\left(\frac{\pi\bar{s}_c}{2}\right)\bar{A}(\bar{s}_c) - \bar{A}^6(\bar{s}_c)\left(\frac{3\bar{g}}{5}\right)^4 * \cos^4\left(\frac{\pi\bar{s}_c}{2}\right) - 3\left(\frac{d\bar{A}}{d\bar{s}}\right)^4_{\bar{s}=\bar{s}_c}\left(1 - \frac{4\bar{g}}{5\pi}\sin\left(\frac{\pi\bar{s}_c}{2}\right)\right) = 0. \qquad (3.37)$$

In particular, for the linearly varying loop with

$$\bar{A}(\bar{s}) = 1 + \frac{(a-1)}{2}\bar{s}, \quad a > 0,$$

equation (3.35) becomes

$$4\left[\frac{(a-1)}{2}\right]^3\frac{3\bar{g}}{5}\cos\left(\frac{\pi\bar{s}_c}{2}\right)\left[1 + \frac{(a-1)}{2}\bar{s}_c\right] - \left[1 + \frac{(a-1)}{2}\bar{s}_c\right]^6\left(\frac{3\bar{g}}{5}\right)^4\cos^4\left(\frac{\pi\bar{s}_c}{2}\right) - 3\left[\frac{(a-1)}{2}\right]^4\left[1 - \frac{4\bar{g}}{5\pi}\sin\left(\frac{\pi\bar{s}_c}{2}\right)\right] = 0. \qquad (3.38)$$

This determines $\bar{s}_c$ in terms of the parameters a and $\bar{g}$, and then $\bar{v}_c$, $\bar{v}_0^*$ follow from (3.19) and (3.21), the results being shown in Table 3.6

Table 3.6

The variation of $\bar{s}_c$, $\bar{v}_0^*$ and $(p_2/p_0)_{min}$ with a and g for adiabatic flow.

$\bar{g} = \frac{1}{2}$ a	0.8	1.0	1.2	1.5
$\bar{s}_c$	1.18	1.0	0.85	0.59
$\bar{v}_0^*$	0.44	0.52	0.61	0.78
$\left(\frac{p_2}{p_0}\right)_{min}$	0.74	0.77	0.81	0.91

$\bar{g} = 1$						
a	0.5	0.8	1.0	1.2	1.5	2.0
$\bar{s}_c$	1.23	1.07	1.0	0.94	0.86	0.73
$\bar{v}_0^*$	0.24	0.3	0.35	0.39	0.46	0.61
$\left(\frac{p_2}{p_0}\right)_{min}$	0.66	0.61	0.58	0.56	0.55	0.55
$\bar{g} = 2$						
a	0.5	0.8	1.0	1.2	1.5	2.0
$\bar{s}_c$	1.07	1.02	1.0	0.98	0.96	0.93
$\bar{v}_0^*$	0.10	0.12	0.15	0.16	0.18	0.21
$\left(\frac{p_2}{p_0}\right)_{min}$	0.37	0.29	0.28	0.25	0.23	0.20

Only the subsonic solution for $\bar{v}_0^*$ is of interest, corresponding to a flow speed that increases rather than decreases through the critical point. It is noticeable that the range of possible pressure ratios is far greater than for the isothermal case.

3.5 Discussion

Our results for steady siphon flow in symmetric loops indicate that subsonic flows can be maintained when there is no pressure difference between the footpoints. (This is a result of the simplified energy equation; a more realistic equation shows that a departure from the static pressure ratio

(here unity) is necessary to produce a flow:- See Chapter 4.) As soon as a pressure difference is maintained, the resulting steady flow becomes supersonic at the summit and contains a shock wave. The flow is accelerated from the high-pressure footpoint to the low-pressure one. If the pressure difference is too large, the shock moves right down to the base of the loop. As the length of the loop is increased so the base speed ($\bar{v}_0^*$) falls in value and the range of allowable pressure ratios increases. If the summit cross-sectional area is large enough the flow speed possesses a minimum value at some point on the upflowing leg.

It is instructive to compare the dynamic solutions presented here with hydrostatic solutions. For an isothermal loop of uniform area, the density behaves as

$$\bar{n}_{static} = \exp\left(-\frac{2\bar{q}}{\pi}\sin\left(\frac{\pi\bar{s}}{2}\right)\right), \tag{3.39}$$

provided velocities are neglected. One may write equation (3.23) in the form

$$\bar{n} = \exp\left(-\frac{2\bar{q}}{\pi}\sin\left(\frac{\pi\bar{s}}{2}\right) - \frac{1}{2}\left(\bar{v}^2 - \bar{v}_0^2\right)\right)$$

$$= \bar{n}_{static}\exp\left(-\frac{1}{2}\left(\bar{v}^2 - \bar{v}_0^2\right)\right). \tag{3.40}$$

Since $\bar{v} > \bar{v}_0$ all along the loop, then

$$\bar{n} < \bar{n}_{static},$$

and the density is lowered all along the loop. One may show a similar result for adiabatic flow.

An attempt has been made by Noci (1981) to compare his siphon flow results with observations. He calculates the

E.U.V. emission measure and, since the emission measure depends on n^2, one would expect a large flow to produce an observable difference. Noci finds that, whereas subsonic flows give rise to small differences from the static case, supersonic flows show large variations and can be regarded as a signature for such flows. However, ionisation equilibrium has been assumed in these calculations and with some ions (e.g. Si_{XII}), substantial errors could be incurred. This has been considered by Raymond and Dupree (1978) and Joselyn et al. (1979) and should be incorporated in future calculations.

We have discussed adiabatic siphon flow in a purely coronal context so far, but such flows could occur elsewhere in the solar atmosphere wherever pressure differences exist. In particular, siphon flows have been proposed as an explanation for Evershed flow in sunspots (Meyer and Schmidt, 1968; Maltby, 1975). On expects such a flow to be along a rapidly diverging flux tube (such as discussed in Section 3.3.2) due to the large decrease in magnetic field as one leaves a sunspot. The converse applies to the inward flow. In fact, siphon flow would only appear to explain the inward flow, the outward case having $p_2 \gg p_0$.

In the next Chapter we improve the present simplified model by incorporating the energetics of the system.

Chapter 4: STEADY-STATE FLOWS IN CORONAL MAGNETIC LOOPS: II THE ENERGETICS OF THE FLOW

4.1 Introduction

In Chapter 3, the theory of isothermal and adiabatic siphon flows was developed, and the next step is to examine how these results are altered by the adoption of a full energy equation. However, it is necessary to discuss briefly the energetics of static coronal loops first: an extensive recent review has been given by Monsignori-Fossi (1981), so we shall just outline the basic properties.

For a static loop of length 2L and negligible gravity (i.e. uniform pressure) the equations of state (3.4), momentum (3.1) and energy (3.5) reduce to a single differential equation in temperature,

$$\frac{d}{ds}\left(10^{-6}T^{5/2}\frac{dT}{ds}\right) = \frac{p^2\chi T^{\alpha-2}}{4k_B^2} - \frac{ph}{2k_B T} \quad , \tag{4.1}$$

which is to be solved subject to the boundary conditions

$$\left.\begin{aligned} T &= T_0 \quad , \quad s = 0 \quad , \\ \frac{dT}{ds} &= 0 \quad , \quad s = L \quad , \end{aligned}\right\} \tag{4.2}$$

the summit temperature gradient vanishing due to the imposed symmetry around the loop summit (See Vesecky et al., 1979 for a discussion of non-symmetric solutions). If T_0 is taken as 10^6 K, the solutions of this equation depends on three parameters; the pressure, p, the loop length, 2L and the mechanical heating, h, (Hood and Priest, 1979a). (An additional parameter is the form of the heating function: we have chosen the heating as constant per unit mass.)

However, by choosing T_0 as 10^6 K, the problem of treating the narrow transition zone has been avoided and several authors (Rosner et al., 1978, Vesecky et al., 1979, Landini and Monsignori-Fossi, 1981 and Serio et al., 1981) have modelled loops down to temperatures of 2×10^4 K. The reason for this choice of T_0 is that a temperature plateau is thought to exist at this point (Basri et al., 1979; Vernazza et al., 1981) and so the conductive flux is small there. This has led these authors to propose that at $T = 2 \times 10^4$ K

$$10^{-11} T^{5/2} \frac{\partial T}{\partial s} = 0 , \quad s = 0 . \tag{4.3}$$

Loops satisfying this condition are said to be thermally isolated. However, equation (4.1) is now over-prescribed and so some relationship must exist between the parameters p, L and h. This gives rise to scaling laws between the various parameters (See Rosner et al., 1978; Hood and Priest, 1979a; Roberts and Frankenthal, 1980; Levine and Pye, 1980; Chiuderi et al., 1981), and they may be of use when the error in observations is reduced to make a comparison with such scaling laws worthwhile.

There are, however, serious objections to the use of boundary condition (4.3). All of the calculations involving (4.3) use an optically-thin radiative loss function. Unfortunately, the solar atmosphere below about 5×10^4 K is optically thick, as were the calculations performed that produced the temperature plateau at 2×10^4 K, and it is doubtful whether one can apply an optically thin model to this plateau. For this reason, it seems desirable to either

start modelling above the transition zone or model down to the temperature minimum (Nagai, 1980, Peres et al., 1981). Other transition-zone problems are the presence of non-thermal velocities (Jordan, 1980) and the validity of the fluid equations (Spicer, 1979). In this chapter, we adopt a value for T_0 of 10^6 K.

Equations (4.1) and (4.2) have been solved numerically by Craig et al., (1978), who show that the form of the emission measure does not depend significantly on the form of the heating function, as well as Chiuderi et al., (1981), Hood and Priest (1979a), Roberts and Frankenthal (1980) and Wragg and Priest (1981), who all vary the parameters p, L and h (in the case of Wragg and Priest, gravity is also included).

The thermal stability of coronal loops has been studied by Antiochos (1979), Habbal and Rosner (1979), Hood and Priest (1980a) and Chiuderi et al. (1981). Antiochos and Hood and Priest find that thermally isolated loops are unstable although Antiochos has used an over-simplified radiative loss function (Chiuderi et al., 1981). On the other hand, Habbal and Rosner and Chiuderi et al. found that thermally isolated loops are stable. The analysis of Habbal and Rosner is incorrect due to a restrictive form of the temperature perturbation (Priest, 1981b), but the discrepency between the other analyses is possibly due to a subtle difference in boundary conditions.

Probably the most interesting feature to come out of static loop calculations is the possibility of thermal non-equilibrium. The energy equation (4.1) is non-linear and does not always possess a unique solution. As the loop

pressure is varied, the summit temperature may take on one or three solutions (Figure 4.1). If the loop pressure is too big, the summit temperature (T_1) cannot remain over 10^6 K and drops to below 10^5 K (the evolution of this cooling is studied in Chapter 5). This feature was first discussed in this context by Hood and Priest (1979a), who examined in some detail the existence of multiple solutions to the energy equation.

They also found that non-equilibrium arises if the length is increased or heating decreased. Hood and Priest (1979a) and Roberts and Frankenthal (1980) demonstrated the existence of non-equilibrium analytically, and Wragg and Priest (1981) showed that hydrostatic loops possessed the same feature. The difference between instability and non-equilibrium is as follows. With instability, an equilibrium (whose existence may be unlikely) becomes unstable and may evolve to a new equilibrium, possibly at a slow rate. With non-equilibrium, no equilibrium actually exists and the evolution may be much more violent than with instability.

In this chapter, we examine how the solutions of the static energy balance equation are affected by a steady flow, how the adiabatic and isothermal results change and how the presence of steady flows alters the onset of non-equilibrium.

4.2 Basic equations

The loop geometry is the same as in Chapter 3, namely semi-circular (although we also examine a loop in which gravity is neglected in Section 4.5), and the cross-sectional area may vary along the loop length. The basic equations are

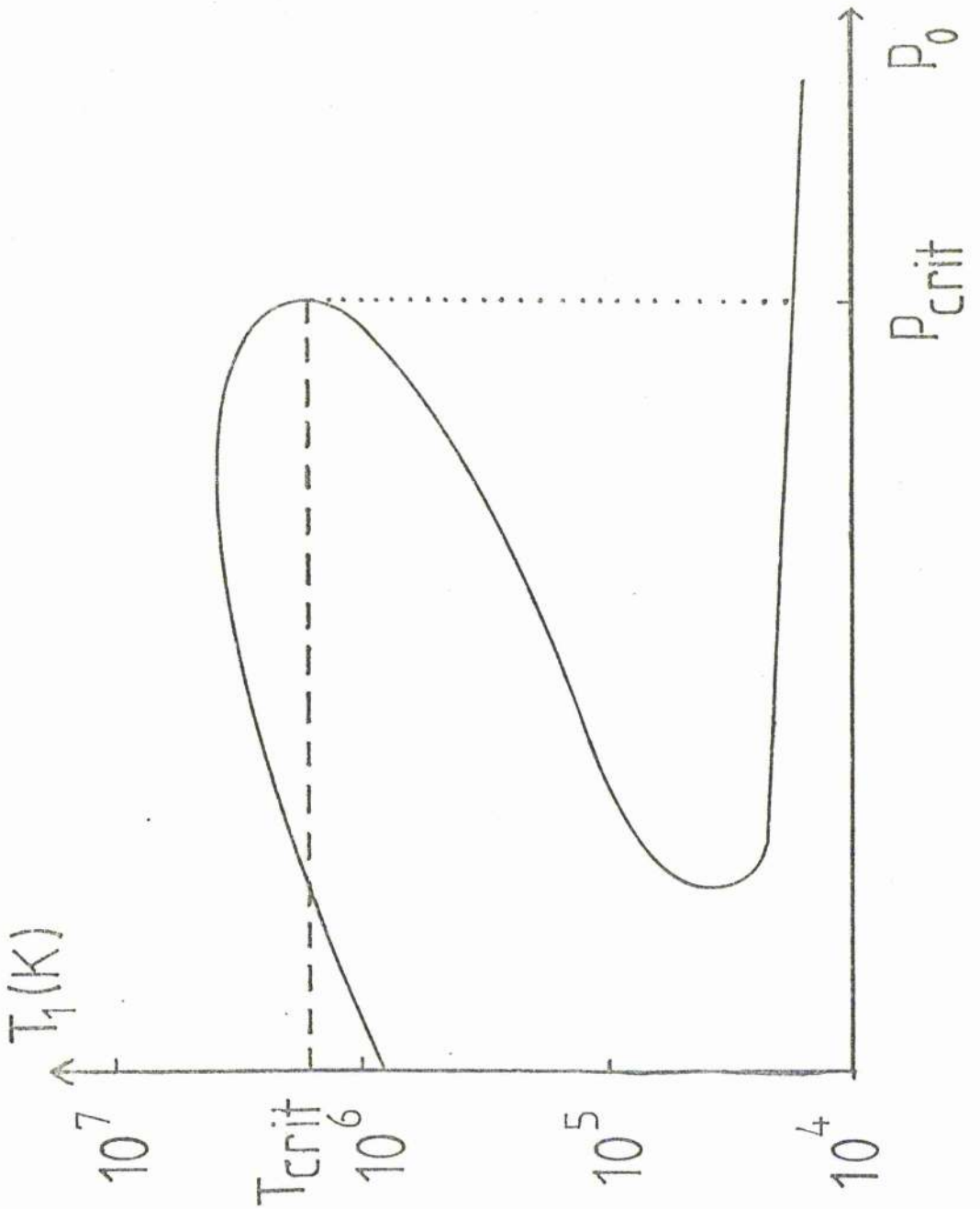

Figure 4.1 The summit temperature (T_1) of a coronal loop as a function of the (uniform) pressure. At the point (p_{crit}, T_{crit}) point no hot solutions exist and the loop cools to below 10^5 K.

(3.1) - (3.5) of Chapter 3 along with boundary conditions (3.6): we restate them here for convenience. The equations of continuity, momentum, state and energy are

$$\frac{\partial}{\partial s}(\rho v A) = 0, \tag{4.4}$$

$$\rho v \frac{\partial v}{\partial s} = -\frac{\partial p}{\partial s} - \rho g \cos\left(\frac{\pi s}{2L}\right), \tag{4.5}$$

$$p = 2nk_B T, \tag{4.6}$$

$$\frac{n^{\gamma} v}{\gamma - 1}\frac{\partial}{\partial s}\left(\frac{p}{n^{\gamma}}\right) - \frac{1}{A}\frac{\partial}{\partial s}\left(10^{-11} A T^{5/2}\frac{\partial T}{\partial s}\right) = nh - n^2 \chi T^{\alpha}, \tag{4.7}$$

subject to

$$\left.\begin{aligned} T = T_0, \quad n = n_0, \quad s = 0, \\ T = T_2, \quad n = n_2, \quad s = 2L. \end{aligned}\right\} \tag{4.8}$$

These are non-dimensionalised as follows :

$$\bar{s} = s/L, \quad \bar{v} = v/c_{s0}, \quad \bar{n} = n/n_c, \quad \bar{T} = T/T_0,$$

$$c_{s0}^2 = \frac{2k_B T_0}{m_H}, \quad \bar{A} = A/A_0, \quad \bar{\chi} = \frac{\chi T_0^{\alpha}}{\chi_0 T_0^{\alpha_0}},$$

$$\bar{L}^2 = L^2\left(\frac{\chi_0 n_c^2 T_0^{\alpha_0 - 7/2}}{10^{-11}}\right), \quad \bar{h} = \frac{h}{(n_c \chi_0 T_0^{\alpha_0})},$$

$$\bar{F}_0 = \left(\frac{c_{s0}^3 n_c m_H L}{10^{-11} T_0^{7/2}}\right), \quad \bar{g} = \frac{m_H g L}{2k_B T_0}.$$

Here, $\bar{L}^2$ is the ratio of radiation to conduction, $\bar{h}$ is the

ratio of heating to some reference radiative loss and $\bar{F}_0$ is the ratio of the conduction to enthalpy. $\bar{g}$ represents the importance of gravity (as in Chapter 3), c_{so} is the base sound speed, and zero subscripts represent footpoint values. n_c is a coronal reference density (taken as 5×10^{14} m^{-3}) which should not be confused with the base density (n_o) which may vary.

Combining equations (4.4) - (4.8) gives two equations,

$$\frac{d\bar{n}}{d\bar{s}} = \frac{\bar{n}}{\left(\bar{T} - \left(\frac{\bar{V}_o \bar{n}_o}{\bar{n}\bar{A}}\right)^2\right)} \left[-\frac{d\bar{T}}{d\bar{s}} + \left(\frac{\bar{n}_o \bar{V}_o}{\bar{n}\bar{A}}\right)^2 \frac{1}{\bar{A}} \frac{d\bar{A}}{d\bar{s}} - \bar{g} \cos\left(\frac{\pi \bar{s}}{2}\right) \right] , \tag{4.9}$$

and

$$\bar{n}_o \bar{V}_o \bar{F}_o \left(\frac{1}{\gamma - 1} \frac{d\bar{T}}{d\bar{s}} - \frac{\bar{T}}{\bar{n}} \frac{d\bar{n}}{d\bar{s}} \right) - \frac{d}{d\bar{s}} \left(\bar{A} \bar{T}^{5/2} \frac{d\bar{T}}{d\bar{s}} \right) = \bar{A} \bar{L}^2 \left(\bar{n} \bar{h} - \bar{n}^2 \bar{\chi} \bar{T}^{\alpha} \right) . \tag{4.10}$$

$\bar{F}_o$ and $\bar{g}$ can be written in terms of $\bar{L}$ as follows

$$\left.\begin{aligned} \bar{F}_o &= \frac{c_{so}^3 n_c m_H}{10^{-11} T_o^{7/2}} \left[\frac{10^{-11} T_o^{7/2 - \alpha_o}}{\chi_o n_c^2} \right]^{1/2} \bar{L} = a\bar{L} , \\ \bar{g} &= \frac{m_H g}{2 k_B T_o} \left[\frac{10^{-11} T_o^{7/2 - \alpha_o}}{\chi_o n_c^2} \right]^{1/2} \bar{L} = b\bar{L} , \end{aligned}\right\} \tag{4.11}$$

and equations (4.9) and (4.10) can be written in terms of four parameters ($\bar{n}_o$, $\bar{L}$, $\bar{h}$ and $\bar{v}_o$). One can understand

the meaning of these parameters physically as follows. $\bar{n}_o$ will be determined possibly by photospheric processes twisting up and relaxing the magnetic field and hence altering the gas pressure and density. L is determined by the magnetic structure of the loop, $\bar{h}$ by the (unknown) heating mechanism and $\bar{v}_o$ by the footpoint pressure ratio. Thus all four parameters may perhaps be physically independent.

4.3 Analytical solutions

4.3.1 The asymmetric role of conduction

We first discuss how the position of the sonic point is affected by the inclusion of an energy equation. The flow becomes sonic when $d\bar{v}/d\bar{s}$ (or $d\bar{n}/d\bar{s}$) is undefined, and, for a loop of uniform area, equation (4.9) implies that

$$\left.\begin{aligned} \frac{d\bar{T}}{d\bar{s}} &= -\bar{\gamma}\cos\left(\frac{\pi \bar{s}_{crit}}{2}\right), \\ \text{and} \qquad \bar{T} &= \left(\frac{\bar{v}_o \bar{n}_o}{\bar{n}}\right)^2, \end{aligned}\right\} \qquad (4.12)$$

at this point. Clearly, the sonic point no longer occurs at the summit and its position depends on the temperature profile. If $d\bar{T}/d\bar{s} > 0$, then $\bar{s}_{crit} > 1$ and if $d\bar{T}/d\bar{s} < 0$, $\bar{s}_{crit} < 1$.

If we consider a loop with $T_2 > T_o$, then $d\bar{T}/d\bar{s}$ will be positive for most of the loop and the sonic point lies on the downflowing leg. This will produce a smaller range of supersonic flows; the analagous effect was found in Section 3.3.2. for a converging loop.

In general one cannot find the sonic point analytically but the numerical calculation is relatively simple. The effect of coupling in the energy equation to the siphon flow

problem is to remove the symmetric features outlined in Chapter 3, but in doing so, it allows us to find wholly subsonic flows for a loop of uniform area. It is also worth pointing out that the critical point and the temperature maximum will not generally coincide.

4.3.2 Order-of-magnitude

In the following two sections, we analyse equations (4.9) and (4.10) by different approaches. In Section 4.3.3, the parameter $\bar{L}$ is assumed small but first a simple order-of-magnitude analysis is attempted.

It is assumed that the velocities in the loop are small so that terms of order $\bar{v}_o^2$ in the momentum equation can be neglected but those of order $\bar{v}_o$ in the energy equation retained. Also, if gravity and area variations are neglected, (4.9) becomes

$$\bar{p} = \bar{p}_o = \text{constant}, \tag{4.13}$$

and (4.10) reduces to

$$\frac{d}{d\bar{s}}\left(\bar{T}^{5/2}\frac{d\bar{T}}{d\bar{s}}\right) - \frac{\bar{F}_o \bar{n}_o \bar{v}_o \gamma}{\gamma-1}\frac{d\bar{T}}{d\bar{s}} = \frac{1}{\bar{L}^2 \bar{n}_o^2}\left(\bar{\chi}\bar{T}^{\alpha-2} - \frac{\bar{h}}{\bar{n}_o \bar{T}}\right), \tag{4.14}$$

where $\bar{n}_o = \bar{p}_o$.

The temperature maximum, $\bar{T}_m$, will not be located at the summit, but at some distance d beyond it, as shown in Figure 4.2. The temperature gradient is approximated by

$$\left.\begin{aligned} \frac{1}{\bar{L}}\frac{d\bar{T}}{d\bar{s}} &= \frac{\bar{T}_m - 1}{\bar{L} + d} \\ \text{up to and} \\ \frac{1}{\bar{L}}\frac{d\bar{T}}{d\bar{s}} &= \frac{1 - \bar{T}_m}{\bar{L} - d} \end{aligned}\right\} \tag{4.15}$$

beyond the temperature maximum.

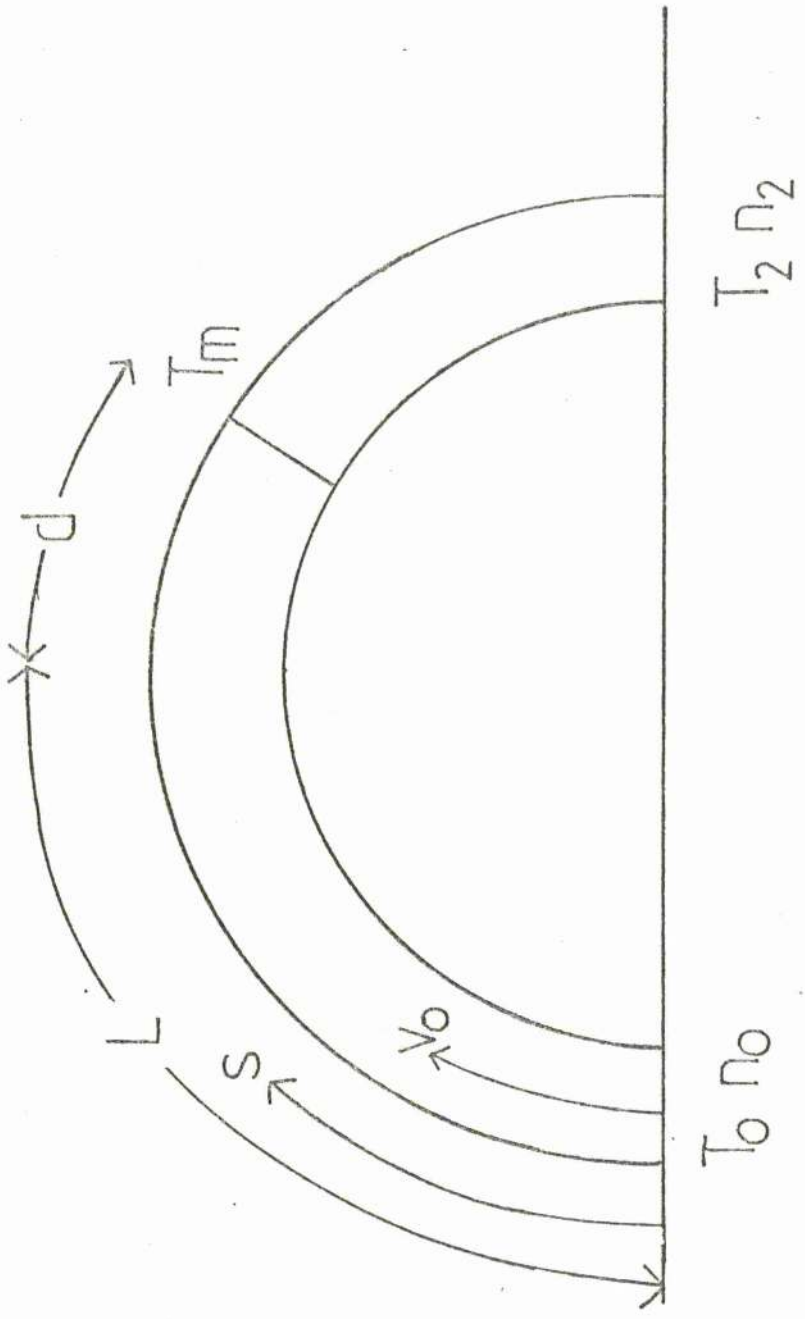

Figure 4.2 The notation for a loop of length 2L, with the position from one footpoint measured by the co-ordinate s and the quantities at the two footpoints denoted by subscripts 0 and 2. The temperature maximum (T_m) is located a distance d beyond the summit.

Equation (4.14) is then written as two equations

$$\frac{(1-\bar{T}_m)\bar{T}_m^{5/2}}{(L\pm d)^2} - \frac{\bar{L}^2\bar{n}_0^2}{L^2}\left(\bar{\chi}\bar{T}_m^{\lambda-2} - \frac{\bar{h}}{\bar{n}_0\bar{T}_m}\right) \mp$$

$$\mp \frac{\bar{F}_0\bar{v}_0\bar{n}_0\gamma(\bar{T}_m-1)}{L(L\pm d)(\gamma-1)} = 0 ; \qquad (4.16)$$

subtracting gives an expression for d:

$$\frac{d}{L} = \frac{\gamma\bar{v}_0\bar{F}_0\bar{T}_m^{\lambda}(\bar{T}_m-1)}{2(\gamma-1)\bar{L}^2\bar{n}_0\left[\frac{\bar{h}\bar{T}_m}{\bar{n}_0} - \bar{\chi}\bar{T}_m^{\lambda}\right]} , \qquad (4.17)$$

and so (4.16) determines $\bar{T}_m$.

Equation (4.17) immediately shows that the shift in maximum temperature beyond the summit is directly proportional to the flow along the loop and inversely proportional to the base density, heating and loop length. This is shown in Figure 4.3. Also, as expected, when $\bar{v}_0 \to 0$, d also tends to zero and the results of Hood and Priest (1979a) are recovered.

4.3.3 Small-parameter expansion in $\bar{L}$

A common approach in solving complicated non-linear systems of ordinary differential equations is to examine the solution when one of the governing parameters of the system is small. On use of (4.11), equations (4.9) and (4.10) can be written in terms of $\bar{L}$ (for uniform area) as

$$\frac{d\bar{n}}{d\bar{s}} = \frac{\bar{n}}{\left(\bar{T} - \left(\frac{\bar{v}_0\bar{n}_0}{\bar{n}}\right)^2\right)}\left[-\frac{d\bar{T}}{d\bar{s}} - b\bar{L}\cos\left(\frac{\pi\bar{s}}{2}\right)\right] , \qquad (4.18)$$

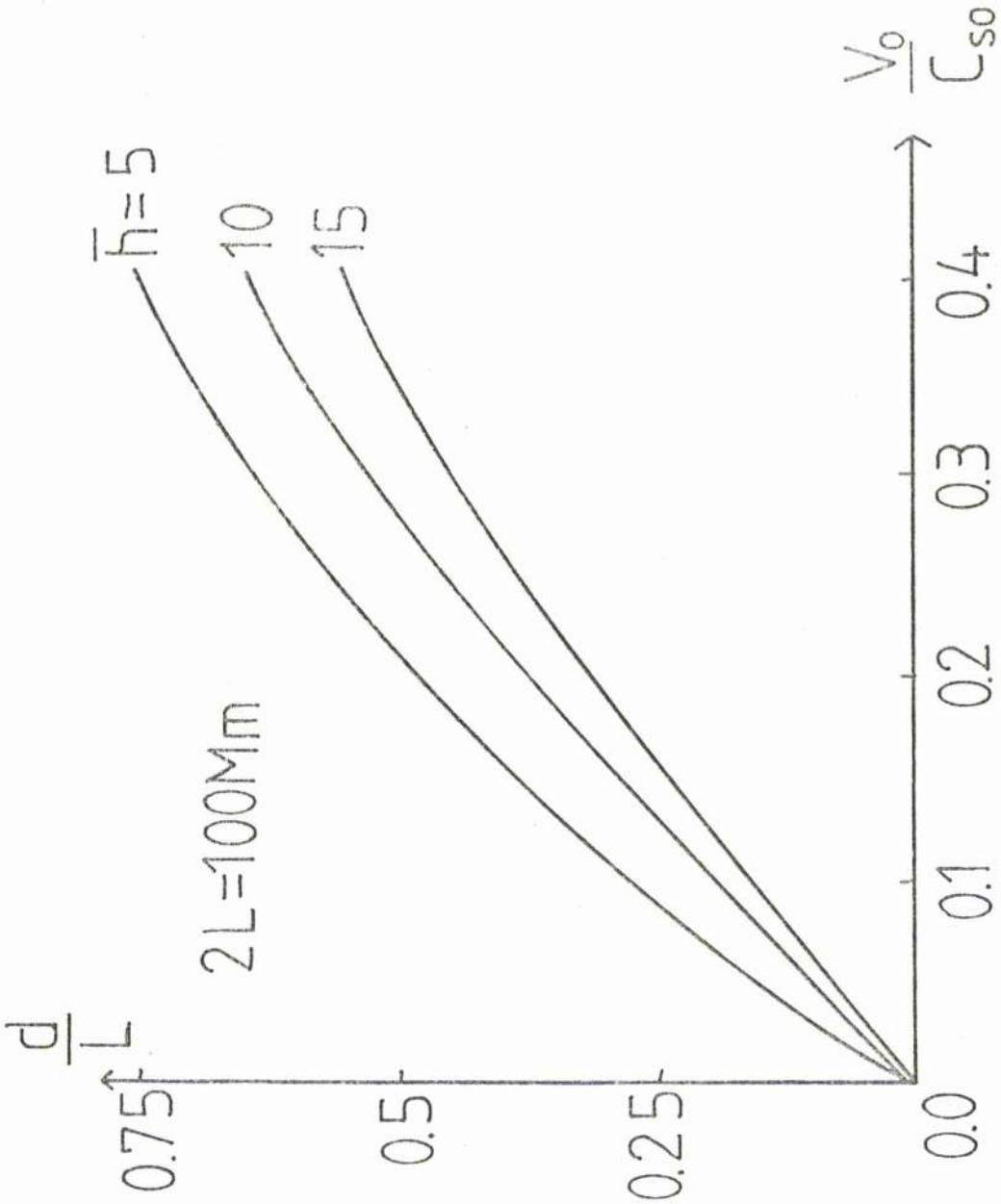

Figure 4.3 The shift, d, of the temperature maximum from the summit as a function of the base velocity (v_0) for a loop of base density 5×10^{14} m^{-3} and length 100Mm ($=10^8$m). The curves show the variation for three values of the heating ($\bar{h}$). The base sound speed (c_{s0}) is 120 km s^{-1} for $T_0=10^6$K.

and

$$\bar{n}_o \bar{V}_o \alpha \bar{L} \left[\frac{1}{\gamma - 1} \frac{d\bar{T}}{d\bar{s}} - \frac{\bar{T}}{\bar{n}} \frac{d\bar{n}}{d\bar{s}} \right] - \frac{d}{d\bar{s}} \left(\bar{T}^{5/2} \frac{d\bar{T}}{d\bar{s}} \right) =$$

$$= \bar{L}^2 \left(\bar{n} \bar{h} - \bar{n}^2 \bar{\chi} \bar{T}^{\alpha} \right) . \qquad (4.19)$$

The limit $\bar{L} \ll 1$ occurs when the loop is so short that conduction dominates. (In doing such an expansion, it is assumed that $\bar{n}_o$ is of order unity).

An expression for $\bar{L}$ in terms of L with T_o taken as 10^6 K is

$$\bar{L}^2 = 1.7 \times 10^{-4} L^2 ,$$

where L is measured in Mm, and so

$$L \lesssim 10 - 15 \text{ Mm} .$$

Consider the following solutions to (4.18) and (4.19):

$$\left. \begin{aligned} \bar{T}(\bar{s}) &= \sum_{i=0}^{N} \bar{L}^i \bar{t}_i(\bar{s}) , \\ \bar{n}(\bar{s}) &= \sum_{i=0}^{N} \bar{L}^i \bar{n}_i(\bar{s}) , \end{aligned} \right\} \qquad (4.20)$$

subject to the boundary conditions

$$\left. \begin{aligned} \bar{T}(0) &= \bar{T}(2) = 1 , \\ \bar{n}(0) &= \bar{n}_0 , \\ \bar{n}(2) &= \bar{n}_2 . \end{aligned} \right\} \qquad (4.21)$$

The solutions to $O(\bar{L}^2)$ are

$$\bar{T} = 1 + \bar{L}^2 \left[\left(\frac{\bar{s}^2}{2} - \bar{s} \right) \left(\bar{n}_o^2 \bar{\chi} - \bar{n}_o \bar{h} \right) + \right.$$

$$\left. - \frac{4ab \bar{n}_o \bar{V}_o}{\pi^2 (1 - \bar{V}_o^2)} \left(\cos \frac{\pi \bar{s}}{2} - 1 + \bar{s} \right) \right] + O(\bar{L}^3) ,$$

(4.22)

and

$$\frac{\bar{n}}{\bar{n}_0} = 1 - \frac{2h\bar{L}}{\pi(1-\bar{v}_0^2)}\sin\left(\frac{\pi\bar{s}}{2}\right) + \frac{\bar{L}^2}{(1-\bar{v}_0^2)}\left[\left\{\frac{4h^2\bar{v}_0^2}{\pi^2(1-\bar{v}_0^2)}\sin^2\left(\frac{\bar{s}\pi}{2}\right)+\right.\right.$$

$$+\left(\frac{\bar{s}^2}{2}-\bar{s}\right)\left(\bar{n}_0^2\bar{\chi}-\bar{n}_0\bar{h}\right) - \frac{4ab\bar{v}_0\bar{n}_0}{\pi^2}\left(\cos\left(\frac{\pi\bar{s}}{2}\right)-\right.$$

$$\left.\left.-1+\bar{s}\right)+\frac{4b}{\pi^2}\sin^2\left(\frac{\pi\bar{s}}{2}\right)\right\}\Bigg] + O(\bar{L}^3), \qquad (4.23)$$

where α has been set equal to zero.

(4.23)

Differentiating (4.22) with respect of $\bar{s}$ gives

$$\frac{d\bar{T}}{d\bar{s}} = \bar{L}^2\left[(\bar{n}_0^2\bar{\chi}-\bar{n}_0\bar{h})(\bar{s}-1) - \frac{4ab\bar{v}_0\bar{n}_0}{\pi^2(1-\bar{v}_0^2)} *\right.$$

$$\left. * \left(1-\frac{\pi}{2}\sin\left(\frac{\pi\bar{s}}{2}\right)\right)\right],$$

which is zero at some point, $\bar{s} > 1$. Thus the maximum temperature now lies on the downflowing leg, provided the radiation is less than the heating at the base (generally true in the corona). However, one cannot deduce anything about the pressure ratio, since, to $O(\bar{L}^2)$, $\bar{n}_0 = \bar{n}_2$.

Consider now boundary conditions which allow the temperature to vary between footpoints, such as

$$\left.\begin{aligned}\bar{T}(0) &= 1,\\ \bar{T}(2) &= 1+\bar{L}\Theta,\end{aligned}\right\} \qquad (4.24)$$

To order $\bar{L}$, the solutions are

$$\bar{T} = 1+\bar{s}\frac{\bar{L}}{2}\Theta, \qquad (4.25)$$

$$\frac{\bar{n}}{\bar{n}_0} = 1 - \frac{\bar{L}}{(1-\bar{v}_0^2)}\left[\frac{\Theta\bar{s}}{2} + \frac{2b}{\pi}\sin\left(\frac{\pi\bar{s}}{2}\right)\right] . \tag{4.26}$$

Hence, the temperature increases or decreases linearly along the loop. The footpoint density $\bar{n}_2$ is given by

$$\bar{n}_2 = \bar{n}_0\left(1 - \frac{\bar{L}\Theta}{(1-\bar{v}_0^2)}\right) , \tag{4.27}$$

and the pressure ratio is

$$\frac{\bar{p}_2}{\bar{p}_0} = \bar{n}_0\left(1 - \frac{\Theta\bar{L}\bar{v}_0^2}{(1-\bar{v}_0^2)}\right) . \tag{4.28}$$

Thus, if $\bar{T}_2 > \bar{T}_0$, a flow will be driven from left to right in Figure 4.2 provided $\bar{p}_2 < \bar{p}_0$. One must solve (4.27) to obtain $\bar{v}_0$ which gives the correct $\bar{n}_2$. Finally, if the temperature is given by (4.25), the sonic point is given by the solution of (4.12) in the form

$$\bar{s}_{crit} = \frac{2}{\pi}\cos^{-1}\left(-\frac{\Theta}{2b}\right) ,$$

so $\bar{s}_{crit} > 1$, as expected from Section 4.3.1.

4.4 Numerical solutions

We wish to solve (4.9) and (4.10) subject to boundary conditions (4.8). Firstly (4.9) and (4.10) must be written as first-order differential equations,

$$\frac{d\bar{n}}{d\bar{s}} = \frac{\bar{n}}{\left(\bar{T} - \left(\frac{\bar{v}_0\bar{n}_0}{\bar{n}\bar{A}}\right)^2\right)}\left[\frac{\bar{W}}{\bar{A}}\bar{T}^{-5/2} + \left(\frac{\bar{n}_0\bar{v}_0}{\bar{n}\bar{A}}\right)^2\frac{1}{\bar{A}}\frac{d\bar{A}}{d\bar{s}} - \bar{Q}\cos\left(\frac{\pi\bar{s}}{2}\right)\right] , \tag{4.29}$$

$$\bar{n}_0 \bar{v}_0 \bar{F}_0 \left[\frac{1}{\gamma-1} \frac{\bar{W}}{\bar{A}\bar{T}^{5/2}} - \frac{\bar{T}}{\bar{n}} \frac{d\bar{n}}{d\bar{s}} \right] - \frac{d\bar{W}}{d\bar{s}} =$$

$$= \bar{A}\bar{L}^2 \left(\bar{n}\bar{h} - \bar{n}^2 \bar{\chi} \bar{T}^{\alpha} \right) , \tag{4.30}$$

$$\frac{d\bar{T}}{d\bar{s}} = \frac{\bar{W}\bar{T}^{-5/2}}{\bar{A}} . \tag{4.31}$$

If $\bar{g} \neq 0$, this system has no critical points (i.e. $d\bar{n}/d\bar{s}$, $d\bar{T}/d\bar{s}$ and $d\bar{W}/d\bar{s}$ never vanish simultaneously). If, however, $\bar{g} \equiv 0$, then the system must be examined for critical points. Assuming that all velocities are subsonic, the pressure is then constant and (4.29) - (4.31) reduce to,

$$\bar{n}_0 \frac{\bar{v}_0 \bar{F}_0 \gamma}{\gamma-1} \frac{\bar{W}}{\bar{A}\bar{T}^{5/2}} - \frac{d\bar{W}}{d\bar{s}} = \bar{L}^2 \left(\bar{p} \frac{\bar{h}}{\bar{T}} - \bar{p}^2 \bar{\chi} \bar{T}^{\alpha-2} \right) , \tag{4.32}$$

$$\frac{d\bar{T}}{d\bar{s}} = \bar{W}\bar{T}^{-5/2} . \tag{4.33}$$

If $\bar{v}_0 \equiv 0$, Hood and Priest found that the critical point is a centre point (if $\alpha < 1$) or a saddle point (if $\alpha > 1$), the centre point corresponding to coronal values of α. When $\bar{v}_0 \neq 0$ the critical point is given by

$$\left. \begin{aligned} \bar{W}_c &= 0 , \\ \bar{T}_c &= \left(\frac{\bar{\chi}\bar{p}}{\bar{h}} \right)^{-\frac{1}{\alpha-1}} , \end{aligned} \right\} \tag{4.34}$$

and close to the critical point, equations (4.32) and (4.33) are

$$\frac{d\bar{\xi}}{d\bar{s}} = \bar{\omega} \bar{T}_c^{-5/2} , \tag{4.34}$$

$$\frac{d\bar{\omega}}{d\bar{s}} = \bar{L}^2\bar{\rho}^2(\alpha-1)\bar{\chi}\bar{T}_c^{\alpha-2}\bar{t} + \frac{\bar{n}_0\bar{v}_0\gamma\bar{F}_0\omega\bar{T}_c^{-5/2}}{\gamma-1}, \qquad (4.35)$$

where

$$\bar{t} = \bar{T} - \bar{T}_c,$$
$$\bar{\omega} = \bar{W} - \bar{W}_c.$$

Assuming that solutions near the critical point behave as $e^{\lambda\bar{s}}$ this gives

$$\lambda = -\frac{\bar{F}_0\bar{v}_0}{2}\bar{T}_c^{-5/2} \pm \left(\bar{\rho}^2\bar{L}^2\bar{\chi}\bar{T}_c^{\alpha-11/2}(\alpha-1)\right)^{1/2}.$$

If $\alpha < 0$ (as in the corona), then the centre point of Hood and Priest has now become a spiral point. Thus the symmetry present in the static case has been lost.

To solve (4.29) - (4.31) we prescribe $\bar{n}_0$ and $\bar{T}_0$ and iterate $(d\bar{T}/d\bar{s})_{\bar{s}=0}$ to obtain $\bar{T}_2$. Different values of $\bar{v}_0$ give different values of $\bar{n}_2$ and hence a range of pressure ratios is found. We use a standard Runge-Kutta scheme to solve this system. In Sections 4.4.1 - 4.4.4, T_0 is fixed as 10^6 K and n_0 as 5×10^{14} m^{-3} (so that $\bar{n}_0 = \bar{T}_0 = 1$). Then Section 4.5 discusses the consequences of varying $\bar{n}_0$. We first examine how a flow affects a given static temperature profile with $T_0 = T_2$, then relax this constraint and investigate the range of siphon flows produced by different boundary conditions, and finally re-examine the cases of loops with varying area discussed in Chapter 3.

4.4.1 The effect of flows on a static loop

Wragg and Priest (1981) have investigated the energetics of loops in hydrostatic equilibrium. Such a loop is chosen

here with a summit temperature of 2×10^6 K and then the footpoint pressure, P_2, is gradually decreased. A flow will develop and we here examine how a steady flow modifies the static loop properties. Figures 4.4a,b show the behaviour of the loop temperature and density (dashed lines are the static case, solid ones the dynamic case). As predicted in Section 4.3, the position of the temperature maximum is moved along the downflowing leg and its value is decreased giving an asymmetric temperature profile. This asymmetry can be explained by the fact that the convective term in the energy equation acts as a heat sink when the temperature gradient is positive and as a source when negative. In other words, the decrease in temperature occurs because a flow tends to suck up cool matter towards the summit and transport hot material away from it. Figure 4.4a also shows that conduction is enhanced along the downflowing leg.

The density is enhanced along some of the upflowing leg (Fig. 4.4b), but for the rest of the loop it is decreased, as mentioned in Chapter 3. The density minimum (and hence velocity maximum) is moved to the downflowing leg, as mentioned in Section 4.3. Figure 4.4c shows the variation in the shift of maximum temperature, d, beyond the summit as a function of the footpoint upflow, $\bar{v}_o$, and hence pressure ratio. For a given loop length, an increase in pressure ratio increases both the base velocity and the position of maximum temperature from the loop summit. This continues until $\bar{v}_o$ reaches its critical value (see Chapter 3): at this point, the flow can become supersonic at the sonic point and shocked solutions

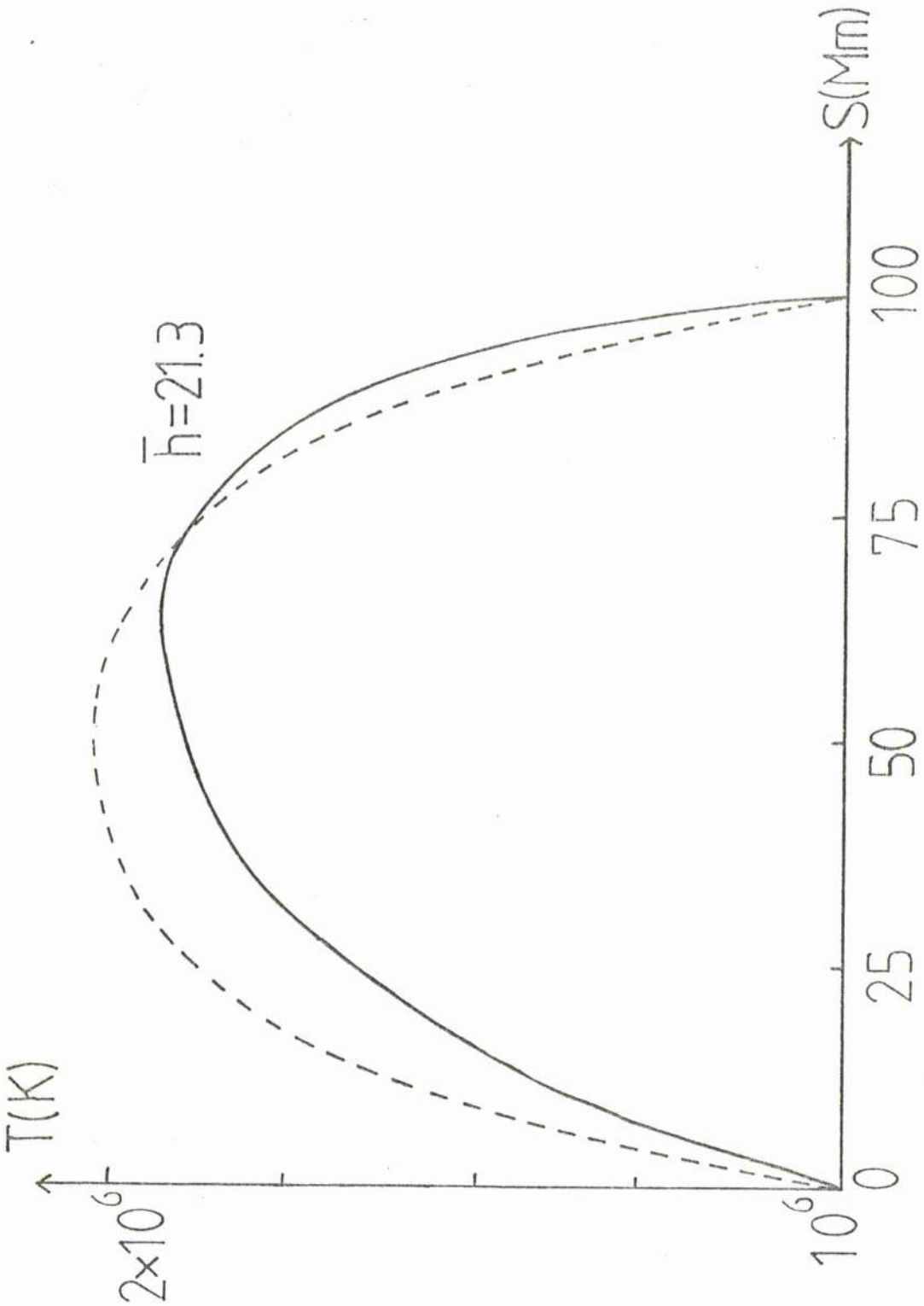

Figure 4.4a The effect of a subsonic flow on the temperature profile of a static loop of length 2L and uniform area. The heating is chosen to give a static summit temperature of 2×10^6 K. The static solution is shown by a dashed curve and a solution with base velocity of $v_o=0.2\ c_{so}$ by the solid curve.

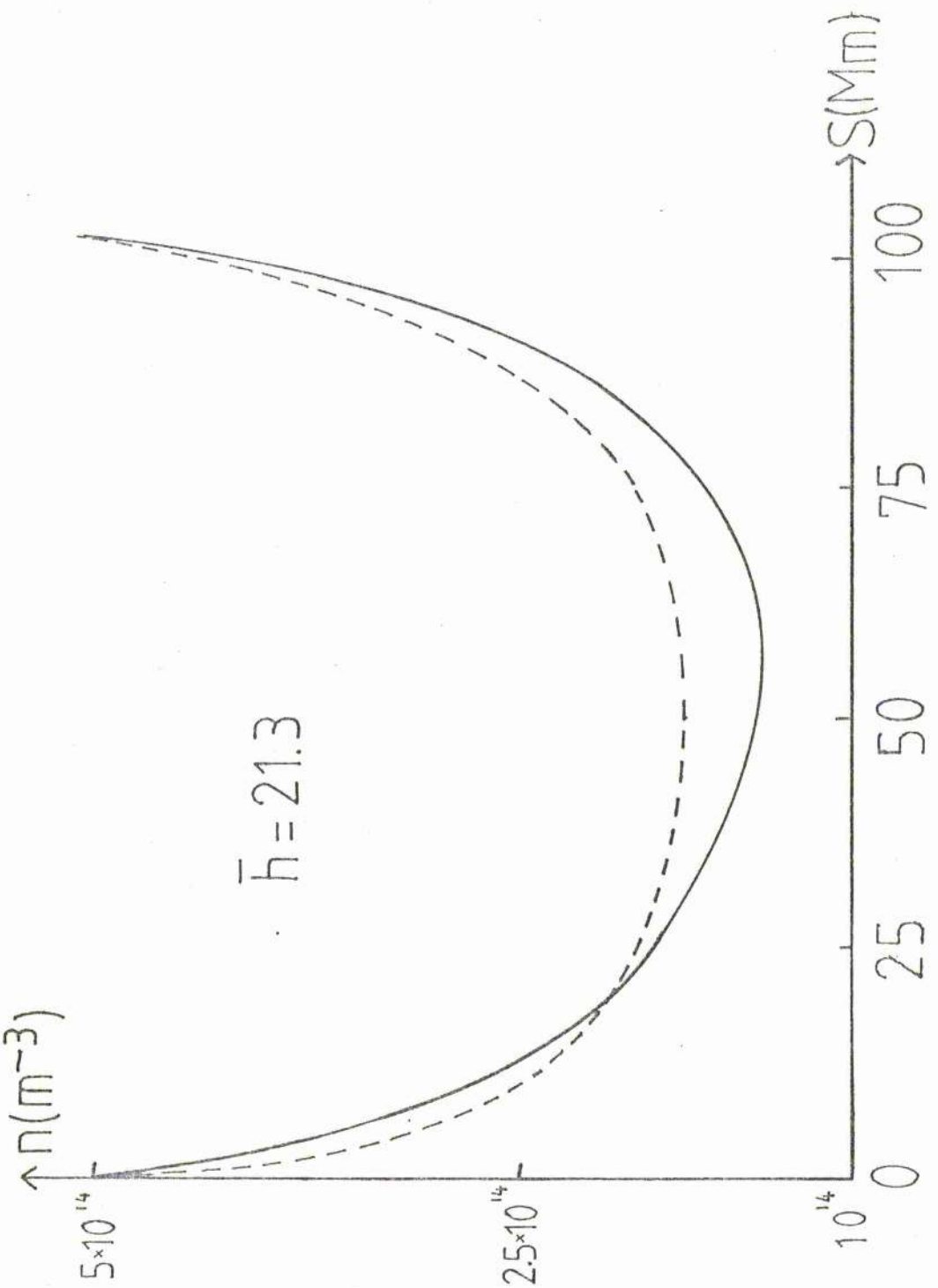

Figure 4.4b The effect of a subsonic flow on the density profile of a static loop of length 2L and uniform area. The notation is as in Figure 4.4a.

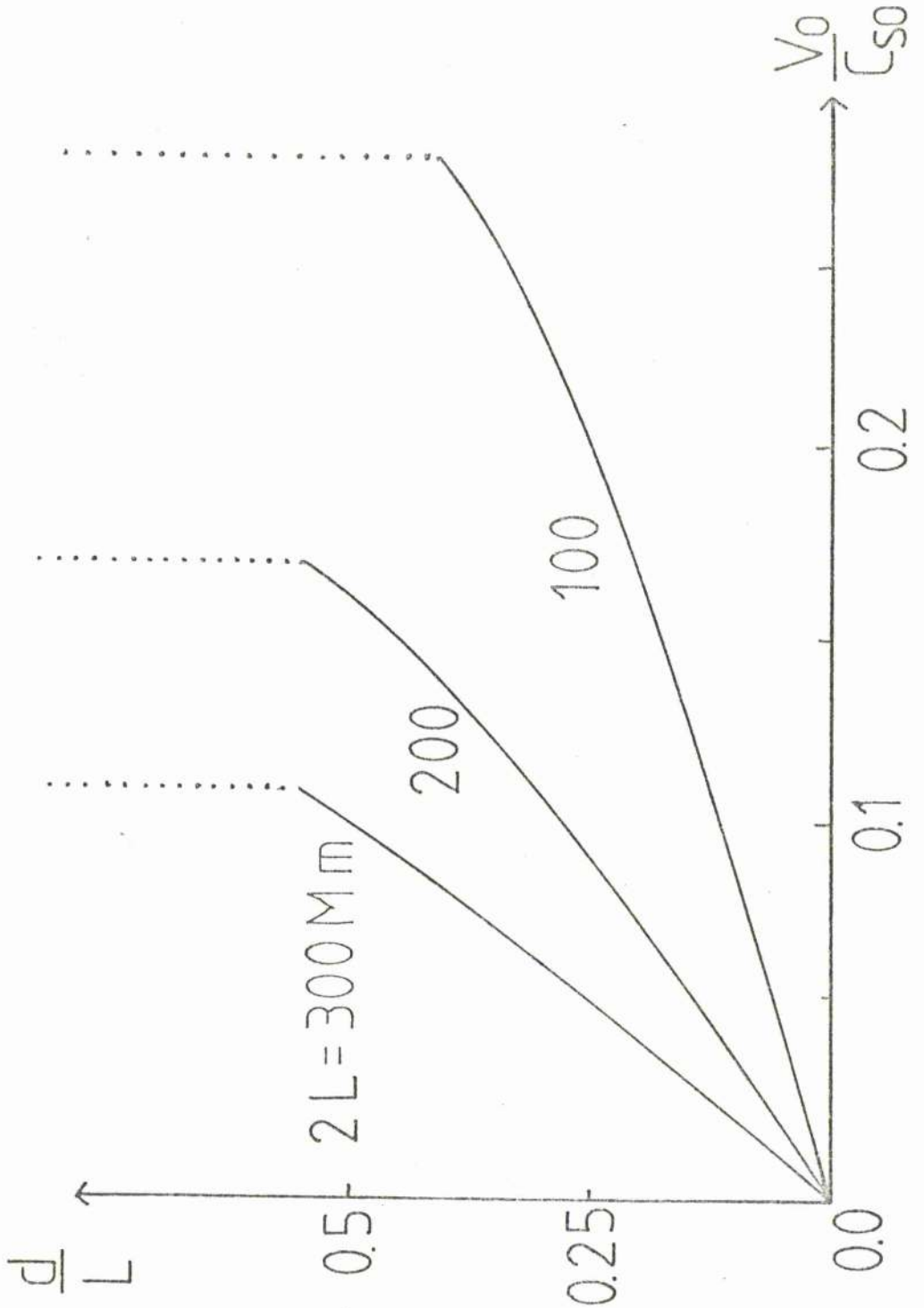

Figure 4.4c The variation with the base velocity v_o/c_{so} of the distance d of the maximum temperature from the loop summit. The heating is chosen to give a summit temperature of 2×10^6 K when $v_o = 0$. The base sound speed (c_{so}) is 120 km s^{-1} and shocked solutions are shown by dotted lines.

become possible. The position of maximum temperature is then the shock position.

It should be pointed out that, as L varies, then so does the heating necessary for a summit temperature of 2×10^6 K, and so equation (4.17) is not relevant. It is interesting also to note that the values of the heating necessary to give summit temperatures of 2×10^6 K are seemingly rather high ($\bar{H} = 21.3$ for L = 50Mm). This means that, at 10^6 K, the heating input is over 20 times the radiative loss at the footpoint. However, if one scales the heating against the temperature at 2×10^4 K (and assumes the pressure is constant between 10^6 and 2×10^4 K) then $\bar{H} \simeq 1$ at 2×10^4. Thus, the non-dimensionalisation is somewhat misleading.

4.4.2 The range of possible flows for uniform area

Having discussed the general effect of steady flows on a static loop we now examine the range of flows driven by a variation of the boundary conditions, (4.8).

Considering firstly subsonic flows, the solid lines in Figure 4.5 show the solutions generated by given footpoint temperature and pressure ratios: the curves have been drawn for different values of $\bar{v}_o$ (i.e. for given base mass fluxes). The first thing to point out is that the upper curve, denotes hydrostatic equilibrium. Hence, if one has two footpoints of a loop rooted in regions of different temperature (possibly due to different levels of magnetic activity), then hydrostatic equilibrium is only achieved incidentally. If one of the footpoint temperatures ($\bar{T}_2$, say)

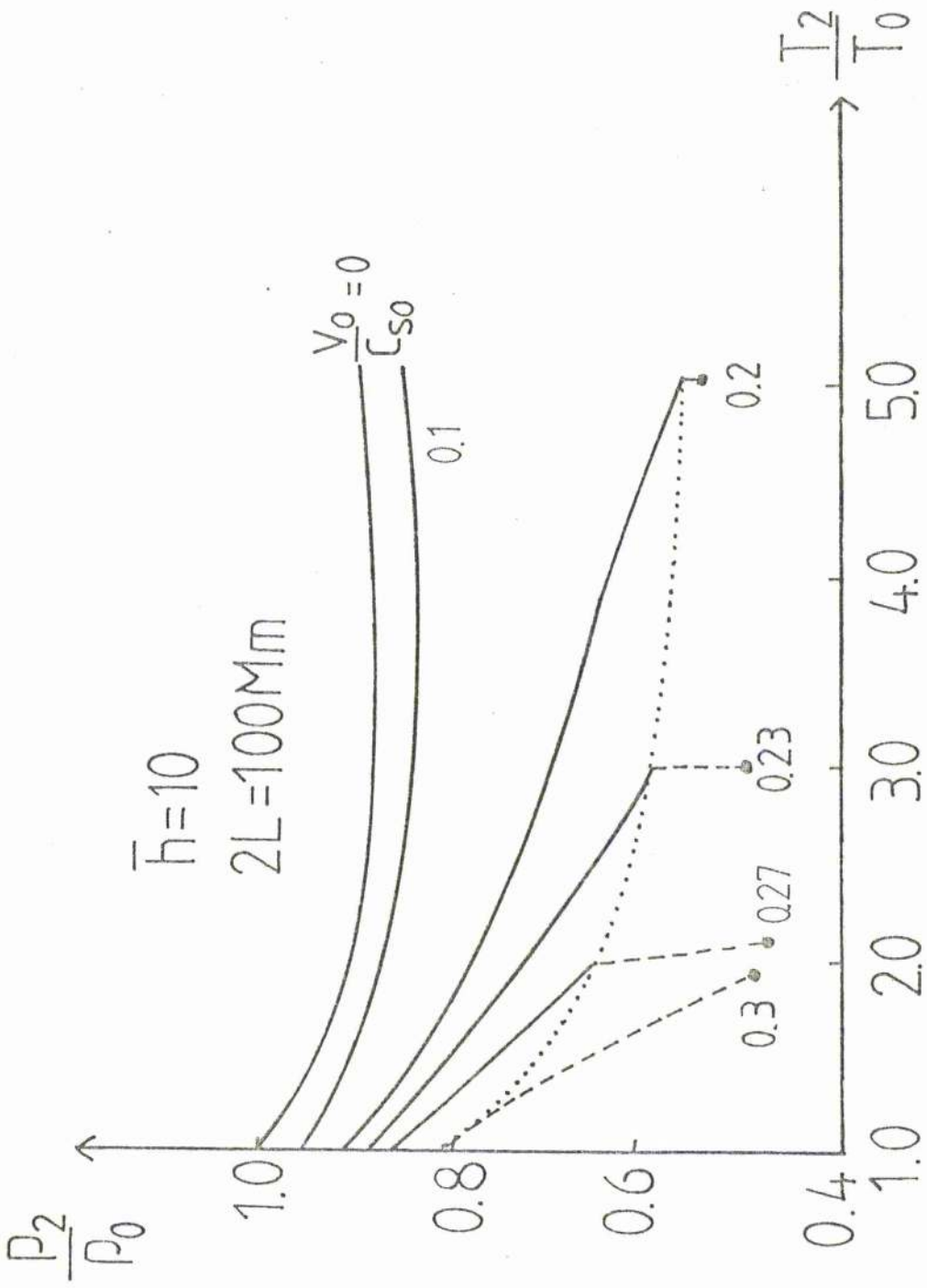

Figure 4.5 The footpoint pressure ratio (p_2/p_0) as a function of the footpoint temperature ratio (T_2/T_0) for a loop of uniform area. It has a length of 100Mm, a base number density of 5×10^{14} m^{-3}, a base temperature of 10^6 K and a dimensionless heating of 10. The upper curve denotes the case of hydrostatic equilibrium, while the other curves are labelled with the values of the base velocity (v_0), and the dotted line is the limit of the subsonic solutions. The dashed lines denote shocked solutions, and the dots at their ends denote the limit when the shock has moved down to the base.

is increased, then the range of possible subsonic solutions increases and the pressure ratio necessary for a shocked flow decreases.

One can hence make the following comment about static loop modelling. The static loop models considered by many authors (see Section 4.1) comprise only one of a large family of solutions. The symmetric static boundary condition, $T_2 = T_o$, $p_2 = p_o$ represent only one point in the $\bar{p}_2 - \bar{T}_2$ phase plane and it seems most unlikely that the Sun should always provide footpoint conditions representing static solutions. Hence, the general dynamic solutions discussed here may be of great relevance to coronal loops.

Figures 4.6a,b show the temperature and velocity profiles along a loop for different values of $\bar{T}_2$. In Figure 4.6a when $\bar{T}_2 = 2$, the temperature no longer possesses a maximum but increases all along the loop. This seems to suggest that, as $\bar{T}_2$ is increased, conduction becomes the most important term in the energy equation. On the other hand, Figure 4.6b shows that the velocity always possesses a maximum (See equation 4.12). This implies that there will always be a subsonic - supersonic transition point, the position of which is given by the solution of (4.12).

As pointed out above, the position of the sonic point cannot be found analytically but a numerical calculation is relatively straightforward. Like Chapter 3, the unshocked subsonic - supersonic solution permits only one value of $\bar{n}_2$, and so a shock-wave is necessary in the downflowing leg to satisfy the boundary conditions at $\bar{s} = 2$. The jump relations across such a shock are given by equations (2.54) - (2.56).

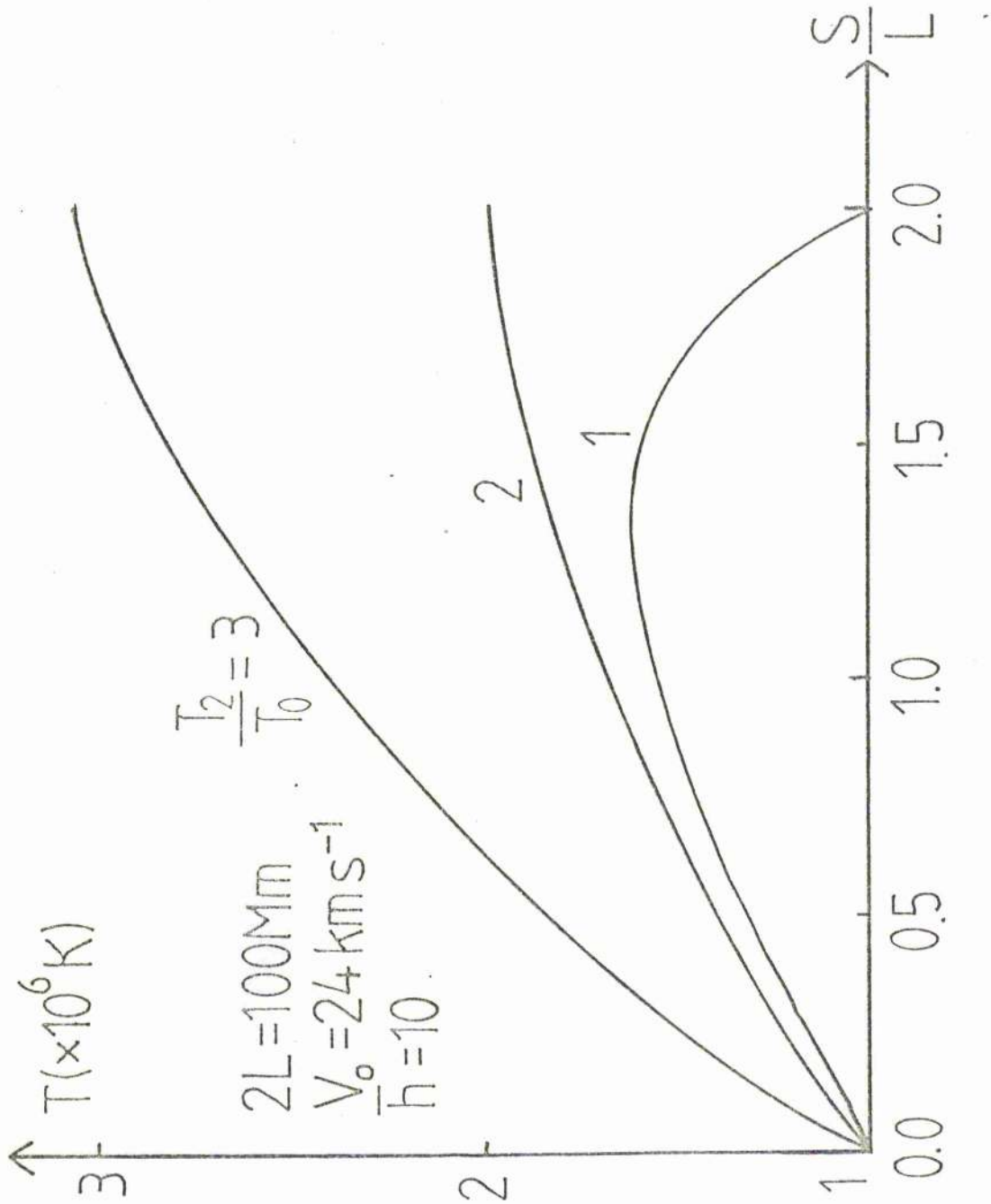

Figure 4.6a The temperature profile in a loop of uniform area and length 100Mm with a siphon flow driven along it. The base density is 5×10^{14} m^{-3}, base temperature 10^6 K and base velocity 24 km s^{-1}. The dimensionless heating is 10 and different curves represent different footpoint temperature ratios.

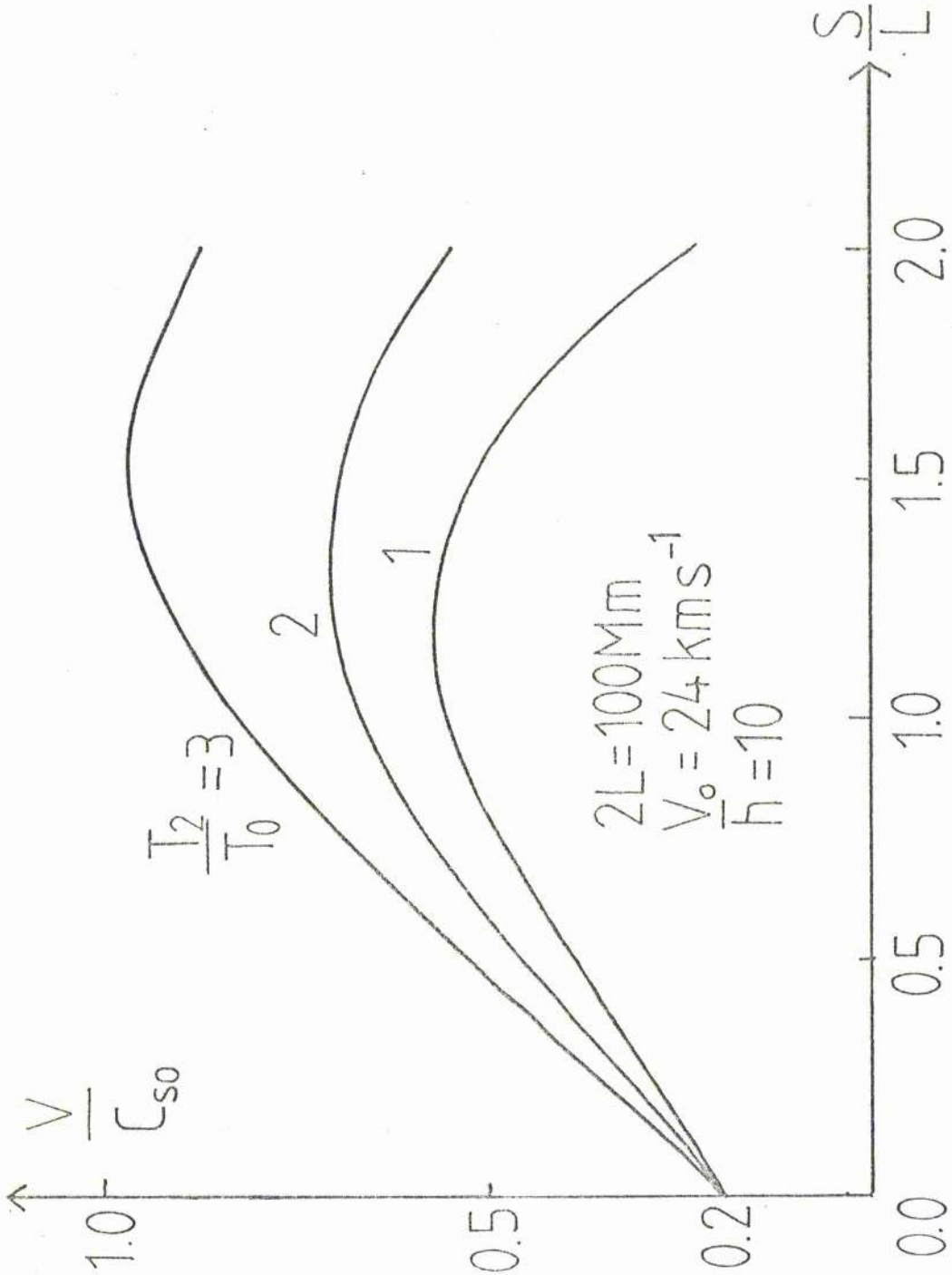

Figure 4.6b The velocity profile in a loop of uniform area and length 100Mm with a siphon flow driven along it. The notation is as in Figure 4.6a.

(The shock is isothermal, since the medium external to the shock possesses finite thermal conductivity (Section 2.4).)

The critical solution (i.e. the one to pass through the sonic point) is specified by a single base velocity and conductive flux for given boundary conditions. Once through the sonic point, the solutions are generated as follows. For a given shock position, the conductive flux out of the shock is automatically determined, and so also is the footpoint temperature, $\bar{T}_2$. If one then varies the shock position, a range of pressure and temperature ratios will be generated. The shocked solutions are shown by dashed curves in Figure 4.5 (the dotted line denoting the lower limit of the purely subsonic solutions). Clearly, the importance of this form of solution has diminished with the introduction of the full energy equation, but, where $T_2 \approx T_0$, the shocked solutions still contribute substantially to the possible range of flows. The large dots in Figure 4.5 indicate that the shock has reached the end of the loop: this is the <u>minimum allowable pressure ratio</u>,

4.4.3 <u>Loops with varying cross-sectional area</u>.

I: <u>Symmetric area</u>

In Chapter 3, we examined siphon flow in loops whose area diverged up to the summit and then converged, having the form

$$\bar{A}(\bar{s}) = 1 + (k-1)\sin^2\left(\frac{\pi\bar{s}}{2}\right) ;$$

hence the magnetic field is k times weaker at the summit than at the base. Wragg and Priest (1981) examined the statics of such loops and found that, as the summit area

increases, the temperature also increases but the density decreases. Also, in Chapter 3, we found that an increase in area resulted in an increase in the range of possible loop flows and a decrease in velocity all along the loop.

In Table 4.1, the effect on the maximum temperature of area divergence is shown.

Table 4.1

Symmetric loops whose area is k time bigger at the loop summit than at either footpoint. The variation with k and base speed ($\bar{v}_o$) of the maximum temperature ($\bar{T}_m$). The loop has a length 2L = 100Mm, dimensionless heating 10 and a base sound speed c_{so} = 120 km s^{-1}.

$\frac{v_o}{c_{so}}$ \ k	1	2	3
0	1.68	1.79	1.96
0.1	1.66	1.78	1.95
0.2	1.60	1.75	1.94
0.3	-	1.69	1.93
0.4	-	1.60	1.91

As k increases, so the maximum temperature rises, but as the pressure ratio decreases so this maximum falls although if k = 3 it is roughly constant. This is exactly what is expected if the results of Wragg and Priest and Section 4.4.2 of this chapter are combined. Figure 4.7a shows the shift of the maximum temperature from the summit as a function of base velocity. The greater the loop divergence, the smaller d becomes. One can interpret this in terms of the conduction

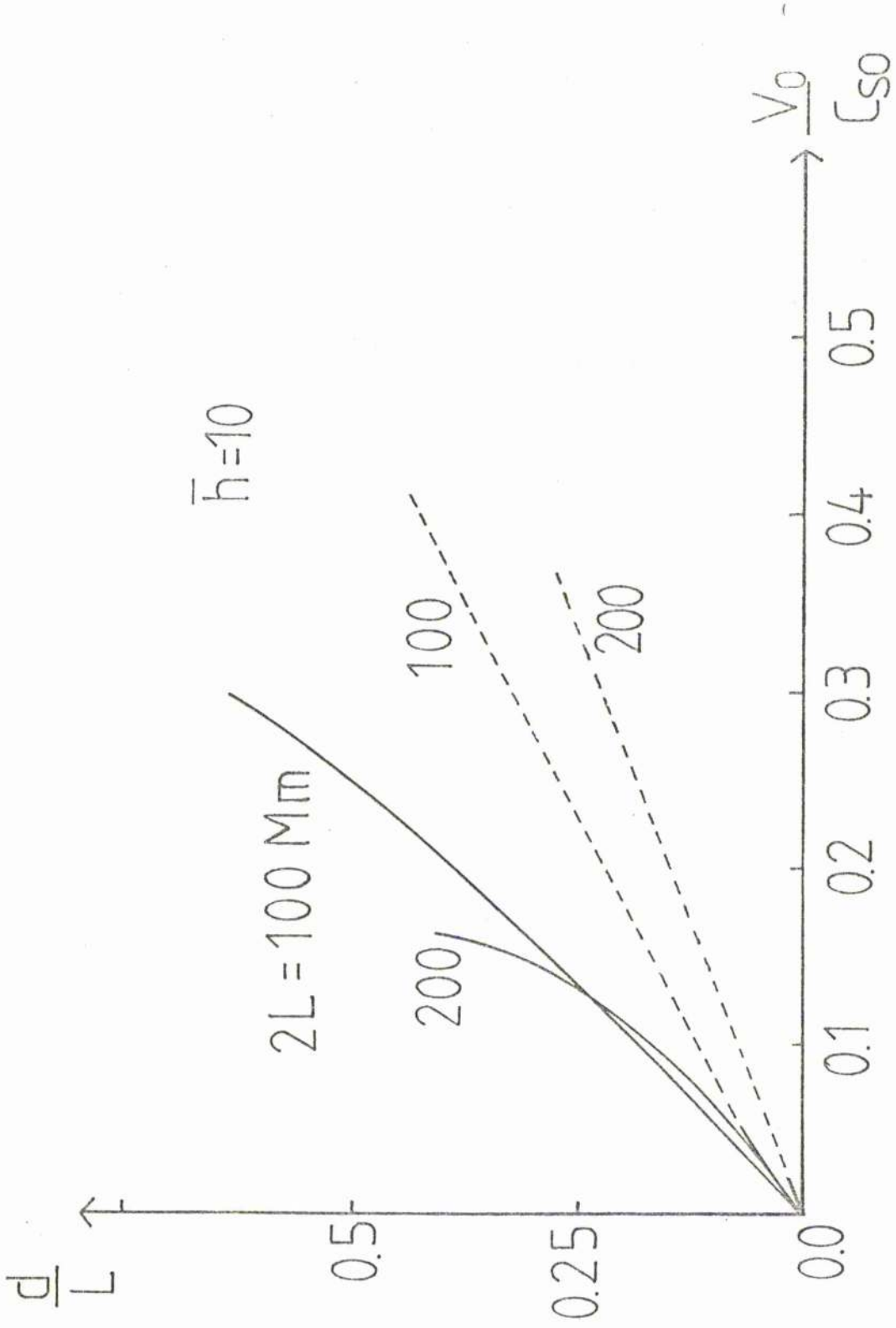

Figure 4.7a Siphon flow in a symmetric loop whose summit area is bigger than the footpoint by a factor k. The variation with the base velocity (v_o) of the distance (d) from the summit of the temperature maximum for loops of length 100 and 200 Mm; solid curves are for k = 2 and dashed ones for k = 5. The dimensionless heating ($\bar{h}$) is 10.

term in the energy equation which may be written as

$$\frac{d}{d\bar{s}}\left(\bar{A}\bar{T}^{5/2}\frac{d\bar{T}}{d\bar{s}}\right) = \bar{A}\frac{d}{d\bar{s}}\left(\bar{T}^{5/2}\frac{d\bar{T}}{d\bar{s}}\right) + \bar{T}^{5/2}\frac{d\bar{T}}{d\bar{s}}\frac{d\bar{A}}{d\bar{s}} \quad . \qquad (4.36)$$

The second term on the right-hand side will act as a heating term when $d\bar{T}/d\bar{s}$ and $d\bar{A}/d\bar{s}$ are positive (having the same sign as $\bar{h}\bar{n}$), and so, from the order-of-magnitude relationship (4.17), an increase in $\bar{h}$ decreases d.

Figure 4.7b shows the velocity profile along a typical loop. As in the adiabatic case, the velocity along much of the loop is reduced below the uniform area case, except for a small region near the footpoints. This is because the bulk of the divergence of the loop takes place away from the footpoints and we expect the flow near the footpoints to be similar to the uniform case. Also, the sonic point occurs near the downflowing footpoint and so shocked flows are largely irrelevant.

4.4.4 Loops with varying cross-sectional area.

II:- Diverging or converging areas

In Chapter 3, as well as symmetric loops, we considered converging and diverging loops whose area behaves as

$$\bar{A}(\bar{s}) = 1 + (a-1)\bar{s}^2 \quad ,$$

where $0 < a < 1$ gives converging loops and $a > 1$ gives diverging loops. It will be recalled that for a diverging loop, no subsonic flows with a pressure ratio less than unity are found.

Again, the effect of modelling the energetics can be predicted from equation (4.36). For a diverging loop

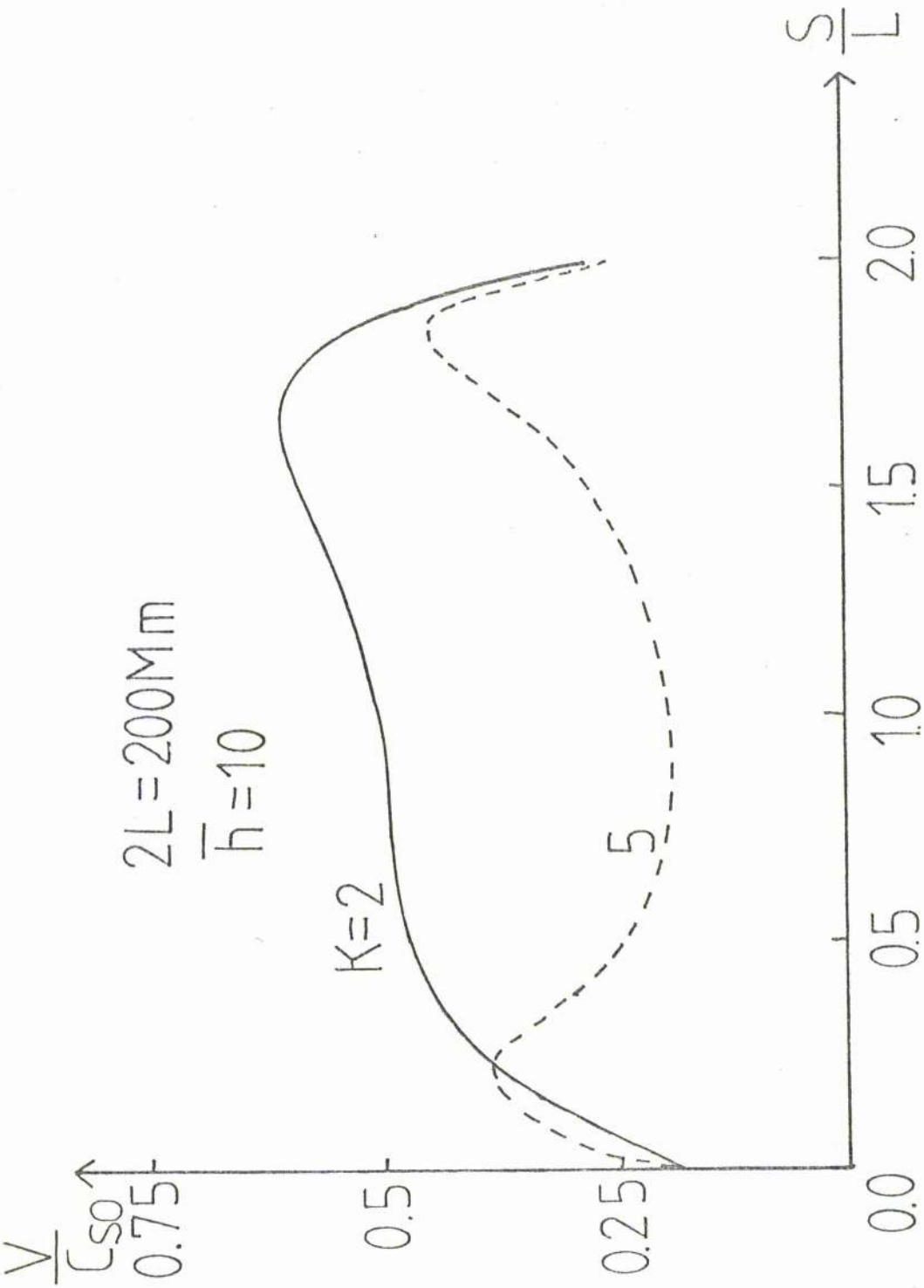

Figure 4.7b The velocity profile for a symmetric loop of length 200mm. The notation is as in Figure 4.7a.

$(d\bar{A}/d\bar{s}>0)$, one has an extra heating term in equation (4.31) and so the loop temperature will be raised above the uniform area case up to the temperature maximum and lowered beyond it; the converse holds for a converging loop. The sonic point is now given by

$$\left.\begin{aligned} \bar{T} &= \left(\frac{\bar{v}_o \bar{n}_o}{\bar{n}\bar{A}}\right)^2 , \\ \frac{d\bar{T}}{d\bar{s}} - \left(\frac{\bar{n}_o \bar{v}_o}{\bar{n}\bar{A}}\right)^2 \frac{1}{\bar{A}} \frac{d\bar{A}}{d\bar{s}} &+ \bar{q} \cos\left(\frac{\pi \bar{s}}{2}\right) = 0 , \end{aligned}\right\} \qquad (4.32)$$

and so for a diverging loop this point is shifted further along the downflowing leg compared with the uniform case: the converse holds for a converging loop.

The results for two specific cases are shown in Table 4.2.

Table 4.2

The properties of loops with a non-uniform area which increases by a factor a from one footpoint to another. The variation of the position (d) and the magnitude (T_m) of the maximum temperature and the pressure ratio as a function of the starting velocity for two loop lengths. The dimensionless heating is 10 and the base temperature 10^6 K.

(a) 2L=100Mm

a	v_o(km s^{-1})	d(Mm)	T_m(10^6 K)	p_2/p_o
2	12.0	1.5	1.67	0.987
	24.0	10.0	1.64	0.962
0.5	12.0	15.0	1.66	0.939
	24.0	31.5	1.47	0.851

(b) 2L=200Mm

a	v_o(km s^{-1})	d(Mm)	$T_m(10^6 K)$	p_2/p_o
2	12.0	10.0	2.10	0.953
	24.0	21.0	1.99	0.843
0.5	12.0	39.0	2.06	0.865
	18.0	51.0	1.98	0.821

For the diverging loop (a = 2), one now has subsonic solutions, but the position of maximum temperature is moved toward the summit. This is a consequence of the role of divergence as shown in equation (4.31), as is the increase in maximum temperature. The converse holds for converging loops.

4.5 The possibility of a thermal catastrophe

In the introduction, it was mentioned that, due to the non-linear nature of the energy equation, there need not exist a unique solution. This phenomenon was called thermal non-equilibrium, and it is of interest to investigate the effect that a steady flow has on the conditions for its onset. However, since the term non-equilibrium is not appropriate for a dynamical system, we shall here refer to the lack of solutions as thermal catastrophe. In this section, we show analytically and numerically how a steady flow affects the previous results. Also, the loop considered will experience a negligible gravitational force, for analytical simplicity.

4.5.1 Analytical solutions

In this section, the order-of-magnitude form of the

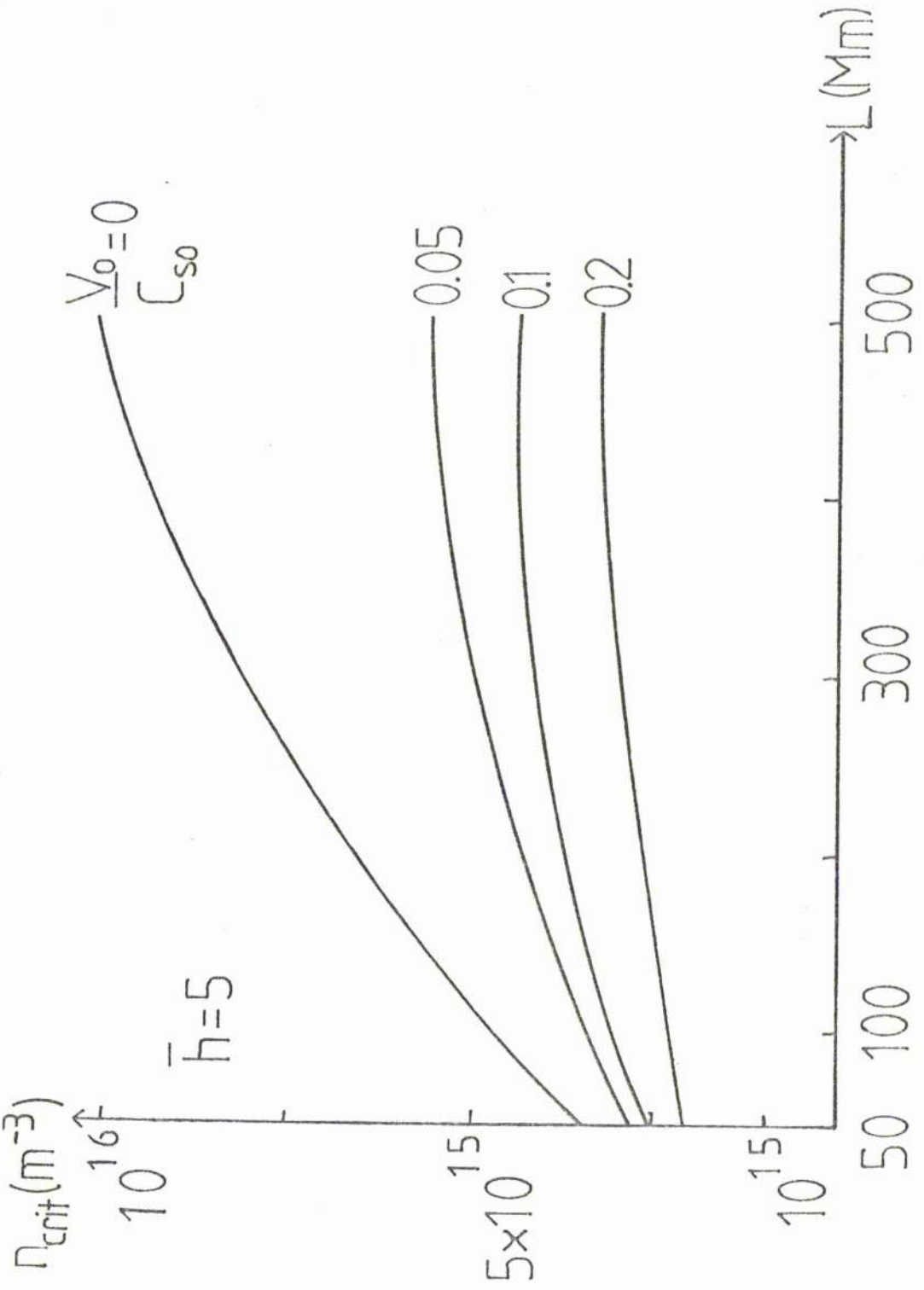

Figure 4.8b The variation with the loop half-length (L) and base velocity (v_o) of the density (n_{cr}) at which a non-steady flow sets in. The notation is as in Figure 4.8a.

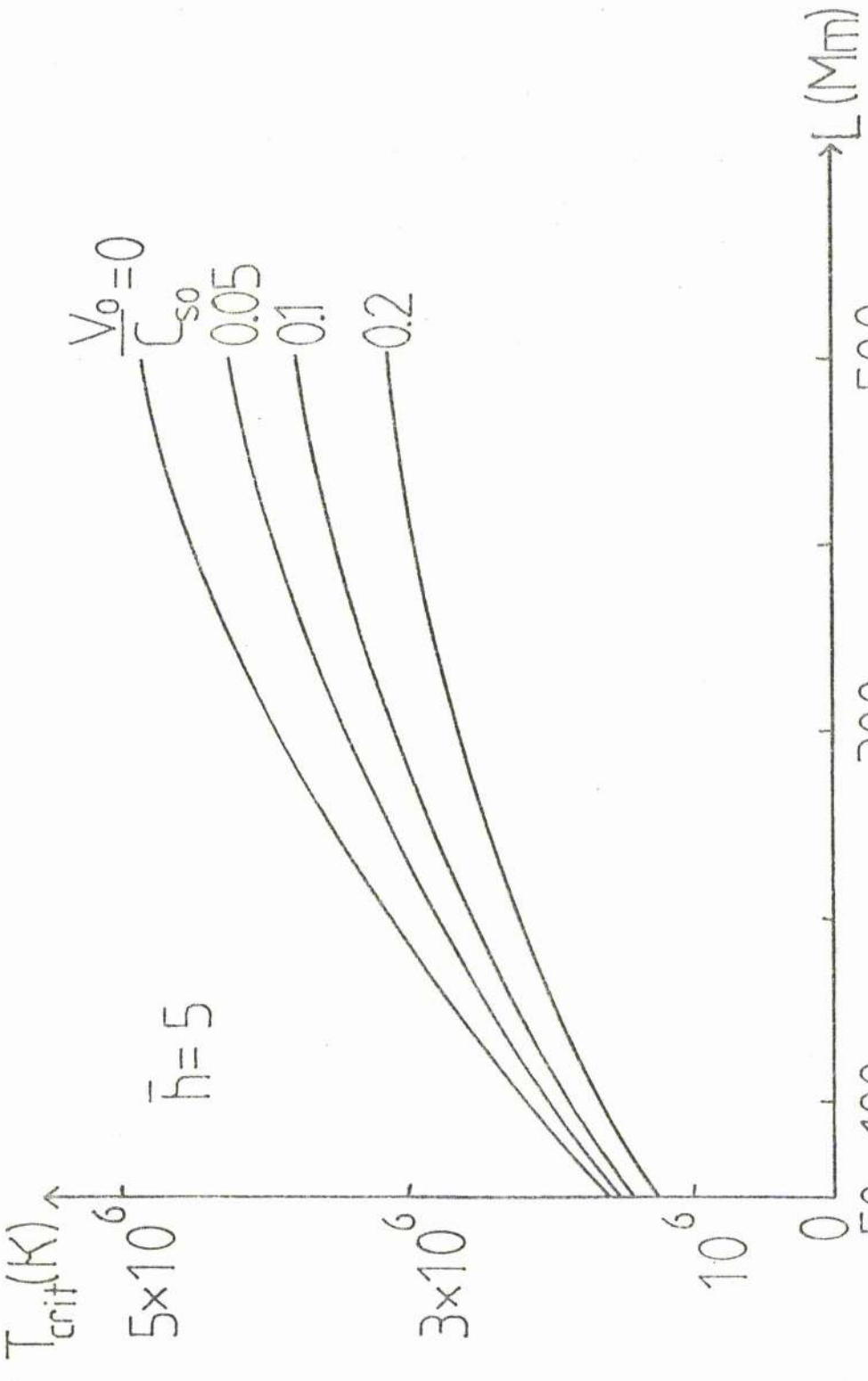

Figure 4.8a The variation with the loop half-length (L) and base velocity (v_o) of the temperature (T_{cr}) at which a non-steady flow sets in. The heating h is taken as 5 and the base sound speed is 120 km s^{-1}.

energy equation (4.16), is used to derive some elementary results. If one increases the base density ($\bar{n}_o$) in a loop with a hot temperature ($\gtrsim 10^6$K) one eventually reaches a point where, if $\bar{n}_o$ is increased further, no steady solution exists to the energy equation. At this point, $d\bar{T}_m/d\bar{n}_o$ is infinite, and so, differentiating equation (4.16) with respect to $\bar{n}_o$ gives, (on setting $\alpha = 0$),

$$\bar{n}_{crit} = \frac{\bar{T}_{crit}^{7/2}\,(11\bar{T}_{crit} - 9)}{2\left[\frac{\bar{h}\bar{L}^2}{\bar{L}^2}(L+d)^2 - \frac{\bar{F}_o\bar{V}_o\gamma(L+d)}{(\gamma-1)\,L}(3\bar{T}_{crit}^2 - 2\bar{T}_{crit})\right]} \qquad (4.33)$$

$$\frac{d}{L} = \frac{(3\bar{T}_{crit}^2 - 2\bar{T}_{crit})\,\bar{F}_o\bar{V}_o\gamma}{2(\gamma-1)\,\bar{h}\bar{L}^2}, \qquad (4.34)$$

where $\bar{n}_{crit}$ and $\bar{T}_{crit}$ are the base density and maximum temperature at the point when $d\bar{T}_m/d\bar{n}_o$ is infinite.

One can then solve equations (4.16), (4.33) and (4.34) to give d, $\bar{T}_{crit}$ and $\bar{n}_{crit}$. The results are shown in Figure 4.8. As expected, the introduction of a steady flow reduces the threshold for catastrophe considerably: a moderate flow of 50 km s^{-1} at the base lowers the critical base density by almost an order of magnitude.

4.5.2 Numerical solutions

The conclusions of the previous section may be confirmed by numerical solution of the energy equation, the results being shown in Figure 4.9. Once again, it may be seen that a flow of around 50 km s^{-1} can reduce the critical density

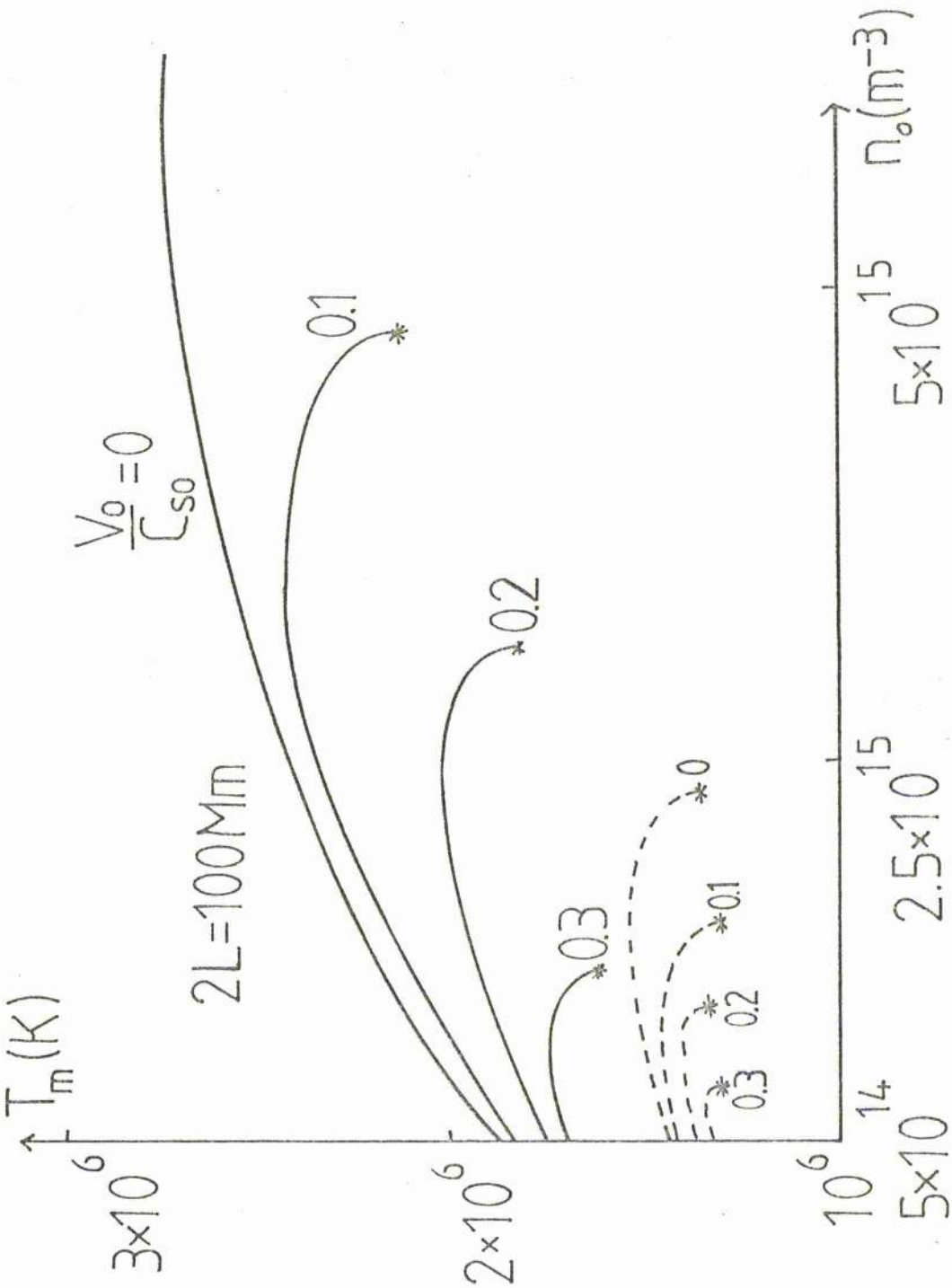

Figure 4.9 The temperature maximum (T_m) as a function of the base density (n_0) for a heating (Ĥ) of 4 (dashed curves) and 10 (solid curve). The onset of a thermal catastrophe is indicated by a star. The coronal reference density is taken as 5×10^{14} m^{-3}; the loop area is uniform, and several starting velocities (v_0) are taken; the base sound speed is 120 km s^{-1}.

by an order of magnitude.

It was suggested by Hood and Priest (1979a) that a hot ($\gtrsim 10^6$ K) steady flow could develop in a static loop that had undergone non-equilibrium. The results of this section show that this is impossible since a steady flow lowers the level of catastrophe below that of a static loop. In Chapter 5, we discuss the possible evolution after non-equilibrium.

4.6 Discussion and conclusions

In the last two chapters, the theory of steady flows in coronal loops has been examined in some depth. The adiabatic theory developed in Chapter 3 suggested the existence of solutions involving a subsonic-supersonic transition and shocks: due to the simplicity of the energy equation chosen, these were the only solutions possible if the footpoint pressure ratio was less than unity.

Calculations in Chapter 4 involving a more realistic energy equation have indicated that wholly subsonic solutions do exist but that the shocked solutions are still an important part of the total range of flows. The shocks are necessary in order to satisfy the imposed footpoint boundary conditions, and are gas dynamic shocks in the adiabatic case and isothermal ones when thermal conduction is important. In Chapter 4, it was found that a wide range of boundary conditions can be satisfied, and we again stress the point that it is extremely unlikely that the Sun can ever prescribe boundary conditions which give rise to static loops. This is further evidence that the corona is not a quiet, static, well-behaved atmosphere, but an active and dynamic structure. We return to this theme

in the next chapter.

It is of interest to compare the adiabatic results with those derived using the full energy equation. The first thing to note is that the loop temperature profiles bear little resemblance to each other. This is because in this chapter we have not considered the parameter range which makes the adiabatic law a good approximation to the energy equation and it would be of interest to investigate the parameters more fully. The adiabatic law arises if both $1/\bar{n}_o\bar{F}_o$ and $\bar{n}_o\bar{L}^2/\bar{F}_o$ are much smaller than unity. On the other hand, the adiabatic theory predicts the density and velocity behaviour fairly well. The concept of sonic points and shocked solutions carries over, the density behaviour in both cases is similar and the simple adiabatic equation enabled us to see the effect of area variations clearly. Thus, in all aspects except the temperature behaviour, the adiabatic calculations provide basic information which could well have been missed had numerical calculations been started straightaway.

Our calculations have tended to concentrate on the role of flows rather than on varying the other parameters. These have been studied at length by Hood and Priest (1979a) and Wragg and Priest (1981), and the behaviour of the solutions is well tabulated. In particular, our heating, $\bar{h}$, has always been taken so that the loop temperatures are between 1.5 and 3×10^6 K in reasonable agreement with observations of interconnecting, quiet and active region loops.

We now turn to discuss siphon flows in terms of more general theory and observations of coronal loops. Firstly, it should be said that little evidence of siphon flow has

been seen so far, (see Livingston and Harvey, 1981), although Noci (1981) has suggested that observations in some loops where only half a loop is seen may be evidence of supersonic flows, (and so decreased emission), on the downflowing leg. The main reason for this lack of observations is that instrumentation has often not been designed to pick up Doppler shifts in the corona: indeed, it is often hard enough to see individual loops at all. It is hoped that one day instrumentation will improve sufficiently for further searches to be made on coronal loops for this sort of flow. However, a vast number of flows have been observed at transition zone temperatures (see Section 1.3); and it may be that these upflows and downflows are part of a larger coronal network of steady or transient flows.

One of the original reasons for studying coronal loops was to try and obtain information about the functional form of the heating mechanism. In fact, this has been a largely unsuccessful exercise and it now seems to be accepted (Chiuderi et al., 1981) that the accuracy of the observations is not good enought to deduce anything. Chiuderi et al. parametrise their heating function as

$$H = H_0 T^{\chi}$$

and determine from observations that $-2.2 < \chi < 6.7$, so from the observational side, one can learn little. In fact, there are other reasons why little can be learnt at present, and that is that too many of the parameters in the equations are unable to be determined to any accuracy by present observations. For example, varying the cross-sectional area, height or magnitude of heating in a model will produce <u>different</u> results to compare with observations and none of these quantities can

be determined observationally to any accuracy at present. One must now add a siphon flow to this list of parameters. Varying footpoint conditions can produce a flow, and this produces alterations in any given model. It is therefore possible to vary any one of three or four parameters to give a model loop which may agree with current observations. To try to vary one parameter to match observations, when in fact any one of four can vary reduces comparison to a meaningless exercise given present observations. Future observations should be able to pin down flows, loop geometry and pressure to much greater accuracy and one could then learn something useful about loop models.

Another problem is that loops are often part of more general coronal arcades and observations refer to the whole arcade rather than separate loops. In turn, this raises the problem of how a coronal arcade (a collection of loops) can be modelled. Priest and Smith (1979) have modelled static coronal arcades, and we now discuss how a siphon flow can be included in such a model.

Assume that a constant pressure difference is imposed along the entire footpoints of the arcade. Then the higher loops are longer, and for some length of loop, shocked solutions will become necessary. Hence, one has a sequence of subsonic solutions topped by shocked ones as shown in Figure 4.10a - this picture results if one considers separate flux-tubes representing thermally-isolated field-lines. One possible <u>global</u> picture is shown in Fig. 4.10b. The shocks will not act as separate gas-dynamic ones but as <u>slow oblique M.H.D. shock</u>, as is obvious if one joins the gas shocks up. We now have a much more complicated 2-dimensional problem

(a)

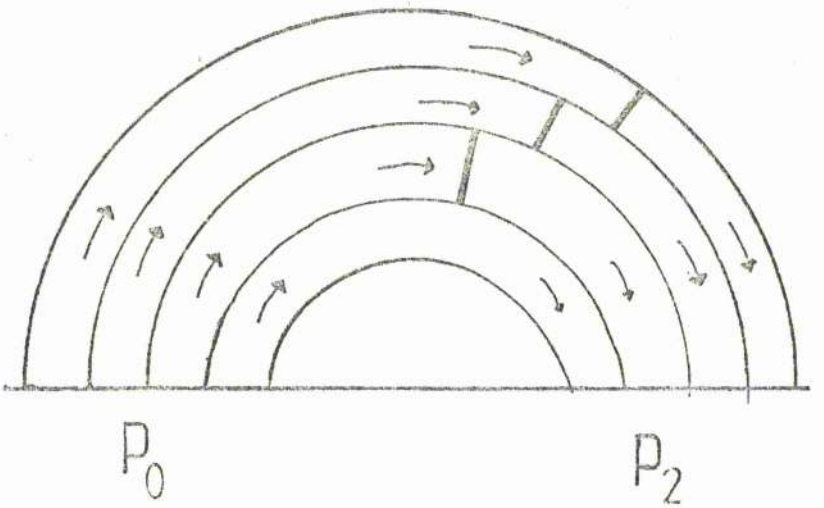

(b)

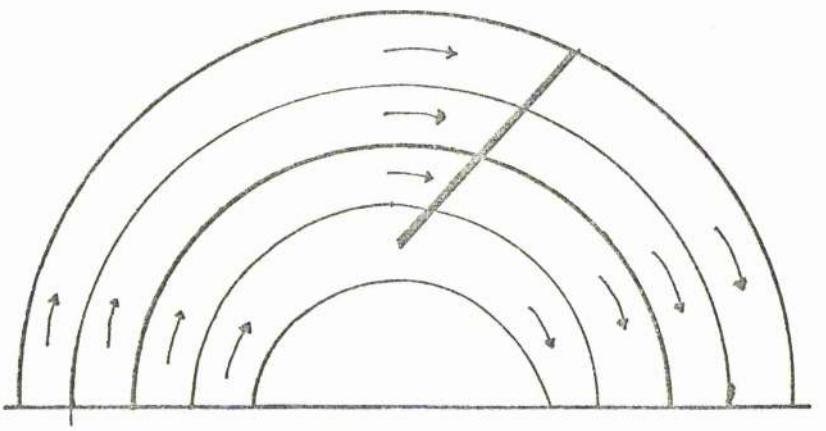

Figure 4.10 (a) The structure of siphon flow in a coronal arcade if one considers the arcade as comprising a group of flux tubes. Above a certain length of flux-tube shocks are necessary to satisfy the boundary conditions. These are gas dynamic shocks, situated at the necessary distance along each flux tube and are shown by solid lines.

(b) The global picture of siphon flow in a coronal arcade. Instead of separate flux tubes, the global magnetic field is considered and the local gas dynamic shocks are replaced by a single, slow, oblique M.H.D. shock, shown by a solid line.

and this cautions against constructing simplistic one-dimensional loops. Another possible application of siphon flows is in the formation of quiescent prominences. We return to this subject in Chapter 5.

Finally, it is of interest to suggest some ways in which a siphon flow can be generated. One way is by photospheric motions compressing the magnetic field and the plasma in it: the enhanced pressure could then be relaxed by a flow from the compressed point. Alternatively, a diverging photospheric flow could reduce the pressure at one of the footpoints. Supergranular motion (typically 500 m s^{-1}) could drive a downflow of this velocity in the intense tubes that make up the boundary of a supergranule cell and, due to viscous coupling, maintain a pressure in those tubes, which may be loop footpoints. Also, the pressure at a footpoint could be enhanced by local heating there.

In conclusion, siphon flows emphasise the dynamic aspect of the corona and should warn against constructing simplified static loop models.

Chapter 5: THERMAL NON-EQUILIBRIUM I: COOLING OF HOT LOOPS

In Chapter 4, it was mentioned that the static energy equation did not always possess a unique solution and that if the parameters governing the loop structure exceeded certain critical values, then no hot ($T_1 > 10^6$K) solutions exist and the loop cools to below 10^5 K. This was referred to as thermal non-equilibrium. In this Chapter, we discuss the evolution of a loop from the non-equilibrium point and suggest some possible consequences of the cooling.

5.1 Introduction

In previous chapters it has been stressed that the closed-field regions of the solar corona are structured as loops or arcades. The recent Skylab mission has emphasised the dynamic nature of the corona (Priest, 1981b) and in Chapters 3 and 4 the theory of steady-state flows in coronal loops was developed. However, most of the flows observed in coronal loops are of a transient nature: in this Chapter we discuss a possible source of these flows, namely thermal non-equilibrium.

Recent observations of the corona (Foukal, 1975, Jordan, 1975) have indicated that some loops have cool cores. These cores are present in sunspot loops and have temperatures below 10^5 K and pressures typically a tenth of the ambient coronal pressure. The loops are typically 100 Mm long and 10 Mm wide (Priest, 1978). An important question is - how do these cool cores form? Since thermal conduction is negligible across a field line, the cores are insulated from the ambient hot

coronal medium but their method of formation is more puzzling. Other cool structures such as prominences and coronal rain are also very evident in the solar corona. Clearly, conduction will also insulate them, but again, their method of formation is an open question. In this Chapter, thermal non-equilibrium in coronal loops or arcades is suggested as a possible method of formation of all these cool structures.

Hood and Priest (1979a) have discussed non-equilibrium in uniform-pressure coronal loops at some length. They find that, if the heating is decreased or the pressure increased sufficiently, then the loop no longer possesses an equilibrium with a temperature of order 10^6 K and cools to a new equilibrium with a temperature below 10^5 K. A similar result also holds for variations in length: if the heating at the loop base is less than the optically-thin radiative loss there, then the stretching of a short loop or the contraction of a long one produces thermal non-equilibrium. This behaviour carries over to hydrostatic loops (Wragg and Priest, 1981) and to loops with siphon flows along them (Chapter 4).

Figure 5.1 shows the variation of the summit temperature with the uniform loop pressure. The value p_{crit} is the pressure at which thermal non-equilibrium occurs, and the dashed line shows the path that is followed as the loop seeks a cool equilibrium solution under the assumption of constant pressure. However, the lower equilibrium will be hydrostatic due to the small scale-height there and so the uniform-pressure assumption breaks down.

In this Chapter, we follow the evolution of the cooling after non-equilibrium occurs.

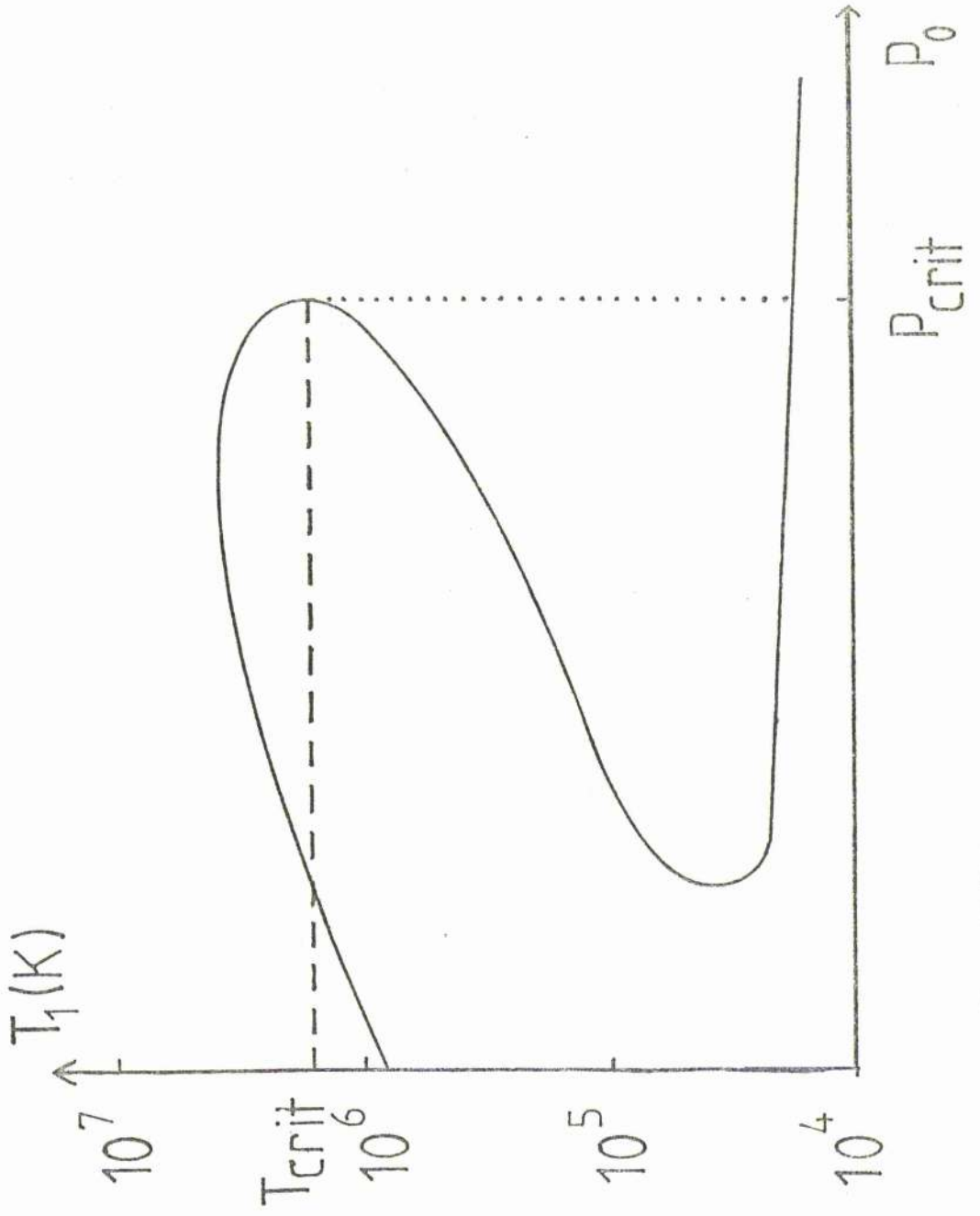

Figure 5.1 The form of the equilibrium summit temperature (T_1) of a coronal loop as a function of its base pressure. When the point (p_{crit}, T_{crit}) is reached, the plasma cools along the dotted line to a new equilibrium below 10^5 K.

5.2 General theory

5.2.1 Basic equations

The equations of unsteady one-dimensional gas-dynamics in a loop of length 2L are momentum (1.25), continuity (1.26), state (1.27) and energy (1.30), which may be written as

$$m_H n \frac{Dv}{Dt} = - \frac{\partial p}{\partial s} - m_H n g f(s), \tag{5.1}$$

$$\frac{Dn}{Dt} = - \frac{n}{A} \frac{\partial}{\partial s}(vA), \tag{5.2}$$

$$p = 2 n k_B T, \tag{5.3}$$

$$\frac{-k_B n}{\gamma - 1} \frac{DT}{Dt} - 2 k_B T \frac{Dn}{Dt} = \frac{1}{A} \frac{\partial}{\partial s}\left(10^{-11} A T^{5/2} \frac{\partial T}{\partial s}\right) - n^2 \chi T^{\alpha} + H(p,T), \tag{5.4}$$

along a field-line.

Here,

$$\frac{D}{Dt} = \frac{\partial}{\partial t} + v \frac{\partial}{\partial s},$$

$$f(s) = \frac{\underline{B} \cdot \hat{\underline{z}}}{|\underline{B}|},$$

and

$$A = A(s).$$

Hence f(s) is just a geometrical factor representing the loop structure and A(s) is the prescribed cross-sectional area. (In Chapters 3 and 4, we took f(s) = cos(πs/2L) for a semi-circular loop.) These equations are non-dimensionalised

as follows,

$$\bar{T} = T/T_0 \,, \quad \bar{n} = n/n_c \,, \quad \bar{P} = P/P_c \,, \quad \bar{A} = A/A_0 \,,$$

$$\bar{V} = V/c_{s0} \,, \quad \bar{t} = t/\tau_{rad} \,, \quad \bar{s} = s/L \,, \quad \tau_s = L/c_s \,,$$

$$c_{s0}^2 = P_c/(m_+ n_c) \,, \quad \bar{\chi} = \frac{\chi T_0^{\alpha}}{\chi_0 T_0^{\alpha_0}} \,, \quad \tau_{cond} = \frac{P_c L^2}{10^{-11} T_0^{7/2}} \,,$$

$$\tau_{heat} = \frac{P_c}{H(P_c, T_0)} \,, \quad P_c = 2 k_B n_c T_0 \,, \quad \tau_{rad} = \frac{P_c}{n_c^2 \chi T_0^{\alpha}} \,,$$

$$\lambda = \tau_s/\tau_{rad} \,, \quad \bar{L}^2 = \tau_{cond}/\tau_{rad} \,, \quad \bar{h} = \tau_{rad}/\tau_{heat} \,, \quad \bar{q} = q/c_{s0} \,.$$

In these expressions, subscripts zero denote quantities evaluated at the loop base: in particular, T_0 is taken as 10^6 K. Subscripts c refer to a reference value, and, in particular, n_c is taken as 5×10^{14} m^{-3}, a typical coronal number density.

Hence, equations (5.1) - (5.4) are

$$\lambda \bar{n} \frac{\partial \bar{v}}{\partial \bar{t}} + \bar{n} \bar{v} \frac{\partial \bar{v}}{\partial \bar{s}} = - \frac{\partial \bar{p}}{\partial \bar{s}} - \bar{q} \bar{n} f(\bar{s}) \,, \tag{5.5}$$

$$\lambda \frac{\partial \bar{n}}{\partial \bar{t}} + \frac{\partial}{\partial \bar{s}} (\bar{n} \bar{v}) = 0 \,, \tag{5.6}$$

$$\bar{P} = \bar{n} \bar{T} \,, \tag{5.7}$$

$$\bar{L}^2 \left[\frac{\gamma}{\gamma - 1} \frac{\bar{P}}{\bar{T}} \left(\frac{\partial \bar{T}}{\partial \bar{t}} + \frac{\bar{v}}{\lambda} \frac{\partial \bar{T}}{\partial \bar{s}} \right) - \left(\frac{\partial \bar{P}}{\partial \bar{t}} + \frac{\bar{v}}{\lambda} \frac{\partial \bar{P}}{\partial \bar{s}} \right) \right] =$$

$$= \bar{T}^{5/2} \frac{\partial^2 \bar{T}}{\partial \bar{s}^2} + \frac{5}{2} \bar{T}^{3/2} \left(\frac{\partial \bar{T}}{\partial \bar{s}} \right)^2 - \bar{L}^2 \left(\bar{P}^2 \bar{\chi} \bar{T}^{\alpha - 2} - \bar{h}(\bar{P}, \bar{T}) \right) , \tag{5.8}$$

if area variations are neglected.

As it stands, this is a complicated set of partial differential equations that are difficult to solve either analytically or numerically. However, progress can be made by using an order-of- magnitude approach for the spatial derivatives, which enables equations (5.5) - (5.8) to be reduced to a set of ordinary differential equations in time. Hence, instead of taking a large number of grid points in the s-direction, we take just three, namely the two footpoints ($\bar{s} = 0, 2$) and the loop summit ($\bar{s} = 1$). If some variable ($\bar{\psi}$) varies spatially, our differencing gives

$$\left.\begin{aligned} \frac{\partial \bar{\psi}}{\partial \bar{s}} &= \frac{\bar{\psi}_2 - \bar{\psi}_0}{2} , \\ \frac{\partial^2 \bar{\psi}}{\partial \bar{s}^2} &= \bar{\psi}_2 - 2\bar{\psi}_1 + \bar{\psi}_0 . \end{aligned}\right\} \qquad (5.9)$$

One expects such a scheme to be valid when $\bar{\psi}_1$ is close to $\bar{\psi}_0$ and $\bar{\psi}_2$: however, the accuracy seems to be good even when they differ considerably (Hood, 1980; Hood and Priest, 1981).

If symmetry is assumed around the loop summit then, for all time

$$\left.\begin{aligned} \bar{n}_0 &= \bar{n}_2 , \\ \bar{T}_0 &= \bar{T}_2 , \\ \bar{v}_1 &= 0 , \end{aligned}\right\} \qquad (5.10)$$

and, evaluating all quantities at the summit, equations (5.5)-(5.8) may be approximated by the following three ordinary differential equations for $\bar{T}_1$, $\bar{n}_1$ and $\bar{v}_0$:

$$\lambda \bar{n}_1 \frac{\partial \bar{v}_0}{\partial \bar{t}} = \bar{n}_1 \bar{v}_0^2 + 2(\bar{n}_0 - \bar{n}_1 \bar{T}_1) + \bar{g} \bar{n}_1 \left.\frac{\partial f}{\partial \bar{s}}\right|_{\bar{s}=1} , \qquad (5.11)$$

$$\lambda \frac{\partial \bar{n}_1}{\partial \bar{t}} = \bar{n}_1 \bar{v}_0 , \qquad (5.12)$$

$$\frac{\partial \bar{T}_1}{\partial \bar{t}} = \frac{(\gamma-1)}{\bar{n}_1}\left[\bar{T}_1 \frac{\partial \bar{n}_1}{\partial \bar{t}} + 2\bar{T}_1^{5/2}\frac{(1-\bar{T}_1)}{\bar{L}^2} - \right.$$

$$\left. - \bar{n}_1^2 \bar{\chi} \bar{T}_1^{\alpha} + \bar{h}(\bar{p}_1, \bar{T}_1) \right] . \qquad (5.13)$$

These three equations form the basis of our discussion in the following two chapters. It should be noted that the momentum equation (5.5) is satisfied identically on applying (5.10), and so we have differentiated (5.5) with respect of $\bar{s}$ and then applied (5.10) to obtain (5.11).

The order-of-magnitude approximation means that we cannot model steep gradients or shocks: its justification is that it gives qualitative trends which are an essential preparation to the full numerical solution that should be subsequently attempted. It is essentially a more rigorous form of dimensional analysis.

5.2.2 The conditions for non-equilibrium

Hood and Priest (1979a) have derived values of the critical pressure, length and heating necessary for non-equilibrium. Since we are using a different and more accurate radiative loss function than the one they used these results are rederived. The order-of-magnitude and static ($\frac{\partial}{\partial \bar{t}} \equiv 0$) form of equations (5.11) and (5.13) are

$$2(\bar{n}_0 - \bar{n}_1 \bar{T}_1) + \bar{\zeta} \bar{n}_1 f'(\bar{\zeta}) = 0 , \qquad (5.14)$$

$$2\bar{T}_1^{5/2}(1-\bar{T}_1) = \bar{L}^2(\bar{\rho}_1^2\bar{\chi}\bar{T}_1^{\alpha} - \bar{h}) , \qquad (5.15)$$

for heating constant per unit volume. If $\bar{g}$ is small, then the pressure is constant ($\bar{p} = \bar{p}_0$), and equation (5.15) is

$$2\bar{T}_1^{5/2}(1-\bar{T}_1) = \bar{L}^2(\bar{p}^2\bar{\chi}\bar{T}_1^{\alpha-2} - \bar{h}) . \qquad (5.16)$$

Further, if $0.562 \leq \bar{T}_1 \leq 2$ then $\alpha = 0$ and $\bar{\chi} = 1$ and equation (5.16) may be analysed as follows.

(a) Non-equilibrium due to increase in pressure

Non-equilibrium occurs when $d\bar{T}_1/d\bar{p}$ is infinite (Figure 5.1); the critical temperature is given by

$$\bar{T}_{crit}^{5/2}(9 - 11\bar{T}_{crit}) = -2\bar{L}^2\bar{h} , \qquad (5.17)$$

and the critical pressure follows from solving equation (5.17). The special case of $\bar{h} = 0$ gives

$$\left.\begin{aligned} \bar{T}_{crit} &= \frac{9}{11} , \\ \bar{p}_{crit} &= \left(\frac{9}{11}\right)^{3/2}\frac{4}{11\bar{L}^2} . \end{aligned}\right\} \qquad (5.18)$$

(b) Non-equilibrium due to increase or decrease of length

In this case, non-equilibrium occurs when $d\bar{T}_1/d\bar{L}$ is infinite and the critical temperature is the solution of

$$\left(\frac{\bar{h}}{\bar{p}^2}\right)(7\bar{T}_{crit}^3 - 5\bar{T}_{crit}^2) = 11\bar{T}_{crit} - 9 . \qquad (5.19)$$

This has no solution if $\bar{h} > \bar{p}^2$ and so non-equilibrium only occurs if $\bar{h} < \bar{p}^2$. If $\bar{h} < \bar{p}^2$, $\bar{T}_{crit}$ can take on two values (Hood and Priest, 1979) so that non-equilibrium occurs if a long loop is contracted or a short loop stretched. The

critical length is obtained from (5.16) and for the case of no heating,

$$\left.\begin{aligned} \bar{T}_{crit} &= \frac{q}{\mu} \\ \bar{L}^2_{crit} &= \frac{4}{\mu \bar{\rho}^2}\left(\frac{q}{\mu}\right)^{9/2}. \end{aligned}\right\} \qquad (5.20)$$

(c) Non-equilibrium due to decrease of heating

Non-equilibrium occurs when $d\bar{T}_1/d\bar{h}$ is infinite, so the critical temperature is given by

$$\bar{T}_{crit}^{5/2}\left(1-\bar{T}_{crit}\right) = -2\bar{L}^2\,\bar{h}_{crit}.$$

Non-equilibrium can only exist if

$$\bar{\rho}^2\bar{L}^2 > \frac{4}{\mu}\left(\frac{q}{\mu}\right)^{9/2}. \qquad (5.21)$$

5.2.3 Thermal stability of critical points

Having derived the position of the critical points, we now investigate their thermal stability. Assuming uniform pressure, the time-dependent energy equation (5.13) reduces to

$$\frac{d\bar{T}_1}{d\bar{t}} = \frac{(\gamma-1)}{\gamma\bar{\rho}} F(\bar{\rho}, \bar{h}, \bar{L}, \bar{T}_1), \qquad (5.22)$$

where

$$F(\bar{\rho}, \bar{h}, \bar{L}, \bar{T}_1) = \bar{T}_1\left[2\frac{\bar{T}_1^{9/2}}{\bar{L}^2}(1-\bar{T}_1) - \bar{\rho}^2\chi\bar{T}_1^{\alpha-2} + \bar{h}\right]. \qquad (5.23)$$

If $\bar{T}_{10}$ is the equilibrium temperature, then

$$F(\bar{\rho}, \bar{h}, \bar{L}, \bar{T}_{10}) = 0. \qquad (5.24)$$

Following Smith and Priest (1977), the stability of (5.22) may be tested by perturbing the temperature as

$$\bar{T}_1 = \bar{T}_{10} + C e^{\bar{\sigma}\bar{t}} , \qquad (5.25)$$

where C is a constant and $\bar{\sigma}$ is a non-dimensional growth rate. Expanding (5.22) in a Taylor series about $\bar{T}_{10}$ gives

$$\bar{\sigma} = \frac{(\gamma-1)}{\gamma \bar{p}} \left(\frac{\partial F}{\partial \bar{T}_1} \right)_{\bar{T}_1 = \bar{T}_{10}} ,$$

where $\bar{\sigma} > 0$ (< 0) implies instability (stability). Thus the stability is directly related to the slope of the curves in Figure 5.1. The growth-rate, $\bar{\sigma}$ is given by

$$\bar{\sigma} = \frac{(\gamma-1)}{\gamma \bar{p}} \left[\frac{\bar{T}_{10}^{5/2} (5 - 7\bar{T}_{10})}{\bar{L}^2} - \bar{p}^2 \bar{\chi} \bar{T}_{10}^{\alpha-2} (\alpha - 2) \right] . \qquad (5.26)$$

However, this analysis fails at the critical point $(\bar{T}_{crit}, \bar{p}_{crit})$, which is neutrally stable on a linear analysis since $\partial F / \partial \bar{T}_1$ vanishes there. Quadratic stability may be investigated by approximating equation (5.22) by

$$\frac{d\bar{T}_1}{d\bar{t}} = \frac{(\bar{T}_1 - \bar{T}_{10})^2}{2} \left(\frac{\partial^2 F}{\partial \bar{T}_1^2} \right)_{\bar{T}_1 = \bar{T}_{crit}}$$

where

$$\left(\frac{\partial^2 F}{\partial \bar{T}_1^2} \right)_{\bar{T}_1 = \bar{T}_{crit}} = \frac{(\gamma-1) \bar{T}_{crit}^{3/2}}{\gamma \bar{p} \bar{L}^2} \left[5(7 - 2\alpha) + 7 \bar{T}_{crit} (2\alpha - 9) \right] . \qquad (5.27)$$

In the corona,

$$\alpha \leq 0 ,$$

$$(\bar{T}_{crit})_{min} = \frac{11}{13} ,$$

and so

$$\left(\frac{\partial^2 F}{\partial \bar{T}_1^2} \right)_{\bar{T}_{crit}} < 0 .$$

If $\bar{T}_1 < \bar{T}_{crit}$, the plasma continues to cool, and if $\bar{T}_1 > \bar{T}_{crit}$ it will return towards equilibrium. Thus, the critical point is quadratically unstable and cooling occurs rather than heating.

5.3 Analytical considerations

Provided that flows are subsonic and gravity is negligible, the order-of-magnitude equations reduce to (5.22) and (5.23). These equations are amenable to analytical treatment in a few special cases.

Expanding the right-hand side of equation (5.22) in a Taylor series about the critical temperature, $\bar{T}_{crit}$, gives

$$F(\bar{p}, \bar{h}, \bar{L}, \bar{T}_1) = F(\bar{p}, \bar{h}, \bar{L}, \bar{T}_{crit}) + (\bar{T}_1 - \bar{T}_{crit}) \left(\frac{\partial F}{\partial \bar{T}_1}\right)_{\bar{T}_1 = \bar{T}_{crit}} + \frac{(\bar{T}_1 - \bar{T}_{crit})^2}{2} \left(\frac{\partial^2 F}{\partial \bar{T}_1^2}\right)_{\bar{T}_1 = \bar{T}_{crit}} + \cdots \quad (5.28)$$

Assume that the pressure attains its critical value ($\bar{p}_{crit}$) and is then increased beyond this by a factor ε, such that

$$\bar{p} = \bar{p}_{crit}(1 + \varepsilon),$$

so that we are in a region where no neighbouring equilibrium exists. Such an increase could result either from slow photospheric motions compressing the loop or from small-scale motions in the loop itself but ε need not be small. Since no static solution exists, the loop must cool (as discussed in Section 5.2)

Because $\bar{T}_{crit}$ is the critical temperature, it satisfies

$$F(\bar{p}_{crit}, \bar{h}, \bar{L}, \bar{T}_{crit}) = 0, \quad (5.29)$$

and equation (5.28) can be written in the form

$$F(\bar{p}, \bar{h}, \bar{L}, \bar{T}_1) = a_1(\bar{T}_{crit}, \bar{p}_{crit}, \bar{L}, \bar{h}, \varepsilon) + (\bar{T}_1 - \bar{T}_{crit})\, a_2(\bar{T}_{crit}, \bar{p}_{crit}, \bar{L}, \bar{h}, \varepsilon) + \frac{(\bar{T}_1 - \bar{T}_{crit})^2}{2}\, a_3(\bar{T}_{crit}, \bar{p}_{crit}, \bar{L}, \bar{h}, \varepsilon) \,. \tag{5.30}$$

Hence, (5.22) can be integrated to give $\bar{T}_1$ as an implicit function of time:

$$\bar{t} = \frac{2\bar{p}\gamma}{(\gamma-1)(4a_1a_3 - a_2^2)^{1/2}} \tan^{-1}\left[\frac{(\bar{T}_{crit} - \bar{T}_1)(4a_1a_3 - a_2^2)^{1/2}}{a_2(\bar{T}_{crit} - \bar{T}_1) - 2a_1}\right]. \tag{5.31}$$

Here, a_1, a_2 and a_3 are given by

$$\left.\begin{aligned} a_1 &= -\bar{p}_{crit}^2\, \bar{X}\, \bar{T}_{crit}^{\alpha-1} f(\varepsilon) = \bar{a}_1 f(\varepsilon) \,, \\ a_2 &= -\bar{p}_{crit}^2\, \bar{X}\, \bar{T}_{crit}^{\alpha-2} (\alpha-1) f(\varepsilon) = \bar{a}_2 f(\varepsilon) \,, \\ a_3 &= -\frac{\bar{p}_{crit}^2}{2}\, \bar{X}\, (\alpha-1)(\alpha-2)\, \bar{T}_{crit}^{\alpha-3} [g(\varepsilon)]^2 + \\ &\quad + \frac{\bar{T}_{crit}^{3/2}}{4\bar{L}^2}(35 - 63\bar{T}_{crit}) \,, \end{aligned}\right\} \tag{5.32}$$

where

$$\left.\begin{aligned} f(\varepsilon) &= \varepsilon(2+\varepsilon) \,, \\ g(\varepsilon) &= (1+\varepsilon)^2 \,. \end{aligned}\right\} \tag{5.33}$$

Similar expressions can be found when $\bar{L}$ or $\bar{h}$ attain critical values, as follows, where

$$\bar{L} = \bar{L}_{crit}(1 \pm \varepsilon),$$

depending upon whether the loop is stretched or contracted and

$$\bar{h} = \bar{h}_{crit}(1 - \varepsilon).$$

(a) $\bar{L}$ critical

$$\left.\begin{aligned} a_1 &= (\bar{h}\bar{T}_{crit} - \bar{\chi}\bar{T}_{crit}^{\alpha-1}\bar{p}^2) f(\varepsilon) = \bar{a}_1 f(\varepsilon), \\ a_2 &= -\bar{p}^2\bar{\chi}\bar{T}_{crit}^{\alpha-2}(\alpha-1) f(\varepsilon) = \bar{a}_2 f(\varepsilon), \\ a_3 &= -\bar{p}^2(\alpha-1)(\alpha-2)\frac{\bar{\chi}}{2}\bar{T}_{crit}^{\alpha-3}[g(\varepsilon)]^2 + \\ &\quad + \frac{\bar{T}_{crit}^{3/2}(35 - 63\bar{T}_{crit})}{4\bar{L}^2_{crit}}, \end{aligned}\right\} \quad (5.34)$$

(b) $\bar{h}$ critical

$$\left.\begin{aligned} a_1 &= \varepsilon\bar{T}_{crit}\bar{h}_{crit}, \\ a_2 &= \varepsilon\bar{h}_{crit}, \\ a_3 &= -(\alpha-1)(\alpha-2)\frac{\bar{\chi}\bar{p}^2\bar{T}_{crit}^{\alpha-3}}{2} + \\ &\quad + \frac{\bar{T}_{crit}^{3/2}(35 - 63\bar{T}_{crit})}{4\bar{L}^2}. \end{aligned}\right\} \quad (5.35)$$

Use may now be made of (5.31) - (5.35) to deduce several simple results.

5.3.1 Estimate of cooling times

First, let us assume that $\varepsilon \ll 1$ and discuss the case when the pressure becomes critical (the procedure is the same if $\bar{L}$ or $\bar{h}$ attain critical values).

The time ($\bar{\tau}_{cool}$) for the loop to cool ($\bar{T}_1 \ll \bar{T}_{crit}$) may be estimated by setting $\bar{T}_1 \approx 0$ in equation (5.30) so that

$$\bar{\tau}_{cool} \approx \frac{\bar{p}_{crit}\,\pi\,\gamma}{(8\bar{a}_1 a_3)^{1/2}(\gamma-1)}\left[\frac{1}{\varepsilon^{1/2}} - \frac{2(\bar{a}_2\bar{T}_{crit} - 2\bar{a}_1)}{(4\bar{a}_1 a_3)^{1/2}}\right] + \\ + O(\varepsilon^{1/2}). \qquad (5.36)$$

Similar expressions of the form

$$\bar{\tau}_{cool} \approx \frac{\bar{p}\,\pi\,\gamma}{(\gamma-1)(8\bar{a}_1 a_3)^{1/2}}\left[\frac{d}{\varepsilon^{1/2}} + e\right], \qquad (5.37)$$

exist for a critical $\bar{h}$ or $\bar{L}$, where d and e are functions of $\bar{a}_1$, $\bar{a}_2$ and a_3. In general, if we assume that a smooth evolution brings about non-equilibrium, then ε will be small and relations (5.36) and (5.37) will be valid.

To investigate the cooling time when $\varepsilon = O(1)$, consider an idealised loop with no heating ($\bar{h} = 0$). Setting $\alpha = 0$ (valid if $0.562 \leq \bar{T}_{crit} \leq 2$) the critical temperature, pressure and length are given by equations (5.18) and (5.20). Using these results in equation (5.31) gives for $\bar{p}_{crit}$

$$\bar{\tau}_{cool} \approx \frac{\gamma}{\gamma-1}\left[\frac{4\bar{L}^2 g(\varepsilon)}{f(\varepsilon)(9/11)^{1/2}(4/11)\delta}\right]^{1/2} \tan^{-1}\left(\frac{\delta^{1/2}}{3f(\varepsilon)^{1/2}}\right), \qquad (5.38)$$

and for $\bar{L}_{crit}$,

$$\bar{\tau}_{cool} \approx \frac{2\gamma}{(\gamma-1)\bar{p}}\frac{(9/11)^2}{f(\varepsilon)^{1/2}\bar{\xi}^{1/2}} \tan^{-1}\left(\frac{\bar{\xi}^{1/2}}{3f(\varepsilon)^{1/2}}\right), \qquad (5.39)$$

where

$$\delta = \delta(\varepsilon) = 2(g(\varepsilon))^2 + 91 - f(\varepsilon),$$

and

$$\bar{\xi} = \bar{\xi}(\varepsilon) = 4(g(\varepsilon))^2 - \frac{91}{4} - f(\varepsilon).$$

Thus, instead of a relationship of the form

$$\bar{\Sigma}_{cool} \sim \frac{1}{\xi^{1/2}} \quad ,$$

which holds when $\xi \ll 1$, we now have an expression behaving as

$$\bar{\Sigma}_{cool} \sim \frac{1}{\xi^{1/2}(2+\xi)^{1/2}} \quad .$$

So, as ξ increases, the rate at which $\bar{\Sigma}_{cool}$ decreases slows down. Although this result has been derived for the particular case $\bar{h} = 0$, it seems likely that a similar result holds for non-zero values of the heating

5.3.2 Initial evolution of cooling

As a final analytical result, consider how the loop cools just after equilibrium is lost. Assuming uniform pressure, equations (5.22) and (5.23) may be solved by expanding $\bar{T}_1$ in a power series as

$$\bar{T}_1 = \bar{T}_{crit} + \xi \bar{T}_{11} + \xi^2 \bar{T}_{12} + \cdots \qquad (5.40)$$

where ξ is the perturbation beyond equilibrium of the critical parameter $\bar{p}$, $\bar{L}$ or $\bar{h}$. Substituting (5.40) into (5.22) gives a system of equations in $\bar{T}_{11}$, $\bar{T}_{12}$, etc ---, which can be solved analytically. The conditions that the loop is in equilibrium at the critical point and that $\partial F/\partial \bar{T}_1$ vanish there give two equations for $\bar{T}_{crit}$ and $\bar{p}_{crit}$, namely

$$2\bar{T}_{crit}^{5/2}(1-\bar{T}_{crit}) = \bar{L}^2(\bar{p}_{crit}^3 \bar{\chi} \bar{T}_{crit}^{\alpha-2} - \bar{h}) \, ,$$

and

$$\bar{T}_{crit}^{5/2}(5-7\bar{T}_{crit}) = \bar{p}_{crit}^2 \bar{L}^2 \bar{\chi} (\alpha-2) \bar{T}_{crit}^{\alpha-2} \, .$$

Substituting into (5.22) gives (for $\alpha = 0$),

$$\bar{T}_1 = \bar{T}_{crit} - \varepsilon\bar{t}\left(\frac{(\gamma-1)\bar{p}_{crit}}{\gamma\bar{T}_{crit}}\right) + O(\varepsilon^2). \qquad (5.41)$$

One thus has a linear decrease in temperature with time, directly proportional to the perturbation of the critical pressure and the critical pressure itself. This solution is valid provided

$$\bar{t} \lesssim \frac{\gamma\bar{T}_{crit}}{(\gamma-1)\bar{p}_{crit}} .$$

Otherwise, a more detailed analysis is needed due to the non-uniformity of our expansion.

Finally, it may be noted that an examination of the continuity equation (5.12) in the form

$$\bar{v} = -\frac{1}{\varepsilon\bar{T}_1}\frac{d\bar{T}_1}{d\bar{t}} ,$$

shows that an upflow is driven when the temperature decreases in time.

5.4 Numerical results:- A more detailed cooling analysis

The equations of motion are governed by three time-scales, namely the conduction (τ_c) radiative (τ_R) and sound travel (τ_s) times, defined as

$$\left.\begin{aligned} \tau_c &= \frac{3pL^2}{2\times10^{-11}T^{7/2}} , \\ \tau_R &= \frac{3p}{2n^2\chi T^{\alpha}} , \\ \tau_s &= L/c_s , \end{aligned}\right\} \qquad (5.42)$$

and in the corona, these are roughly of the same order. Consequently, little analytical progress can be made beyond that outlined in Section 5.3. Recently, Antiochos (1980)

has obtained useful separable solutions in the regime of radiatively-dominated cooling, but to study non-equilibrium we must follow the evolution from the start when radiation does not dominate.

Equations (5.11) - (5.13) are to be solved numerically subject to the following initial conditions at $\bar{t} = 0$:

$$\left.\begin{aligned} \bar{T}_1 &= \bar{T}_{crit}, \\ \bar{n}_1 &= \frac{\bar{n}_0}{\bar{T}_{crit}}, \\ \bar{v}_0 &= 0. \end{aligned}\right\}$$

For now, we neglect the effects of gravity and flux-tube divergence. The critical pressure and temperature are found by solving equations (5.16) and (5.17) and then the pressure is written as

$$\bar{p} = \bar{p}_{crit}(1+\varepsilon).$$

The numerical results are shown in Figures 5.2a-c for a loop of half-length 50Mm and heating, $\bar{h} = 2$ ($\bar{h} = 1$ corresponds to a heating H of 2.5×10^{-6} Wm^{-3}). Figure 5.2a shows the variation of temperature with time for several perturbations. Clearly, the results depend strongly on ε (as was found by Smith and Priest, 1977, in the analogous problem for neutral sheets). The time for the temperature to fall below 2.5×10^4 K (defined as τ_{cool}) increases dramatically as ε decreases.

The cooling occurs in two distinct phases. A slow fall in temperature, the expression for which is given by equation (5.41) is followed by a rapid cooling when the temperature drops from 8×10^5 K to below 10^5 K in a few minutes. The second phase of the cooling is driven by

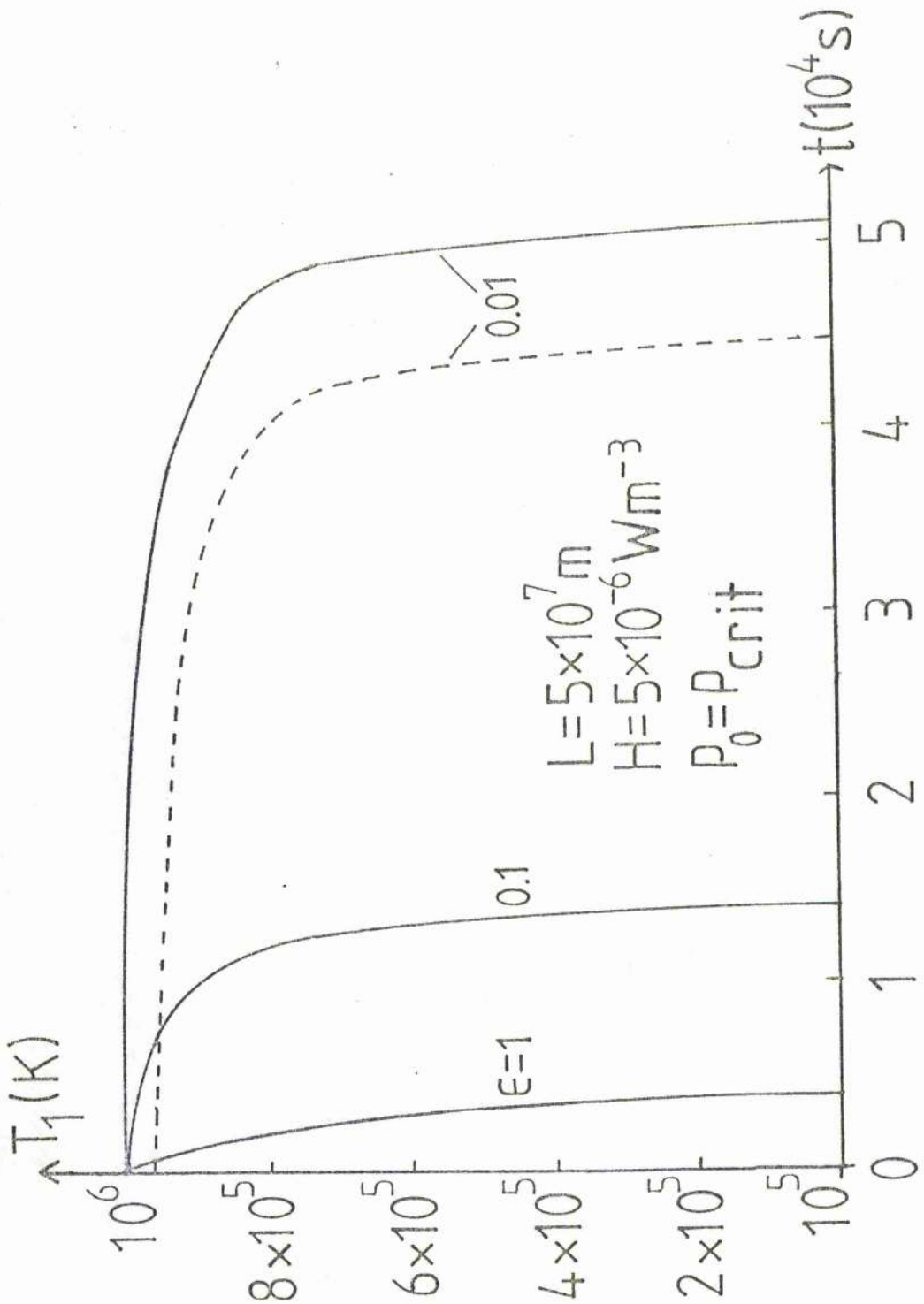

Figure 5.2a The variation with time of the summit temperature of a coronal loop whose pressure has been increased beyond its equilibrium by a factor ε. The loop is of half-length 50 Mm. It has a constant heat input of 5×10^{-6} Wm^{-3} ($\tilde{h} = 1$ corresponds to $H = 2.5 \times 10^{-6}$ W m^{-3}) and a 'base' temperature of 10^6K. The dashed curve is for a semi-circular loop with the effect of gravity included.

the large increase in radiation below 8×10^5 K and the resulting rapid energy loss. Thus, non-equilibrium gives similar results to linear instability up to a certain point, after which a violent non-linear evolution occurs.

The corresponding behaviour of the summit density and base velocity are shown in Figures 5.2b and c. Initially the loop cools very slowly with the pressure remaining roughly constant but driving a small upflow. However, during the non-linear phase, the summit pressure falls off quickly driving a large upflow which results in a substantial increase in the summit density. The time taken to fall from 7.5×10^5 K to below 2×10^4 K is a small part of the total cooling time if $\epsilon \ll 1$, so we expect equation (5.31) and the (uniform pressure) approximations derived from it in Section 5.3 to be fairly accurate.

The dotted curve in Figure 5.2a shows the effect of including gravity in a semi-circular loop where $\bar{g} = 1$ and

$$f(\zeta) = \cos\left(\frac{\pi\zeta}{2}\right).$$

Gravity decreases the critical temperature but raises the critical base pressure (Cragg and Priest, 1982a) and hence increases the radiative loss function. The loop then cools more quickly, but gravity should not affect the dynamics until the temperature is of order 10^5 K. Gravity will cause cool, dense plasma to fall until hydrostatic equilibrium is reached, but by then, the field configuration may have altered (see Section 5.5).

Figures 5.3 and 5.4 give the variation of the cooling time (τ_{cool}) with the loop half-length, L, and the heating

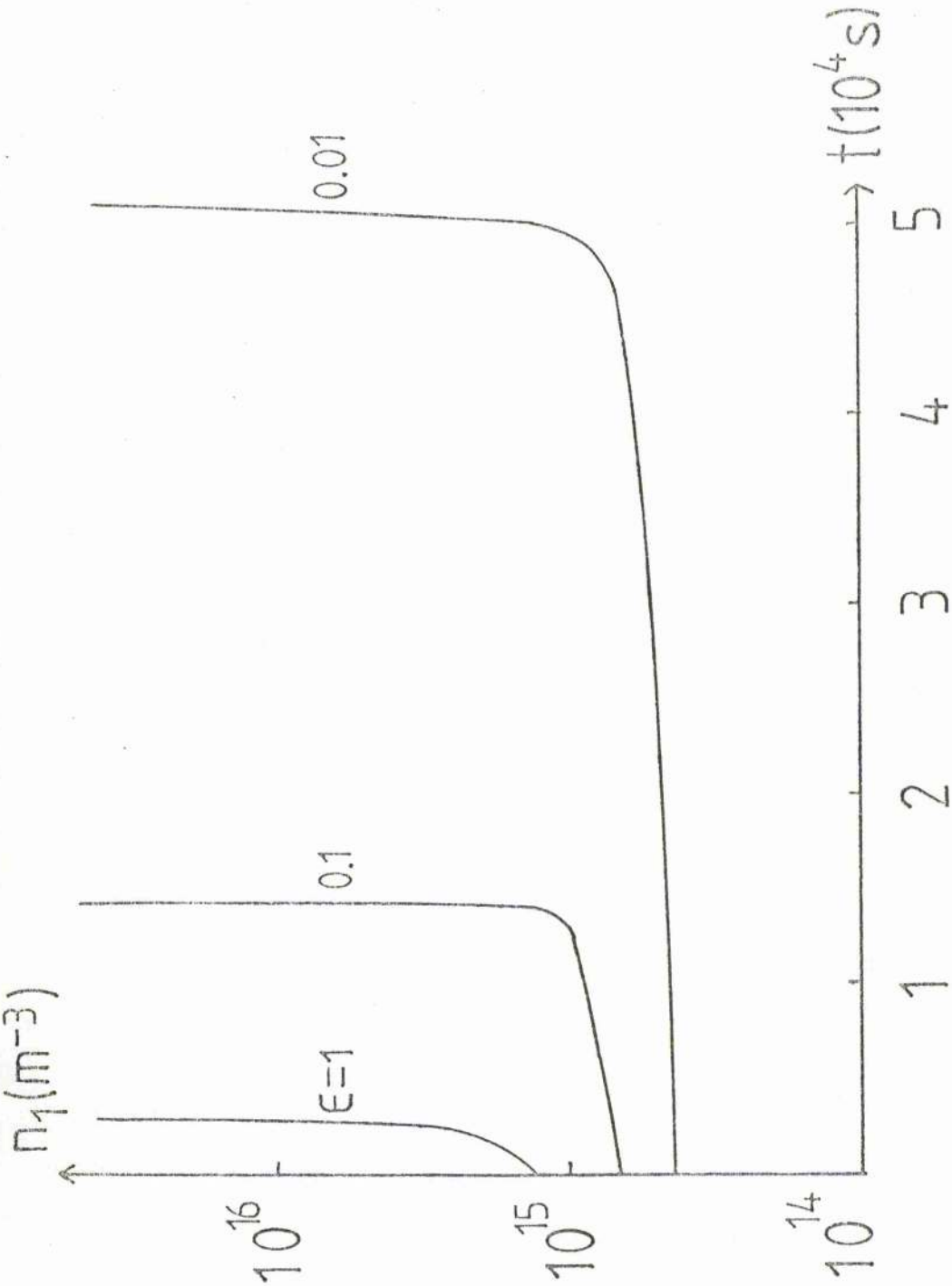

Figure 5.2b The variation with time of the summit density of a coronal loop whose pressure has been increased beyond its equilibrium by a factor ϵ. The notation is as in Figure 5.2a.

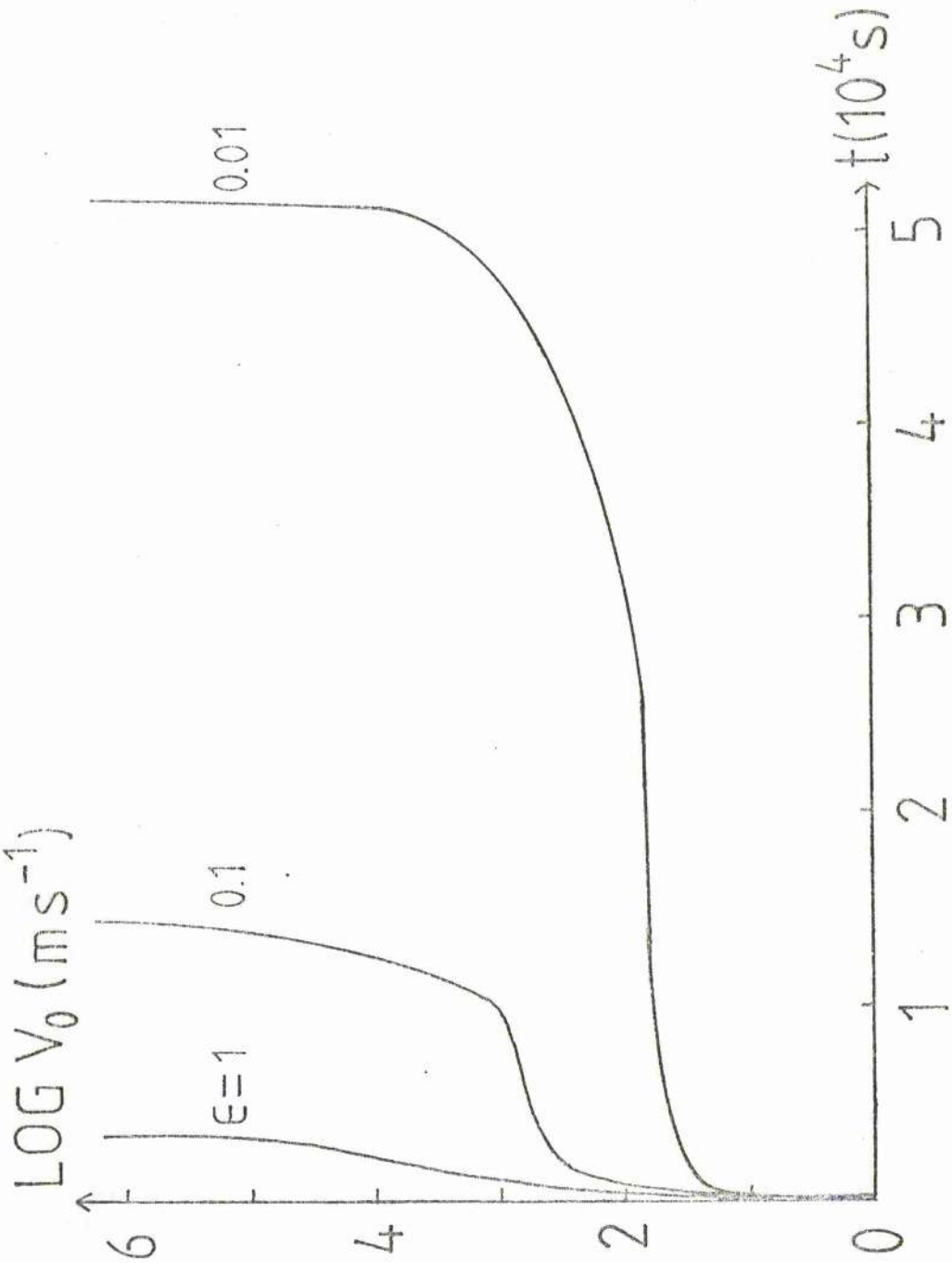

Figure 5.2c The variation with time of the base velocity of a coronal loop whose pressure has been increased beyond its equilibrium by a factor ϵ. The notation is as in Figure 5.2a.

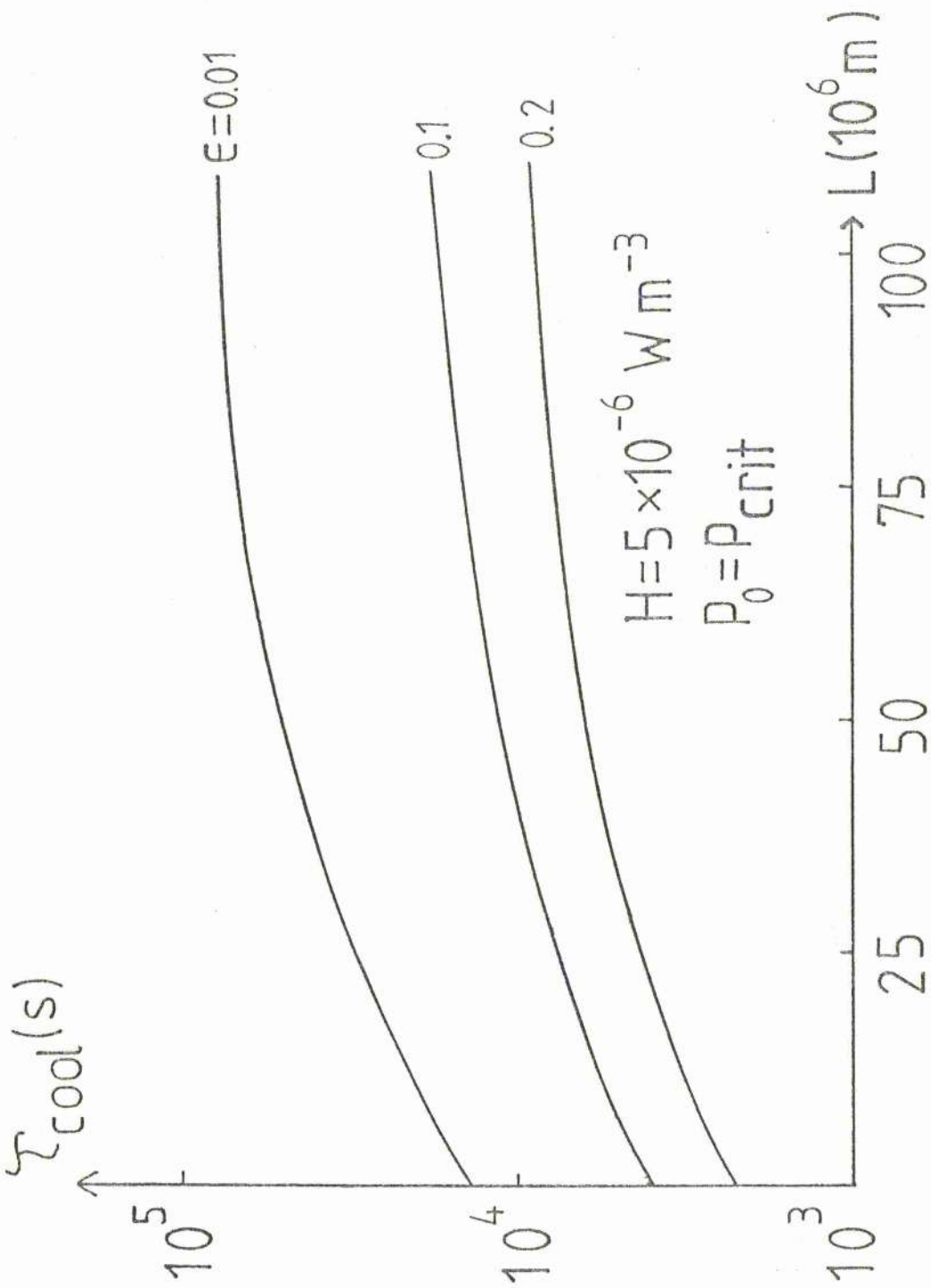

Figure 5.3 The cooling time, τ_{cool}, (defined as the time taken for the temperature to fall from its critical value to 12,500 K) as a function of the loop half-length L(in Mm) for three values of ε, the perturbation from the critical pressure. The heating and base density are the same as Figure 5.2.

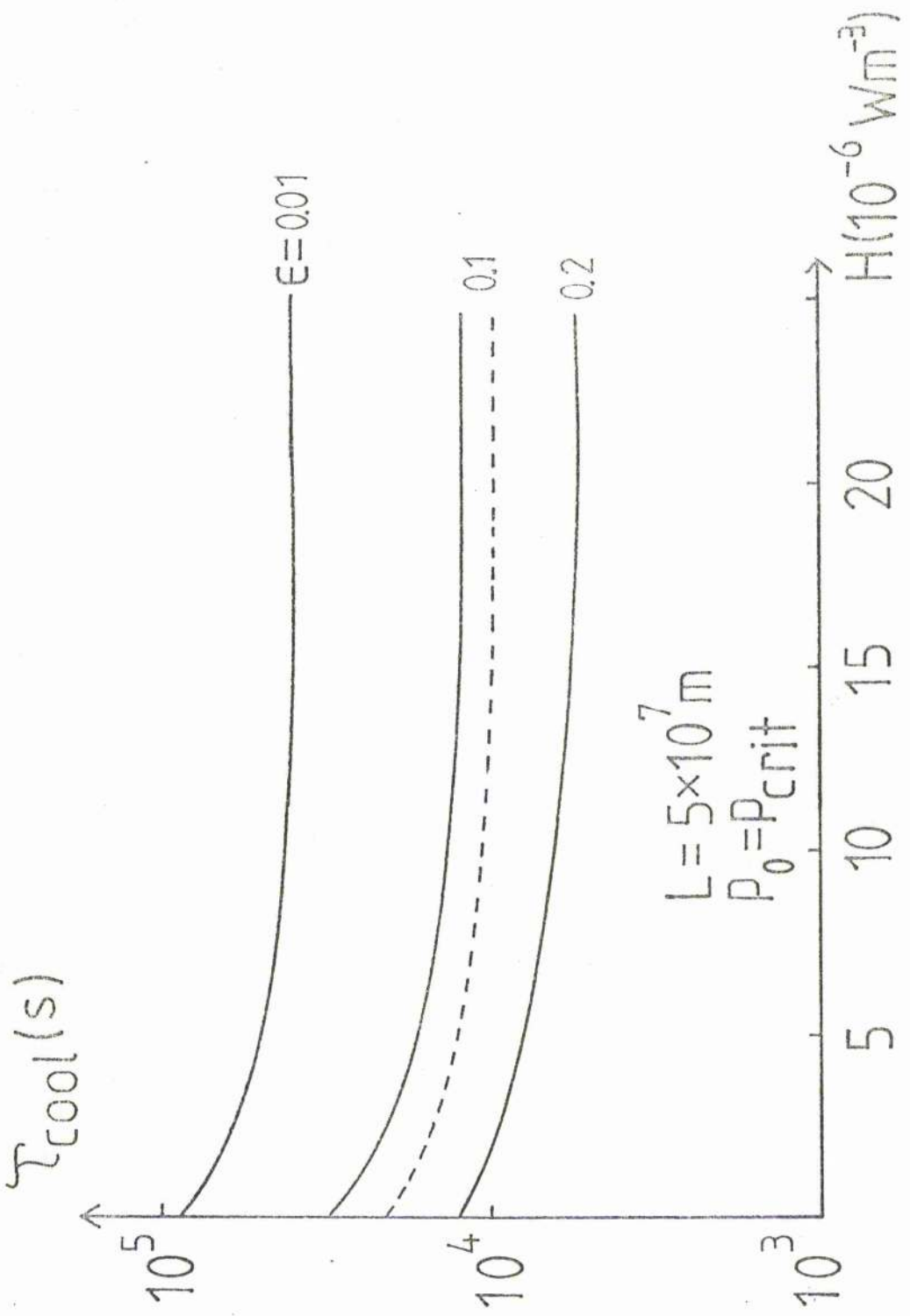

Figure 5.4 τ_{cool} as a function of the mechanical heating (H) for three values of ε. The loop half-length is 50Mm. The dashed curve denotes the analytic value of τ_{cool} derived from Equation (5.36).

$\bar{h}$, respectively. Increasing the length results in an increase in cooling time, since longer loops possess lower values of $\bar{p}$ crit and higher values of $\bar{T}$ crit, thus lowering the radiative loss. Increasing $\bar{L}$ also decreases the loss due to conduction. The difference in τ_{cool} between loops of 10 and 100Mm length is just less than a factor of ten, giving good agreement with the analytic result (5.37).

Increasing the heating, however, lowers the cooling time. This is a seemingly contradictory result since, by increasing $\bar{h}$, one is depositing more energy in the loop. The contradiction can be explained as follows. An increase in $\bar{h}$ raises $\bar{p}$ crit sufficiently to increase the value of radiation and overcome the increase in heating. The variation in τ_{cool} with heating is not large: the dashed curve is the analytic estimate for small values of ε derived in Section 5.3.2.

The case of $\bar{L}$ becoming critical is shown in Figure 5.5. $\bar{L}$ is only critical if $\bar{h} < \bar{p}^2$, and a loop can undergo non-equilibrium either by stretching or contraction. The cooling time has been calculated from the analytic approximation (5.30). The lower branch of the curves are for a loop being stretched such that

$$\bar{L} = \bar{L}_{crit}(1+\varepsilon)$$

and the upper branch for a loop that has been contracted. Thus, longer loops take longer to cool, but the variation along the lower branch is small.

The case of $\bar{h}$ becoming critical is not so interesting, since only one critical value exists provided (5.21) is satisfied.

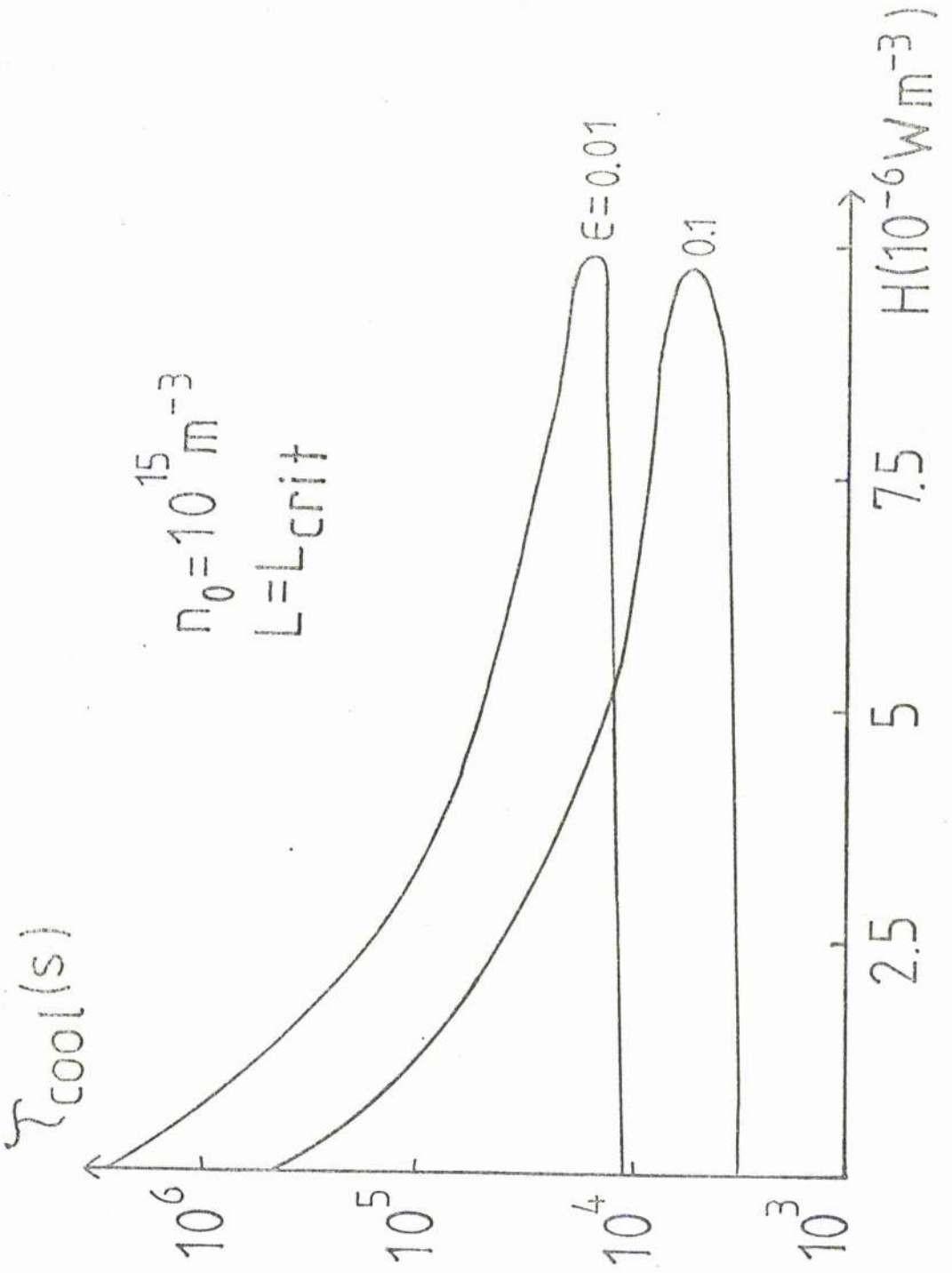

Figure 5.5 The analytic cooling time from (5.36) as a function of the heating, H, for a loop whose length has become critical. The upper half of each curve has had the length shortened by a factor ε below the critical value, whereas the lower half has been lengthened by ε. The base density has been taken as 10^{15} m^{-3}.

5.5 Discussion and conclusions

In this chapter we have discussed the possibility of a coronal loop undergoing thermal non-equilibrium if the pressure or length are increased byond certain critical values. The time for the loop to cool below 2×10^4 K is strongly parameter-dependent, but the cooling times generally lie in the range 5000 s $\rightarrow 10^5$ s. The most important parameter is ε, the magnitude by which the parameter ($\bar{p}$, $\bar{L}$ or $\bar{h}$) is pushed beyond the critical point, and for $\varepsilon \ll 1$ the cooling time is typically in the range mentioned. Downflows are expected to occur only when the plasma is cool enough ($T \lesssim 10^5$ K) for gravity to become important, but this phase has not been studied in detail. The results obtained are relevant to a number of observed physical processes in the solar corona, namely the formation of quiescent prominences, the presence of cool cores in some coronal loops (Foukal, 1975) and the loop evacuation observed by Levine and Withbroe (1977).

Priest and Smith (1979) pointed out that, if the footpoints of a coronal arcade are sheared enough, a cool region forms at the arcade summit. This was suggested as a means for the formation of a quiescent prominence. Our single field-line model here may represent a single part of the arcade, and it has been shown that thermal non-equilibrium provides a means of achieving the high densities observed in prominences (typically 10^{16} - 10^{17} m^{-3}; Tandberg-Hanssen, 1974). The proposed scenario is shown in Figure 5.6a. The high density is achieved by a siphon mechanism, which operates when the loop summit temperature and pressure fall

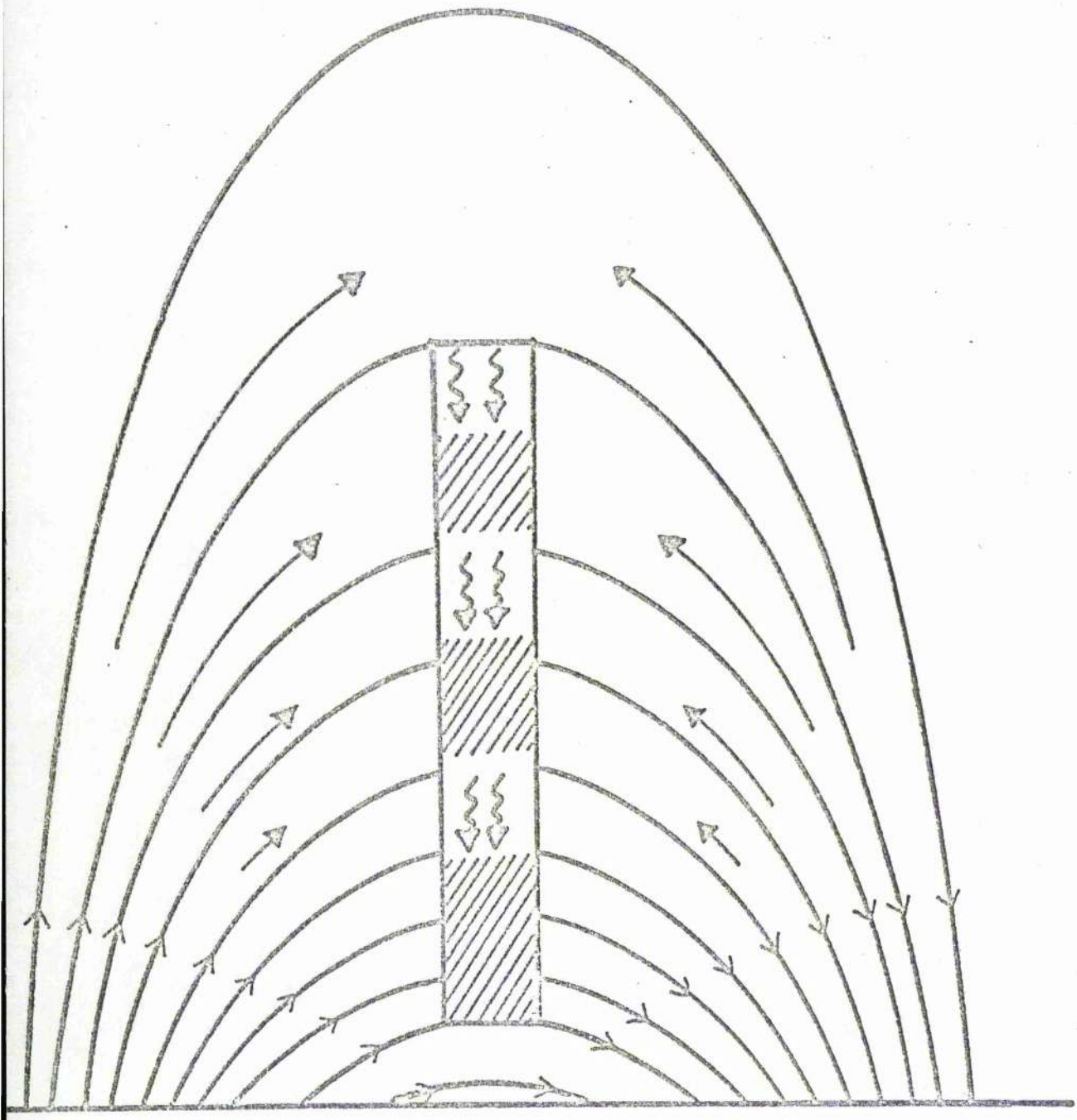

Figure 5.6a A possible dynamic prominence formation model. As a result of thermal non-equilibrium, a pressure gradient drives material along a field line from the photosphere to the loop summit where it cools to below 10^5K. If enough material collects, the field lines may sag and support a quiescent prominence. Subsequently, plasma is lost by dribbling through the field lines, but it is replaced by new plasma sucked up along the field lines from the sides. (From Priest and Smith, 1979).

so that a pressure gradient exists between the summit and the base, driving plasma upwards. The densities produced in this way are high (Figure 5.2b), typically above 10^{16} m^{-3} and the subsequent evolution is expected to be complicated. We suggest that, when the density is high enough, the force-free condition in the loop breaks down, so that the field lines sag and support the prominence (Kippenhahn and Schluter, 1957; Milne et al., 1979). It should be pointed out that this is not the same mechanism as that of Pikl'ner (1971). He generated an upflow by the inhibition of mechanical heating at the arcade summit, whereas the above process can result from a smooth evolution which suddenly undergoes non-equilibrium. The time of formation of such a prominence lies between 10^4 and 5×10^4 s, in agreement with the generally accepted values. The important feature of non-equilibrium is the sudden, non-linear development when the temperature falls from 8×10^5 K. A linear analysis would give substantially longer times for the temperature to fall below 10^5 K - in this respect our results are analogous to the numerical calculations of Hildner (1974) who found a similar rapid fall in temperature.

A possible steady-state is shown in Figure 5.6b. The material is continually sucked up by a siphon mechanism and becomes supersonic at the appropriate point along the loop as in Chapter 4. The flow is shocked by a slow oblique M.H.D. shock and then enters the prominence. Hence one can keep a large quiescent prominence continually supplied with plasma.

Foukal (1975) observed cool, low-pressure cores in some sunspot loops and thermal non-equilibrium is a possible

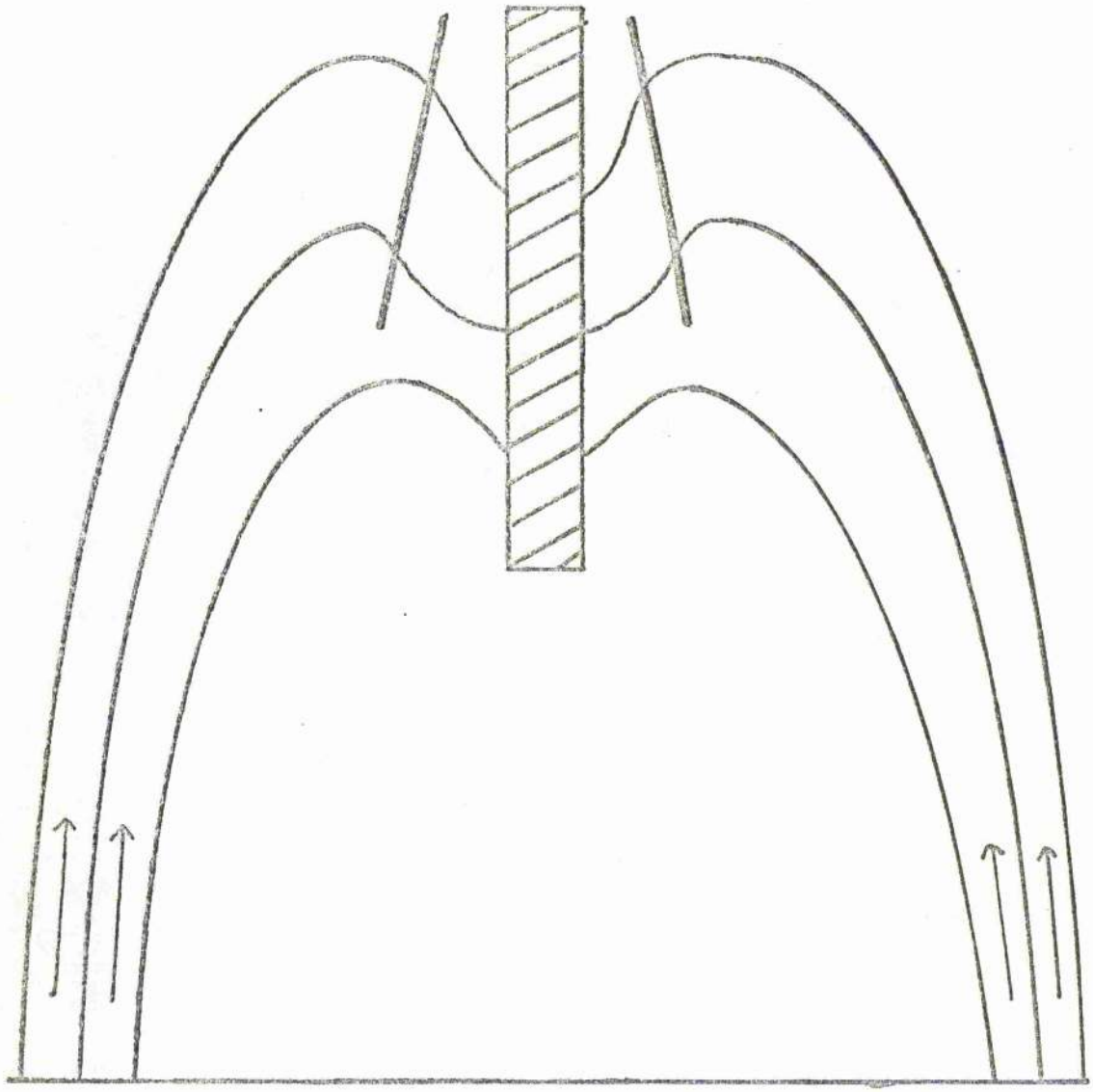

Figure 5.6b A possible steady-state prominence model. A siphon flow driven by a pressure gradient flow up the field lines, becomes sonic and is shocked by slow M.H.D. shocks (solid lines) before entering the prominence.

mechanism for their formation. One can visualise a loop being slowly twisted up until the critical pressure (or length) is reached and then, once this value is exceeded, the loop cooling down to 10^5 K or below. Our calculations can easily explain the temperature-pressure behaviour but the density is somewhat harder to understand, since we predict large-scale upflows. However, it is likely that gravity will cause the material to fall eventually and a continually dynamic state may persist. A full numerical code able to deal with shocks would be needed to simulate this. In fact, the behaviour of a loop after non-equilibrium will depend on the magnitude of the gas pressure and magnetic field at the summit and also on the magnetic field structure. The important parameter is the summit value of the plasma beta ($\beta = 2\mu p/B^2$). If non-equilibrium occurs in a loop then either a cool core or a dense filament (or prominence) will form. For small values of β, the transverse force balance across the loop will still be force-free and any evolution will occur along the field line. However, if β is of order unity due to a large pressure increase, then it is possible that the field lines may become deformed and a dense condensation result around the loop summit; supported by the magnetic field. We interpret this as being a cool filament. On the other hand, if the field line in our model is part of a coronal arcade (as in Figure 5.6a, b) we expect the scenario discussed earlier to arise. This serves to emphasise the inherent multi-dimensional nature of coronal loops and cautions against constructing too simple a model.

The event observed by Levine and Withbroe (1977) has

been connected with thermal non-equilibrium by Hood and Priest (1979a) and Roberts and Frankenthal (1980). These authors considered that the downflows observed could be explained by loop plasma falling under gravity after non-equilibrium had occurred. Downflows are observed at temperatures of 10^5 - 5 x 10^5 K and we point out that at no stage did our calculations produce downflows at these temperatures. Gravity does not become a dominating mechanism until below 10^5 K and so we must regard the link between the Levine-Withbroe event and non-equilibrium as unproved at this stage.

In conclusion, thermal non-equilibrium in coronal loops seems to be of considerable importance in the formation of cool structures in the solar corona. It has the attraction that no violent event is needed to trigger the cooling. One just needs a smooth variation in one of the parameters such that it exceeds a certain critical value and a thermal catastrophe results. It produces large-scale flows and could be partly responsible for the largely dynamic state of the solar corona, (e.g. Priest, 1981b).

CHAPTER 6: THERMAL NON-EQUILIBRIUM:- II - A MECHANISM FOR THE SIMPLE-LOOP FLARE

6.1 Introduction

As noted in Chapter 1, solar flares may be generally split into two types:- the simple-loop (compact) flare and the large 2-ribbon flare. The simple loop flare occurs in a magnetic loop which remains essentially unchanged in structure throughout the flare. The temperature is seen to rise to over 10^7 K within a few minutes and the emission measure, which is defined by Craig (1981, p.230) in its simplest form as

$$\int n_e^2 \, dV ,$$

rises to typically 10^{55} m^{-3}, attaining its maximum a few minutes after the temperature maximum (Milkey et al., 1971; Datlowe et al., 1974; Moore and Datlowe, 1975; Figure 6.1). The electron number density lies typically in the range $5 \times 10^{16} < n < 5 \times 10^{17}$ m^{-3}.

It is generally considered that such flares occur due to a rapid release of magnetic energy (e.g. reviews by Brown and Smith 1980; Van Hoven, 1981), and that such an energy release results in the thermal evolution discussed above. Models for this evolution have been reviewed by Craig (1981) and have usually proceeded along the following lines. The equations of one-dimensional gas-dynamics are first derived and an initial equilibrium is set up. The heating is then rapidly increased, due to magnetic energy release or particle acceleration, and the subsequent evolution followed. This procedure has been used by Kostyuk and Pikel'ner (1975), Nagai (1980) and Craig and MacClymont (1981). An alternative approach is to look at the nature of

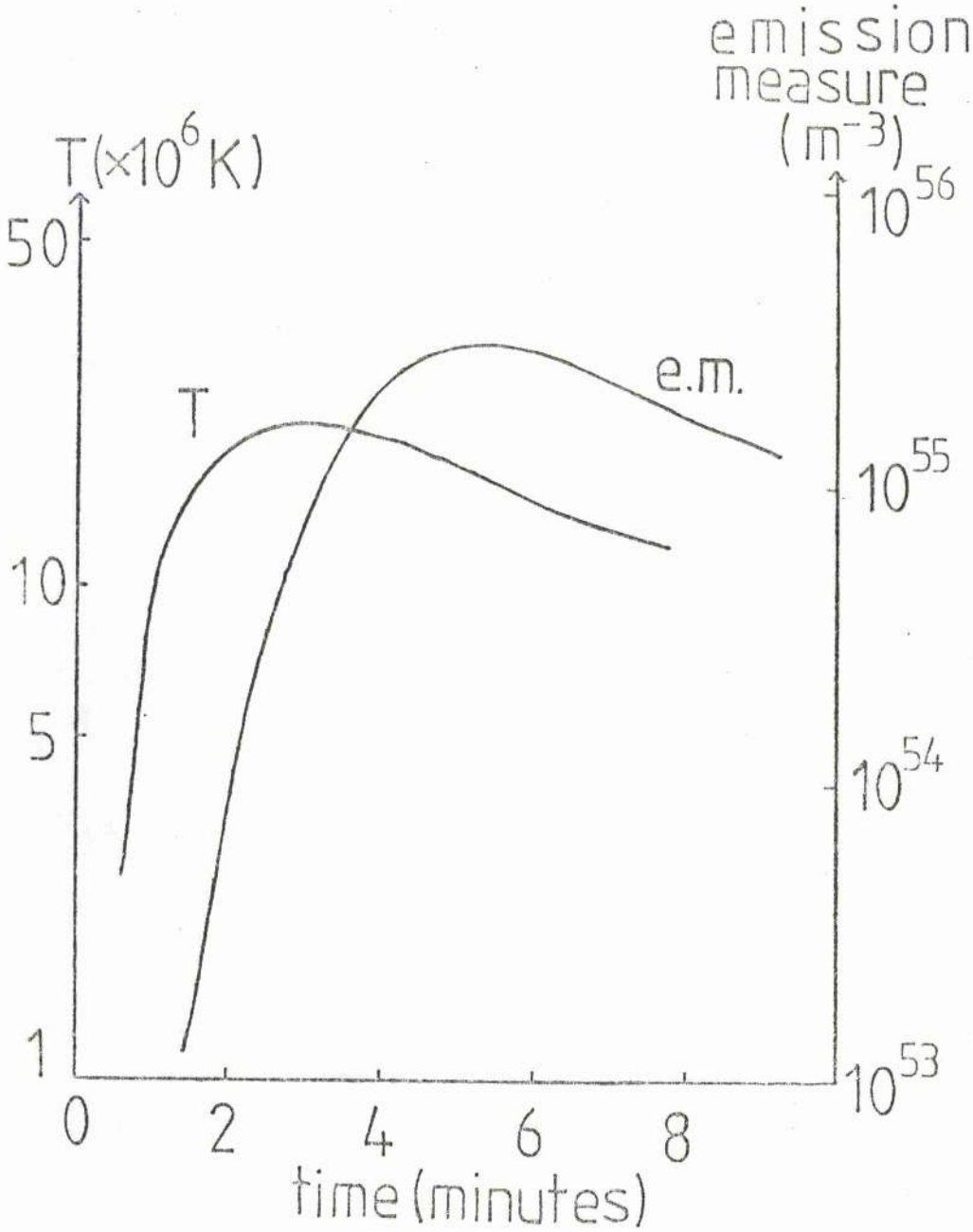

Figure 6.1 Evolution of temperature and emission measure for a typical simple-loop flare. The temperature attains its maximum value when the emission measure is still rising.

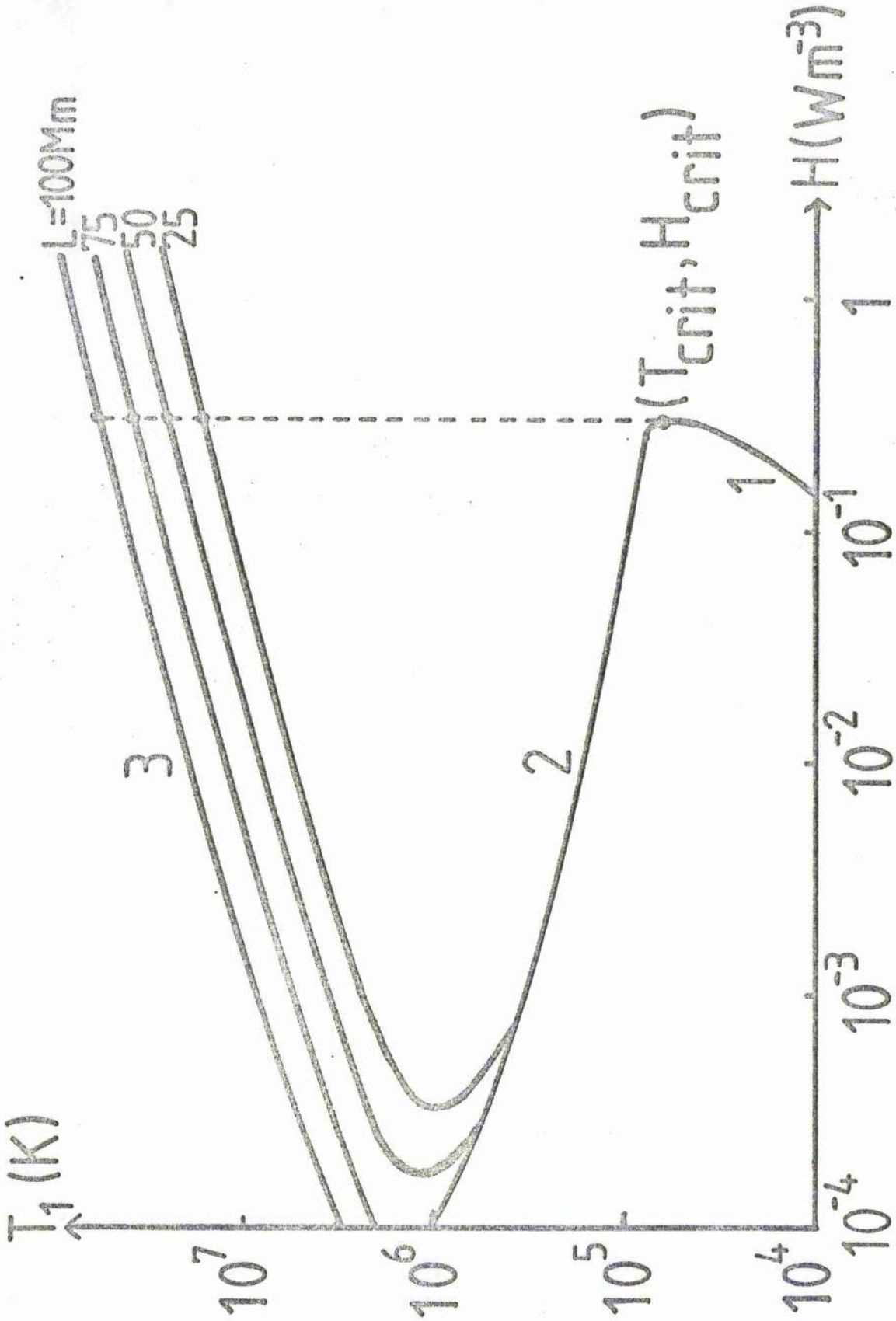

Figure 6.2 The equilibrium curves for a uniform-pressure loop of length 2L for different values of L in Mm (1Mm = 10^6m). As one increases the heating (H) for the cool solutions, the summit temperature (T_1) increases slowly along the lower curve up to the point (T_{crit}, H_{crit}) when no neighbouring equilibrium solution exists. The loop heats up to a new temperature (T_f), whose value depends on L. The base temperature, T_0, is here taken as 2×10^4 K.

the static energy balance equation (Hood and Priest, 1981) and so in this chapter, we discuss this alternative trigger for the simple-loop flare.

Hood and Priest (1981) have suggested that thermal non-equilibrium in cool loops may be responsible for some flares. The magnetic field is assumed to play a purely passive role by channelling heat. It is interesting to note that Cheng and Widing (1975) in their study of simple-loop flares found that several of these flares had " no obvious evidence of particle acceleration," suggesting a passive role for the electric (and magnetic) field. The cool loops (such as those observed by Foukal (1975) and discussed in the previous chapter) have temperatures of $2 - 5 \times 10^4$ K and their energy balance is between heating and radiation, as shown by the lowest curve of Figure 6.2. If the heating is increased, then the summit temperature rises until it reaches 8×10^4 K. Beyond this point, the radiative loss does not increase with temperature (Figure 1.1), and any additional energy deposited cannot be radiated away. Thermal conduction is negligible so no equilibrium exists and flaring occurs. Hood and Priest found that the loop heated up to over 10^7 K, but their analysis looks at only uniform pressure solutions of the static energy equation. The high-temperature solution is the top curve in Figure 6.2, and the path the flare follows is shown by a dashed line.

In this Chapter, we follow the non-linear evolution of this flaring in order to see if the heating can occur quickly enough. The idea is analogous to that discussed in Chapter 5 for the cooling of a loop, but the physics of the non-linear evolution is substantially different in that the flare occurs

over a considerably shorter time-scale.

6.2 Basic equations, time-scales and stability of critical points

6.2.1 Basic equations

Our equations are the same as in Chapter 5, namely the order-of-magnitude equations (5.11) - (5.13),

$$\lambda \bar{n}_1 \frac{d\bar{v}_0}{d\bar{t}} = \bar{n}_1 \bar{v}_0^2 + 2(\bar{n}_0 - \bar{n}_1 \bar{T}_1) + \bar{g}\bar{n}_1 \left.\frac{df}{d\bar{s}}\right|_{\bar{s}=1} , \tag{6.1}$$

$$\lambda \frac{d\bar{n}_1}{d\bar{t}} = \bar{n}_1 \bar{v}_0 , \tag{6.2}$$

$$\frac{d\bar{T}_1}{d\bar{t}} = \frac{(\gamma-1)}{\bar{n}_1}\left[\bar{T}_1 \frac{d\bar{n}_1}{d\bar{t}} + 2\bar{T}_1^{5/2}(1-\bar{T}_1) - \right.$$

$$\left. - \bar{n}_1^2 \bar{\chi} \bar{T}_1^{\alpha} + \bar{h}(\bar{p}_1, \bar{T}_1)\right] , \tag{6.3}$$

restated here for convenience.

Quantities with subscript 1 denote summit values and those with subscript zero denote base ones. λ is the ratio of sound-travel to radiation time-scales, $\bar{L}^{-2}$ is the ratio of conduction to radiation time-scales, $\bar{h}$ is a dimensionless mechanical heating, and $\bar{g}$ is the ratio of loop length to scale height.

6.2.2 Time-scales

During a flare, temperatures range from 10^5 - 10^7 K and densities from 10^{15} - 10^{18} m^{-3}, and it is expected that different time-scales will dominate at different phases of the flare.

The large variation between the time-scales was absent in the case of loop cooling discussed in Chapter 5, when, for the greater part of the calculation all the time-scales were of roughly the same order. The three time-scales, radiative (τ_R), conductive (τ_c) and sound-travel (τ_s), are given by equation (5.42). In Figures 6.3a-c the importance of each time-scale is shown as a function of temperature and density The loop half-length, L, is taken as 20, 50 and 100 Mm respectively.

By far the most interesting region is the bottom one where radiation dominates. The temperature and density here are comparable with those in a cool loop before flaring, and we analyse this region in Section 6.3. Elsewhere, it can be seen that sound waves are easily propagated, and clearly as the temperature increases conduction becomes more important until, for hot, rarefied plasmas, it dominates.

6.2.3 Thermal stability of critical points

In Chapter 5, it was shown that the growth-rate, σ, of perturbations to an equilibrium is given by

$$\sigma = \frac{(\gamma-1)}{\gamma \bar{p}} \left[\frac{\bar{T}_{10}^{-5/2}}{\bar{L}^2} (5 - 7\bar{T}_{10}) - \bar{p}^2 \bar{\chi} \bar{T}_{10}^{\alpha-2} (\alpha - 2) \right]. \qquad (6.4)$$

However, for the flare case, $\bar{L}^2 \gg 1$ and so σ and $\partial F / \partial \bar{T}_1$ are discontinuous when α changes sign. (6.4) indicates that σ is negative when $T_1 < 8 \times 10^4$ K ($\alpha = 2$) and positive when $T_1 > 8 \times 10^4$ K ($\alpha = 0$), and so we write (6.4) as

$$\frac{\partial F}{\partial \bar{T}_1} = \frac{(\gamma-1)}{\gamma \bar{p}} \left[\frac{\bar{T}_1^{5/2} (5 - 7\bar{T}_1)}{\bar{L}^2} + \right.$$

$$\left. + 2\bar{p}^2 \bar{T}_1^{-2} H(T_1 - 8 \times 10^4 K) \right]_{\bar{T}_1 = \bar{T}_{10}}, \qquad (6.5)$$

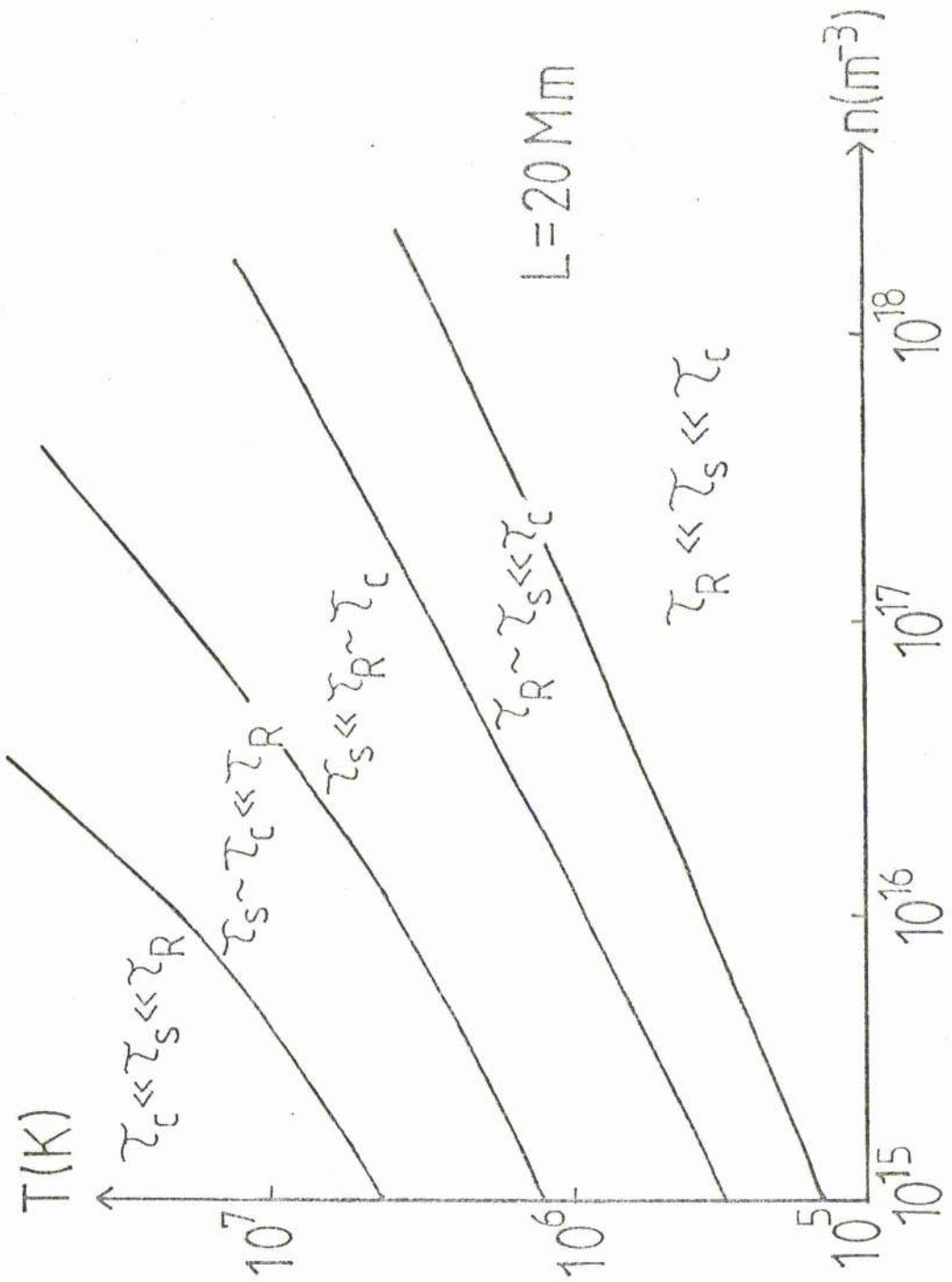

Figure 6.3a The relative importance of the time-scales (τ_s, τ_c, τ_R) for sound travel, conduction and radiation, respectively, as a function of density (n) and temperature (T) for a loop of length 2 x 10^7 m.

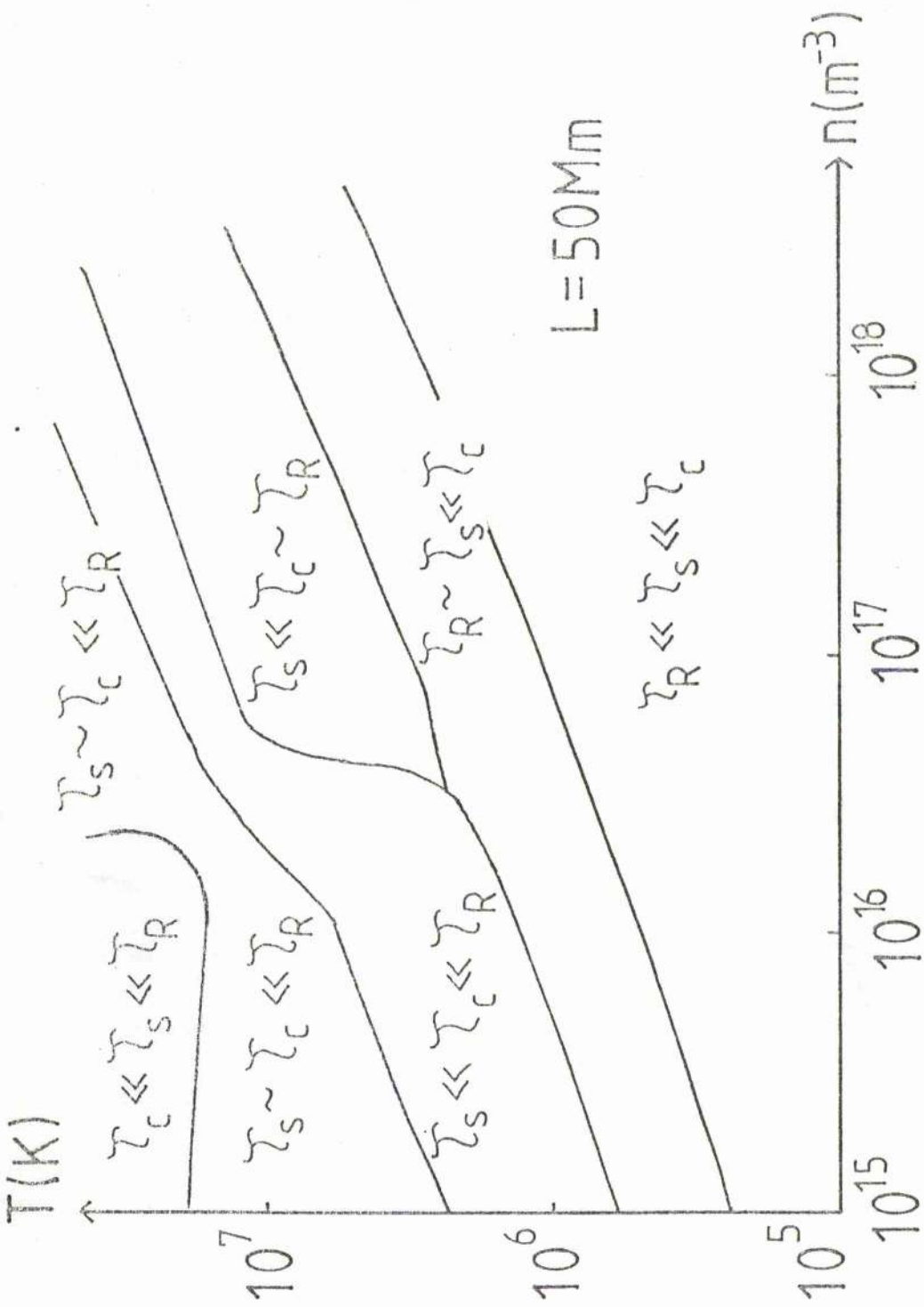

Figure 6.3b As Figure 6.3a with L = 50Mm.

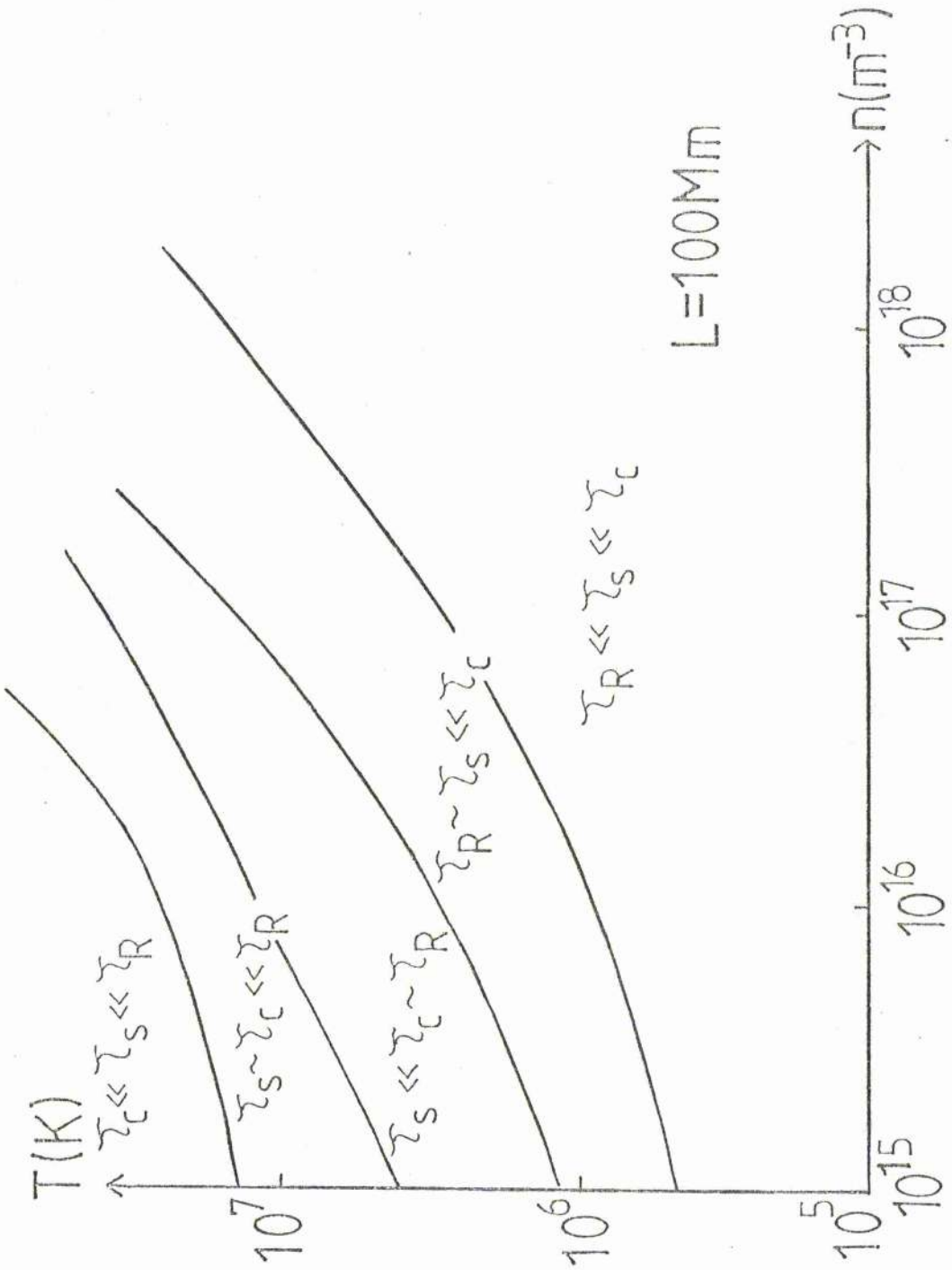

Figure 6.3c As Figure 6.3a with L = 100Mm.

where H represents the Heaviside function. At the critical point, however, $\partial F/\partial \bar{T}_1 = 0$ and quadratic stability may be investigated by writing

$$\frac{d\bar{T}_1}{d\bar{t}} = \frac{(\bar{T}_1 - \bar{T}_{crit})^2}{2}\left(\frac{\partial^2 F}{\partial \bar{T}_1^2}\right)_{\bar{T}_1 = \bar{T}_{crit}} ,$$

where

$$\left(\frac{\partial^2 F}{\partial \bar{T}_1^2}\right)_{\bar{T}_1 = \bar{T}_{crit}} = \frac{(\gamma-1)}{3\bar{p}}\left[\frac{\bar{T}_{crit}^{3/2}}{2\bar{L}^2}\left(5(9-2\alpha) + 7(2\alpha-9)\right) + \frac{2\bar{p}^2}{\bar{T}_{crit}^2}\,\delta(T_1 - 8\times 10^7 K)\right] . \tag{6.6}$$

δ is the delta function, and so (6.6) is positive, and the critical point is quadratically unstable.

6.3 Analytical solution for initial heating

As was mentioned in Section (6.2.2), a cool dense loop will evolve on the radiative time-scale. Since our model proposes that such a loop flares to higher temperatures, we analyse this initial phase. The scaling of the parameters is

$$1 << \lambda << \bar{L}^2 ,$$

and equations (6.1) - (6.3) reduce to

$$\frac{d\bar{v}_0}{d\bar{t}} = O\left(\frac{1}{\lambda}\right) , \tag{6.7}$$

$$\frac{d\bar{n}_1}{d\bar{t}} = O\left(\frac{1}{\lambda}\right) , \tag{6.8}$$

$$\frac{d\bar{T}_1}{d\bar{t}} = \frac{(\gamma-1)}{\bar{n}_1}\left[\bar{h}(\bar{p}, \bar{T}_1) - \bar{n}_1^2 \bar{\chi} \bar{T}_1^{\alpha}\right] + O\left(\frac{1}{\lambda}\right) . \tag{6.9}$$

To zeroth order,

$$\bar{v}_0 = 0, \tag{6.10}$$

$$\bar{n}_1 = \bar{n}_1(\bar{t} = 0), \tag{6.11}$$

$$\frac{d\bar{T}_1}{d\bar{t}} = \frac{(\gamma-1)}{\bar{n}_1}\left(\bar{h} - \bar{\chi}\bar{n}_1^2\bar{T}_1^{\alpha}\right), \tag{6.12}$$

provided the velocity vanishes at the summit. These are also the form of the full, undifferenced equations under the same approximation.

Equation (6.12) can be integrated if α is an integer, and the general solution is given by Gradshteyn and Ryzhik (1980), p.63. However, to model a flare up to temperatures of 2×10^6 K we only need to consider $\alpha = 0$ and $\alpha = -2$ (Table 1.1). The solutions are

$$\bar{t} = \frac{\bar{n}_1}{(\gamma-1)}\frac{(\bar{T}_1 - \bar{T}_{crit})}{(\bar{h} - \bar{n}_1^2)}, \quad 8\times10^4 < T < 2.5\times10^5, \tag{6.13}$$

$$\bar{t} = \bar{t}\left(T_1 = 2.5\times10^5\ \mathrm{K}\right) + \frac{\bar{n}_1}{(\gamma-1)\bar{h}}\left[(\bar{T}_1 - \bar{T}_c) - \left(\frac{\bar{n}_1^2}{\bar{h}}\right)^{1/2}\tanh^{-1}\left\{\frac{\left(\frac{\bar{h}}{\bar{n}_1^2}\right)^{1/2}(\bar{T}_1 - \bar{T}_c)}{\left(1 + \frac{\bar{h}\bar{T}_1\bar{T}_c}{\bar{n}_1^2}\right)}\right\}\right],$$

$$2.5\times10^5 < T < 5.62\times10^5, \tag{6.14}$$

$$\bar{t} = \bar{t}\left(T_1 = 5.62\times10^5\right) + \frac{\bar{n}_1(\bar{T}_1 - \bar{T}_c)}{(\gamma-1)(\bar{h} - \bar{n}_1^2)},$$

$$5.62\times10^5 < T < 2\times10^6, \tag{6.15}$$

where $\bar{T}_c$ represents the temperature at which α changes sign.

Now, suppose that, after reaching the point of non-equilibrium, the heating is increased by a factor ε , such that

$$\bar{h} = \bar{h}_{crit}(1+\varepsilon) , \qquad \varepsilon > 0 ,$$

where $\bar{h}_{crit}$ satisfies

$$\bar{n}_1^2 = \bar{h}_{crit} .$$

since conduction is small at such low temperatures (Figure 6.2). The initial flaring behaviour is given by (6.13) in the form

$$\bar{T}_1 = \bar{T}_{crit}\left(1 + \frac{\varepsilon \bar{t}(\gamma-1)\bar{n}_0}{\bar{T}_{crit}^2}\right) , \tag{6.16}$$

where $\bar{n}_0$ is the base density. Thus, the temperature increases linearly in time, and the rate of increase is proportional to both the base density and heating perturbation. This can be identified as the "preflare phase".

Equation (6.14) may be written as

$$\bar{t} = \frac{(\bar{T}_1 - \bar{T}_{crit})}{(\gamma-1)\bar{n}_0\varepsilon} + \frac{1}{(\gamma-1)\bar{n}_0(1+\varepsilon)}\left[(\bar{T}_1 - \bar{T}_c) - \right.$$

$$\left. - \frac{1}{(1+\varepsilon)} \tanh^{-1}\left(\frac{(1-\varepsilon)(\bar{T}_1 - \bar{T}_c)}{1+(1+\varepsilon)\bar{T}_1\bar{T}_c}\right)\right] . \tag{6.17}$$

Equation (6.17) shows that once the initial (preflare) phase is over, the next stage of temperature rise is approximately independent of ε for $\varepsilon \ll 1$. Beyond this stage, our approximation will not be valid.

In theory, one would extend this analysis by the derivative-expansion method but this yields little further information (Hood and Priest, 1982) since the equations are too complicated to be solved analytically.

6.4 Numerical solution for initial phases of flare

In the previous section, an analytical solution for the initial or preflare stage of the flare was derived, and it is now necessary to solve equations (6.1) - (6.3) numerically in order to find the summit temperature of the flare up to its maximum value.

The point of non-equilibrium is given by

$$\left(\frac{\partial \bar{F}}{\partial \bar{T}_1}\right)_{\bar{T}_1 = \bar{T}_{crit}} = 0 \,,$$

and if $\partial \bar{F}/\partial \bar{T}_1$ changes sign from negative to positive, we move from a stable to an unstable branch of the equilibrium curve (Section 5.2.3). For the radiation law adopted here, this occurs at 8×10^4 K and the critical heating ($\bar{h}_{crit}$) follows from the steady-state energy equation. Thus, all heat deposited in the loop is being radiated away. If the heating is then increased beyond $\bar{h}_{crit}$ by

$$\bar{h} = \bar{h}_{crit}(1+\varepsilon)$$

then the extra energy cannot be radiated away and the loop heats up. Equations (6.1) - (6.3) were integrated numerically by a Runge-Kutta scheme (neglecting gravity and area divergence) subject to initial conditions at $\bar{t} = 0$ of

$$\left.\begin{aligned} \bar{T}_1 &= \bar{T}_{crit} \,, \\ \bar{n}_1 &= \frac{\bar{n}_0}{\bar{T}_{crit}} \,, \\ \bar{V}_0 &= 0 \,, \end{aligned}\right\} \qquad (6.18)$$

and using an initial time-scale of $\bar{t} = 0.01$.

Figure 6.4 shows the variation of the summit temperature with time for several values of the heating perturbation, ε.

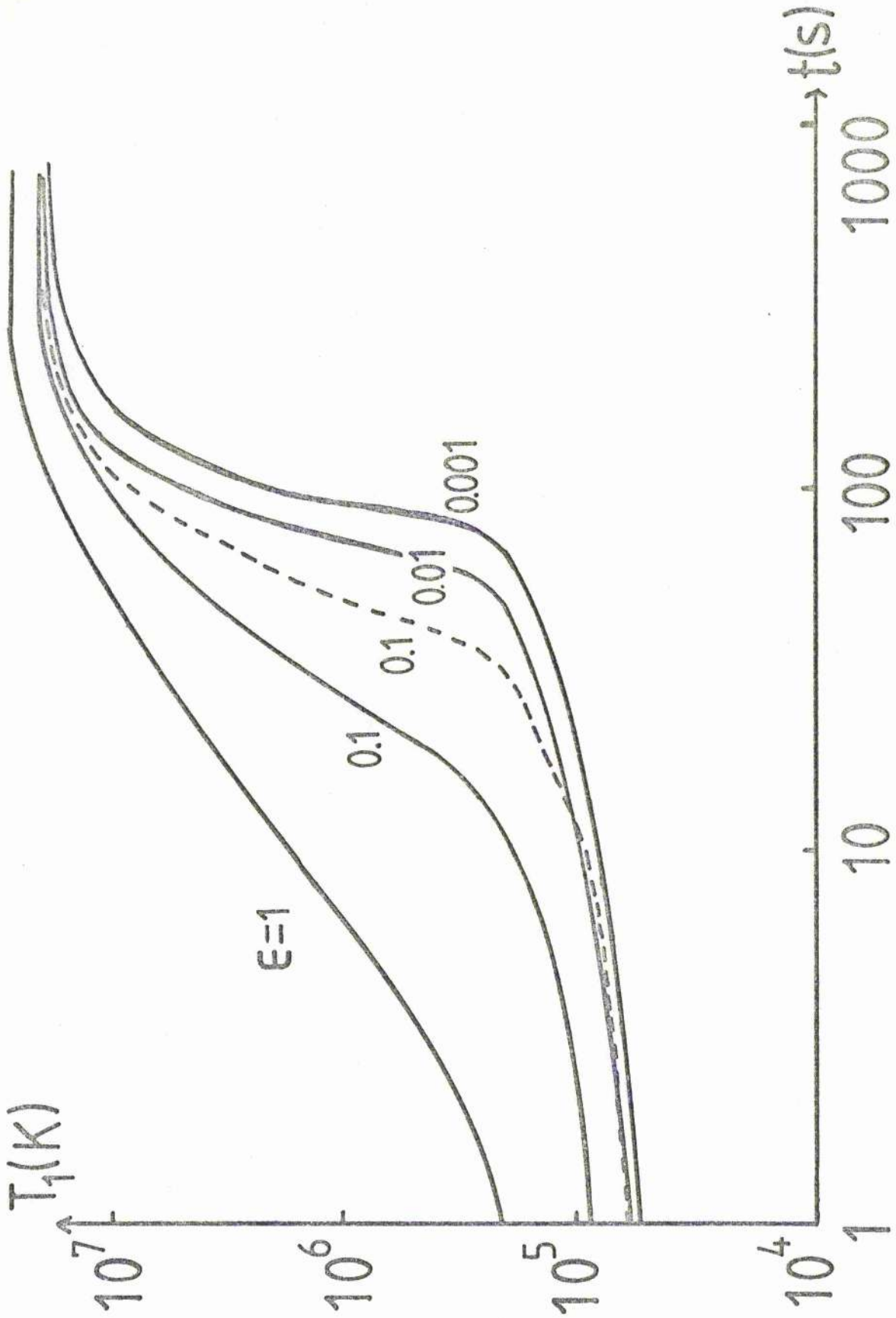

Figure 6.4 The temporal evolution of the summit temperature (T_1) with time (t) as a function of ε, the heating perturbation. The loop has a half-length of 50Mm, base density 2.5×10^{17} m^{-3}, base temperature 2×10^4 K and critical heating 3.2×10^{-1} W m^{-3}.

We have chosen a loop of half-length 50 Mm and base density 2.5×10^{17} m^{-3}. For large increases in heating ($\mathcal{E} \gg 1$), the temperature exceeds 2×10^7 K after approximately 30s, but, as $\mathcal{E}$ is decreased, so the time taken to reach this temperature increases. For small $\mathcal{E}$, the temperature increases in two phases which we identify as the preflare phase and the flash phase (or flare-rise phase). First, there is a slow increase up to 2.5×10^5 K (Equation 6.16), and then there is a very rapid flaring which is initiated when α becomes negative. The duration of the second phase (when the plasma heats up from 2.5×10^5 K to its maximum temperature) is approximately independent of $\mathcal{E}$. The temperature increase is eventually stopped when conduction becomes effective. The phase between the flash-phase and the temperature maximum is referred to as the intermediate phase and is characterised by a slower increase in the temperature. The initial parts of these solutions were checked against the analytic solutions of Section 6.3 and gave good agreement. It should also be pointed out that any value of $\mathcal{E}$ (>0) will give rise to a flare eventually.

The flare rise-time, τ_f, may be defined as the time for the summit plasma to heat from 8×10^4 K to its maximum value (where $d\bar{T}_1/d\bar{t} = 0$). It depends on the physical quantities L, n_0 and $\mathcal{E}$. In Figure 6.5, τ_f is plotted against L for several values of $\mathcal{E}$. Increasing the loop half-length increases both the conduction time-scale and the sound travel-time, so that variations due to both conduction and sound waves take place more slowly. Thus, both the flaring time and flare temperature increase with L. For the values of $\mathcal{E}$ and L considered, τ_f lies within the range 5 - 15 minutes, which is

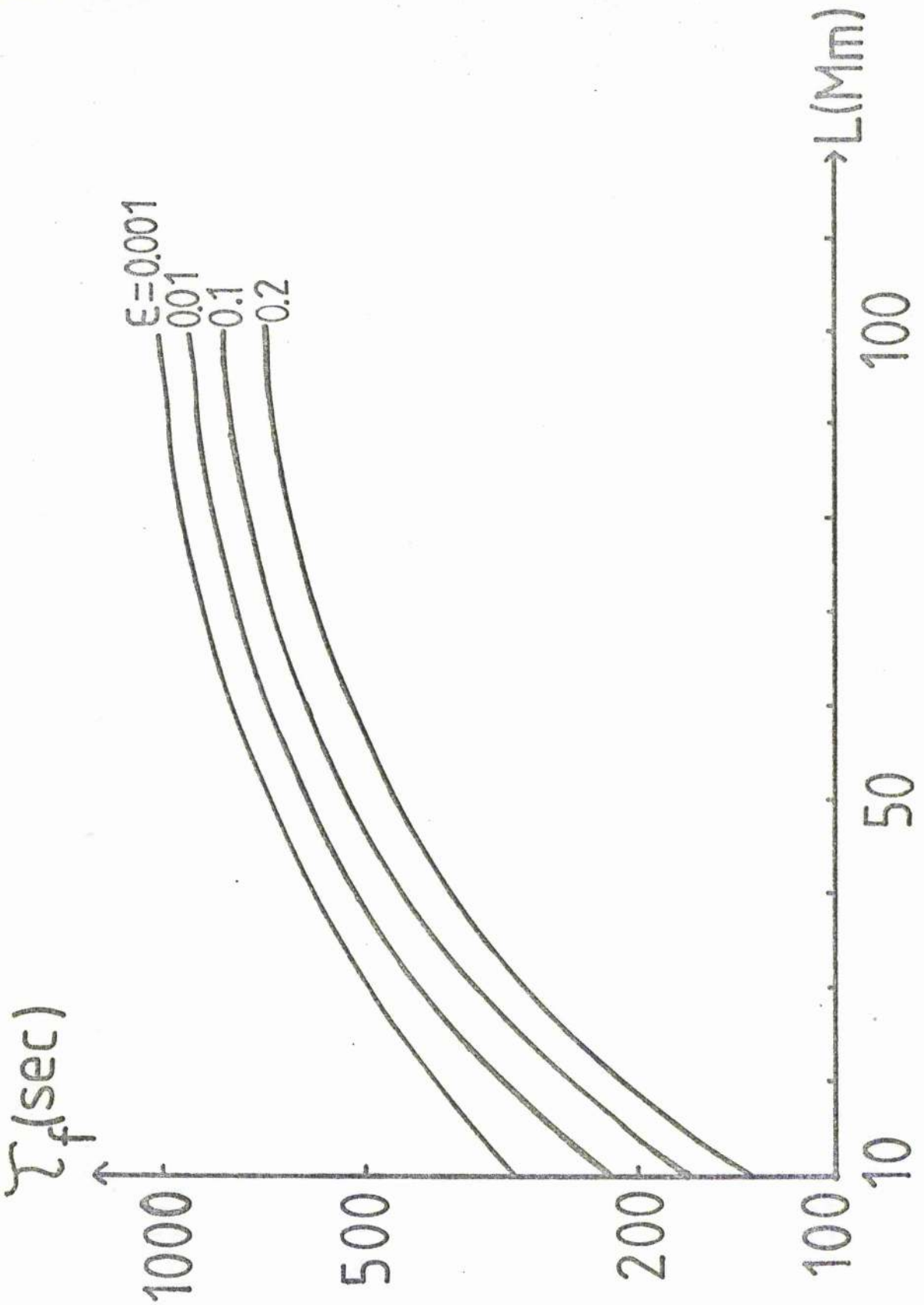

Figure 6.5 The flare rise time-scale (τ_f) as a function of the loop half-length (L) in Mm (=10^6 m) for several values of the perturbation ε. τ_f is defined as the time for the summit temperature to rise from its critical values to its maximum. The base density is 2.5×10^{17} m^{-3} and the base temperature 2×10^4 K.

in reasonable agreement with observations (See Section 6.6).

Figure 6.6 shows the variation of τ_f with the base density (n_0). n_0 may possibly increase as the magnetic field is twisted up due to the conservation of total pressure. However, unlike the case when the length is varied, a change in n_0 does alter the critical (mechanical) heating. If $T_{crit} = 8 \times 10^4$ K, then

$$\bar{h}_{crit} = \frac{\bar{n}_0^2}{\bar{T}_{crit}^2} + O\left(\frac{\bar{T}_{crit}^{7/2}}{\bar{L}^2}\right). \qquad (6.19)$$

In Figure 6.6 it can be seen that τ_f decreases as n_0 increases. Thus flares occurring in active regions with high gas pressures will tend to attain their maximum temperatures more rapidly than those taking place elsewhere.

Figure 6.7 shows the variation of the flare maximum temperature (T_f) with base density for several loop lengths, with ϵ held fixed as 0.1. If n_0 or L are increased, then so does T_f. A simple scaling relationship may be derived from the numerical results, namely

$$T_f \approx 2.6 \times 10^{-7} L^{0.52} n_0^{0.57} \quad K.$$

This may be explained if the plasma reaches a quasi-static equilibrium at its maximum temperature T_f. Such a balance between conduction and heating (See Hood and Priest, 1981) together with equation (6.19) gives the scaling law

$$T_f \approx 2.5 \times 10^{-7} (L n_0)^{4/7} \quad K,$$

where $4/7 \simeq 0.57$. The agreement is therefore reasonable despite the fact that large flows are present during the flare rise. We discuss the role of flows in the next section.

So far we have not discussed the role of gravity and of

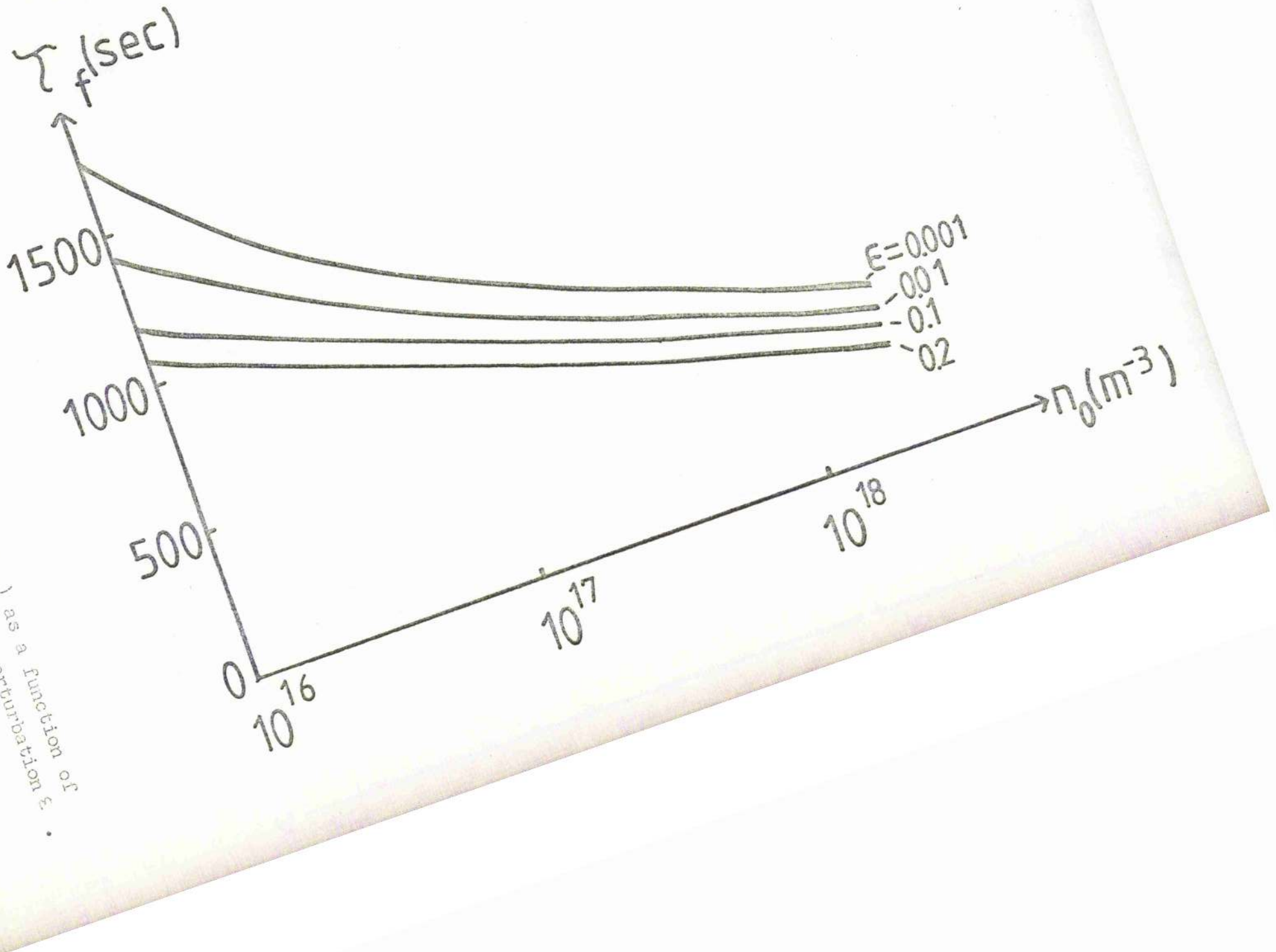

Figure 6.6 The flare time-scale (τ_f) as a function of the base density for several values of the perturbation ε.

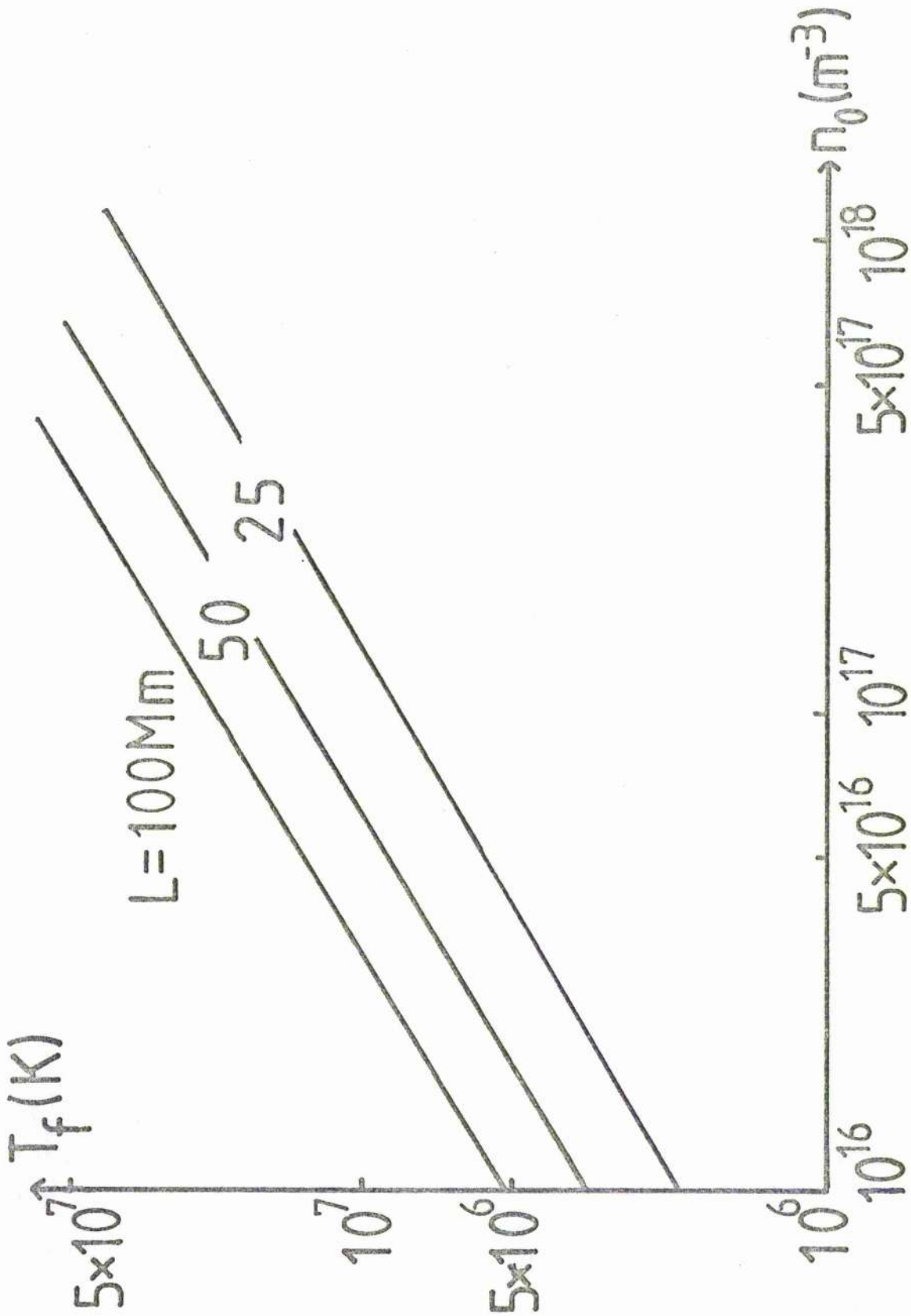

Figure 6.7 The flare temperature (T_f) as a function of the base density (n_0) for several loop half-lengths (L). T_f is the maximum temperature of the summit plasma. The critical heating varies with n_0.

flux tube divergence in flare modelling, but one can make a few simple statements. Gravity is a stabilising effect (Wragg and Priest, 1982a), so one expects τ_f to increase due to a decrease in the initial growth-rate. The main effect of gravity is one of stratification, as seen from the static form of (6.1),

$$\bar{n}_1 = \frac{2\bar{n}_0}{(2\bar{T}_1 - \bar{g}\, f'(\bar{s}=1))} \,, \tag{6.20}$$

where $f'(\bar{s} = 1) < 0$.

(6.20) shows clearly that introduction of stratification reduces the summit density, the magnitude of the reduction depending on the parameter $\bar{g}$. $\bar{g}$ is a measure of the loop-length, L, to the scale-height, and for cool loops, $\bar{g}$ can be large. Thus, gravity is clearly an effect to be included in future calculations. Its inclusion in our numerical code led to an increase in τ_f and a reduction in T_f, both by small amounts.

Flux tube divergence is unimportant at low temperatures but becomes important when large mass fluxes and temperatures occur. Wragg and Priest (1981) show that, if $d\bar{A}/d\bar{s}$ and $d\bar{T}/d\bar{s}$ are both positive, flux tube divergence acts like an additional heat source. Thus, we expect loops with strong divergence to possess higher flaring temperatures.

Up until now we have examined the case when the heating becomes critical, so now let us consider the behaviour when the base density becomes critical instead. It may be shown that the critical values are

$$T_{crit} = 8 \times 10^4 \, K \,,$$

$$\bar{n}^2_{crit} = \bar{h} / (\bar{\chi} \bar{T}^{\alpha-2}_{crit}) \,.$$

Non-equilibrium occurs when the base density, $\bar{n}_0$, is decreased

below its critical value

$$\bar{n}_0 = \bar{n}_{crit}(1-\varepsilon'), \quad \varepsilon' < 1,$$

and the temperature grows initially like

$$\bar{T}_1 = \bar{T}_{crit}\left(1 + \frac{\varepsilon'(2-\varepsilon')}{(1-\varepsilon')}\frac{\bar{t}(\gamma-1)\bar{n}_0}{\bar{T}_{crit}^2}\right), \qquad (6.21)$$

which is simply equation (6.16) with ε replaced by

$$\varepsilon \longrightarrow \frac{\varepsilon'(2-\varepsilon')}{(1-\varepsilon')} .$$

Thus, for $\varepsilon' \ll 1$, the preflare phase proceeds at twice the rate if the density is critical rather than the heating.

Finally, other forms of the heating perturbation may be considered, such as a linear increase to a constant value

$$\bar{h} = \left\{ \begin{array}{ll} \bar{h}_{crit}(1+\varepsilon\bar{t}/\bar{t}_1), & \bar{t} \leq \bar{t}_1, \\ \bar{h}_{crit}(1+\varepsilon), & \bar{t} > \bar{t}_1, \end{array} \right\} \qquad (6.22)$$

or a sinusoidal pulse,

$$\bar{h} = \left\{ \begin{array}{ll} \bar{h}_{crit}\left(1+\varepsilon \sin\left(\frac{\pi\bar{t}}{\bar{t}_1}\right)\right), & \bar{t} \leq \bar{t}_1, \\ \bar{h}_{crit}, & \bar{t} > \bar{t}_1. \end{array} \right\} \qquad (6.23)$$

Little difference was found in the resulting flare parameters for either of those forms, and so we conclude that non-equilibrium will proceed at approximately the same rate no matter how the heating is increased beyond its critical value provided $\varepsilon \ll 1$. This is seen in Figure 6.4 where the dashed curve represents a heating pulse of the form (6.23).

6.5 The behaviour of flare density and velocities

In Sections 6.3 and 6.4 we have obtained solutions of the order-of-magnitude equations for the flare rise, and have shown that the onset of thermal non-equilibrium can give reasonable

values for the flare temperature and rise-time. The subsequent behaviour of the loop density was not discussed, since the assumption of fixed footpoint density and temperature is unlikely to be true. Under our assumed boundary conditions, the behaviour is as follows. After non-equilibrium, the loop summit temperature rises and so does the pressure. A pressure gradient exists between summit and base, driving a downflow and decreasing the density. This downflow possibly is the same as that observed by Lites et al., (1981) which was seen to be of order 70 km s^{-1}. Due to our order-of-magnitude approximation, we cannot follow whether this steepens into a shock. By keeping the base conditions fixed, we always have a pressure gradient between summit and base driving a downflow. However, since an increase in density is observed, this description is clearly inadequate, and we suggest the following alternative.

The downflow steepens and forms a shock which propagates down the loop, impinging upon the chromosphere. The temperature at the loop base is enhanced sufficiently to drive an upflow (which may well be supersonic). We are unable to model this evaporation exactly but can make analytical progress as follows.

Suppose that conduction has not yet become important ($L^{-2} \ll 1$) and that mechanical heating and enthalpy flux provide the main energy deposition or loss. (Radiation falls off as T^{-1} above 8×10^4 K and is assumed unimportant). It is also assumed (for analytical simplicity) that the flows are subsonic and so the pressure is spatially constant. One can then develop separable solutions similar to those of Antiochos (1980) in which heating drives an upflow: by comparison he used radiation to drive a downflow. The equations of momentum, (5.5) state,

(5.7), continuity (5.6) and energy (5.8) are

$$\bar{P} = \bar{P}(\bar{t}), \tag{6.24}$$

$$\bar{P} = \bar{n}\,\bar{T}, \tag{6.25}$$

$$-\lambda \frac{\bar{P}}{\bar{T}} \frac{\partial \bar{T}}{\partial \bar{t}} + \lambda \frac{\partial \bar{P}}{\partial \bar{t}} - \frac{\bar{v}\bar{P}}{\bar{T}} \frac{\partial \bar{T}}{\partial \bar{s}} + \bar{P} \frac{\partial \bar{v}}{\partial \bar{s}} = 0, \tag{6.26}$$

$$\frac{3}{2} \frac{\partial \bar{P}}{\partial \bar{t}} + \frac{5}{2} \frac{\partial \bar{v}}{\partial \bar{s}} \frac{1}{\lambda} = \bar{h}. \tag{6.27}$$

Antiochos (1980) has a radiative loss term on the right-hand side of (6.27) instead of heating.

Eliminating $\bar{v}$ from (6.24) - (6.27) gives

$$\bar{P}\left(\frac{\partial \bar{T}}{\partial \bar{t}} \frac{\partial^2 \bar{T}}{\partial \bar{s}^2} - \frac{\partial^2 \bar{T}}{\partial \bar{s} \partial \bar{t}} \frac{\partial \bar{T}}{\partial \bar{s}} \right) + \frac{\partial \bar{P}}{\partial \bar{t}} \left(\left(\frac{\partial \bar{T}}{\partial \bar{s}} \right)^2 - \frac{2\bar{T}}{5} \frac{\partial^2 \bar{T}}{\partial \bar{s}^2} \right) + \frac{2\bar{h}}{5} \bar{T} \frac{\partial^2 \bar{T}}{\partial \bar{s}^2} = 0. \tag{6.28}$$

Following Antiochos directly, we seek separable solutions of the form

$$\bar{P} = \bar{P}_0 \phi(\bar{t}),$$
$$\bar{T} = \bar{T}_0 \theta(\bar{t}) \xi(\bar{s}),$$

so that

$$\frac{\partial \theta}{\partial \bar{t}} \frac{\phi}{\theta} \left(\xi \frac{\partial^2 \xi}{\partial \bar{s}^2} - \left(\frac{\partial \xi}{\partial \bar{s}} \right)^2 \right) + \frac{\partial \phi}{\partial \bar{t}} \left(\left(\frac{\partial \xi}{\partial \bar{s}} \right)^2 - \frac{2\xi}{5} \frac{\partial^2 \xi}{\partial \bar{s}^2} \right) - \frac{2\xi}{5} \frac{\partial^2 \xi}{\partial \bar{s}^2} = 0, \tag{6.29}$$

where

$$\bar{t} = \frac{\bar{t}\,\bar{h}}{\bar{P}_0}.$$

Separable solutions exist if the time-dependent coefficients are constants, so that

$$\left.\begin{aligned} \bar{p} &= \bar{p}_0(l\bar{t}+1), \\ \bar{T} &= \bar{T}_0(l\bar{t}+1)^{k/l}\,\xi(\bar{s}), \end{aligned}\right\} \qquad (6.30)$$

where k and l are constants whose range of values are to be determined.

Next ξ may be expressed as

$$\frac{d\xi}{d\bar{s}} = \frac{d\xi(0)}{d\bar{s}}\,\xi^{-\frac{n}{m}}, \qquad (6.31)$$

where

$$\left.\begin{aligned} n &= k-l, \\ m &= \tfrac{2}{5}(l+1)-k, \end{aligned}\right\} \qquad (6.32)$$

so that there is a two-parameter family of solutions in terms of k and l.

The allowable values of k and l may be determined as follows. The velocity is given by

$$\bar{v} = \frac{\lambda m\,\xi^{\frac{n}{m}+1}}{5(l\bar{t}+1)\,d\xi(0)/d\bar{s}}, \qquad (6.33)$$

and for evaporation we need $\bar{v} > 0$ which implies that

$$\left.\begin{aligned} &m > 0, \\ \text{or}\quad &k < \tfrac{2}{5}(l+1), \end{aligned}\right\} \qquad (6.34)$$

It is also required from observations that $\bar{p}$ and $\bar{T}$ increase in time and so l and k are positive. Finally, it is required that the differential emission measure (D.E.M.) increase with time (Craig, 1981). The D.E.M. is defined by Craig as

$$\int = \frac{p^2}{2k_B^2 T^2}\,\frac{1}{\left|\frac{dT}{ds}\right|}, \qquad (6.35)$$

where k_B is Boltzmann's constant.

Thus we require

$$k < 1 \ . \qquad (6.36)$$

Equations (6.34) and (6.36) give a restriction on k and l. Figure 6.8 shows the time-dependence of the temperature and velocity (θ ($\bar{t}$) and v ($\bar{t}$)), where

$$\bar{v}(\bar{t}) = \frac{2(2+1) - 5k}{25(l\bar{t}+1)} \ .$$

Clearly the temperature is increasing and the velocity is positive for all time and one has a solution of the form required. The general effect of increasing k is to raise the value of θ and decrease v. This shows that the time-dependent equations permit solutions in which both the temperature rises in time and the velocity is positive (i.e. an upflow), as is required in the intermediate stages of the flare. However, further calculations are required to back up this simple, semi-kinematic aproach.

Further upflows are present in the decay phase. The <u>decay phase</u> can be defined here as the time when the flare temperature is falling and the density is still rising (Figure 6.1). Antiochos and Sturrock (1978) have analytically demonstrated the existence of an upflow in this phase. Again, subsonic flows and constant pressure are assumed and they find that

$$V = \frac{2\times 10^{-11}}{5p} T^{5/2} \frac{dT}{ds} \ .$$

Since heat is being conducted away from the summit, a velocity is driven upwards.

It thus seems that continual mass evaporation is occurring throughout the flare: i.e. from the flash phase until well on into the decay phase.

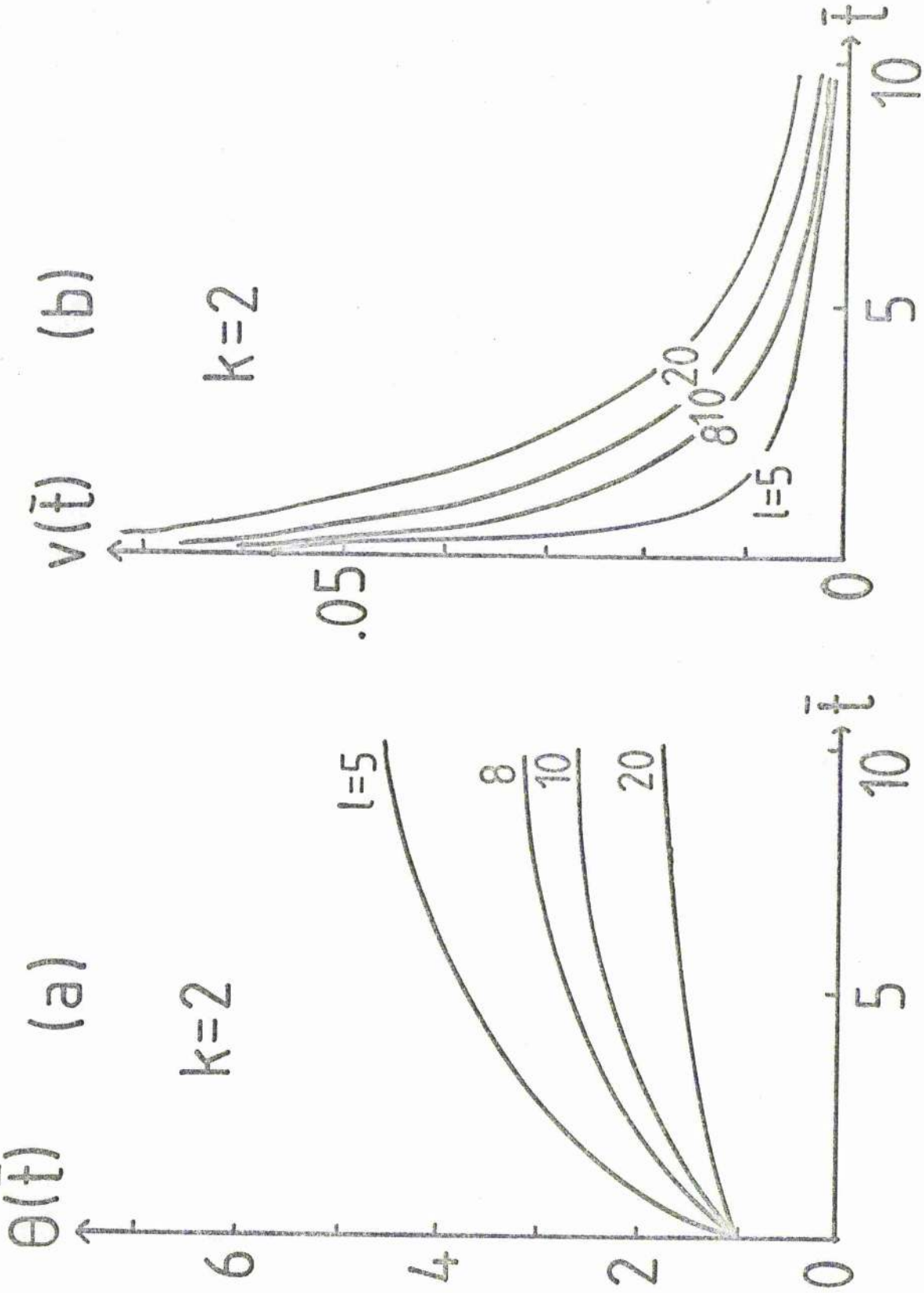

Figure 6.8 (a) The time dependent part, $\theta(\bar{t})$, of the separable solution for the temperature during the intermediate (evaporation) phase as a function of the dimensionless time $\bar{t}$ $(=tH/p_0)$. p_0/H is typically 5 seconds. The parameter k is 2, and l is allowed to vary. (b) The time dependent part, $v(\bar{t})$ of the velocity.

6.6. Discussion and conclusions

In this chapter, we have considered thermal non-equilibrium as a mechanism for the simple-loop flare. If the mechanical heating in a cool loop becomes too big or the density too small, thermal non-equilibrium occurs and the loop flares to temperatures of order 2×10^7 K in a time of between 5 and 10 minutes. Moore and Datlowe (1975), for instance, have examined data from 17 flares occurring between 10th October 1971 and 25th May 1972. They find the loop length lies between 6×10^6 and 10^8 m, and the maximum temperature lies between 10^7 and 2×10^7 K. The duration of the flares in X-rays is between 150 s and 200 s, while the rise-time is typically a few minutes. Our theoretical values give reasonable agreement with such observations.

With the order-of-magnitude approach, we have identified two distinct phases of a simple-loop flare. First of all, the temperature of a cool loop generally rises linearly with time to 2.5×10^5 K, at a slow rate that depends on how the equilibrium was perturbed: this was called the preflare phase. Subsequently, it rises explosively to over 10^7 K in a matter of 60 s: the flash phase. It did not prove possible to examine the behaviour of the flare density in any detail without an ad-hoc adjustment of the base boundary conditions, but a useful analytic solution for an intermediate phase was derived. In this case, an upflow occurred at the same time as a temperature rise.

Clearly, the analysis in this chapter is of a crude nature but it has demonstrated the viability of thermal non-equilibrium as a flare trigger. One must now solve the full set of equations numerically to obtain exact solutions, but this is a procedure

fraught with difficulties. Attempts have been made along these lines by Kostyuk and Pikel'ner (1975), Nagai (1980), Craig and MacClymont (1981) and Wu et al., (1981). Nearly all of these authors have run into computational problems. Kostyuk and Pikel'ner, in an attempt to model the chromosphere realistically, attached a model atmosphere onto the base of the transition zone. They then 'fired' a beam of electrons at the chromosphere and watched the subsequent evolution. The loop flared to 10^7 K in approximately 100 s, but as pointed out by Somov and Syrovatskii (1976), their results are dubious due to the value of their time-step, chosen as 1s. Since the dominant time-scale in a flare is initially the radiative one (Section 6.3) one must choose a time-step much less than this time-scale. The radiative time-scale is of order 1-5 s, and so a time-step of 1 s may miss out information. In fact, a time-step as small as 1/100 s may be needed (MacNiece, 1981).

Nagai followed Kostyuk and Pikel'ner in attaching a model atmosphere and succeeded in avoiding the problem of time-step size. However, Craig (1981) has cast doubt on Nagai's grid spacing in the transition zone. Nagai assumes a release of energy, either at the loop summit or at one of the footpoints, and follows the evolution. A conduction front propagates from summit to base and heats a portion of the chromosphere, which then rushes up the loop with a velocity of up to 400 km s^{-1}. The satisfactory lower atmosphere and time-steps make this the 'best' model produced so far.

Craig and McClymont (1981) consider the evolution of a cool loop after some heat is deposited in it. Their loop is isolated in that no mass is allowed to cross the base, but

the footpoint temperature is allowed to respond to coronal evolution. They find that the loop settles down to a new, hot equilibrium after about 20 minutes. Subsequently, more energy is deposited in the loop and a second new equilibrium arises. They suggest that an infinite number of equilibria can exist for a given loop mass, but attribute this result to lack of numerical resolution in the transition zone. Mragg and Priest (1982b) also point out that all but their first equilibrium are spurious solutions.

Wu et al. (1981) ignore the transition zone by fixing their base temperature at 10^6 K. They then vary this base temperature, and study the loop evolution.

It is clear from the above discussion that the choice of time-step and the ability of a numerical code to model steep gradients is vital in flare simulations. Recent use has been made of the SHASTA code (Boris and Book, 1972) by Hood and Priest (1982) to model flaring due to non-equilibrium. They find the flaring times to be similar to those in this chapter and, like us, are unable to get realistic densities due to the chosen boundary conditions. However, the SHASTA code can cope with shocks well and is of great potential in flare modelling.

The second important problem is one of boundary conditions. In this chapter we have fixed the base conditions for all time and have pointed out the drawbacks of this in Section 6.5. However, Kostyuk and Pikel'ner (1975) and Nagai (1980) have made some progress in this field by attaching a model atmosphere to the base of the transition zone. This enables shocks propagating down the loop to interact

realistically with the upper chromosphere rather than simply being reflected as would occur with a fixed boundary. It is also worth noting that the summit temperature will be independent to a large degree of the base conditions. This is because the time information takes to propagate from summit to base and back will be of roughly the same time as τ_f. Thus we expect that the temperatures and time-scales in this chapter are essentially of the right order since our base conditions are not relevant to the flare-rise phase.

Finally, it is worth comparing briefly the differences between the calculations of Chapters 5 and 6. Despite solving the same equations using the same approximations the physics of the two problems is significantly different. This can be attributed to the different relevant time-scales. In the cooling, all of the time-scales were of order 10^3 s, and so any evolution proceeds slowly. Also, the initial evolution was at constant pressure. In this chapter, the radiative time-scale was initially three orders of magnitude less than the others, typically being a few seconds and any evolution occurred rapidly. It was also of interest to find that the initial evolution was at constant density. This serves to point out that two apparently similar problems in fact exhibit distinct physical behaviour.

Chapter 7: THE HEATING OF "POST"-FLARE LOOPS IN 2 - RIBBON FLARES

7.1 Introduction

As outlined in Chapter 1, 2-ribbon flares are the most energetic events in the solar photosphere and corona releasing up to 3×10^{32} J in a large flare. First of all, a magnetic field eruption takes place, and then, in the place of the pre-flare magnetic field configuration, a system of loops is seen to rise in the atmosphere. These are generally referred to as post-flare loops. In fact, the word 'post' is misleading, because, as pointed out by Pneuman (1981a), the loops are a major part of the flare and their formation accounts for a large energy release.

Our knowledge of "post"-flare loops has increased greatly with the observations from Skylab, and the Kopp-Pneuman (1976) model has been remarkably successful in explaining their basic properties. We return to the Kopp-Pneuman model subsequently but first discuss the observations of "post"-flare loops.

It is instructive to consider first how a preflare magnetic field configuration can erupt. One possible trigger for a 2-ribbon flare is new flux emerging from the solar interior, as described in the emerging flux model of Heyvaerts et al. (1977) and Tur and Priest (1978). The new flux encounters old flux as it rises, and a current sheet forms between old and new flux. When this sheet reaches a certain height in the atmosphere, thermal equilibrium ceases to exist: the sheet heats up and becomes turbulent, triggering a fast

reconnection in the large-scale overlying field. An alternative mechanism involves the M.H.D. instability of coronal loops and arcades: Hood and Priest (1979b, 1980b) included the dominant stabilising feature of photospheric line-tying, and found that, if a plage filament situated in a coronal arcade is twisted too much or lifted too high, then it becomes unstable and erupts outwards. Pneuman (1980) has also examined the eruption of arcades and showed on the basis of an order-of-magnitude analysis that a prominence with its overlying field would erupt outwards.

In this chapter we shall assume that, after a filament eruption, the magnetic field is dragged open to form a large-scale current sheet configuration as shown in Figure 7.1. This subsequently relaxes by reconnection through a series of configurations shown in Figure 7.2 as the field closes back down.

The recent Skylab workshop on solar flares (Sturrock, 1980) has provided a wealth of data on "post"-flare loops. For example, those of the 29th July, 1973 flare have been described in a series of papers by Nolte et al. (1979), Petrasso et al. (1979) and Svestka (1978). In the initial stages of the flare, the temperature was at least 10^7 K. After 3 hours it had fallen to 5×10^6 K at the summit and 3.5×10^6 K at the footpoints, while the corresponding electron densities were 7×10^{15} m^{-3} and 7.5×10^{15} m^{-3}. As the "post"-flare loop system increased in size, the temperature continued to decrease slowly: 12 hours after the flare start, the summit and footpoint values were still 4.5×10^6 K and 3.1×10^6 K, respectively, while the corresponding densities

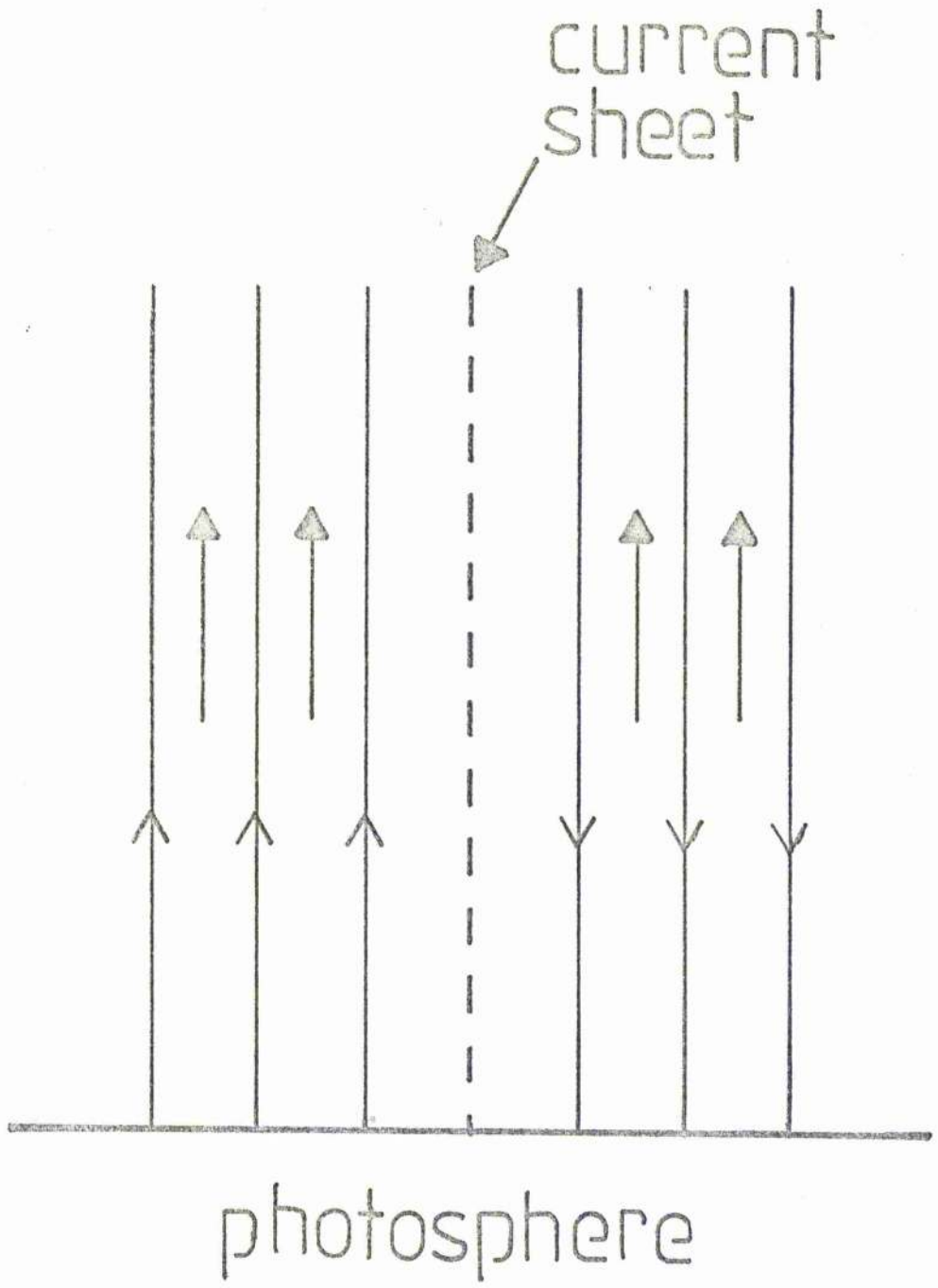

Figure 7.1 The open-field configuration that is produced by a filament eruption. The thick-headed arrows represent a solar wind outflow.

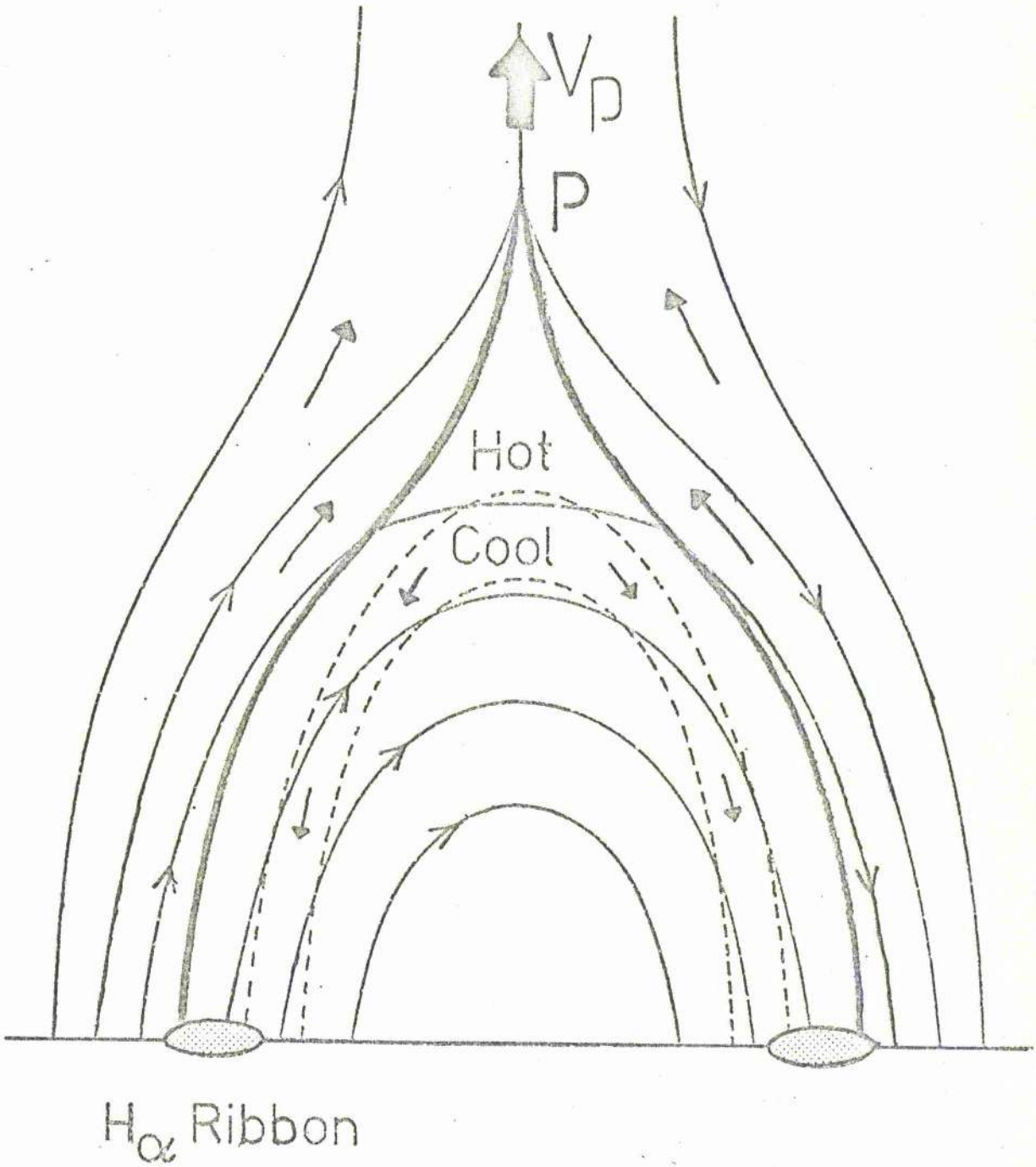

Figure 7.2 The rising system of "post"-flare loops some time later during the reconnection process as the field closes back down. The neutral point P is rising vertically with a speed v_p, trailing two slow M.H.D. shock-waves behind it (thick solid curves). A solar-wind upflow is present along the outer field lines. Below the shocks there lies a hot, compressed loop. Below the hot loop, there is a loop of plasma that has cooled and is falling, as seen in H_α.

were 5×10^{15} m^{-3} and 6×10^{15} m^{-3}. Within the errors quoted by Petrasso et al. (1979), the density therefore remains roughly constant and the temperature decreases slightly as the flare progresses. The height of the soft X-ray loops was observed to be approximately 30,000 km after three-and-a-half hours and 106,000 km after 12 hours, (Nolte et al, 1979). For the first 3 hours, the average speed of rise was approximately 10 km s^{-1} and for the next 9 hours it was only of order 0.5 km s^{-1}. Early on in the flare, however, the loops could have been rising as fast as 40 km s^{-1} or more. Moore et al. (1980) give the best fit to their observations of the rise speed as

$$V = 34.7 \exp(-t^{0.46}) , \qquad (7.1)$$

where t is in units of 20 minutes and v is in km s^{-1}.

The values of the physical parameters in the ambient medium outside the loop system are a little uncertain. The magnetic field strength probably lies between 10 and 100 gauss, while typical values for the density and temperature in the active-region corona are 2×10^{15} m^{-3} and 2×10^{6} K. This corresponds to a plasma beta ($\beta = 2\mu p / B^2$) of 0.1 - 0.01 (but see Section 7.3).

The mass of a typical system of "post"-flare loops was estimated by Kleczek (1964) to be of order 10^{12} - 10^{13} Kg and by Pneuman to be even greater (7.5×10^{15} Kg). This is of the order of the total coronal mass and therefore it is unlikely to be of coronal origin.

The model of Kopp and Pneuman was developed to explain this observation. They considered a system of rising loops

and solved the equations of motion in the following kinematic manner. The equations of continuity and momentum were first reduced to those holding along an isolated field line, and the magnetic field configuration was prescribed as a function of space and time. It comprised a region of closed field lines (the loops) whose height rose with time and a region of open (radial) field lines. Hence the rate of rise of the neutral point, P, at the top of the loops, was prescribed.

These equations were solved, and it was found that as a flux tube (defined as the region between two field lines) moved towards the neutral point, its width increased greatly, hence generating a large upflow. Just before reconnection, the mass flux entering this flux tube was 12 times greater than at t = 0. When the field lines reconnected, this enhanced solar wind outflow was trapped in the loops.

By this simple idea, Kopp and Pneuman found that they could trap over 10^{12} Kg in the loops - short of that required but a great deal better than obtained by any previous theoretical calculation. Once the field line closed, a gas dynamic shock propagated down the loop bringing to rest the upflowing plasma and heating it. However, if one does not think in terms of flux tubes but rather considers the global M.H.D. picture, these gas shocks will become an oblique M.H.D. shock, as shown in Figure 7.2. The temperature obtained by Kopp and Pneuman for the loops is far too low and gas dynamic shocks can never explain the loops temperature but the use of M.H.D. shocks gives a clear source of additional energy namely the magnetic field.

In this chapter, we construct firstly a local model of

these shocks to show that the correct temperatures may be obtained, and then we apply the general theory to the 2-ribbon flare of 29th July 1973. Finally, a global model of the reconnection is constructed.

Recent order-of-magnitude calculations by Pneuman (1981a) have shown that ohmic dissipation can account for the energy release in the loops. The analysis presented here shows in detail how the energy is actually released in the slow shocks.

7.2 The slow shock model

As pointed out in Section 7.1, the original Kopp-Pneuman model was defective in that the plasma was heated by gas shocks propagating down individual flux tubes rather than M.H.D. shocks propagating outward and upward across the incoming field. In a magnetic medium there are no purely gasdynamic shocks since they became magnetoacoustic ones.

Locally-straight sections of these shocks are shown in Figure 7.3. In a frame of reference fixed to the Sun (Figure 7.3a), the Y-type (or cusp-type) neutral point P (and the shocks) are seen to rise with speed v_p, while the loops below the shocks are stationary. The fluid ahead of the shocks moves with velocity components $v_{||}$ along the field and $v_{\perp}$ normal to it. In a frame of reference moving with P and the shocks (Figure 7.3b), the plasma ahead of the shocks has an extra downflow component v_p and the plasma below the shocks is moving down with speed v_p.

Using the notation of Chapter 2 (Figure 2.1), the normal and tangential components of the incident velocity in the shock frame (Figure 7.3b) may be written

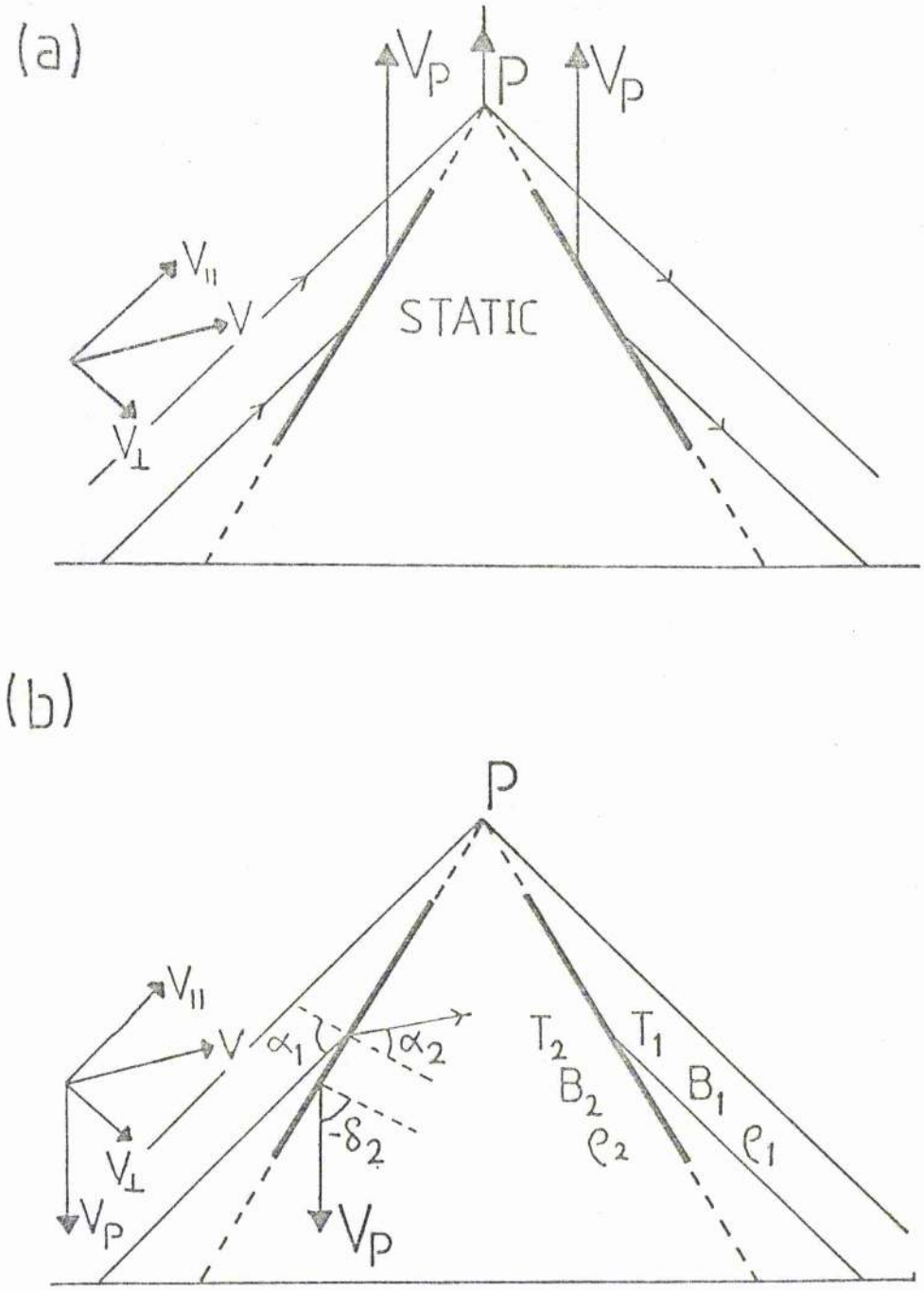

Figure 7.3 The notation for locally straight parts of the shocks in Figure 7.2: (a) in a rest frame, where the flow velocity ahead of the shocks has components $v_{||}$ and $v_\perp$ along and perpendicular to the magnetic field; (b) in a frame of reference moving upwards at speed v_p with the shocks and the neutral point P. . The thick lines represent shocks, the thin continuous lines the magnetic field and the solid-headed arrows the various flow components.

$$\left.\begin{aligned} V_{1n} &= V_{\parallel}\cos\alpha_1 + V_{\perp}\sin\alpha_1 + V_p\cos\delta_2 \,, \\ V_{1t} &= V_{\parallel}\sin\alpha_1 - V_{\perp}\cos\alpha_1 - V_p\sin\delta_2 . \end{aligned}\right\} \qquad (7.1)$$

Note that $v_{\perp}$ may be negative provided $v_{\parallel}$ and v_p are so large that v_{1n} is still positive. It is then possible to solve the shock relations derived in Chapter 2 and so deduce $v_{\parallel}$ and $v_{\perp}$ from (7.1). For given values of $v_{\parallel}$, $v_{\perp}$, β_1, T_1, α_1 and ϱ_1 the aim is to solve the jump relations for v_p, T_2, α_2, δ_2, ϱ_2 and B_2. Since the shock is of the slow type, the field is refracted towards the normal by the shock passage (Section 2.3.2) and releases magnetic energy to heat the plasma.

The input parameters may vary over wide ranges and it is important to note the range of interest. The neutral point speed (v_p) is expected to lie between 1 km s^{-1} or less and, say, 50 km s^{-1} or even more. The parallel flow speed must not be too much larger than the sound speed, in general line with the Kopp-Pneuman concept. For the ambient temperature (T_1), density (n_1), and beta (β_1), values of 2 - 2.5 x 10^6 K, 2 - 4 x 10^{15} m^{-3} and 0.01 - 0.1 are expected for the active region corona, where this process is taking place. Solutions with v_p small enough were found only for α_1 close to $\pi/2$ and $v_{\perp}$ relatively small, so that the shock is propagating at a small angle of inclination to a slowly collapsing field. This parameter range unfortunately does not allow a simple analytical solution of the shock jump relations. The problem is due to α_1 being close to $\pi/2$. As was pointed out, the low-beta calculations break down in this limit.

We thus solved equations (2.36), (2.37) and (2.39)

numerically and the effect of varying the parameters ($v_{||}$, $v_{\perp}$, α_1, β_1) have been plotted in Figures 7.4, 7.5 and 7.6. In fact, v_{1n} and v_{1t} were specified with $v_{||}$ and $v_{\perp}$ following from (7.1) as

$$v_{||} = \frac{v_{1n}\cos\alpha_1 + v_{1t}\sin\alpha_1}{v_p\cos(\alpha_1 + \delta_2)},$$

$$v_{\perp} = \frac{v_{1n}\sin\alpha_1 - v_{1t}\cos\alpha_1}{v_p\sin(\alpha_1 + \delta_2)}.$$

First of all, Figures 7.4 and 7.5 show the variation of the loop temperature (T_2) and the neutral-point speed (v_p) with $v_{||}$ and $v_{\perp}$ for $\beta_1 = 0.1$ and 0.01. $v_{\perp}$ is a measure of the speed of collapse of the field lines. Increasing $v_{\perp}$ raises the reconnection rate and the magnetic energy release, which results in a higher temperature (T_2). It also increases v_p and δ_2 so that the shocks move closer together. The relevant value of β_1 close to the shocks is rather uncertain, both because the magnetic field strength is not very well known and also because the values ahead of the shocks may differ substantially from the ambient coronal value, since the flux tubes diverge just before reconnecting (Kopp and Pneuman, 1976). The effect of lowering β_1 from 0.1 to 0.01 is to change T_2 only slightly and to decrease v_p substantially for a given inflow; also, the switch-off speed increases. Increasing $v_{||}$ tends to increase both v_p and T_2, although at $\beta_1 = 0.01$, v_p is approximately constant.

Figure 7.6 gives the results of varying α_1 for a fixed value of $v_{\perp}$ ($= v_{\perp}^*$). ($v_{\perp}^*$ is the value of $v_{\perp}$ that makes δ_2 zero), and $\beta_1 = 0.01$. As α_1 increases from 87° towards 90°, T_2

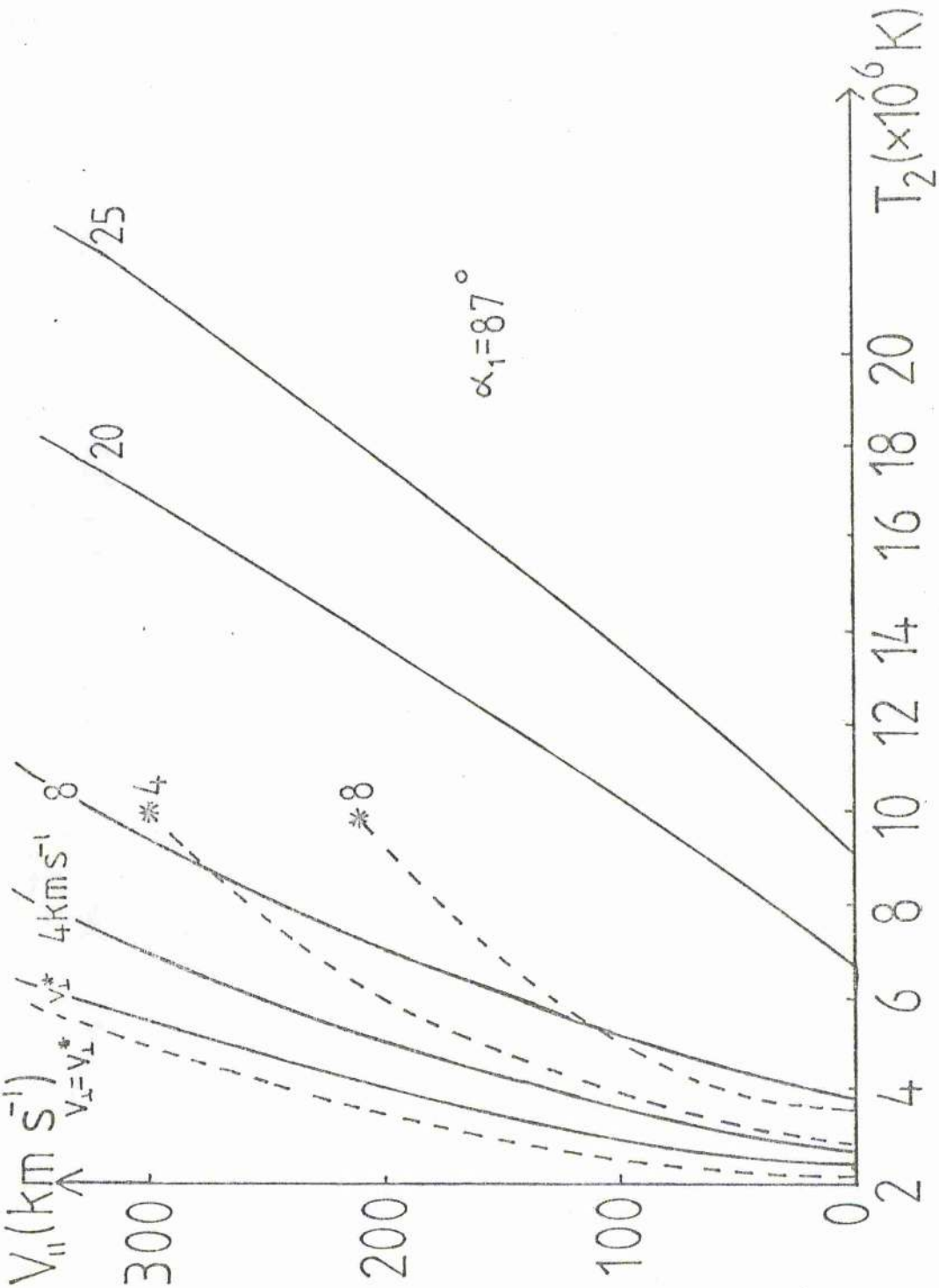

Figure 7.4 The effect of the parallel upflow (v_{11}) and the field line speed ($v_\perp$) on the loop temperature (T_2). Solid lines are for $\beta_1 = 0.01$, and the dashed lines represent $\beta_1 = 0.1$. In each case the magnetic field incidence (α_1) to the shock is 87° and the sound speed (c_{s1}) for a temperature of 2×10^6 K is about 200 km s^{-1}. $v_\perp^*$ is the smallest allowable value of $v_\perp$: it makes $\delta_2 = 0$ and so switches off the tangential flow component.

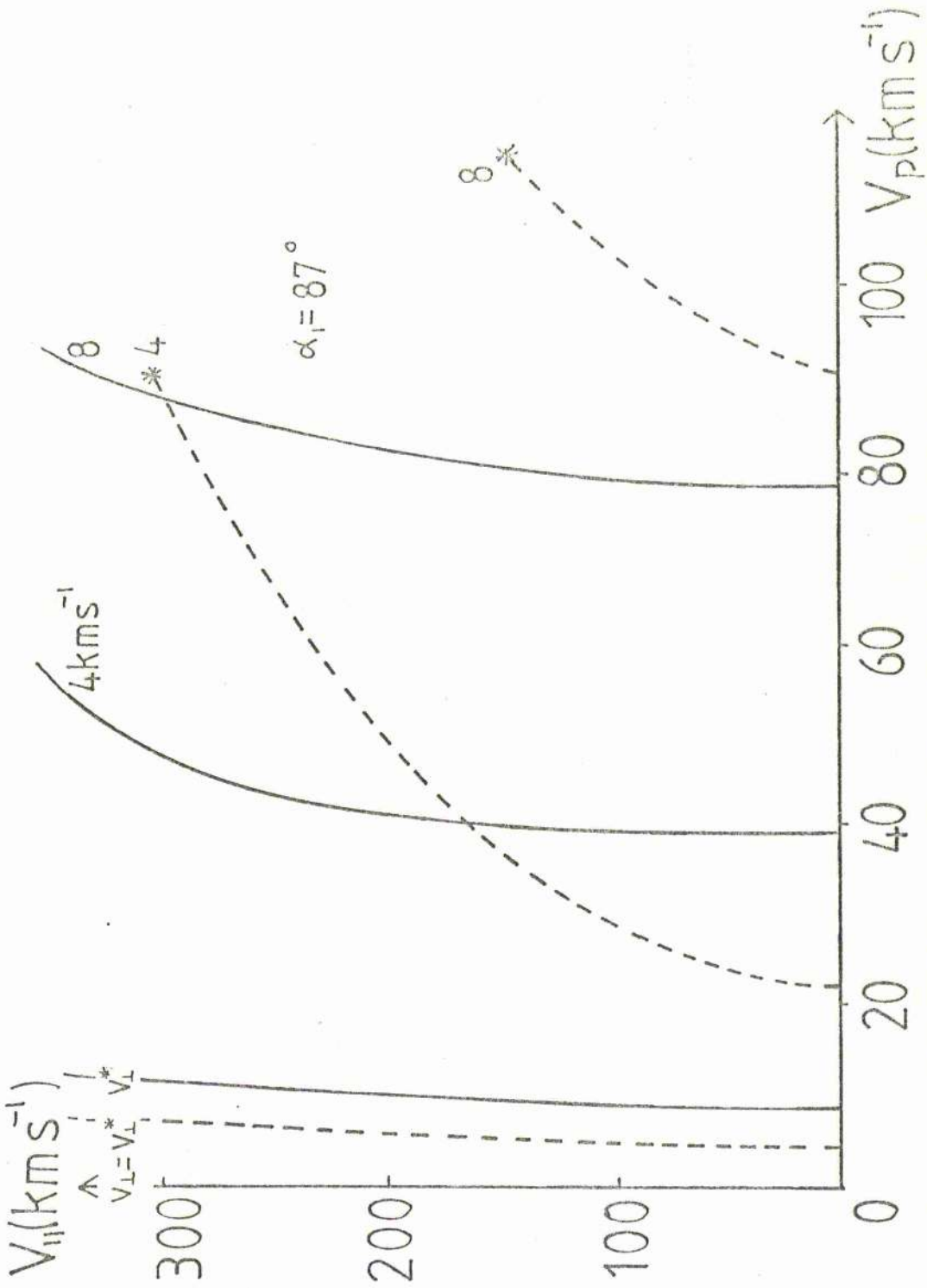

Figure 7.5 The effect of the parallel upflow ($v_{||}$) and the field line speed ($v_\perp$) on the neutral point speed (v_p). The notation is the same as in Figure 7.4.

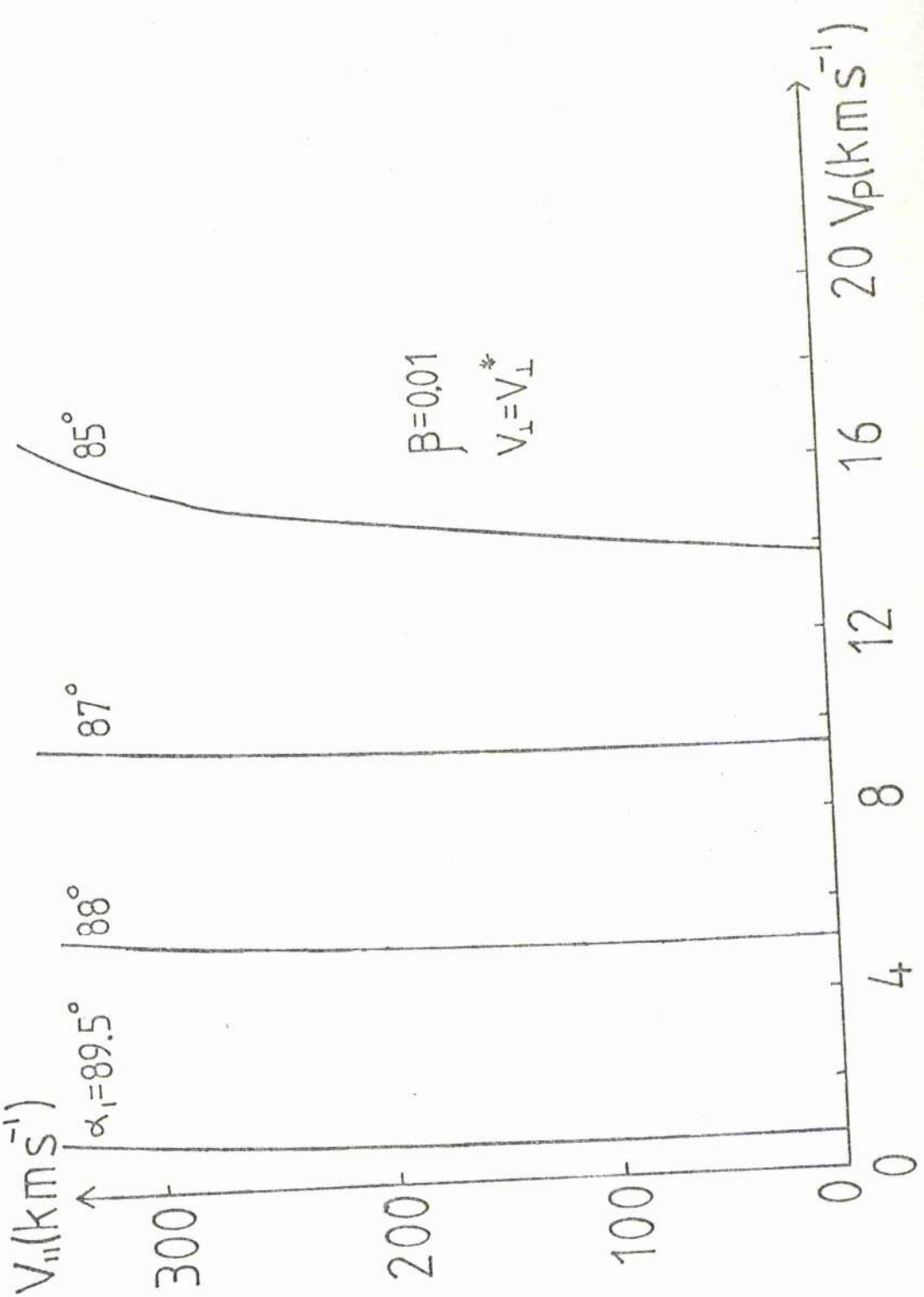

Figure 7.6 The neutral point speed (v_p) as a function of the upflow speed ($v_{\parallel}$), for several values of α_1. The plasma beta is 0.01 and the perpendicular inflow velocity is the minimum value ($v_\perp^*$).

increases only slightly and so is not shown, but v_p decreases markedly to values as low as the 0.5 - 1 km s^{-1} that one finds in the late stages of "post"-flare loop evolution.

It is now desirable to apply these results to a specific flare.

7.3 The evolution of the "post"-flare loops of 29th July, 1973

In Section 7.1, the basic details of this large flare were outlined and it is now the intention to see how well our slow-shock model can simulate the loop temperature and upward rise speed. The rise speed, V_p, is given by Moore et al. (1980) and is shown as a function of time in Figure 7.7. The temperature after the first 3 hours is given by Petrasso et al. (1979) is shown as large dots on Figure 7.8. Both the rise speed and temperature may be accounted for by slow shock heating as follows. For the first hour, it is necessary to have field line speeds (v_1) larger than the minimum value (v_1^*), so we have prescribed α_1 to be 87° and v_{11} to be $1.3c_{s1}$ and have deduced from Figure 7.5 the variation $v_\perp(t)$ which produces $v_p(t)$ shown in Figure 7.7. Then Figure 7.4 has been used to deduce the resulting loop temperatures (T_2) shown in Figure 7.8. For the first 30 minutes, we have taken $v_\perp$ to be between 20 and 10 km s^{-1}. This gives temperatures of over 10^7 K for the first 15 minutes (not shown) and between 10^7 and 8×10^6 K for the next 15. The values of v_p are rather high (60 km s^{-1}) for this period. After 30 minutes, $v_\perp$ is below 10 km s^{-1} and is chosen to give the observed v_p.

It is interesting to note that very early in the flare,

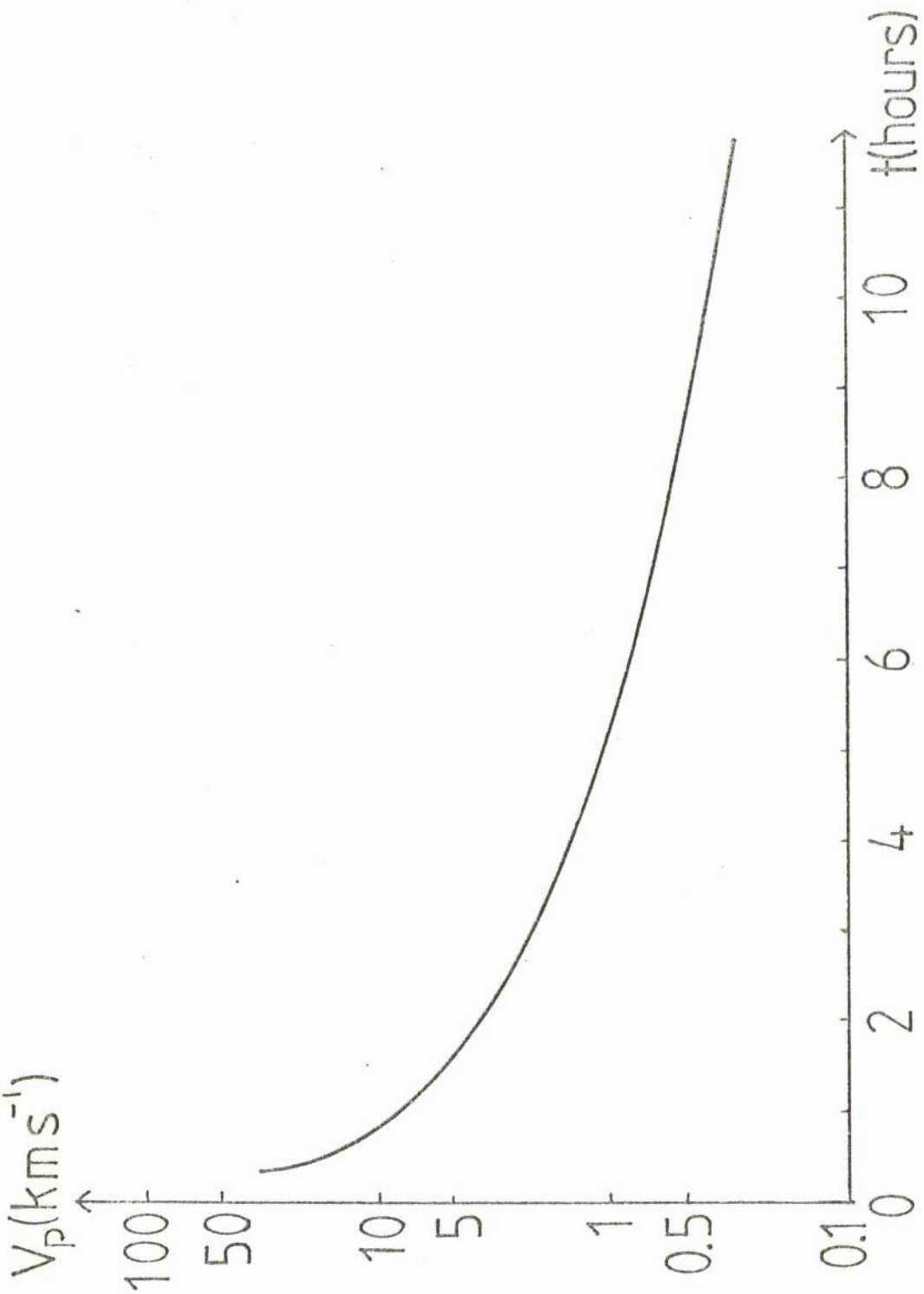

Figure 7.7 The observed neutral point rise-speed (v_p) as a function of time after flare onset for the "post"-flare loops of 29 July, 1973. (After Moore et al. 1980).

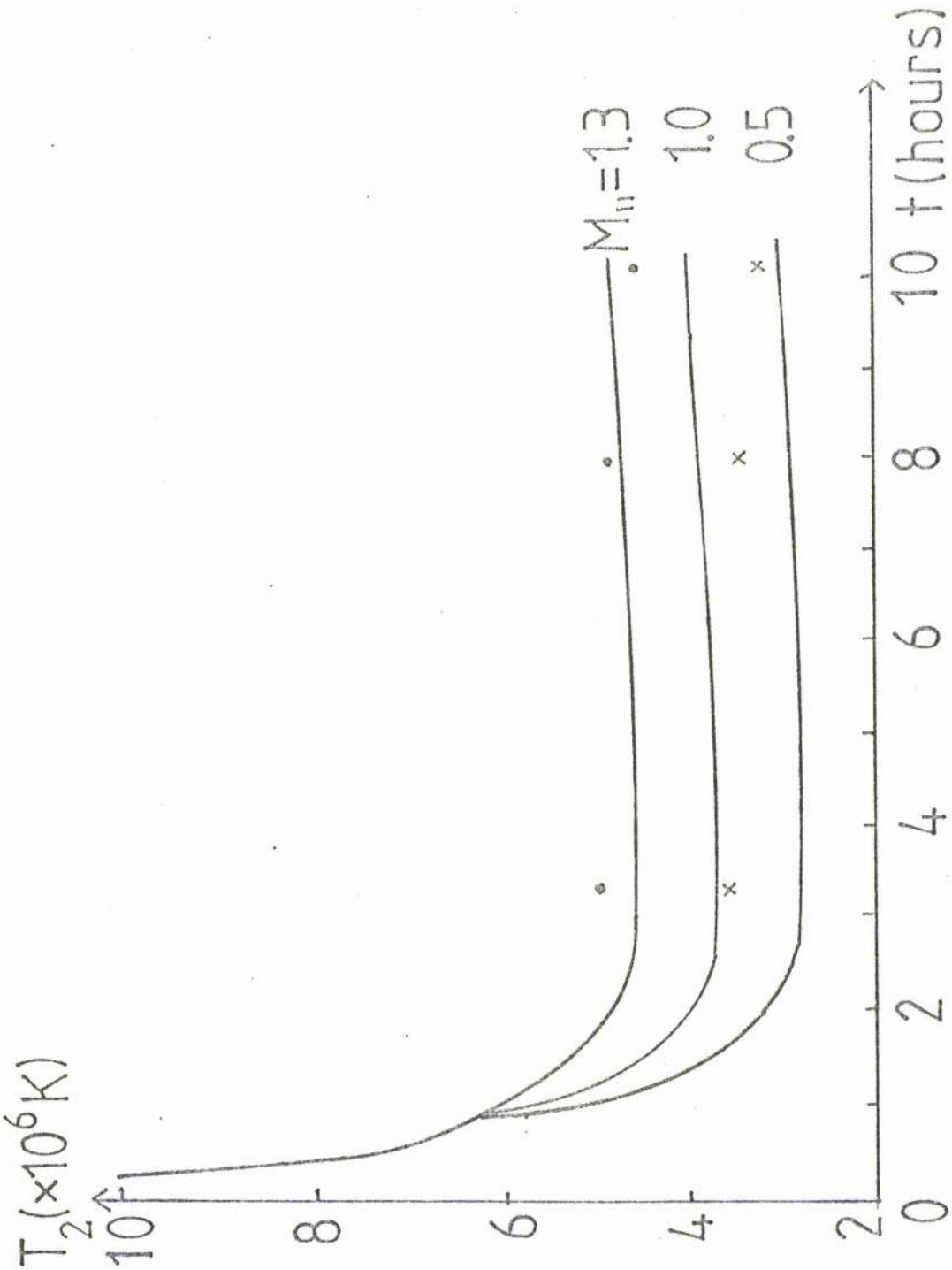

Figure 7.8 The temperature evolution predicted by slow-shock heating with ambient beta (β_1) of 0.01, For the first hour we have put $\alpha_1 = 87^\circ$ and $M_{11} = (v_{11}/c_{s1}) = 1.3$. Thereafter $v_1 = v_1^*$ and the results for several values of M_{11} are shown. (The sound speed (c_{s1}) for a temperature of 2×10^6 K is about 200 km s^{-1}).

reconnection could be proceeding even faster than mentioned above, and, if the shock approaches switch-off conditions, temperatures of order 10^8 K are possible if $\beta_1 = 0.01$. Such temperatures are tentatively claimed in new results from the Solar Maximum Mission (Machado, 1980).

For the remaining time we have assumed that $v_\perp = v_\perp^*$ and used Figure 7.6 to deduce the angle of inclination $\alpha_1(t)$ that produces the rise-speed $v_p(t)$ shown in Figure 7.7. Then, the resulting temperature $T_2(t)$ has been deduced for several values of M_{11} ($= v_{11}/c_{s1}$), as shown in Figure 7.8. It can be seen that after 3 hours, values of $\alpha_1 = 87^\circ$, $M_{11} = 1.3$ and $M_{11} = 0.9$ will reproduce the observed v_p and T_2 at the summit and footpoint, respectively; whereas after 10 hours $\alpha_1 = 89.5^\circ$, $M_{11} = 1.0$ is needed at the summit and $M_{11} = 0.5$ at the footpoints. In fact, $v_\perp$ will decrease steadily to $v_\perp^*$ giving a smooth decrease in T_2 rather than the jump to $v_\perp^*$ after 1 hour portrayed here. Also, for an ambient coronal density of 3×10^{15} m^{-3}, our model produces loop densities of typically 9×10^{15} m^{-3} at the summit after one hour, decreasing to 6×10^{15} m^{-3} at the summit and to 5×10^{15} m^{-3} at the base after 10 hours. The base density is somewhat low, but could easily be enhanced by evaporation of chromospheric material (See Section 7.5).

It should be pointed out that other values of the parameters can also reproduce the observations, but the above estimates do demonstrate the viability of slow-shock heating.

7.4 The global reconnection process

In this section we shall construct a simple global model for the reconnection that is believed to be taking place above

a "post"-flare loop system as the field closes back down and the neutral point rises. Steady reconnection at an X-type neutral point is thought to occur by the mechanism of Petschek (1964) (see, e.g., Vasyliunas, 1975), and this has been put on a firmer mathematical foundation for both incompressible and compressible plasmas by Soward and Priest (1977, 1982). In these models, one generally quotes the maximum reconnection rate as the principal result, and for the Petschek model, it is typically a small fraction of the Alfvén speed at large distances away from the reconnection region. This parameter is a measure of how fast magnetic flux can be convected inward to the diffusion region where the field lines actually break and reconnect. However, the analytical model of Soward and Priest is rather complicated, and so we turn here to the simpler model proposed by Sonnerup (1970). Not only are the slow shocks of the Petschek model present but expansion waves have also been introduced. These originate outside the diffusion region and are physically unrealistic. However, Sonnerup (1973) has justified their use by stating that they may be regarded as a lumping together of all interactions ahead of the shocks. The invoking of this second discontinuity meant that Sonnerup could construct solutions where the magnetic field and velocity are uniform in each region between the discontinuities and are related to the external conditions by a simple matching across the discontinuities (which, in the incompressible case are just Alfvén waves). The compressible version of this model (Yang and Sonnerup, 1976) is complicated and requires the simultaneous solution of four ordinary differential equations for the expansion fan.

Sonnerup found a maximum reconnection rate of order the Alfvén speed, much larger than that discovered by Petschek. However, Forbes (1981) has pointed out to the author that this discrepency may be due to the different locations at which the reconnection rate is measured. The Sonnerup rate may only be valid in the external region close to the diffusion region whereas the Petschek rate is valid far from the origin. Hence an Alfvénic inflow near the diffusion region may be a manifestation of the Petschek inflow far away.

One effect which makes "post"-flare reconnection different from conventional reconnection models is the presence of a strong solar-wind flow along the ambient field. Such a flow has already been partially included in the Sonnerup model by Mitchell and Kan (1978). Figure 7.9 shows the geometry in a frame moving with the shocks and with an upflow in the inflowing region (1). This model is a simplified case of the general Mitchell and Kan formulation. They allowed two regions with different densities and vertical inflow velocities to reconnect, with the aim of simulating magnetopause reconnection. The general problem is thus asymmetric about both x and y axes. For the case of equal inflow densities and velocities, the problem is greatly simplified. After matching across the two waves PA and PB and for a downflow V_p in region 3 we find:

$$
\left.
\begin{aligned}
V_{2x} &= V_{A1} A_1 (k-1)/2 , \\
V_{2y} &= -V_{A1} \left(1 + \xi (k-1)/2 \right) , \\
V_p &= V_{A1} / k , \\
\tan\theta_1 &= \xi / A_1 , \\
\tan\theta_2 &= \left(\xi + \frac{2}{k+1} \right) / A_1 , \\
\tan\theta_3 &= \left(\xi + \frac{2}{k} \right) / A_1 ,
\end{aligned}
\right\} \qquad (7.2)
$$

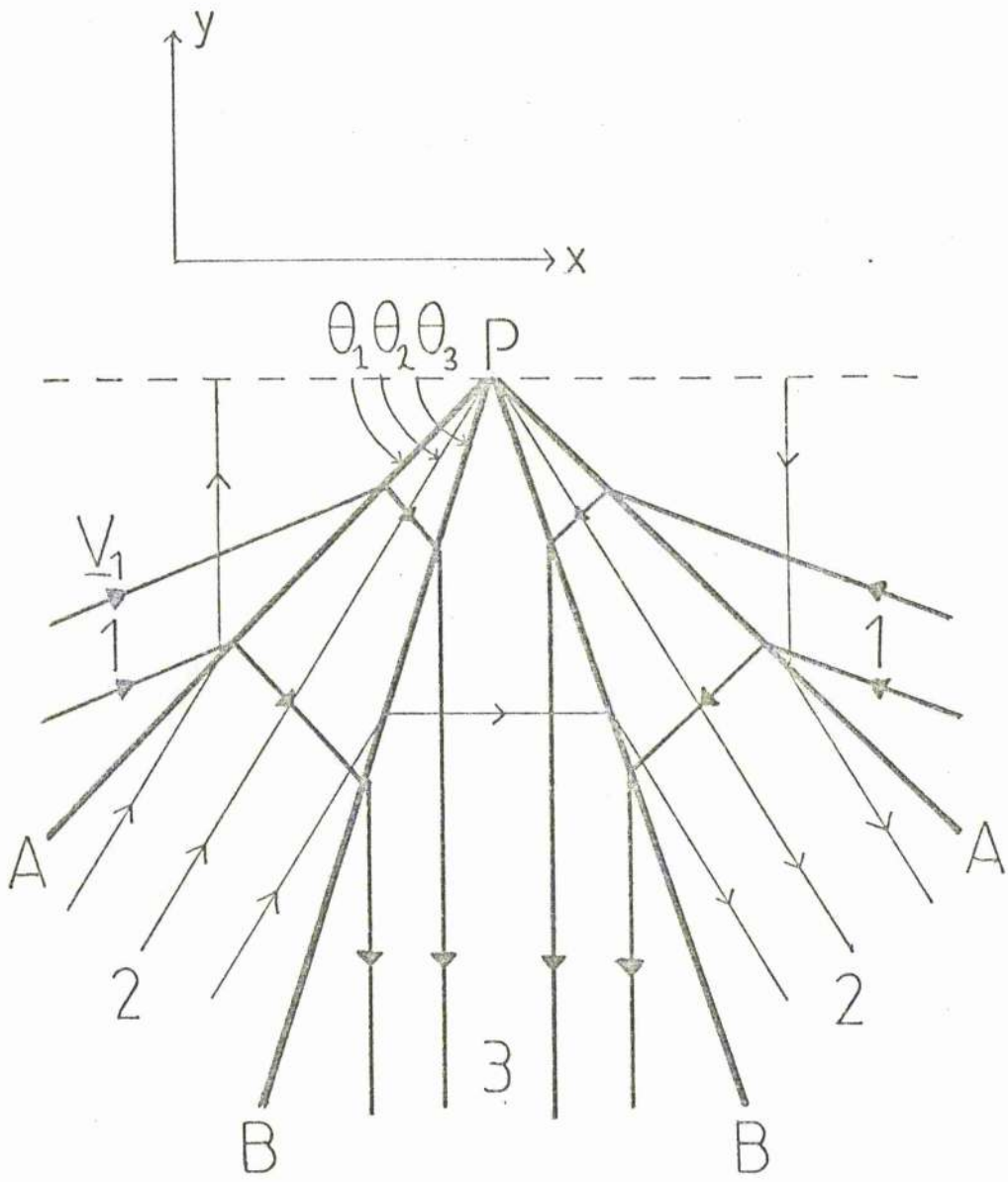

Figure 7.9 An incompressible reconnection geometry in a frame moving upwards at v_p (like Figure 7.3b). The lines PA and PB represent Alfvén waves and (artificial) Alfvén waves, which would become slow shocks and (artificial) expansion waves in the compressible case. Note also that v_{1y} may be directed in either the positive or negative y-direction.

$$B_2 = B_1\left[1 + \xi(k+1) + (A^2+\xi^2)\frac{(k+1)^2}{4}\right]^{1/2},$$

$$B_3 = B_1 k A_1,$$

where

$$\xi = 1 - \frac{v_{1y}}{v_{A1}},$$

$$A_1 = \frac{v_{1x}}{v_{A1}}, \tag{7.3}$$

$$k = \frac{1}{1+(1+\xi)^{1/2}}. \tag{7.4}$$

In these equations, v_{A1} is the inflow Alfvén velocity. In a fixed frame of reference (Figure 7.3a), the y-components of velocity are

$$v_{2y}' = v_{2y} + v_p,$$

$$v_{1y}' = v_{1y} + v_p, \tag{7.5}$$

where v_{1y} represents the y-component of the solar-wind flow. After eliminating v_p, v_{1y}' and ξ between (7.2) - (7.5) we obtain an equation relating K and v_{1y}'/v_{A1}, namely

$$k = \frac{1}{1+\left(2 + \frac{v_{1y}'}{v_{A1}} + \frac{1}{k}\right)^{1/2}}, \tag{7.6}$$

which may be solved to give

$$k = \frac{3}{2\left(1-\frac{v_{1y}'}{v_{A1}}\right)}\left[-1 \pm \left(1 + \frac{4}{9}\left(1 - \frac{v_{1y}'}{v_{A1}}\right)\right)^{1/2}\right], \tag{7.7}$$

for the transformed frame.

Furthermore, the constancy of total pressure (gas plus magnetic) across both PA and PB gives

$$p_3 + \frac{B_3^2}{2\mu} = p_2 + \frac{B_2^2}{2\mu} = p_1 + \frac{B_1^2}{2\mu}.$$

After using (7.2) for B_2 and B_3, we find

$$\frac{p_3}{p_1} = 1 + \frac{1}{\beta_1}(1 - K^2 A_1^2),$$

$$\frac{p_2}{p_1} = 1 - \frac{1}{\beta_1}\left[\xi(K+1) + (A^2+\xi^2)\frac{(K+1)^2}{4}\right].$$

Now (4.2), (4.6) and (4.7) may be solved to give θ_1, θ_2, θ_3 and p_3 in terms of the reconnection rate A_1 and the inflow v_{1y}'. As A_1 increases, so the angles θ_1, θ_2, θ_3 decrease and the waves spread out, a behaviour which is typical of reconnection models. As the solar-wind flow (v_{1y}') increase, so the angles increase (Figure 7.10) and and system of Alfvén waves closes up, which was expected from the results of Section 7.2. At the same time the neutral point speed (v_p) was found to increase so that the system of loops rises more quickly. Also, the pressure p_3 increases with v_{1y}' and is strongly dependent on β_1.

7.5 Discussion and conclusions

On the basis of a simple model we have shown in this Chapter that the heating and rise-speed of "post"-flare loops can, in all stages of their evolution, be attributed to slow M.H.D. shock waves, hence removing a major problem in the Kopp and Pneuman (1976) model. By varying the inflow parameters, a wide range of loop temperatures can be obtained. These parameters include the upflow (v_{11}) along the field, the rate of collapse ($v_\perp$) of the field and the inclination α_1 of the shock normal to the field.

The analysis of the present chapter ignores many potentially important effects, however, and it is instructive to

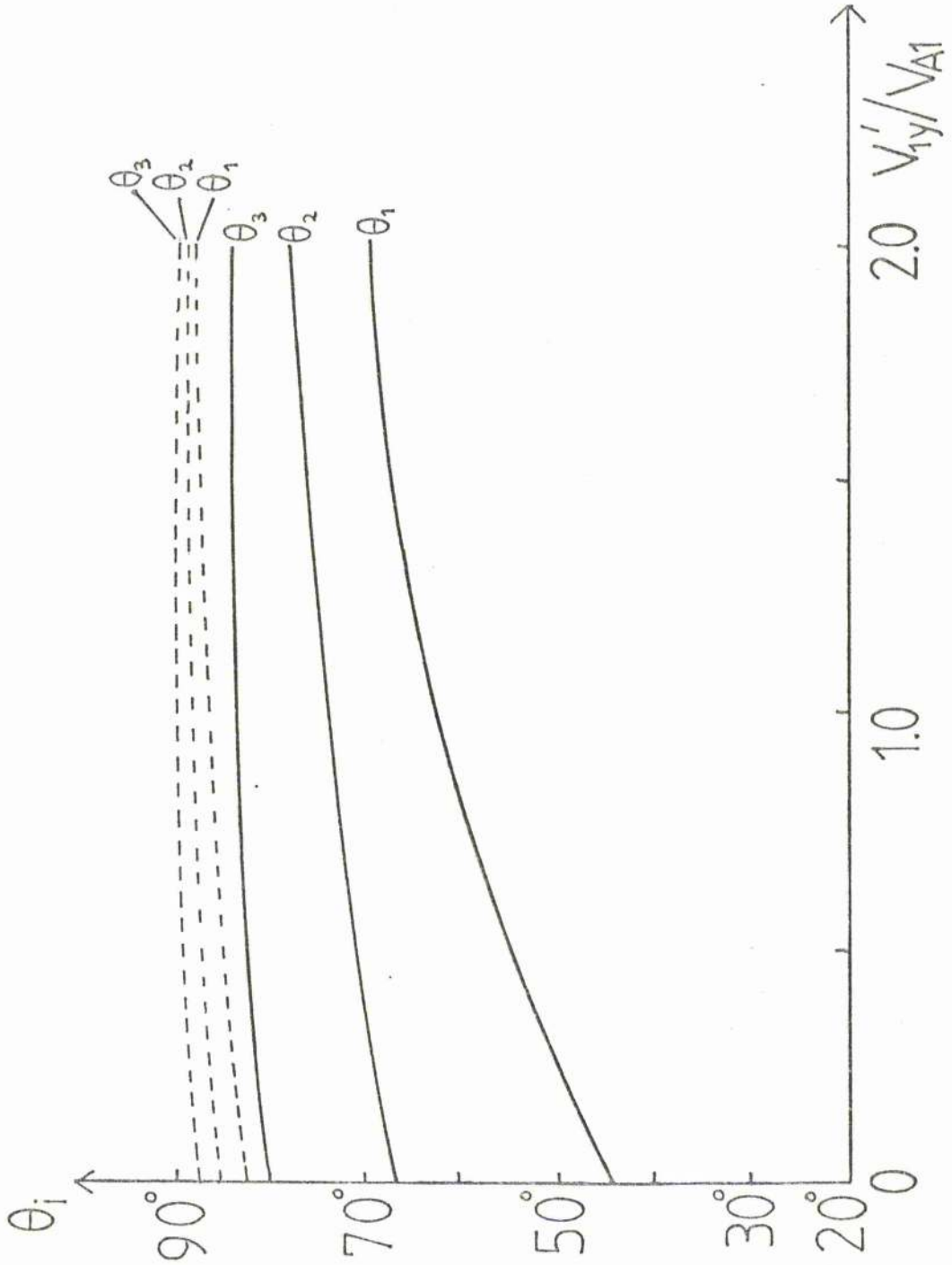

Figure 7.10 The variation of the angles of inclination θ_1, θ_2, θ_3 of the Alfvén waves PA, PB and the seperatrix to the horizontal as a function of the solar wind upflow speed v_{1y}'. v_{A1} is the ambient Alfvén speed and the reconnection rate A_1 is taken as 1.0 (solid) and 0.1 (dashed).

discuss them. It is desirable to solve the full two-dimensional, resistive, time-dependent, compressible problem numerically to see what effects have been missed by the above kinematic analysis and also by the calculations of Kopp and Pneuman. (Indeed, this is in the process of being undertaken by Forbes, 1982). One of the most interesting problems concerns the effect that line-tying of the magnetic field to the photosphere has on the reconnection rate. This seems to be one of the reasons for the non-uniform rate of reconnection (and hence the rate of rise of the loops). A second problem concerns the role of fast magnetoacoustic waves generated at the reconnection site. Slow waves generated here steepened into shocks but an interesting question concerns whether fast waves can propagate outward to warn the incoming flow that a shock lies ahead of it. It is possible that such waves could alter the configuration. Another problem concerns the source of the mass of the loops. While the Kopp-Pneuman mechanism is able to trap a considerable amount of material, it is now generally considered that this is not enough. Pneuman (1981b) has suggested that chromospheric evaporation is the principle mass source but the relative contributions of both sources have not been studied in detail. However, it would be desirable for observations to detect upflows either inside or outside the reconnected region.

Finally, it will be most interesting when more flare observations become available to test the model proposed in this Chapter.

Chapter 8: MAGNETIC NON-EQUILIBRIUM AND EXPLOSIVE PHENOMENA

8.1 Introduction

Well before the launch of the Skylab satellite, a large number of eruptive and explosive phenomena were known to exist on the Sun, including surges, sprays (or eruptive active prominences), eruptive quiescent prominences and coronal transients. Surges are streams of plasma rising vertically from the chromosphere at velocities between 50 and 200 km s^{-1}. They reach a height of between 20,000 and 200,000 km and are then seen to fall back along the same trajectory. A surge has a temperature of typically 8×10^3 K, a magnetic field of 30 G and a number density of typically 10^{18} m^{-3} (Rust et al., 1980). Sprays are similar to surges except that they are ejected at higher speeds (600 km s^{-1}) and do not return to the sun. They have temperatures in the range 10^4 - 10^5 K and magnetic fields as big as 100 G.

Eruptive prominences are larger-scale events. They have a fairly weak magnetic field ($\simeq$10 G) and rise into the corona at 200 km s^{-1}. Their temperature and density are similar to a surge but they do not return to the Sun after eruption.

A coronal manifestation of an eruptive process is a coronal transient (Pneuman, 1978). These typically have temperatures of 10^6 K and a weak field (only $\simeq$ 2G). They are much larger than any of the other eruptive events and eject up to 10^{13} Kg into interplanetary space.

In this chapter, we shall discuss how a static magnetic

field can erupt due to excess gas pressure and possibly give rise to such explosive phenomena. The structure of a pre-eruptive magnetic field may be given by the magnetostatic equation

$$\nabla p = \underline{J} \times \underline{B} + m_H n \underline{g} \quad , \tag{8.1}$$

where

$$\underline{J} = \frac{\nabla \times \underline{B}}{\mu} \quad , \tag{8.2}$$

and

$$\nabla . \underline{B} = 0 \quad . \tag{8.3}$$

Taking the scalar product of $\underline{B}$ with (8.1) gives

$$\frac{dp}{ds} = - m_H n g \, (\hat{\underline{z}} . \hat{\underline{s}}) \quad , \tag{8.4}$$

where $\underline{s}$ is the coordinate measured along a field-line and $\hat{\underline{z}}$ is the unit-vector in the vertical direction. (8.4) shows that hydrostatic balance holds along any given field line, and, if the plasma is isothermal, it can be integrated to give

$$p = p_0 e^{-z/\Lambda} \quad , \tag{8.5}$$

where Λ is the scale-height, defined as

$$\Lambda = c_s^2 / g \quad .$$

Consider now a structure that is much longer than it is high or wide, so that variations along the horizontal (x-axis) can be ignored. Then, quantities depend only on y and z, and so the magnetic field, B, may be written as

$$\underline{B} = \left(B_x(y,z) \, , \, \frac{\partial A(y,z)}{\partial z} \, , \, - \frac{\partial A(y,z)}{\partial y} \right) \quad , \tag{8.6}$$

where A is the z-component of the vector potential. The components of (8.1) reduce to

$$\frac{\partial A}{\partial y}\frac{\partial B_x}{\partial z} = \frac{\partial B_x}{\partial y}\frac{\partial A}{\partial z}, \tag{8.7}$$

$$\frac{\partial p}{\partial y} = -\frac{1}{2}\frac{\partial}{\partial y}B_x^2 - \frac{\partial A}{\partial y}\nabla^2 A, \tag{8.8}$$

$$\frac{\partial p}{\partial z} = -\frac{1}{2}\frac{\partial}{\partial z}B_x^2 - \frac{\partial A}{\partial z}\nabla^2 A - \frac{\rho m_H g}{2k_B T}. \tag{8.9}$$

Now $p = p(A, Z)$ from (8.4) and $B_x = B_x(A)$ from (8.7) so (8.5) is

$$p(A, z) = p_0(A)\, e^{-z/\Delta},$$

and (8.8) or (8.9) reduce to

$$\nabla^2 A + \frac{1}{2}\frac{d}{dA}\left(B_x^2(A)\right) = -\mu\frac{\partial}{\partial A}p(A, z). \tag{8.10}$$

If we assume also that the scale-height is much greater than any vertical variations then both the gas pressure and field in the x-direction are <u>constant</u> along any flux surface and (8.10) reduces to

$$\nabla^2 A = -\frac{d}{dA}\left(\frac{B_x^2(A)}{2} + \mu p(A)\right), \tag{8.11}$$

and if $p(A)$ and $B_x^2(A)$ are prescribed, then in theory it should be possible to solve this equation. Equation (8.11) is in general non-linear and need not have a unique solution. It may be written in dimensionless form

$$\nabla^2 \bar{A} = -\frac{d}{dA}\left[\frac{\bar{B}_x^2(\bar{A})}{2} + \beta\bar{p}(\bar{A})\right], \tag{8.12}$$

where

$$\beta = \frac{\mu p_0}{B_0^2} , \quad \bar{A} = \frac{A}{B_0 h} , \quad \bar{p} = \frac{p}{p_0} ,$$

$$\bar{y} = \frac{y}{h} , \quad \bar{z} = \frac{z}{h} , \quad \bar{B}_x = \frac{B_x}{B_0} .$$

and p_0, B_0 and h are scaling factors.

We discuss this equation briefly in Section 8.3. However analytic solutions of (8.12) are complicated and do not give much physical insight to the problem. Instead, we first discuss some simpler solutions to (8.1), which, although restrictive, do give us a clear view of the problem.

8.2 Cylindrically symmetric equilibrium models

8.2.1 General Theory

We first discuss some simple models for cylindrically symmetric magnetic fields in which the gas pressure is prescribed and the magnetic field deduced. If the magnetic field is assumed to be purely azimuthal (Figure 8.1a), then the momentum equation reduces to

$$\frac{d}{dr}\left(\mu p + \frac{B_\phi^2}{2}\right) = -\frac{B_\phi^2}{r} \qquad (8.13)$$

This is non-dimensionalised as follows:

$$\bar{p} = p/p(r=1) , \quad \bar{B} = B/B(r=1) ,$$

so that (8.13) is

$$\frac{d}{dr}\left(\beta\bar{p} + \bar{B}_\phi^2\right) = -\frac{2\bar{B}_\phi^2}{r} , \qquad (8.14)$$

where

$$\beta = \frac{2\mu p(r=1)}{B_\phi^2(r=1)}$$

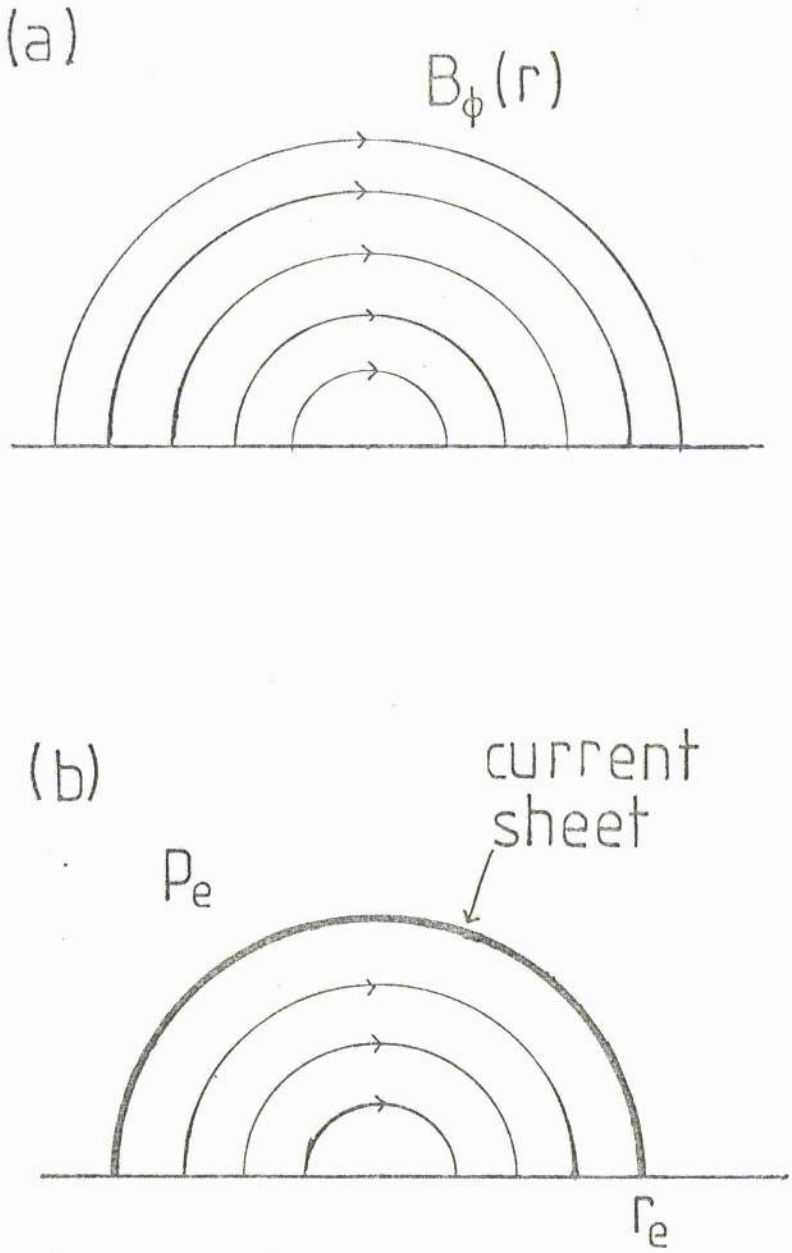

Figure 8.1
(a) A cylindrically-symmetric arcade with a purely azimuthal magnetic field.
(b) An azimuthal magnetostatic field confined at a distance r_e by a pressure p_e.

and r is non-dimensionalised against some length-scale l.

If the gas pressure is imposed everywhere, then (8.14) integrates to give

$$\bar{B}_\phi^2 = \frac{C}{r^2} - \beta\bar{p} + \frac{\beta}{r^2}\int 2\rho r \, dr \qquad (8.15)$$

where C is a constant of integration.

One can thus pick $\bar{p}(r)$, and use (8.15) to evaluate the properties of the magnetic field. In practice, the Sun will prescribe both the pressure and normal component of magnetic field at the photosphere but our assumption of cylindrical symmetry means that we cannot prescribe both of these.

8.2.2 Special Cases

(a) Consider first the case of $\bar{p}$ being imposed as

$$\bar{p} = \frac{4}{(1+r^2)^2} \qquad (8.16)$$

so that the pressure falls from the origin to infinity. Integrating (8.15) gives

$$\bar{B}_\phi^2 = \frac{1}{r^2} + \beta\frac{(3r^2+1)(r^2-1)}{r^2(1+r^2)^2}, \qquad (8.17)$$

so that, as $\beta \to 0$, we recover a potential field as expected. Considering the behaviour of $\bar{B}_\phi^2$ near the origin, it can be seen that

$$\bar{B}_\phi^2 \approx \frac{1}{r^2}(1-\beta) + O(r^2),$$

so that we require $\beta < 1$ for equilibrium.

A more general case of (8.16) is

$$\bar{p} = \frac{2^n}{(1+r^2)^n}$$

which gives

$$\bar{B}_\phi^2 = \frac{c}{r^2} - \frac{2^n \beta (1 + n r^2)}{(1+r^2)^n r^2 (n-1)} \quad , \quad n \neq 1 ,$$

$$\bar{B}_\phi^2 = \frac{c}{r^2} - \frac{2\beta}{r^2(1+r^2)} \left[r^2 - (1+r^2) \log(1+r^2) \right] , \quad n = 1 .$$

Evaluating C from the condition that $\bar{B}_\phi = 1$ at $r = 1$ gives

$$\bar{B}_\phi^2 = \frac{1}{r^2} + \frac{\beta}{(n-1) r^2 (1+r^2)^n} \left[(n+1)(1+r^2)^n - 2^n (n-1)(1+2r^2) \right] ,$$

$$n \neq 1 ,$$

$$\bar{B}_\phi^2 = \frac{1}{r^2} + \frac{\beta}{r^2(1+r^2)} \left[2(1+r^2) \log(1+r^2) - r^2 (1+r^2) \right] ,$$

$$n = 1 .$$

Close to the origin, the restriction on β becomes

$$\beta < \frac{(n-1)}{2^n (n-1) - (n+1)} , \quad n \neq 1 ,$$

which becomes more severe as n increases. For $n = 1$, there is no restriction on β.

These solutions may also de derived from equation (8.12) by a method first discussed by Low (1977), however the above derivation is somewhat simpler.

(b) One interesting case of the previous Section is to consider a magnetic field given by (8.17) surrounded at some distance r_e by a field-free gas. We wish to ascertain whether a body of plasma can be contained if its internal pressure is pumped up. Assuming that the field is given by (8.17) and the pressure by (8.16) then a current sheet exists at $r = r_e$ as shown in Figure 8.1b. Pressure balance must hold across this sheet and if the external presure is given by p_e, pressure balance implies

$$\bar{p}_e = \left[\bar{p} + \frac{\bar{B}_\phi^2}{\beta} \right]_{r=r_e} ,$$

where $\bar{p}_e = p_e/p_1$. Hence, C in (8.15) is determined by the pressure-balance at r_e rather than by normalisation at r = 1. (8.15) becomes

$$\bar{B}_\phi^2 = \beta \bar{p}_e \left(\frac{r_e^2}{r^2} \right) + \frac{4}{r^2(1+r_e^2)} - \frac{4\beta(1+2r^2)}{(1+r^2)r^2} ,$$

where, if r_e is fixed an equilibrium exists provided

$$\beta < \frac{1}{(1+r_e^2)(4-\bar{p}_e r_e^2)} .$$

So, for a chosen r_e, increasing β means that the plasma can no longer be contained. Also, increasing p_e allows higher values of pressure to be contained.

(c) A further possible form of the imposed pressure is to consider the pressure at the dimensionless distance r = 1 to be fixed and to vary the pressure toward the origin trigonometrically. Such a pressure is

$$\frac{p(r)}{p_1} = a - (1-a)\cos(\pi r) , \qquad (8.18)$$

where p_1 is the pressure at r = 1. a is a constant such that the pressure changes smoothly from unity at r = 1 to 2a - 1 at the origin. Equation (8.15) may be integrated immediately to give

$$\bar{B}_\phi^2 = \frac{1}{r^2} + 2\beta \left[\frac{1}{2r^2} - \frac{1}{2}\left\{ a + (a-1)\cos(\pi r) \right\} + \right.$$

$$\left. \frac{a(r-1)}{r^2} + \frac{(a-1)}{r^2}\left\{ \frac{\sin(\pi r)}{\pi} + \frac{1}{\pi^2}(\cos(\pi r) + 1) \right\} \right] , \qquad (8.19)$$

where $\bar{B}_\phi$ and β are defined in Section (8.2.1). We now

examine (8.19) to determine whether any values of a or β preclude the existence of fields. Near the origin, (8.19) behaves as

$$\bar{B}_\phi^2 \approx \frac{1}{r^2}\left[1 + \beta + 2\beta\left(\frac{2(a-1)}{\pi^2} - a\right)\right],$$

and so if

$$\beta > \frac{\pi^2}{(4-\pi^2) + 2a(\pi^2-2)},$$

no physically relevant solutions exist.

Rewriting in terms of a, this becomes

$$a > \frac{\pi^2\left(\frac{1}{\beta}+1\right) - 4}{2(\pi^2-2)}, \qquad (8.20)$$

for the non-existence of solutions. So if either a or β are held fixed and the other is increased, non-equilibrium will eventually result due to excessive pressure buildup. Figure 8.2 shows the variation of pressure and magnetic field with radius for such a configuration. The gas pressure is fixed at r = 1 and is allowed to vary at the origin. When the condition (8.20) on a is violated, no field can be constructed. It is also worth noting that such fields have been discussed in the context of coronal loops by Chiuderi et al., (1977).

(d) We have explicitly shown that magnetic non-equilibrium occurs in three specific cases of an imposed pressure distribution. However, one can pick many other possible values of p(r) and some of these will give rise to non-equilibrium too. For example, if

$$\bar{p} = e^{1-r}$$

no solutions exist if

$$\beta > \frac{1}{(2e-5)}$$

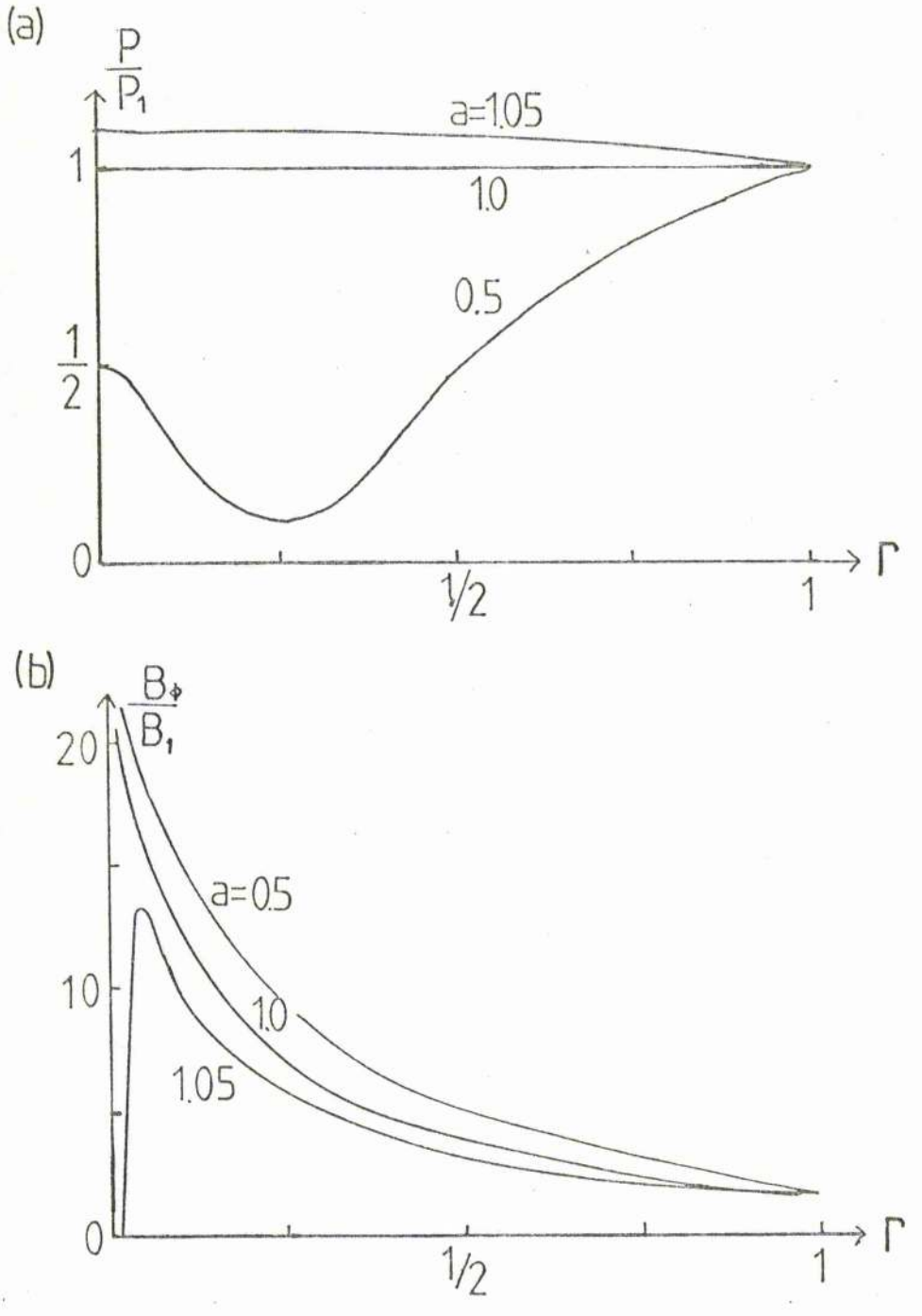

Figure 8.2 (a) The pressure and (b) the magnetic field given by equations (8.18) and (8.19), respectively, as functions of the dimensionless radius, r. Several values of a are shown and β is taken as 1.0.

and one could continue generating such solutions in many other cases.

The next development must be the inclusion of gravity into such an analysis, but a stratified atmosphere introduces complications into these simple calculations. In particular gravity does not act in a cylindrically-symmetric manner and so the simple calculations there will have to be modified. Also, it is of importance to follow the evolution in time of these structures after the onset of non-equilibrium.

8.3 General two-dimensional solutions

As noted in Section 8.1, the equilibrium of a magneto-static field can be written in terms of a single elliptic partial differential equation (8.12). (See Tsinganos (1981) for a more general outline of this approach). Equation (8.12) is, in general, non-linear and need not possess a unique solution and progress towards solving it has proceeded furthest for the case of force-free fields ($\beta = 0$). This has been considered by Low and Nakagawa (1975), Low (1977) and Heyvaerts et al., (1979). These authors have simplified (8.12) by writing

$$\bar{B}_x^2 = \lambda f(A) , \qquad (8.21)$$

where increasing λ represents an increase in $\bar{B}_x$. They find that, if λ is too big, no solutions exist to (8.12), and they interpret the maximum as the onset for a flare due to excess footpoint shearing. This conclusion has been criticised by Jockers (1978) and Priest and Milne (1980), who note that $\bar{B}_x(A)$ attaining a maximum does not correspond to a maximum shear.

$\bar{P}(A)$ has been prescribed by Birn et al., (1978) and Low (1980), and, unlike the force-free case, the physical meaning of increasing $\bar{p}(A)$ is clear. If $\bar{p}(A)$ is too big, the field cannot contain the excess gas pressure and will blow out.

The two cases of breakdown of magnetostatic and force-free equilibria are related by the following simple relationship

$$\beta_{max} = \frac{\lambda}{2}_{max} ,$$

provided

$$\bar{\beta}_x^2(A) = \bar{p}(A).$$

A particular case is given by Birn et al., who assume

$$\bar{p} = \frac{2}{c}\left[\frac{2a\cosh b}{r\pi\cosh\left(\frac{2b\phi}{\pi} - b\right)}\right]^2 ,$$

and obtain

$$\bar{A} = \frac{2}{c}\log\left[\frac{r\pi\cosh\left(\frac{2b\phi}{\pi} - b\right)}{2a\cosh b}\right] ,$$

where b is a solution of

$$b = a\sqrt{\frac{c\beta}{2}}\cosh b$$

If $a = c = 1$, solutions exist if $\beta \lesssim 1$. In terms of the physical parameters, this gives

$$n \gtrsim 6 \times 10^{20}\left(\frac{B^2}{T}\right),$$

for eruption where B is measured in Gauss. For B = 10 G, $T = 10^6$, $n \gtrsim 6 \times 10^{16}$ m^{-3}, a density which is achieved in the corona during flares. If T is lower, say 10^4 K, (as in the photosphere) then $n \gtrsim 6 \times 10^{18}$, a typical photospheric density.

8.3.1 Separable solutions

Approximation (8.21) is, in fact, a rather severe

restriction and attempts have been made to overcome it by looking for separable solutions to the force-free equations (Priest and Milne, 1980). This is easily extended to cylindrical magnetostatic fields in two dimensions.

The non-dimensional form of equation (8.1) is

$$\beta \nabla \bar{p} = (\nabla \times \bar{\underline{B}}) \times \bar{\underline{B}} \quad ,$$

where

$$\beta = \frac{\mu p(r=1, \phi=0)}{B^2(r=1, \phi=0)} \quad , \qquad \bar{p} = \frac{p}{p(r=1, \phi=0)} \quad ,$$

$$\bar{B} = \frac{B}{B(r=1, \phi=0)} \quad .$$

The r and ϕ components are just

$$\beta \frac{\partial \bar{p}}{\partial r} = - \frac{\bar{B}_\phi}{r} \left[\frac{\partial}{\partial r}(r \bar{B}_\phi) - \frac{\partial \bar{B}_r}{\partial \phi} \right] \quad , \tag{8.22}$$

$$\bar{B}_r \frac{\partial \bar{p}}{\partial r} + \frac{\bar{B}_\phi}{r} \frac{\partial \bar{p}}{\partial \phi} = 0 \quad , \tag{8.23}$$

and flux conservation gives

$$\frac{\partial}{\partial r}(r \bar{B}_r) + \frac{\partial \bar{B}_\phi}{\partial r} = 0 \quad . \tag{8.24}$$

Assuming separable solutions

$$\bar{p} = p(r) \Pi(\phi),$$
$$\bar{B}_r = R_r(r) \bar{\Phi}_r(\phi),$$
$$\bar{B}_\phi = R_\phi(r) \bar{\Phi}_\phi(\phi),$$

gives (8.22) - (8.24) as

$$\frac{\bar{\Phi}_\phi^2}{\Pi R_r} \frac{d}{dr}(r R_\phi) + \frac{r \beta}{R_\phi R_r} \frac{dp}{dr} = \ell = \frac{\bar{\Phi}_\phi}{\Pi} \frac{d \bar{\Phi}_r}{d \phi} \quad , \tag{8.25}$$

$$\frac{R_r r}{R_\phi p} \frac{dp}{dr} = n = - \frac{\bar{\Phi}_\phi}{\bar{\Phi}_r \Pi} \frac{d \Pi}{d \phi} \quad , \tag{8.26}$$

$$\frac{1}{R_\phi}\frac{d}{dr}(rR_r) = m = -\frac{1}{\Phi_r}\frac{d\Phi_\phi}{d\phi}\,, \tag{8.27}$$

where l, n and m are constants of separation. This system is separable if

$$\frac{\Phi_\phi^2}{\Pi} = \text{const.}\,, \tag{8.28}$$

or

$$\frac{1}{R_r}\frac{d}{dr}(rR_\phi) = \text{const.} \tag{8.29}$$

(a) $\Phi_\phi^2/\Pi = \text{const.}$

Consider solutions with

$$\Phi_\phi^2 = \Pi\,,$$

The ϕ - equations give

$$\left.\begin{aligned}\Phi_\phi &= \cos l\phi\,,\\ \Phi_r &= \sin l\phi\,,\\ \Pi &= \cos^2 l\phi\,,\end{aligned}\right\} \tag{8.30}$$

and the r-equations

$$\left.\begin{aligned}R_r &= \frac{1}{r}J_l(l\sqrt{2\beta}\,r)\,,\\ R_\phi &= \frac{1}{l}\frac{d}{dr}\left[J_l(l\sqrt{2\beta}\,r)\right]\,,\\ P &= \left[J_l(l\sqrt{2\beta}\,r)\right]^2\,,\end{aligned}\right\} \tag{8.31}$$

where J_1 is the l-th order Bessel function (Abramowitz and Stegun p. 362).

These are just the magnetostatic analogy of the linear (constant -α) force-free field and always give equilibrium.

(b) Solutions subject to (8.29)

Consider the case when

$$\frac{d}{dr}(rR_\phi) = kR_r\,, \tag{8.32}$$

where k is a constant. The radial equations give

$$\left.\begin{aligned} R_r &= r^{-1-k}, \\ R_\phi &= -r^{-1-k}, \\ P &= r^{-2(1+k)}, \end{aligned}\right\} \tag{8.32}$$

and the ϕ-equations give

$$\frac{d^2\bar{\Phi}_\phi}{d\phi^2} + k^2\bar{\Phi}_\phi + \beta\lambda^2 k\,|\bar{\Phi}^{2/k}|\bar{\Phi}_\phi = 0, \tag{8.34}$$

$$\bar{\Pi} = \lambda\,|\bar{\Phi}_\phi|^{2\left(\frac{1}{k}+k\right)}, \tag{8.35}$$

$$\bar{\Phi}_r = -\frac{1}{k}\frac{d\bar{\Phi}_\phi}{d\phi}, \tag{8.36}$$

where λ is a constant of integration. Equation (8.34) is the same as the force-free equation with λ replaced by $\beta\lambda^2$. Equation (8.34) can be solved analytically if $k = -\frac{1}{2}$ and it can be shown that β lies in the range

$$0 < \beta\lambda^2 \leq 1,$$

for solutions to exist. Hence if the pressure is too big, magnetostatic equilibrium breaks down.

8.4 A simple time-dependent model

Consider a magnetic arcade with a uniform magnetic field B and cross-sectional width d. The arcade is so long that any variations along it may be ignored. If this arcade is situated in a field-free region with pressure p_0 below it and p_e above it, then equilibrium exists if the pressure gradient across the arcade is balanced by the tension exerted by the field (as shown in Figure 8.3a). If the arcade has a radius of curvature r and fixed footpoints separated by a distance 2a, then $r^2 = (a^2+h^2)$. There therefore exists

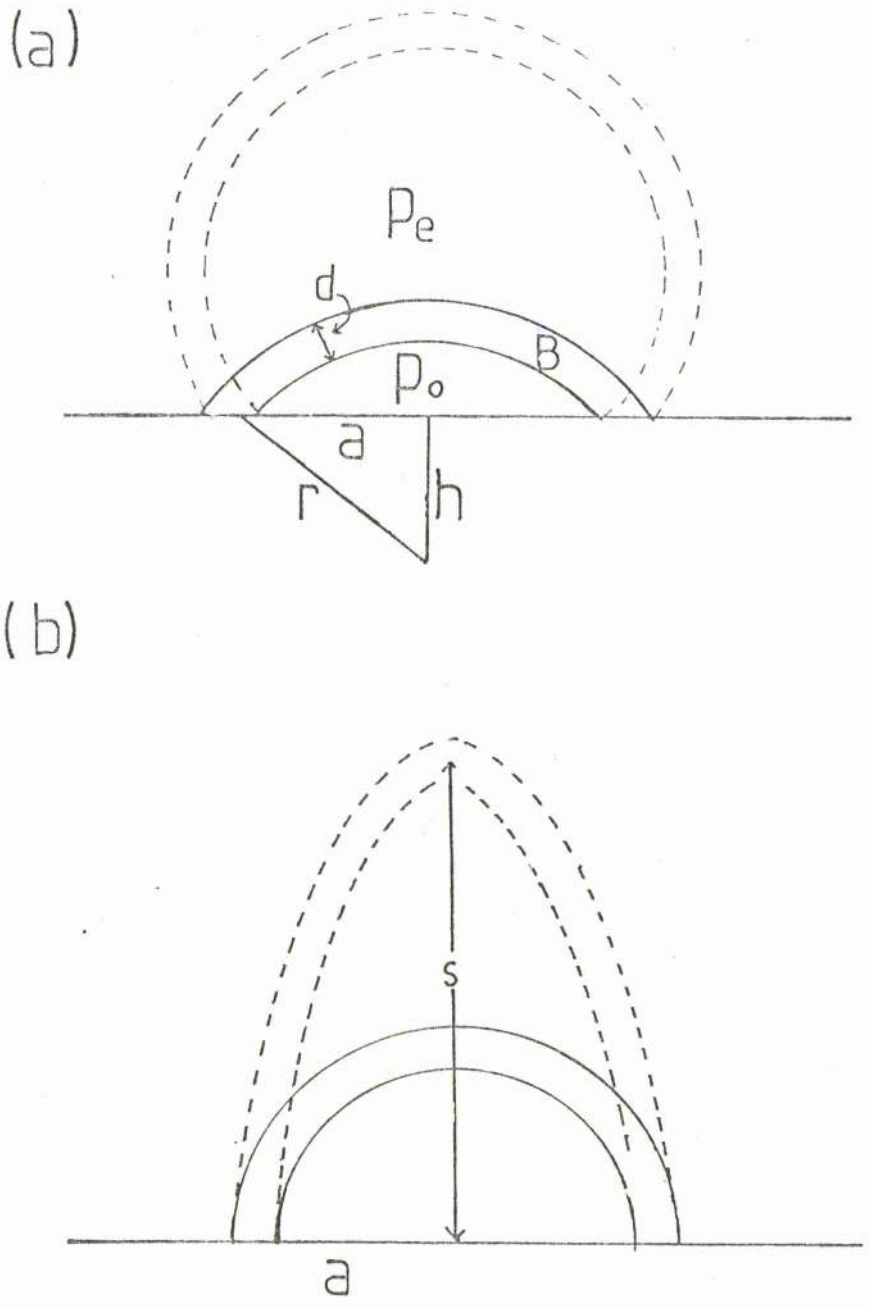

Figure 8.3
(a) Magnetic arcade of width d and field strength B set in a field-free medium with pressure p_o below the loop and p_e above it. The footpoints are separated by a distance 2a and the loop has radius $r^2 = a^2 + h^2$. The dotted lines denote a second equilibrium, the centre of the loop being a distance h above the footpoints.
(b) The arcade as a time $t > 0$. The footpoints are separated by a fixed distance a but the arcade has become elliptical with major radius s and minor radius a. The dashed lines denote the arcade at time $t = 0$. The pressure, p_o, has been increased byond its critical value by a factor ξ.

for any value of |h|, two possible equilibrium configurations, one with $h < 0$ and the other with $h > 0$ as in Figure 8.3a.

Equilibrium is given by

$$\frac{p_o - p_e}{d} = \frac{B^2}{\mu r} \quad , \tag{8.37}$$

and h is determined by

$$h = \pm a \left[\left(\frac{B^2 d}{a \mu} \right)^2 \frac{1}{(p_o - p_e)^2} - 1 \right] . \tag{8.38}$$

If a, B and d are kept fixed, when $p_o - p_e$ becomes too big, h no longer has a real value. Thus, for either configuration shown in Figure 8.3a as $p_o - p_e$ increases, h tends to 0 and the loop becomes semi-circular. When the critical value of $p_o - p_e$, given by

$$(p_o - p_e)_{crit} = \frac{B^2 d}{a \mu} \quad , \tag{8.39}$$

is exceeded no equilibrium is possible. This can be understood physically since the magnetic tension exerted by the arcade field can no longer confine the plasma in the field-free region below the arcade.

The magnetic energy is given by

$$W_m = \int_V \frac{B^2}{2\mu} \, dV \tag{8.40}$$

where V represents the volume permeated by the field. For the arcade case, W_m is just

$$W_m = \begin{cases} \frac{B^2 d L}{\mu} (a^2 + h^2)^{1/2} \tan^{-1}(a/h) , & h < 0, \\ \frac{B^2 d L}{\mu} (a^2 + h^2)^{1/2} \left(\pi - \tan^{-1}(a/h) \right) , & h > 0, \end{cases} \tag{8.41}$$

where L is the length of the arcade, so h = 0 is not a maximum of the magnetic energy.

The thermal energy density is given by

$$E = \frac{3p_0}{2}, \qquad (8.42)$$

so the onset of non-equilibrium does correspond to a maximum in E. The respective energies are shown in Figure 8.4.

Consider now what happens if $(p_0 - p_e)$ is increased beyond its critical value by a factor ε such that

$$p_0 = \left(p_e + \frac{B^2 d}{a\mu}\right)(1+\varepsilon). \qquad (8.43)$$

A very simple time-dependent model may be constructed as follows. Assume that, for all time, d (and hence B) remain fixed. (This is a great simplification and may or may not be justifiable: future calculations are needed to check this). Assume also that as the arcade evolves, it behaves as an ellipse, centre the photosphere (Figure 8.3b) so that

$$r = s(t), \qquad (8.45)$$

where s = a at t = 0 and r is the coordinate of the summit. The radius of curvature of an ellipse of form $x^2/a^2 + y^2/b^2 = 1$ is

$$R_c = \frac{\left[1 + (dy/dx)^2\right]^{3/2}}{(d^2y/dx^2)}, \qquad (8.46)$$

and so, at the summit, $R_c = a^2/s(t)$. Hence, as the ellipse rises, R_c decreases and the effect of magnetic tension increases.

We assume that the mass below the arcade is constant in time and for an isothermal plasma, this gives

$$p_0 = \frac{a^2 p_0(t=0)}{a\, s(t)}. \qquad (8.47)$$

Finally, the mass in the arcade is also held constant in time,

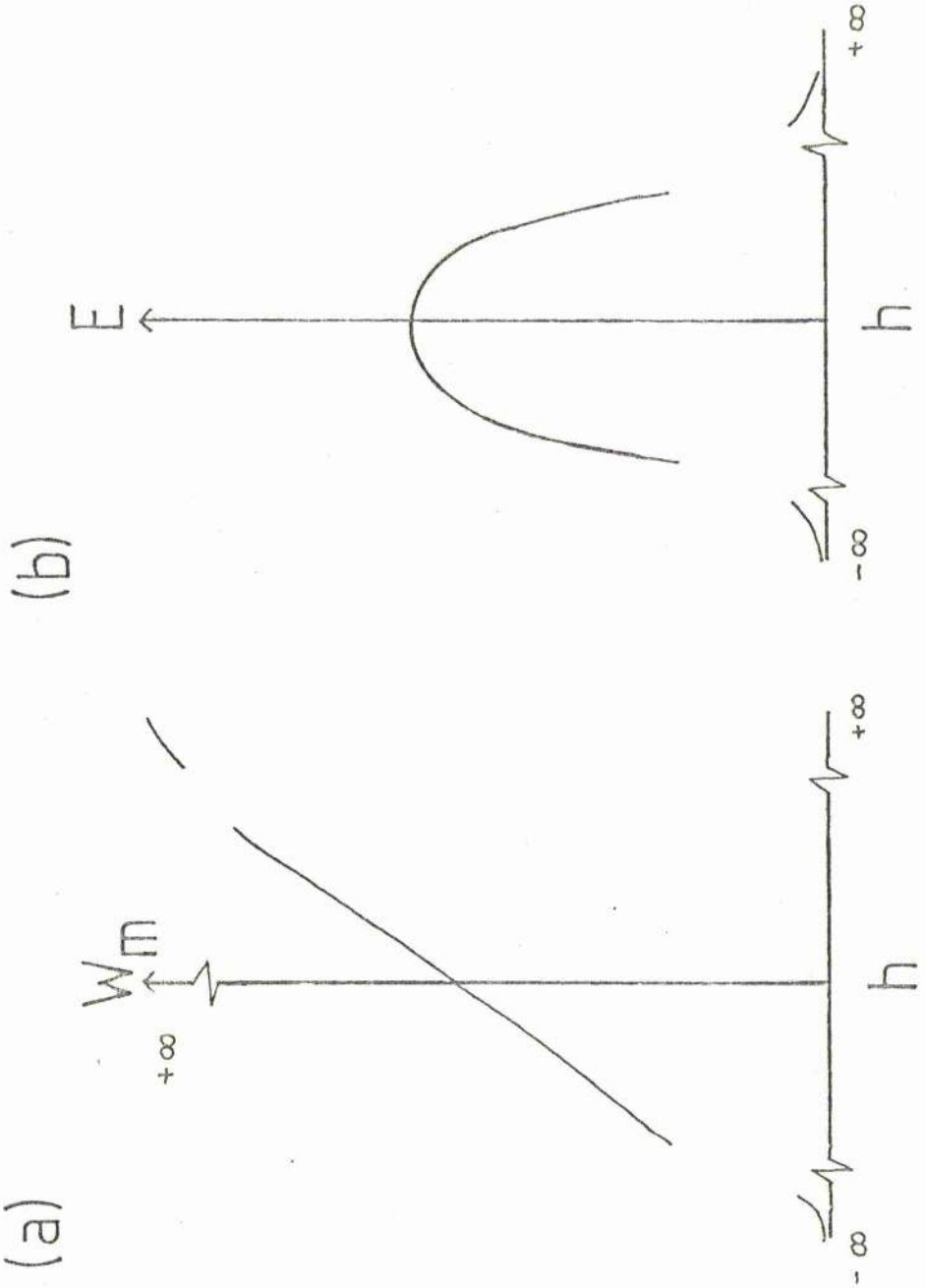

Figure 8.4
(a) The form of the magnetic energy in the loop as a function of h.
(b) The form of the energy density, E, due to the pressure p_o as a function of h.

so

$$\rho = \frac{a\,\rho(t=0)}{\left[\frac{1}{2}(a^2+s^2)\right]^{1/2}}\,, \tag{8.48}$$

where $\frac{1}{2}(a^2+s^2)^{\frac{1}{2}}$ is length of the ellipse.

Considering force-balance around the summit gives

$$\frac{\rho_o a}{\left[\frac{1}{2}(a^2+s^2)\right]^{1/2}}\frac{d^2s}{dt^2} = \frac{1}{d}\left[\frac{a\,p(t=0)}{s} - p_e\right] - \frac{\beta^2 s}{\mu a^2}\,, \tag{8.49}$$

and, writing (8.49) in terms of the sound speeds inside and the arcade, $c_{so}^2 = p_o/\rho_o$, $c_{se}^2 = p_e/\rho_o$ respectively and the Alfvén speed, $v_A = B^2/\mu\rho_o$ gives

$$a\frac{d^2s}{dt^2} = \frac{1}{d}\left[\frac{c_{so}^2}{\sqrt{2}s}(a^2+s^2)^{1/2} - \frac{c_{se}^2}{\sqrt{2}}(a^2+s^2)^{1/2}\right] - \frac{v_A^2}{a^2\sqrt{2}}(a^2+s^2)^{1/2}\,s\,. \tag{8.50}$$

Integrating once gives

$$\frac{a}{2}\left(\frac{ds}{dt}\right)^2 = \frac{c_{so}^2 a}{\sqrt{2}d}\left[(a^2+s^2)^{1/2} - a\sinh^{-1}\left(\frac{a}{s}\right)\right] - \frac{c_{se}^2}{2\sqrt{2}d}\left[s(s^2+a^2)^{1/2} + a^2\sinh^{-1}\left(\frac{s}{a}\right)\right] - \frac{v_A^2}{3\sqrt{2}a^2}(a^2+s^2)^{3/2} + \text{const.}\,, \tag{8.51}$$

where the constant is determined by the condition,

$$\frac{ds}{dt} = 0\,, \quad t = 0\,.$$

This gives, on application of the equilibrium condition (8.44), and after extensive algebra,

$$\frac{1}{2}\left(\frac{ds}{dt}\right)^2 = \left(c_{se}^2 + v_A^2\frac{d}{a}\right)(1+\varepsilon)\left[(a^2+s^2)^{1/2} - a\sinh^{-1}\left(\frac{a}{s}\right)\right] - \frac{c_{se}^2}{2\sqrt{2}d}\left[\frac{s}{a}(s^2+a^2)^{1/2} + a\sinh^{-1}\left(\frac{s}{a}\right)\right] - \frac{v_A^2}{3\sqrt{2}a^3}(a^2+s^2)^{3/2} +$$

$$+\frac{c_{se}^2 a}{2\sqrt{2}d}\left[3\sinh^{-1}1-\sqrt{2}\right]+\frac{V_A^2}{\sqrt{2}}\left[-\frac{\sqrt{3}}{2}+\sinh^{-1}1\right]-$$

$$-\frac{\xi a}{d}\left(c_{se}^2+V_A^2\frac{d}{a}\right)\left(1-\frac{\sinh^{-1}1}{\sqrt{2}}\right). \qquad (8.52)$$

(8.52) is an equation for the velocity of the summit of the arcade and the velocity can be shown to be zero at some point s_{max}. Hence, the arcade travels upward initially until the external pressure and magnetic tension increase and prevent the arcade from rising further and the arcade will then fall back. This is what is seen to happen in a surge. For $c_{se}^2 = v_A^2 = 50$ km s^{-1}, d = 10Mm and a = 50Mm, one finds that s_{max} is 30 Mm for $\xi = 0.2$.

8.5 Conclusions

In this Chapter the magnetostatic equation (8.1) has been solved analytically for several cases and the feature of magnetostatic non-equilibrium shown to exist. This non-equilibrium may be interpreted as saying that the plasma can no longer be contained by the magnetic field and must evolve, on the fast magnetoacoustic timescale. We have been mainly concerned with demonstrating the existence of non-equilibrium than in calculating specific values of parameters but it does appear that if $\beta \geq 1$ then the possibility of non-equilibrium is always present. Values of β as large as this are not generally expected in the high corona, where magnetic non-equilibrium is likely to be due more often to excessively sheared footpoints (Priest and Milne, 1980). However in the photosphere and chromosphere values of β as high as one are

to be expected.

The next question is to consider how this non-equilibrium manifests itself observationally. As mentioned in the introduction, sprays and surges are eruptions from the chromosphere and their temperatures are characteristic of the chromospheric values. We suggest that one possible explanation of these eruptive phenomena is that magnetostatic non-equilibrium occurs and material is ejected at high speed from the photosphere as shown in Section 8.4. The speed of ejection depends on the local conditions in the region of non-equilibrium. It is indeed possible that surges and sprays could both be manifestations of magnetic non-equilibrium with a different parameter range in each case. However, using the typical values of physical quantities quoted by Rust et al., (1980), it may be seen that surges have a plasma beta some two orders of magnitude higher than sprays and are hence the more likely candidate. Zirin (1974) has also studied surges and notes that the erupting material is well confined and flows outward in a collimated way. This suggests that the magnetic field surrounding the surge remains roughly vertical, inhibiting lateral motions.

This is the situation modelled in Section (8.4) where it was found that after non-equilibrium, the plasma could only rise to a certain height. However, this calculation is very idealised and a much more rigorous analysis is needed before any conclusions are drawn.

It is also important to consider whether all our magnetostatic fields are stable. The most important feature of any such analysis is photospheric line-tying and the results of

Hood and Priest (1979b, 1980a) suggest that this is the dominant effect. We thus expect the fields discussed to possess great stability.

In this Chapter, we have just scraped the surface of what is a large subject and have contented ourselves with showing that the well-known phenomenom of force-free non-equilibrium carries over to magnetic fields containing pressure gradients.

Chapter 9: SUMMARY AND CONCLUSIONS

In this thesis, several dynamic phenomena have been discussed, and it is the aim of the present chapter to summarise briefly the various results and suggest how the work described can be improved upon and extended.

Chapter 2 provides an extensive review of the behaviour of shock waves. The well-known results of gas shocks were stated, and then an analysis of slow magnetohydrodynamic shocks was undertaken. We relaxed the usual assumption of aligned incident field and flow (or vanishing electric field) and undertook analytical and numerical solutions of the full jump relations. It was found that considerable plasma heating can be obtained under these circumstances. In particular, when the tangential component of the magnetic field is switched off, a temperature ratio of $2/(5\beta_1)$ across the shock becomes possible for $\beta_1 \ll 1$. It was thus suggested that slow shocks are a very effective heating mechanism and could be responsible (in part) for coronal heating.

Chapters 3 and 4 discussed steady flows in coronal loops: the so-called siphon flows. Chapter 3 considered adiabatic and isothermal flows. The energy equation was here replaced by the simple polytropic law $p = Kn^{\gamma}$ where $\gamma = 1$ and $\gamma = 5/3$ were considered. The equations of momentum, continuity and state were solved along a single field line subject to prescribed foot-point pressures. It was found that, for a loop of uniform cross-sectional area there exists no wholly subsonic flows with a pressure ratio less than unity. Therefore, for a given sub-unity pressure

ratio, the flow undergoes a subsonic-supersonic transition at the loop summit and is decelerated on the downflowing leg by a standing shock to give the required boundary condition.

Several different loop cross-sectional areas were also considered. In particular, a loop whose area converges from one footpoint to another was found to allow pressure ratios with wholly subsonic solutions. However, a diverging loop permits only shocked ones. The effect of the flow is to lower both density and temperature below their static levels, suggesting that such siphon flows should be observable, due to the drop in emission measure (Noci, 1981).

Chapter 4 extended this theory to include a realistic energy equation. Such an equation incorporates terms representing thermal conduction, optically thin radiation and a mechanical heating term which is constant per unit mass. The full set of steady-state equations was solved numerically subject to fixed temperatures and densities at the footpoints. A large range of footpoint boundary conditions were found to be satisfied by loops having siphon flows, suggesting that the static loop models previously considered (Hood, 1980 and references therein) are only one of a large range of possible coronal loop solutions. Also, the need for shocked solutions was removed, although they still can occur for large pressure ratios. A flow was also found to reduce the maximum loop temperature and move it to some position on the downflowing leg, thus creating asymmetric temperature profiles. The onset for thermal non-equilibrium in a loop (see below) was found to be enhanced by the presence of a steady flow.

The work on siphon flows can be extended in the

following ways:

(i) It is necessary to find out how siphon flows actually arise, and this can be done by a time-dependent calculation in which one starts with a static loop and then gradually reduces one of the footpoint pressures. A flow will start, and it is of interest to see how long it takes before a steady flow is set up if at all.

(ii) Improvements in coronal loop observations are necessary before one can expect to detect such a flow, but recent eclipse photographs (Livingston and Harvey, 1981) have provided the first evidence of coronal siphon flows. It is important to calculate the deviation from the predicted emission which a flow would cause and the work of Noci is a first step in this direction.

(iii) It is desirable to model steady-state siphon flows down to the base of the transition zone instead of starting at $T = 10^6$ K. This will enable us to see whether the large number of observed transition zone flows are, in fact, part of a wider circulation. It seems unlikely that steady or quasi-steady flows are not occurring in coronal loops due to the continually changing nature of the loop base. It is thus hard to believe that loops are always static, and there seems little doubt that flows from one end of the loop to the other do exist provided the base conditions remain steady for a few sound-travel times (typically a sound-travel time is between 5 and 20 minutes).

In Chapter 5, the cooling of a coronal loop due to thermal non-equilibrium was examined. Hood and Priest (1979a) showed that, if the pressure in a coronal loop became too

large, then it is unable to maintain a temperature of over 10^6 K and cools to below 10^5 K. Using an order-of-magnitude scheme, we followed the non-linear evolution of the cooling. It was found that the loop cools slowly from typically 10^6 K to 7.5×10^5 K and then cools non-linearly to below 10^4 K in a matter of a few minutes. It was suggested that, depending on the loop geometry, the result could either be a cool loop core as observed by Foukal (1975) or a prominence supported by a coronal arcade.

This simple analysis should be developed along the following lines:

(1) A full numerical solution should be attempted of the one-dimensional equations. This is well within the resources of current computers, and it should be able to follow the evolution for a considerable time. Such a code should enable one to model the transition zone down to the temperature minimum and recent work of Peres et al., (1981) has made this a practical proposition. They have developed a piecewise radiative loss function for temperatures down to the temperature minimum based on the calculations of Vernazza et al. (1981), and such a loss function can be easily included into current codes.

(2) Fuller M.H.D. simulations of arcades and loops would enable us to see exactly how (and whether) it is necessary to couple in the magnetostatics to the energetics. The single-field line model is only of use if a field is approximately force-free, and it is not always clear that this is the case.

Chapter 6 discussed another aspect of thermal non-equilibrium, namely the suggestion that it is responsible for the

compact flare. In a cool loop, heating approximately balances radiation, and, if the heating becomes too big, the input cannot be radiated away and the loop heats up. The loop flares to over 10^7 K in typically 5 minutes, in good agreement with flare rise-time observations. The evolution was followed by using the same order-of-magnitude approximation as in Chapter 5, and it was suggested that this gives a reasonable approximation to the temperature behaviour but a poor approximation for the density. The following improvements are likely to be of use:

(1) As in Chapter 5, a full numerical code is needed and preliminary results (Hood and Priest, 1982) are encouraging.

(2) The question of base boundary conditions is of vital importance. It is clear that any disturbance generated in the corona must be allowed to interact as far down as the temperature minimum if necessary. Thus one must construct a lower atmosphere, such as suggested by Peres et al. (see above). This is somewhat simpler than the approach undertaken by Nagai (1980), but the end result should be similar.

(3) Gravity should be included fully since the scale-height is small in cool regions.

(4) Area divergence should be considered. However, it is important to remember that the flaring loop must remain force-free for all time, and a rapid area divergence could give rise to very weak fields, and a situation of magneto-static rather than force-free equilibrium could arise, casting doubt on single field line models.

(5) It should be remembered that thermal non-equilibrium is just one possible trigger for the compact flare. Other models of energy release such as the kink instability (Hood and Priest, 1979b) and tearing modes (Spicer, 1977) are also important. Therefore one should also try to develop further models of the response of hot loops to an energy input. (See Craig, 1981, for a review of current work on this subject).

Chapter 7 re-examined the Kopp-Pneuman model for "post"-flare loops. Kopp and Pneuman (1976) suggested that "post"-flare loops are heated by gas-dynamic shocks but the temperatures obtained this way are nowhere near high enough. Instead, it is suggested that the loops are heated by two slow M.H.D. shocks extending from the Y-type neutral point. Using the theory of Chapter 2, temperatures of up to 10^7 K and neutral point speeds of 1 km s^{-1} were found and the model was then applied to the 29th July 1973 flare.

Clearly, a full 2-dimensional, compressible M.H.D. calculation is desirable, but this gives rise to considerable numerical problems. Also, it will be of interest to compare this model with other observations of "post"-flare loops to test its more general applicability.

Finally, Chapter 8 examined magnetostatic non-equilibrium. It was shown analytically that magnetostatic equilibrium could break down if the gas pressure becomes too large in certain magnetic structures. Both one-and two-dimensional models were examined, and it was suggested that non-equilibrium is a possible explanation of surges and sprays. This work can be regarded as a preliminary analysis and future work should include:

(1) A further examination of existence theorems that can be applied to the equation

$$\nabla^2 A = -\lambda \xi(A)$$

Bicnet al. (1978) have made some progress, and further results by Edenstrasser (1980) should be considered to see if they can be applied to solar magnetic fields.

(2) Further simple time-dependent analyses following the ideas of Pneuman (1980) may give a rough guide to the evolution of a magnetic field after non-equilibrium has occurred.

(3) A numerical solution of the time-dependent equations seems feasible if the initial field can be expressed in simple analytical form.

REFERENCES

Antiochos, S.K.: "The stability of solar coronal loops" Astrophys. J. 232, L125-129, (1979).

Antiochos, S.K.: "Radiative-dominated cooling of the flare corona and transition region" Astrophys. J. 241, 385-393, (1980).

Antiochos, S.K. and Sturrock, P.A.: "Evaporative cooling of flare plasma" Astrophys. J. 220, 1137-1143, (1978).

Basri, G.S., Linsky, J., Bartoe, J-D.F., Brueckner, G.E. and Van Hoosier, M.E.: "L_α rocket spectra and models of the quiet and active solar chromosphere based on partial redistribution diagnostics" Astrophys. J. 230, 924-949, (1979).

Bazer, J. and Ericson, W.B.: "Hydromagnetic shocks" Astrophys. J. 129, 758-785, (1959).

Birn, J., Goldstein, H. and Schindler, K.: "A theory of the onset of solar eruptive processes." Solar Phys. 57, 81-101. (1978).

Boris, J.P. and Book, D.L.: "Flux-corrected transport 1. SHASTA, a fluid transport algorithm that works" J. Comp. Phys. 11, 38-69, (1972).

Boyd, T.J.M. and Sanderson, J.J.: "Plasma Dynamics", Nelson, (1969).

Brown, J.C.: "The interpretation of spectra, polarization and directivity of solar hard X-rays" in S.R. Kane (ed) 'Solar gamma, X-ray and EUV emission', D. Reidel, IAU Symposium 68, 245-282, (1975).

Brown, J.C. and Smith, D.F.: "Solar Flares" Rep. Prog. Phys. 43, 125-197, (1980).

Brown, J.C., Smith, D.F. and Spicer, D.S.: "Solar flare observations and their interpretations" in S. Jordan (ed) 'The Sun as a star' NASA, p.181-227 (1981).

Bruner, E.C., Chipman, E.G., Lites, B.W., Rottman, G.J., Shine, R.W., Athay, R.G. and White, O.R.: "Preliminary results from OSO-8: Transition zone dynamics over a sunspot" Astrophys. J. 210, L97-L101, (1976).

Bruzek, A. and Durrant, C.J.: 'An Illustrated Glossary of Solar and Solar Terrestial Physics' D. Reidel, (1977).

Chase, R.C., Krieger, A.S., Svestka, Z. and Vaiana, G.S.: "Skylab observations of X-ray loops connecting separate active regions" Space Res. 16, 917-922, (1976).

Cheng, C-C. and Widing, K.G.: "Spatial distribution of XUV emission in solar flares" Astrophys. J. 201, 735-739, (1975).

Cheng, C-C., Feldman, U. and Doschek, G.A.: "What produces the high densities observed in solar flare plasma?" Astron. Astrophys. 97, 210-212, (1981).

Chiuderi, C., Giachetti, R. and Van Hoven, G.: "The structure of coronal loops - I Equilibrium Theory" Solar Phys. 54, 107-122, (1977).

Chiuderi, C., Einaudi, G. and Tricelli-Ciamponi, G.: "What can we learn from static models of coronal loops?" Aston. Astrophys. 97, 27-32, (1981).

Cox, D.P. and Tucker, W.H.: "Ionisation equilibrium and radiative cooling of a low density plasma" Astrophys. J. 157, 1157-1167, (1969).

Craig, I.J.D.: "Simple loop flares: thermal evolution" in S.R. Priest (ed), 'Solar Flare Magnetohydrodynamics' Gordon and Breach, p 277-336, (1981).

Craig, I.J.D., McClymont, A.N. and Underwood, J.H.: "The temperature and density structure of active region coronal loops" Aston. Astrophys. 70, 1-10, (1978).

Craig, I.J.D. and McClymont, A.N.: "The dynamic formation of quasi-static active region loops" Solar Phys. 70, 97-113, (1981).

Curle, S.N.: 'Modern Fluid Dynamics' Van Nostrad (1971).

Datlowe, D.W., Hudson, H.S. and Peterson, L.E.: "Observations of solar X-ray bursts in the energy range 5-15 Ke V" Solar Phys. 35, 193-206, (1974).

Edenstrasser, J.W.: "Unified treatment of symmetric MHD equilibria" J. Plasma Phys. 24, 299-313, (1980).

Forbes, T.G.: Private Communication (1981).

Forbes, T.G.: Paper in preparation, (1982).

Foukal, P.V.: "The temperature structure and pressure balance of magnetic loops in active regions" Solar Phys. 43, 327-336, (1975).

Foukal, P.V.: "The pressure and energy balance of the cool corona over sunspots" Astrophys. J. 210, 575-581, (1976).

Foukal, P.V.: "Magnetic loops, downflows and convection in the solar corona" Astrophys. J. 223, 1046-1057, (1978).

Gradshteyn, I.S. and Ryzhik, I.M.: 'Tables of Integrals, Series and Products' Academic Press, (1980).

Glencross, W.M.: "Plasma flow along sheared magnetic arches within the solar corona" Astron. Astrophys. 83, 65-72, (1980).

Habbal, S.R. and Rosner, R.: "Thermal instabilities in magnetically confined plasmas - solar coronal loops" Astrophys. J. 234, 1113-1121, (1979).

Haugen, E.: "On the chromospheric velocity field in sunspot regions" Solar Phys. 9, 88-101, (1969).

Heyvaerts, J., Priest, E.R., and Rust, D.M.: "An emerging flux model for the solar flare phenomenon "Astrophys. J. 216, 123-137, (1977).

Heyvaerts, J., Larsy, J.M., Schatzman, M. and Witomsky, G.: "Solar flares: blowing up of force-free magnetic configurations" Preprint, (1979).

Hildner, E.: "The formation of solar quiescent prominences by condensation" Solar Phys. 35, 123-136, (1974).

Hood, A.W. and Priest, E.R.: "The equilibrium of solar coronal magnetic loops" Astron. Astrophys. 77, 233-251, (1979a).

Hood, A.W. and Priest, E.R.: "Kink instability of solar coronal loops as the cause of solar flares" Solar Phys. 64, 303-321, (1979b).

Hood, A.W.: "Solar Coronal Loops" Ph.D. Thesis, St. Andrews University, (1980).

Hood, A.W. and Priest, E.R.: "Are solar coronal loops in thermal equilibrium?" Astron. Astrophys. 87, 126-131, (1980a).

Hood, A.W. and Priest, E.R.: "Magnetic instability of coronal arcades as the origin of 2-ribbon flares" Solar Phys. 66, 113-134, (1980b).

Hood, A.W. and Priest, E.R.: "Thermal non-equilibrium: a trigger for solar flares?" Solar Phys. (1981).

Hood, A.W. and Priest, E.R.: Paper in preparation (1982).

Jeffrey, A. and Taniuti, T.: 'Non-Linear Wave Propagation' Academic Press, (1964).

Jockers, K.: "Bifurcation of force-free magnetic fields: a numerical approach" Solar Phys. 56, 37-53, (1978).

Jordan, C.: "The structure of solar active regions from EUV and soft X-ray observations" in S.R. Kane (ed) 'Solar gamma, X-ray and EUV emission', D. Reidel, IAU Symposium 68, p.109-131.

Jordan, C.: "The energy balance of the solar transition region" Astron. Astrophys. 86, 355-363, (1980).

Joselyn, J.A., Munro, R.H. and Holzer, T.E.: "Mass flow and the validity of ionisation equilibrium on the sun" Solar Phys. 64, 57-69, (1979).

Kippenhahn, R. and Schluter, A.: "Eine theorie der solaren filamente" Z. Astrophys. 43, 36 (1957).

Kleczek, J.: "Mass balance in flare loops" in W. Hess (ed) 'AAS-NASA Symposium on Solar Flares' p. 77-80, (1964).

Kopp, R.A. and Pneuman, G.W.: "Magnetic reconnection in the corona and the loop prominence phenomenon" Solar Phys. 50, 85-98, (1976).

Kopp, R.A. and Holzer, T.E.: "Dynamics of coronal hole regions - I Steady polytropic flow with multiple critical points". Solar Phys. 49, 43-56, (1976).

Kostyuk, N.D. and Pikel'ner, S.B.: "Gasdynamics of a flare region heated by a stream of high-velocity electrons" Sov. Astron. 18, 590-599, (1975).

Landau, L.D. and Lifschitz, E.M.: 'Fluid Mechanics' (1959).

Landini, M. and Monsignori-Fossi, B.C.: "Energy balance and the structure of coronal loops" (1981).

Levine, R.H. and Withbroe, G.L.: "The physics of an active region loop system" Solar Phys. 51, 83-101, (1977).

Levine, R.H. and Pye, J.P.: "The coronal and transition zone temperature structure of a solar active region" Solar Phys. 66, 39-60, (1980).

Livingston, W. and Harvey, J.: "Preliminary results from eclipse corona velocity observations", to appear in 'Proc. International Symp. on Solar Eclipse', (1981).

Lites, B.W., Bruner, E.C., Chipman, E.G., Shine, R.A., Rottman, G.J., White, O.R. and Athay, R.G.: "Preliminary results from OSO-8: persistent velocity fields in the chromosphere and transition zone" Astrophys. J. 210, L111-L113, (1976).

Lites, B.W., Bruner, E.C. and Wolfson, C.J.: "OSO-8 observations of the impulsive phase of solar flares in the transition zone and corona" Solar Phys. 69, 373-389, (1981).

Loughead, R.E.: "The fibrils around isolated sunspots" Solar Phys. 5, 489-497, (1968).

Low, B.C.: "Evolving force-free magnetic fields. I. The development of the preflare phase" Astrophys. J. 212, 234-242, (1977).

Low, B.C.: "The false equilibrium of a force-free magnetic field" in M. Dryer and E. Tandberg-Hanssen (eds) 'Solar and Interplanetary Dynamics' D. Reidel, IAU Symposium 91, 283-289, (1980).

Low, B.C. and Nakagawa, Y.: "Dynamics of solar magnetic fields. VI. Force-free magnetic fields and the motions of magnetic footpoints" Astrophys. J. 199 237-246, (1975).

Ludford, G.S.: "The structure of a hydromagnetic shock in steady plane motion" J. Fluid Mech. 5, 67-80, (1958).

Lynn, Y.M.: "MHD shocks in non-aligned flows" Phys. Fluids 9, 314-335, (1966).

Machado, M.E.: Private communication (1980).

MacNiece, P.: Private communication (1981).

Maltby, P.: "The chromospheric Evershed flow" Solar Phys. 43, 91-105, (1975).

Marshall, W.: "The structure of MHD shocks" Proc. Roy. Soc. A233, 367-376, (1955)

Meyer, F. and Schmidt, H.U.: "Field-aligned flows in the solar atmosphere" Z. Angew Math. Mech. 48, 218-221, (1968).

Milkey, R.W., Blocker, N.K., Chambers, W.H., Fehlau, P.E., Fuller, J.C. and Kunz, W.E.: "The time-behaviour of temperature and emission measure in X-ray flares" Solar Phys. 20, 400-412, (1971).

Milne, A.M., Priest, E.R. and Roberts, B.: "A Model for quiescent solar prominences" Astrophys. J. 232, 304-317, (1979).

Mitchell, H.G. and Kan, J.R.: "Merging of magnetic fields with field aligned plasma flow components" J. Plasma Phys. 20, 31-45, (1978).

Monsignori-Fossi, B.C.: "The structure of active regions" in Proc 3rd European Solar meeting. (1981).

Moore, R.L. and Datlowe, D.W.: "Heating and cooling of the thermal X-ray plasma in solar flares" Solar Phys. 43, 189-209, (1975).

Moore, R.L. et al. (15 co-authors): in P. Sturrock (ed) 'Skylab Workshop on Solar Flares' Colo. Ass. Univ. Press, p.341-409, (1980).

Nagai, F.: "A model of hot loops associated with solar flares:- I. Gasdynamics in the loops" Solar Phys. 68, 351-379, (1980).

Noci, G. : "Siphon flows on the solar corona" Solar Phys. 69, 63-76, (1981).

Nolte, J.T., Gerassimenko, M., Kriger, A.S., Petrasso, R.D. and Svestka, Z.: "Study of post-flare loops on 29th July 1973 - I. Dynamics of X-ray loops" Solar Phys. 62, 123-132, (1979).

Parker, E.N.: 'Interplanetary Dynamical Processes" Wiley-Interscience, (1963).

Parker, E.N.: 'Cosmical Magnetic Fields' O.U.P. (1979)

Peres, G., Rosner, R., Serio, S. and Vaiana, G.S.: "Closed coronal structures: IV. Hydrodynamical stability and response to heating perturbations" Preprint, (1981).

Petrasso, R.D., Nolte, J.T., Gerassimenko, M., Krieger, A.S., Krogstad, R., Seguin, F.H. and Svestka, Z.: "Study of post-flare loops on 29th July 1973 - II. Physical parameters in the X-ray loops" Solar Phys. 62, 133-144, (1979).

Petschek, H.E.: "Magnetic field annihilation" in W. Hess (ed) 'AAS - NASA Symposium on Solar Flares' p. 425-439, (1964).

Pikel'ner, S.B.: "The origin of quiescent prominences" Solar Phys. 17, 44-49, (1971).

Pneuman, G.W.: "Coronal manifestations of eruptive prominences :- Theory" in E. Jensen, P. Maltby and F. Orrall (eds) 'Physics of Solar Prominences' IAU Colloquium 44, 281-302, (1978).

Pneuman, G.W.: "Eruptive prominences and coronal transients" Solar Phys. 65, 369-385, (1980).

Pneuman, G.W.: "Two-ribbon flares - (post)-flare loops" in E.R. Priest (ed), 'Solar Flare Magnetohydrodynamics', p. 379-428, (1981a).

Pneuman, G.W.: Private Communication, (1981b).

Priest, E.R.: "The solar flare phenomenon" in D.J. Williams (ed), 'Physics of the Solar Planetary Environment' Am. Geophys. Union 1, 144-169, (1976).

Priest, E.R.: "The structure of coronal loops" Solar Phys. 58, 57 - 87, (1978).

Priest, E.R.: 'Solar Flare Magnetohydrodynamics' Gordon and Breach, (1981a).

Priest, E.R.: "Theory of loop flows and instability" in F. Orrall (ed) 'Skylab Workshop on Active Regions', Colo. Ass. Univ. Press, (1981b).

Priest, E.R.: 'Solar Magnetohydrodynamics' D. Reidel, (1982).

Priest, E.R. and Smith, E.A.: "The structure of coronal arcades and the formation of solar prominences" Solar Phys. 64, 267-286, (1979).

Priest, E.R. and Milne, A.M.: "Force-free magnetic arcades relevant to two-ribbon solar flares" Solar Phys. 65, 315-346, (1980).

Raymond, J.C., Cox, D.P. and Smith, D.P.: "Radiative cooling in a low density plasma" Astrophys. J. 204, 290-294, (1976).

Raymond, J.C. and Dupree, A.K.: "C III density diagnostics in non-equilibrium plasmas" Astrophys. J. 222, 379-383, (1978).

Roberts, B. and Frankenthal, S.: "The thermal statics of coronal loops" Solar Phys. 68, 103-109, (1980).

Roseneau, P. and Frankenthal, S.: "Shock disturbances in a thermally conducting solar wind" Astrophys. J. 208, 633-637, (1976).

Roseneau, P. and Frankenthal, S.: "Propagation of MHD shocks in a thermally conducting medium" Phys. Fluids 21, 559-566, (1978).

Rosner, R., Tucker, W.H. and Vaiana, G.S.: "The dynamics of the quiescent solar corona" Astrophys. J. 220, 643-665, (1978).

Rust, D.M. et al. (12 co-authors): "Mass Ejections" in P. Sturrock (ed) 'Skylab Workshop on Solar Flares' Colo. Ass. Univ. Press, p.273-339, (1980).

Schröter, E.H.: "The Evershed effect in sunspots" in J. Xanthakis (ed) 'Solar Physics' Wiley, p.325-351, (1967).

Serio, S., Peres, G., Vaiana, G.S., Golub, L. and Rosner, R.: "Closed coronal structures. II. Generalised hydrostatic model" Astrophys. J. 243, 288-300, (1981).

Sheeley, N.R., Bohlin, J.D., Brueckner, G.E., Purcell, J.D., Scherrer, V. and Tousey, R.: "XUV observations of coronal magnetic fields" Solar Phys. 40, 103-121, (1975).

Smith, E.A. and Priest, E.R.: "The formation of solar prominences by thermal instability in a current sheet" Solar Phys. 53, 25-40, (1977).

Somov, B.V. and Syrovatskii, S.I.: "Physical processes in the solar atmosphere associated with flares" Sov. Phys. Usp. 19, 813-835, (1976).

Sonnerup, B.U.O.: "Magnetic field reconnection" J. Plasma Phys. 4, 161-174, (1970).

Sonnerup, B.U.O.: "Magnetic field reconnection and particle acceleration" in 'High energy phenomena on the Sun' NASA Symposium p.357-376, (1973).

Soward, A.M. and Priest, E.R.: "Fast magnetic field line reconnection" Phil. Trans. Roy. Soc. A284, 369-417, (1977).

Soward, A.M. and Priest, E.R.: "Fast magnetic field line reconnection in a compressible fluid - I. coplanar field lines" Submitted to J. Plasma Phys. (1982).

Spicer, D.S.: "An unstable arch model of a solar flare" Solar Phys. 53, 305-345, (1977).

Spicer, D.S.: "Non-thermal effects associated with steep temperature gradients in the transition zone" Solar Phys. 62, 269-276, (1979).

Spicer, D.S., and Brown, J.C.: "Solar flare theory" in S. Jordan (ed) 'The Sun as a Star' NASA, p.413-470 (1981).

Spitzer, L.: 'Physics of Fully Ionised Gases' Wiley, (1962).

Sturrock, P.: 'Skylab Workshop on Solar Flares' Colo. Ass. Univ. Press, (1980).

Summers, H.P. and McWhirter, R.W.P.: "Radiative power loss from laboratory and astrophysical plasmas" J. Phys. B 12, 2387-2412, (1979).

Svestka, Z.: 'Solar Flares' D. Reidel, (1976).

Svestka, Z.: "The system of post-flare loops on July 29, 1973" contribution to Skylab workshop on Solar Flares, (1978).

Svestka, Z., Krieger, A.S., Chase, R.C. and Howard, R.: "Transequatorial loops connecting McMath regions 12472 and 12474" Solar Phys. 52, 69-90, (1977).

Tandberg-Hanssen, E.: 'Solar Prominences' D. Reidel, (1974).

Tsinganos, K.C.: "Magnetohydrodynamic equilibrium. 1. exact solutions of the equations" Astrophys. J. 245, 764-782, (1981).

Tur, T.J. and Priest, E.R.: "A trigger mechanism for the emerging flux model of solar flares" Solar Phys. 58, 181-200, (1978).

Vasyliunas, V.M.: "Theoretical models of magnetic field line merging" Revs. Geophys. Space Phys. 13, 303-336, (1975).

Van Hoven, G.: "Simple loop flares: magnetic instabilities" in E.R. Priest (ed) 'Solar Flare Magnetohydrodynamics' Gordon and Breach, p.217-275, (1981).

Vernazza, J.E., Avrett, E.H. and Loeser, R.: "Structure of the solar chromosphere. III. Models of the EUV brightness components of the quiet sun" Astrophys. J. Sup. (1981).

Wragg, M.A. and Priest, E.R.: "The temperature and density structure of coronal loops in hydrostatic equilibrium" Solar Phys. 70, 293-313, (1981).

Wragg, M.A. and Priest, E.R.: "Thermal stability of coronal loops in hydrostatic equilibrium" Paper in preparation, (1982a).

Wragg, M.A. and Priest, E.R.: "Thermally isolated solar coronal loops" Submitted to Solar Phys. (1982b).

Wu, S.T., Kan, L.C., Nakagawa, Y. and Tandberg-Hanssen, E.: "Effect of thermal conduction and radiation on the dynamics of a flaring coronal loop" Solar Phys. 70, 137-148, (1981).

Yang, C.K. and Sonnerup, B.U.C.: "Compressible magnetic field reconnection: a slow-wave model" Astrophys. J. 206, 570-582, (1976).

Yeh, T.: "Subsonic flows in the coronal-interplanetary regions of closed field lines" Solar Phys. 55, 241-250, (1977).

Zirin, H.: "Solar Flares" Vistas in Astronomy, 16, 1-34, (1974).